THE TECTONOMETAMORPHIC AND MAGMATIC EVOLUTION OF THE UPPERMOST UNIT IN THE SOUTHERN AEGEAN (CYCLADES AND CRETE)

Dissertation
zur Erlangung des Doktorgrades
der Naturwissenschaften

vorgelegt beim Fachbereich 11
der Johann Wolfgang Goethe-Universität
in Frankfurt am Main

von
Silviu-Octavian Martha
aus Caransebeş

Frankfurt (2017)
(D 30)

vom Fachbereich 11 Geowissenschaften/Geographie der
Johann Wolfgang Goethe-Universität als Dissertation angenommen.

Dekan:	Prof. Dr Peter Lindner
Gutachter:	Prof. Dr Gernold Zulauf
	Prof. Dr Gotthardt Kowalczyk
Prüfungskomission:	Prof. Dr Horst Marschall
	Prof. Dr Peter Prinz-Grimm

Datum der Disputation: 20. November 2017

Dedicat familiei mele
pentru dragostea și sprijinul lor,
și în special bunicilor mei,
Zaharie Novac (1928–2000)
și
Silvia Novac, născută Banda (1934–2015).

Table of contents

1 Introduction

1.1 Motivation and aims

The southern Aegean lies in the back-arc of the Hellenic Subduction Zone, where the African Plate is subducted beneath the Eurasian Plate. Two orogenic domains are distinguished in this realm on Crete and in the Cyclades that formed during progressive nappe stacking in the Eocene to Miocene following the closure of the Pindos Ocean (e.g. Altherr et al. 1982; Seidel et al. 1982); (1) the Cretan nappe pile and (2) the Attico-Cycladic Complex (Fig. 1.1). Despite differences in the tectonometamorphic evolution, similarities regarding the composition and stratigraphy point to a mutual origin of these domains. A connection between the Cretan nappe pile and the Attico-Cycladic Massif is best expressed in the Uppermost Unit of both domains. Exposures of the Uppermost Unit on Crete and in the Cyclades are homologous (e.g. Reinecke et al. 1982; Bonneau 1984). However, the provenance, the stratigraphy and the tectonometamorphic evolution of the Uppermost Unit in the Cyclades and on Crete are only poorly understood and far from consensus.

The Basal and the Cycladic Blueschist units of the Attico-Cycladic Complex as well as the units of the lower nappe system of the Cretan nappe pile were affected by Late Oligocene to Early Miocene metamorphic events (e.g. Altherr et al. 1982; Seidel et al. 1982; Okrusch & Bröcker 1990; Ring et al. 2001). On the other hand, the Uppermost Unit in the Cyclades and the upper nappe system of the Cretan nappe pile that includes the Uppermost Unit and the non-metamorphic Pindos Unit escaped this event. Apatite fission track ages from the Uppermost and Pindos units on Crete show that the upper Cretan nappe system must already have been at upper crustal levels from at least the Late Eocene / Early Oligocene (Thomson et al. 1998, 1999). The Uppermost Unit should therefore have preserved information on the pre-Late Eocene tectonometamorphic evolution of the Hellenides in the southern Aegean.

The Uppermost Unit on Crete is heterogeneous and consists of several subunits that differ in composition and grade of metamorphic overprint. Exposures of the Uppermost Unit (Fig. 1.1) can be found in central and western Crete but also on the islands of Gavdos and Chrysi south of Crete (e.g. Bonneau 1972; Creutzburg & Seidel 1975; Krahl et al. 1982). The most widespread subunit of the Uppermost Unit is the Asterousia Crystalline Complex consisting of amphibolite facies rocks that are intruded by granitoids. Both the amphibolite facies rocks and the granitoids yielded Maasrichtian to Danian K-Ar biotite and hornblende cooling ages (Baranyi et al. 1975; Lippolt & Baranyi 1976; Seidel et al. 1976, 1981; Koepke & Seidel 1984; Langosch et al. 2000). These K-Ar ages were usually interpreted as cooling from amphibolite facies metamorphism (e.g. Seidel et al. 1981). However, this interpretation does not explain, why granitoids in central Crete are usually foliated, while granitoids in eastern Crete

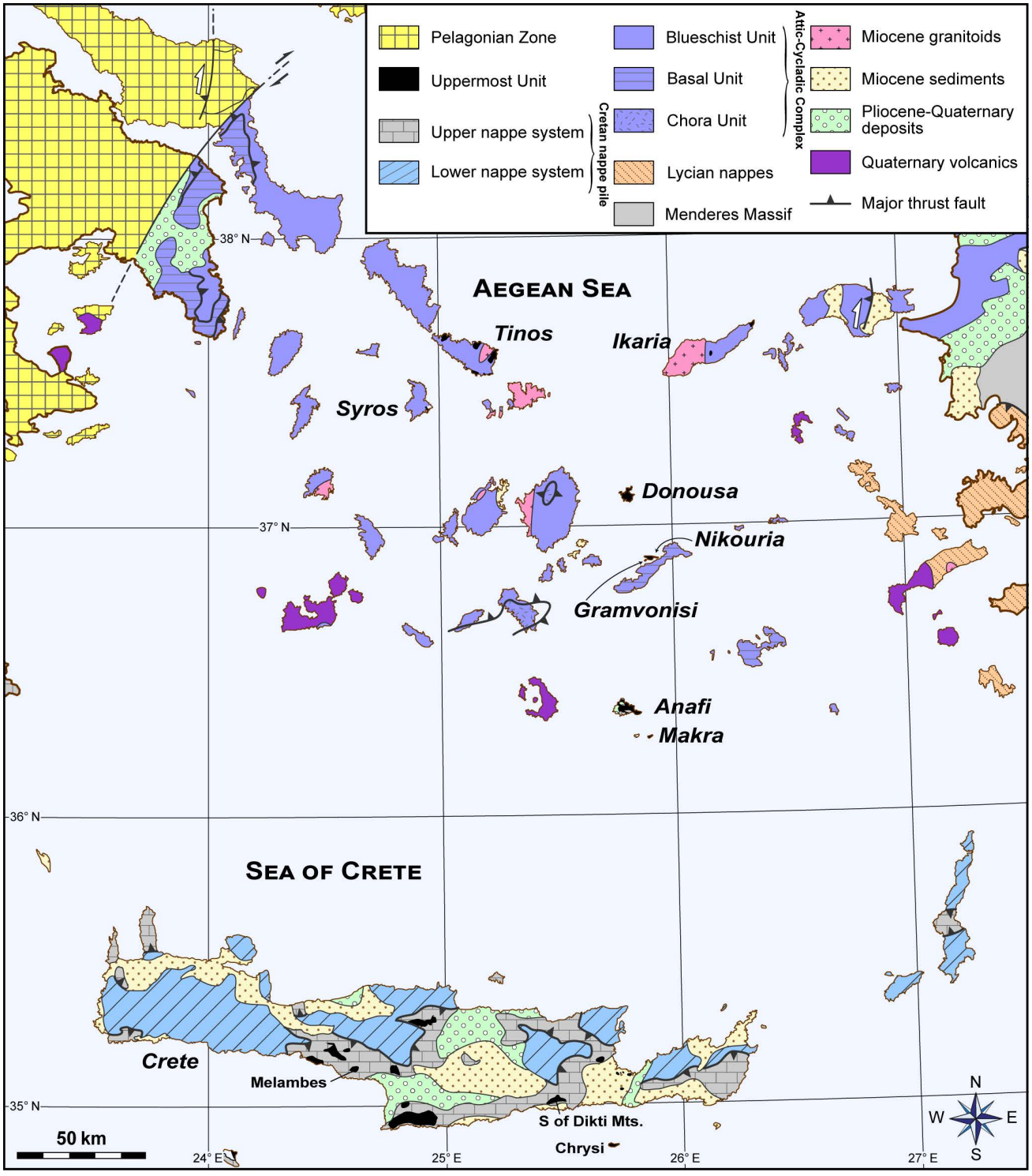

Fig. 1.1 Geological map of the southern Aegean region (modified after Chatzaras et al. 2011) showing exposures assignable to the Uppermost Unit.

lack foliation (e.g. Langosch 1999). Furthermore, the affinity and the tectonometamorphic evolution of the Asterousia Crystalline Complex have only poorly been addressed in previous studies.

In the Cyclades, the Uppermost Unit consists mainly of amphibolite facies metamorphic rocks and granitoid intrusions that were correlated with the Asterousia Crystalline Complex (e.g. Reinecke et al. 1982). Asterousia-type exposures in the Cyclades are reported from the islands of Anafi, Donousa,

Gramvonisi, Ikaria, Makra, Nikouria, Syros and Tinos (Dürr et al. 1978; Altherr et al. 1980; Reinecke et al. 1982; Dürr 1985; Thorbecke 1987). Greenschist facies rocks at the base of the amphibolite facies rocks are known only from the island of Anafi (Reinecke et al. 1982). K-Ar biotite and hornblende ages of metamorphic rocks and granitoids from the Cycladic islands (Dürr et al. 1978; Altherr et al. 1994; Patzak et al. 1994) confirm a correlation with the Asterousia Crystalline Complex on Crete, while K-Ar actinolite ages of greenschist facies rocks from Anafi yield Middle to Late Palaeocene ages (Reinecke et al. 1982).

The provenance of the Uppermost Unit is ambiguous. Hall et al. (1984) suggested the Uppermost Unit to be a large olistostrome within the Late Cretaceous to Eocene Pindos flysch. Tortorici et al. (2012) considered the Uppermost Unit, however, as a remnant of an accretionary wedge complex. The prevelant view believes the Asterousia Crystalline Complex of the Uppermost Unit to be a remnant of the Pelagonian Zone of the Inner Hellenides that has been thrust on top of the Pindos Unit on Crete and on top of the Cycladic Blueschist Unit in the Cyclades (Bonneau 1972, 1982; Reinecke et al. 1982).

The aims of this PhD thesis are to

(1) Decipher the tectonometamorphic evolution of the Asterousia Crystalline Complex and other subunits of the Uppermost Unit in the southern Aegean;

(2) Compare the kinematic and (micro)structural record of exposures of Asterousia-type rock on Crete and in the Cyclades;

(3) Estimate the age of Asterousia-type (meta)igneous intrusions on Crete and in the Cyclades;

(4) Provide a geodynamic model for the early Alpine evolution of the Hellenides in the southern Aegean (mid-Late Cretaceous to Eocene).

To achieve these goals, a multidisciplinary approach of combined structural geology, petrographic and geochronological analyses was applied in several areas, where Asterousia-type rocks crop out.

1.2 Study areas

Fieldwork was carried out in six areas, where Asterousia-type rocks of the Uppermost Unit on Crete and in the Cyclades have been reported by previous authors (Fig. 1.2). These are (1) the island of Anafi; (2) the island of Donousa; (3) the area west of Melambes and (4) the western Asterousia Mountains in central Crete as well as (5) the area of Kritsa and (6) the area between Pefkos, Kalami and Sykologos south of the Dikti Mountains in eastern Crete. Additionally, I had the opportunity to shortly visit Asterrousia-type exposures between Kamares and Magarikari in central Crete and in the area of

Fig. 1.2 Study areas visited in the course of this PhD thesis.

Kalo Chorio and Pachia Ammos in the northern Ierapetra Graben during my field studies. Fieldwork was carried out on Anafi in October 2013 and in the other areas during a three-month ERASMUS-funded project in September to December 2014.

Fieldwork includes sampling, structural mapping and photo documentation. Sampling focused on samples for geochronological analyses (intrusive rocks and metasedimentary rocks) as well as samples for petrographic analyses (metamorphic rocks). For metamorphic rocks, the dip of the foliation, the orientation (up/down) and, where apllicable, the plunge of the mineral/stretching lineation were indicated on the sample, so thin sections could later be produced parallel to the mineral/stretching lineation. Structural measurements include planar (foliation of metamorphic rocks, bedding of flysch, fault planes, shear zones in quartzite, fold planes) and linear (mineral/stretching lineation, slickenside striation, striation on shear zones, fold axes) elements.

In this PhD thesis, the results from three of the areas visited are presented. The areas were chosen carefully as each area represents a different region. The areas considered are the island of Anafi (Cyclades), the area west of Melambes (central Crete) and the area between Pefkos, Kalami and Sykologos south of the Dikti Mountains (eastern Crete), respectively. Taken together and using also published data, a comprehensive overview of the exposures of the Uppermost Unit in the southern Aegean and on the tectonometamorphic and magmatic evolution in the southern Aegean realm during the mid-Late Cretaceous to Late Eocene was achieved. Studies in the areas not considered in this PhD thesis are ongoing.

1.3 Structure of the PhD thesis

The thesis consist of three manuscripts that were submitted to peer-review international journals. One of the manuscripts was published in the *International Journal of Earth Sciences* (chapter 2), while the second manuscript was published in *Gondwana Research* (chapter 3). The third manuscript was submitted to the *Geological Magazine* (chapter 4). The manuscripts address each a different area, where rocks of the Uppermost Unit in the southern Aegean crop out.

In chapter 2, results from the exposures of the Uppermost Unit on the Cycladic island of Anafi (Fig. 1.3) are provided. The new data presented (structural data, petrographic analyses and U-Pb zircon ages) and (re-)evaluation of published data shed some new light on the tectonometamorphic evolution

of the Uppermost Unit in the Cyclades. Granodiorite intrusions inside the Asterousia-type metasediments are shown to have intruded into a magmatic arc setting continuously during the middle to late Campanian. Dykes of monzogranitic composition intruded parts of the succession during the Maastrichtian. Furthermore, it is shown that amphibolite facies metamorphic rocks have been thrust on top of greenschist facies rocks during Palaeocene top-to-the SE mylonitic shearing. Both high-grade and low-grade metamorphic rocks have been thrust on top of Eocene flysch sediments following significant uplift and exhumation under brittle top-to-the SE conditions.

Fig. 1.3 The Rock of Kalamos (470 m) on Anafi consists entirely of marble and is one of the largest monolithic rocks in Europe.

Chapter 3 presents results of studies carried out in the area west of Melambes in central Crete (Fig. 1.4). Field observations, (micro)structural data, petrographic analyses, electron microprobe analysis, electron backscatter diffraction analysis and U-Pb age data show that the exposures of the Uppermost Unit from the study area can be subdivided into two tectonometamorphic subunits. The Uppermost Unit west of Melambes compares well with the exposure on Anafi regarding succession, composition, grade of metamorphic overprint and age of granitoid intrusions inside the amphibolite facies rocks. The new data suggest the existence of an extended magmatic arc along the southern active margin of the Pelagonian-Lycian Block, where the northern part of the Pindos realm was subducted from at least the Santonian. This chapter is the core of this PhD study and presents a new geodynamic model for the tectonometamorphic and magmatic evolution in the southern Aegean realm. Top-to-the SE is shown to have been the dominant shear sense in the southern Aegean from at least the mid-Late Cretaceous until the Late Eocene.

Fig. 1.4 Orthogneiss exposure near the Sotiras chapel west of Melambes.

The Uppermost Unit in the Viannos Municipality between the villages Pefkos, Kalami and Sykologos in eastern Crete (Fig. 1.5) is the focus in chapter 4. Except for greenschist and amphibolite facies rocks, we also studied prehnite-pumpellyite facies rocks assignable to the Arvi Unit. Granitoid intrusions were not observed in the field. However, the occurrence of contact metamorphic chiastolite hornfels with metamorphic grown zircon yielding comparable ages to those obtained from Anafi and west of Malambes indicates the existence of a non-exposed pluton that was probably eroded. The amphibolite facies rocks show evidence for three deformation stages. Our results further suggest that the Uppermost Unit must have been at shallower structural levels in eastern Crete than on Anafi and west of Melambes following amphibolite facies overprint.

Fig. 1.5 View on Kalami and on the Arvi Unit from thr cemetery east of Kalami. Arvi basalt is visible on the bottom right.

Finally, in chapter 5, a summary of this PhD thesis along with an outlook for future research possibilities is provided and in chapter 6, a German translation of chapter 5 is provided. The appendix contains conference abstracts related to this PhD thesis and tables with field data from the three research areas.

Chapter 3 and 4 contain geological maps of the study areas that were produced by Maximilian Fischer and Bastian Wiesenbach (chapter 3) and Jannes J. Binck and Patrick M. Nowara (chapter 4), respectively. Samples mentioned in chapter 3 that are labelled Mel… were collected by Fischer and Wiesenbach, while sample Do513 was collected by Wolfgang Dörr. Thin sections from samples labelled Mel… and described in Wiesenbach (2014) were reproduced and re-examined as the original thin sections were not available. Samples labelled PKS… in chapter 4 were collected by Binck and Nowara, who also produced thin sections of these samples. However, thin section analysis and all other analyses performed on samples labelled PKS… have been conducted by the author of this PhD thesis. The structural data presented in chapter 4 (Figs. 4.2 and 4.3) also uses data collected by Binck and Nowara. However, most of the structural data was collected by the author of this PhD thesis (see appendix B3).

1.4 Conference contributions

During this PhD, four contributions related to this PhD thesis have been made at international conferences, the abstracts of all of which have been published in the abstract volumes of the conferences. The conference abstracts can be found in Appendix A.

Martha, S.O., Binck, J.J., Dörr, W., Gerdes, A., Linckens, J., Nowara, P.M., Xypolias, P. & Zulauf, G. (2016): A Late Cretaceous magmatic arc in the southern Aegean (Crete and Cyclades): constraints on the tectonometamorphic and magmatic evolution of the internal Hellenides. – In: Ortner, H. (ed.): *Abstract volume of GeoTirol2016 – Annual meeting of DGGV and PANGEO Austria, 25–28 September 2016, Innsbruck*, p. 197. Talk.

Martha, S.O., Dörr, W., Linckens, J., Wiesenbach, B. & Zulauf, G. (2016): Structural and U-Pb zircon data from the Asterousia Crystalline Complex of central Crete: Insights on the evolution of the Eastern Mediterranean. – In: Froitzheim, N., Keppler, R., Kleinschrodt, R. McCann, T. & Ballhaus, C. (eds.): *16th Symposium Tectonics – Structural Geology – Crystalline Geology*, p. 34. DOI: 10.13140/RG.2.1.3756.7126. Talk.

Martha, S.O., Zulauf, G., Dörr, W., Xypolias, P., Petschick, R. & Schastok, J. (2015): The Asterousia Crystalline Complex in the Aegean region: insights from structural analyses and U-Pb zircon dating on Anafi Island (Cyclades, Greece). – In: Wagner, J., Elger, K. (eds.) *GeoBerlin2015 – Dynamic Earth from Alfred Wegener to today and beyond – Abstracts. Annual meeting of DGGV and DMG, 4–7 October 2015*. p. 253; Berlin. DOI: 10.2312/GFZ.LIS.2015.003. Talk.

Wiesenbach, B., Martha, S.O., Dörr, Wolfgang, Petschick, R., Xypolias, P. & Zulauf, G. (2014): Structural evolution and kinematics of Pelagonian-type crystalline rocks of central Crete and Anafi Island. – In: Röhling, H.-G. & Zulauf, G. (eds.): GeoFrankfurt 2014 – Dynamik des Systems Erde / Earth Science Dynamics. Abstract volume. – *Schriftenreihe der Deutschen Gesellschaft für Geowissenschaften*, **85**: p. 592. Poster.

1.5 References

Altherr, R., Kreuzer, H., Lenz, H., Wendt, I., Harre, W. & Dürr, S. (1994): Further evidence for a Late-Cretaceous low pressure/high-temperature terrane in the Cyclades, Greece. Petrology and geochronology of crystalline rocks from the islands of Donoussa and Ikaria. – *Chemie der Erde*, **54**: pp. 319–328.

Altherr, R., Kreuzer, H., Wendt, I., Lenz, H., Wagner, G.A., Keller, J., Harre, W. & Höhndorf, A. (1982): A Late Oligocene/Early Miocene high temperature belt in the Attic-Cycladic Crystalline Complex (SE Pelagonian, Greece). – *Geologisches Jahrbuch, Reihe E*, **23**: pp. 97–164.

Altherr, R., Seidel, E., Okrusch, M., Schliestedt, M., Reinecke, T., Kreuzer, H., Harre, W., Klein, H. & Dürr, S. (1980): Metamorphic rocks associated with ophiolites in Greece: petrology and geochronology. – In: Panayiotou, A. (ed.) *International Ophiolite Symposium, Nicosia - Cyprus, 1–8 April, 1979. Abstracts of papers submitted*. Τμήμα Γεωλογικής Επισκόπησης [Geological Survey Department], pp. 9–10; Λευκωσία [Nicosia].

Baranyi, I., Lippolt, H.J. & Todt, W. (1975): Kalium-Argon-Datierungen an zwei Magmatiten von Kalo Chorio, Nord-Ost-Kreta. – *Neues Jahrbuch für Geologie und Paläontologie, Monatshefte*, **5**: pp. 257–262.

Bonneau, M. (1972): La nappe métamorphique de l'Asteroussia, lambeau d'affinités pélagoniennes charrié jusque sur la zone de Tripolitza de la Crète moyenne (Grèce). – *Comptes Rendus de l'Académie des Sciences, série D*, **275**: pp. 2303–2306.

Bonneau, M. (1982): Évolution géodynamique de l'arc égéen depuis le Jurassique supérieur jusqu'au Miocène. – *Bulletin de la Société Géologique de France, série 7*, **24** (2): pp. 229–242.

Bonneau, M. (1984): Correlation of the Hellenide nappes in the south-east Aegean and their tectonic reconstruction. – *Geological Society, London, Special Publications*, **17**: pp. 517–527. DOI: 10.1144/GSL.SP.1984.017.01.38.

Creutzburg, N. & Seidel, E. (1975): Zum Stand der Geologie des Präneogens auf Kreta. – *Neues Jahrbuch für Geologie und Paläontologie, Abhandlungen*, **149** (3): pp. 363–383.

Dürr, S. (1985): *Γεωλογικός χάρτης της Ελλάδος 1:50.000. Φύλλο Αμοργός–Δονούσα [Geological map of Greece 1:50,000. Amorgos–Donoussa sheet]*. – Geological map, Ινστιτούτο γεωλογικών και μεταλλεύτικων έρευνων [Institute of Geology and Mineral Exploration]; Αθήνα [Athens]

Dürr, S., Seidel, E., Kreuzer, H. & Harre, W. (1978): Témoins d'un métamorphisme d'âge crétacé supérieur dans l'Égéide: datations radiométriques de minéraux provenant de l'île de Nikouriá (Cyclades, Grèce). – *Bulletin de la Société Géologique de France, série 7*, **20** (2): pp. 209–213.

Hall, R., Audley-Charles, M.G. & Carter, D.J. (1984): The significance of Crete for the evolution of the Eastern Mediterranean. – *Geological Society, London, Special Publications*, **17** (1): pp. 499–516. DOI: 10.1144/GSL.SP.1984.017.01.37.

Koepke, J. & Seidel, E. (1984): Oberkretazisches Kristallin an der Basis von Ophiolithen der Südägäis: Charakterisierung der Metamorphose-Fazies. – *Tschermaks Mineralogische und Petrographische Mitteilungen*, **33** (4): pp. 263–286. DOI: 10.1007/BF01082673.

Krahl, J., Herbart, H. & Katzenberger, S. (1982): Subdivision of the allochthonous "ophiolites"-bearing formation upon the Pindos Group, southwestern part of central Crete, Greece. *International Symposium on the Hellenic Arc and Trench (H.E.A.T.). April 8–10. 1981, Athens. Proceedings. Volume 1*. Εθνικό Μετσόβιο Πολυτεχνείο [Ethnikó Metsóvio Polytechneío], pp. 324–341; Αθήνα [Athens].

Langosch, A. (1999): *Petrologie der plutonischen Gesteine im oberkretazischen Hochtemperaturkrisallin der Insel Kreta*. – Tectum, 201 p.; Marburg

Langosch, A., Seidel, E., Stosch, H.-G. & Okrusch, M. (2000): Intrusive rocks in the ophiolitic mélange of Crete – Witnesses to a Late Cretaceous thermal event of enigmatic geological position. – *Contributions to Mineralogy and Petrology*, **139** (3): pp. 339–355. DOI: 10.1007/s004100000136.

Lippolt, H.J. & Baranyi, I. (1976): Oberkretazische Biotit- und Gesteinsalter aus Kreta. – *Neues Jahrbuch für Geologie und Paläontologie, Monatshefte*, **7**: pp. 405–414.

Okrusch, M. & Bröcker, M. (1990): Eclogites associated with high-grade blueschists in the Cyclades archipelago, Greece: a review. – *European Journal of Mineralogy*, **2** (4): pp. 451–478. DOI: 10.1127/ejm/2/4/0451.

Patzak, M., Okrusch, M. & Kreuzer, H. (1994): The Akrotiri unit on the island of Tinos, Cyclades, Greece: witness to a lost terrane of Late Cretaceous age. – *Neues Jahrbuch für Geologie und Paläontologie, Abhandlungen*, **194**: pp. 211–252.

Reinecke, T., Altherr, R., Hartung, B., Hatzipanagiotou, K., Kreuzer, H., Harre, W., Klein, H., Keller, J., Geenen, E. & Böger, H. (1982): Remnants of a Late Cretaceous high temperature belt on the island of Anafi (Cyclades, Greece). – *Neues Jahrbuch für Mineralogie, Abhandlungen*, **145** (2): pp. 157–182.

Ring, U., Layer, P.W. & Reischmann, T. (2001): Miocene high-pressure metamorphism in the Cyclades and Crete, Aegean Sea, Greece: Evidence for large-magnitude displacement on the Cretan detachment. – *Geology*, **29** (5): pp. 395–398. DOI: 10.1130/0091-7613(2001)029<0395:MHPMIT>2.0.CO;2.

Seidel, E., Kreuzer, H. & Harre, W. (1982): A Late Oligocene/Early Miocene high pressure belt in the external Hellenides. – *Geologisches Jahrbuch, Reihe E*, **23**: pp. 165–206.

Seidel, E., Okrusch, M., Kreuzer, H., Raschka, H. & Harre, W. (1976): Eo-Alpine metamorphism in the Uppermost Unit of the Cretan nappe system – petrology and geochronology. Part 1. The Léndas area (Asteroúsia Mountains). – *Contributions to Mineralogy and Petrology*, **57** (3): pp. 259–275.

Seidel, E., Okrusch, M., Kreuzer, H., Raschka, H. & Harre, W. (1981): Eo-Alpine metamorphism in the Uppermost Unit of the Cretan nappe system – petrology and geochronology. Part 2. Synopsis of high-temperature metamorphics and associated ophiolites. – *Contributions to Mineralogy and Petrology*, **76** (3): pp. 351–361. DOI: 10.1007/BF00375462.

Thomson, S.N., Stöckhert, B. & Brix, M.R. (1999): Miocene high-pressure metamorphic rocks of Crete, Greece: rapid exhumation by buoyant escape. – *Geological Society, London, Special Publications*, **154** (1): pp. 87–107. DOI: 10.1144/GSL.SP.1999.154.01.04.

Thomson, S.N., Stöckhert, B., Rauche, H. & Brix, M.R. (1998): Apatite fission-track thermochronology of the Uppermost Tectonic Unit of Crete, Greece: implications for the post-Eocene tectonic evolution of the Hellenic Subduction System. – In: van den Haute, P., de Corte, F. (eds.) *Advances in Fission-Track Geochronology*. – Solid Earth Sciences Library, **10**: pp. 187–205.

Thorbecke, G. (1987): *Die Zonengliederung der ägäischen Helleniden und westlichen Tauriden*. – Gesellschaft der Geologie- und Bergbaustudenten in Österreich, 161 p.; Wien

Tortorici, L., Catalano, S., Cirrincione, R. & Tortorici, G. (2012): The Cretan ophiolite-bearing mélange (Greece): a remnant of Alpine accretionary wedge. – *Tectonophysics*, **568**–**569**: pp. 320–334. DOI: 10.1016/j.tecto.2011.08.022.

Wiesenbach, B. (2014): *Kartierung und strukturgeologische Untersuchung des Asteroussia-Kristallins NW von Melambes (Westteil), Kreta*. – Master thesis, Goethe-Universität Frankfurt am Main, 105 p. (unpubl.); Frankfurt am Main

2 New structural and U-Pb zircon data from Anafi crystalline basement (Cyclades, Greece): constraints on the evolution of a Late Cretaceous magmatic arc in the Internal Hellenides

Silviu O. Martha[1], Wolfgang Dörr[1], Axel Gerdes[1], Rainer Petschick[1], Janina Schastok[1], Paraskevas Xypolias[2], Gernold Zulauf[1]

[1]Institut für Geowissenschaften, Goethe-Universität Frankfurt, Altenhöferallee 1, 60438 Frankfurt am Main, Germany. E-mail: s.martha@em.uni-frankfurt.de, w.doerr@em.uni-frankfurt.de, gerdes@em.uni-frankfurt.de, petschick@em.uni-frankfurt.de, schastok@em.uni-frankfurt.de, g.zulauf@em.uni-frankfurt.de

[2]Department of Geology, University of Patras, 26500, Patras, Greece. E-mail: p.xypolias@upatras.gr

Keywords: Anafi • Cyclades • Asterousia Crystalline Complex • Uppermost Unit • U-Pb dating • Structural geology

Published in: *International Journal of Earth Sciences*, **105** (7): pp. 2031–2060. DOI: 10.1007/s00531-016-1346-8.

2.1 Abstract

The Asterousia Crystalline Complex consists of Late Cretaceous amphibolite facies metamorphic rocks and associated granitoids, which can be found in exposures on Crete and the Cyclades (Greece). It is attributed to the Uppermost Unit and therefore to the Pelagonian domain of the Internal Hellenides. The tectonometamorphic evolution of this unit is still a matter of debate. We present new structural and petrological data of Asterousia-type rocks and greenschist facies metamorphic rocks from the island of Anafi in the southern Aegean Sea as well as U–Pb zircon ages of granitoids from Anafi. The crystalline sequence of Anafi rests on top of Eocene flysch and comprises from bottom to top: (a) Anafi Greenschist; (b) Anafi Amphibolite Group (orthoamphibolite with intercalations of metasedimentary rocks at the base); and (c) Chalepa Group (amphibolite facies metasediments with slices of serpentinite and granitoids). LA-ICP-MS and ID-TIMS $^{206}Pb/^{238}U$ zircon ages of granodiorite from the Chalepa Group reveal several similar zircon populations suggesting continuous emplacement of granitoids inside a magmatic arc from ca. 72.5 to 79 Ma. The minimum emplacement age of granodioritic magma, deduced from the $^{206}Pb/^{238}U$ median age of the youngest zircon population, is 72.6 +0.1/−0.2 Ma. Deformation (micro)fabrics of granodiorite result from low strain obtained at T > 600 °C. This along with the U–Pb ages and published K–Ar ages indicates intrusion of the plutonic rocks at deep structural levels followed by very slow cooling. Monzogranitic dykes cutting through granodiorite in north-eastern Anafi are undeformed and yielded a $^{206}Pb/^{238}U$ median age of 69.9 +0.7/−0.7 Ma. Based on the new and published data, the following implications for the tectonometamorphic evolution on Anafi can be made: (1) obduction and accretion of mantle slices (serpentinite) to the Asterousia-type rocks were prior to amphibolite facies metamorphism; (2) intrusion of granitoids during the middle to late Campanian within a magmatic-arc setting and coeval shift of the magmatic arc towards the south; (3) Maastrichtian intrusion of dykes; (4) Palaeocene greenschist facies metamorphism and coeval ductile top-to-the SE thrusting of the Anafi Amphibolite Group on top of the Anafi Greenschist; (5) post-Eocene brittle top-to-the SE thrusting of the Anafi Greenschist and the Anafi Amphibolite Group on top of flysch sediments; (6) clockwise rotation of the system and (Early) Oligocene brittle top-to-the SE thrusting of the Chalepa Group on top of all units mentioned above; and (7) ongoing clockwise rotation of the Aegean block during the Oligocene to early Miocene and change in stress field (NE–SW compression).

2.2 Introduction

The Cyclades in the central-south Aegean region (Fig. 2.1) consist of a stack of nappes that were assembled during Eocene to Oligocene compressive phases (Avigad et al. 1997). Crystalline rocks that

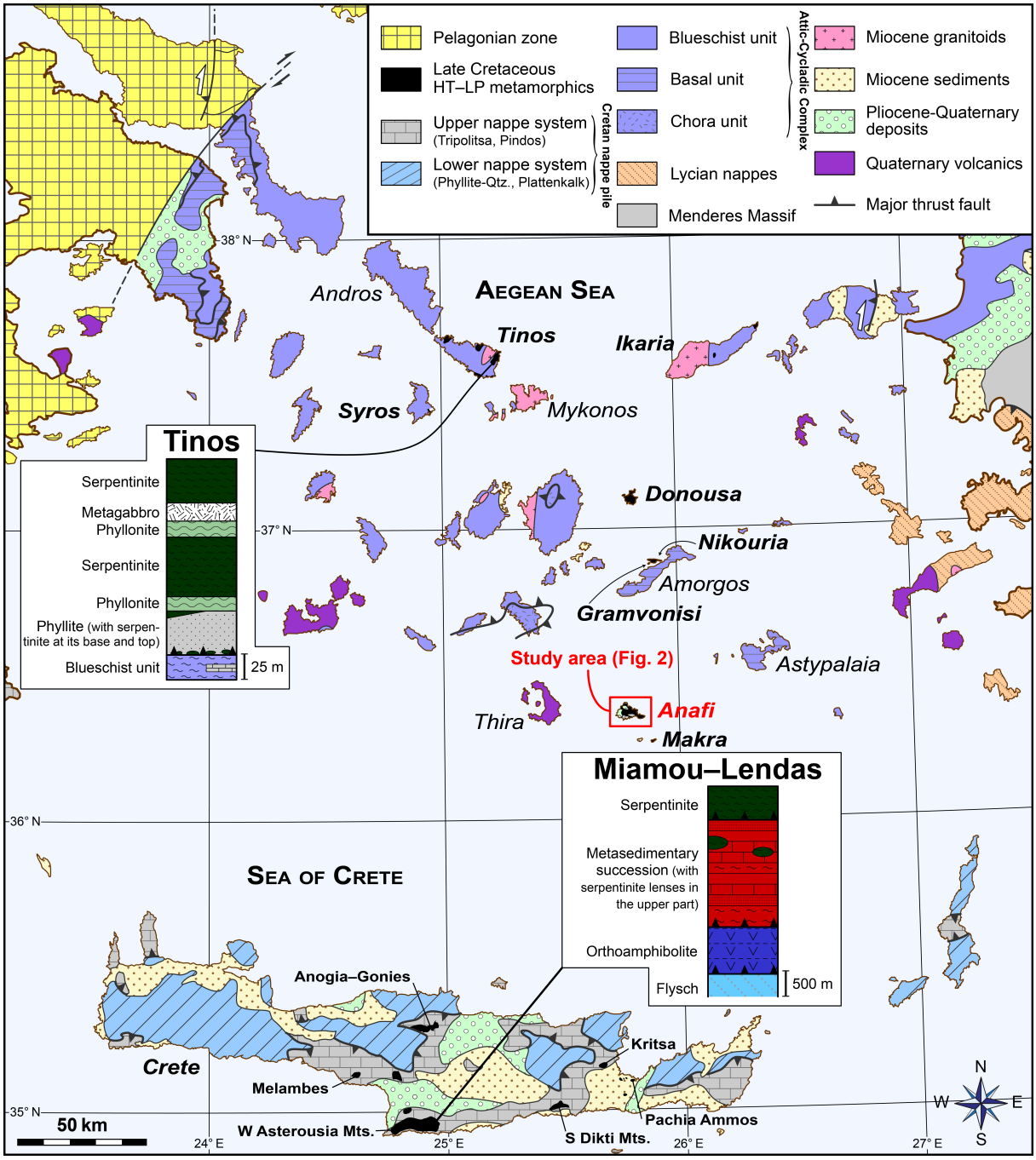

Fig. 2.1 Geological map of the southern Aegean region (modified after Chatzaras et al. 2011). Tectonostratigraphic columns show the succession of the Asterousia Crystalline Complex between Miamou and Lendas in the Asterousia Mts. (after Koepke and Seidel 1984).

underwent Late Cretaceous to Middle Palaeocene high-temperature (HT)–low-pressure (LP) metamorphism and related felsic magmatic rocks are compiled within the so-called Upper Unit (e.g. Dürr et al. 1978a, b; Reinecke et al. 1982; Dürr 1985; Maluski et al. 1987; Altherr et al. 1994; Patzak et al. 1994; Be'eri-Shlevin et al. 2009). The crystalline rocks of the Upper Unit display oceanic and continental affinities and rest tectonically on top of the Cycladic Blueschist Unit occupying the higher structural levels in the nappe pile of the Attic–Cycladic Complex (e.g. Okrusch and Bröcker 1990).

The Upper Unit escaped regional Eocene high-pressure (HP)–low-temperature (LT) metamorphism (Altherr et al. 1979) that affected the other parts of the Attic–Cycladic Complex.

Several workers have proposed that the HT–LP metamorphic rocks of the Cyclades are equivalent to the Asterousia Crystalline Complex of the Uppermost Unit on Crete. The Uppermost Unit is thrust on top of weakly or non-metamorphic rocks of the Cretan nappe pile (i.e. Pindos Unit and Tripolitsa Unit, e.g. Dürr et al. 1978a; Seidel et al. 1981; Reinecke et al. 1982; Bonneau 1984; Altherr et al. 1994; Langosch et al. 2000; Be'eri-Shlevin et al. 2009). In this tectonic context, the Uppermost Unit is considered to belong to the upper plate of the Alpine subduction system in the Aegean region (Bonneau 1984). The rolling back of the subduction zone caused the accretion and the bulk southward translation of Hellenic nappes and was accomplished by the progressive migration of the orogenic front from the north-central Aegean in Late Cretaceous to Eocene times to the south Aegean in Eocene to Miocene times (e.g. Jolivet and Brun 2010). The structural evolution of the Uppermost Unit, especially in the Cyclades, is only poorly understood. This is mainly due to the scarce and limited exposures of the unit in this area and the frequent extensional reworking of the original contact between the Upper Unit and the Cycladic Blueschist Unit.

Pe-Piper and Photiades (2006) and Be'eri-Shlevin et al. (2009) emphasized significant differences in geochemistry, geochronology and metamorphic grade between HT– LP metamorphic rocks of the Upper Unit in the northern (Ikaria, Syros, Tinos; Fig. 2.1) and the southern (Anafi, Donousa, Gramvonisi, Makra, Nikouria; Fig. 2.1) Cyclades. However, the reasons for these differences remain unknown. Furthermore, different interpretations have been proposed for the parent lithotectonic terrane of the Uppermost Unit both in the Cyclades and on Crete. The prevailing view, based primarily on the structural position of the Uppermost Unit as well as on the presence of Late Jurassic ophiolitic bodies, supports a Pelagonian affinity (e.g. Aubouin and Dercourt 1965; Bonneau 1972, 1984; Tortorici et al. 2012). However, the lack of Late Cretaceous magmatism and HT–LP metamorphism in the counterpart Pelagonian massif of mainland Greece put in question this interpretation and point to a correlation of the Uppermost Unit with the Late Cretaceous magmatic arc complexes of northern Turkey (Be'eri-Shlevin et al. 2009).

The present study is focusing on the structural evolution, kinematics and timing of orogenic events as recorded in different types of crystalline rocks exposed on the Cycladic island of Anafi (Fig. 2.2). These rocks prove to be a key in understanding the tectonometamorphic evolution of the upper parts of the Hellenic nappes. For this purpose, we present herein (1) new (micro)structural data from greenschist and amphibolite facies metamorphic rocks, (2) petrographic and XRD data of crystalline rocks and (3) U–Pb ages of zircon separated from granodiorite and monzogranitic dykes.

2.3 Regional Geology

2.3.1 Geological outline of Anafi

Melidonis (1963) provided an account of the geology of Anafi and produced the first detailed geological map, which was revised by Reinecke et al. (1982). According to Reinecke et al. (1982), four main tectonically stacked lithological units can be distinguished, which, from structurally lowest to highest level, are: (a) a flysch formation; (b) a monotonous series of greenschist; (c) a tectonic mélange made up of HT–LP metamorphic rocks, slices of ultramafic rocks, marble, and granitic to dioritic intrusive rocks; and d) Late Miocene (?) to Pleistocene sedimentary deposits (Fig. 2.2).

The *flysch formation* is of Eocene age (Melidonis 1963) and consists of conglomerate, shale, pelite, limy siltstone, and sandstone to greywacke. Blocks of serpentinite occur sporadically throughout the formation, whereas olistostromes and steeply dipping limestone, referred to as 'marbles of Kastelli' (Reinecke et al. 1982), occur in the upper parts. Reinecke et al. (1982) regarded the flysch as probably belonging to one of the flysch sequences of the units below the Asterousia Crystalline Complex on Crete (i.e. Pindos Unit or Tripolitsa Unit; see below), while Soukis and Papanikolaou (2004) correlated it to flysch deposits exposed on Thira and Astypalaia.

Greenschist on top of the flysch sequence is very fine-grained and results from basic volcanic rocks with a mid-ocean ridge basalt (MORB)-type signature (Reinecke et al. 1982). The age of the greenschist facies metamorphism is Middle to Late Palaeocene based on K–Ar ages of actinolite (Reinecke et al. 1982). The provenance of the greenschist is questionable. Reinecke et al. (1982) suggested a correlation with greenschist on Mykonos, while Bonneau (1984) related them with the Arvi Unit on Crete.

The *tectonic mélange* sensu Reinecke et al. (1982) on top of the greenschist is composed of HT–LP metamorphic rocks, marble, granitoids and serpentinized ultramafic rocks. It is regarded as remnants of a Late Cretaceous high-temperature belt, i.e. the Asterousia Crystalline Complex (Reinecke et al. 1982). Reinecke et al. (1982) divided the tectonic mélange into six subunits, which, in structural ascending order, are: (a) massive to strongly foliated, dark orthoamphibolite with chemical affinities to back-arc basin tholeiites and minor intercalations of quartzite, calcsilicate rock and micaschist at the base; (b) slices of variegated HT–LP metamorphic rocks including calcsilicate rock, quartzite, gneiss, micaschist, banded amphibolite and marble; (c) hornblende diorite with cognate inclusions; (d) serpentinized ultramafic rocks, partly cut by plagiogranitic dykes; (e) metachert-bearing marble and gneiss intercalated with amphibolite and calcsilicate rock, intruded by granitoids that are cut by S-type aplitic and pegmatitic dykes in north-eastern Anafi; and (f) white, massive marble on the Kalamos Peninsula (south-eastern Anafi). K–Ar dating of biotite (63.5 ± 0.5 to 65.1 ± 0.6 Ma) and hornblende (65.9 ± 0.5 to 69.3 ± 2.2 Ma) separated from orthoamphibolite and granitoids of the tectonic mélange

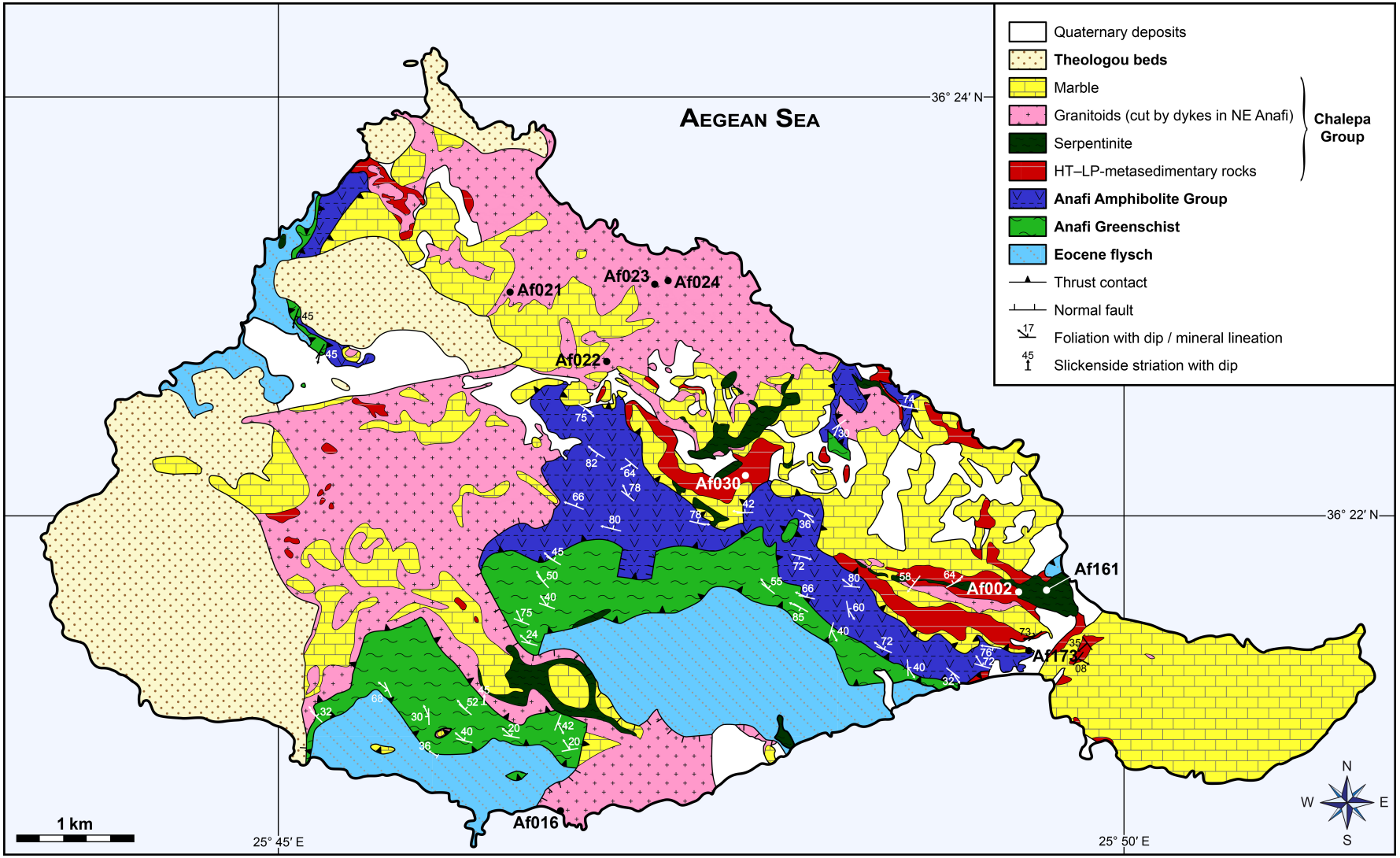

Fig. 2.2 Geological map of Anafi (modified after Reinecke et al. 1982) summarizing structural data (foliation and mineral/stretching lineation of crystalline rocks and slickenside striation) and showing location of samples of igneous rocks and of samples collect.

revealed that cooling of these rocks occurred contemporaneously during the Latest Cretaceous to Early Palaeogene (Reinecke et al. 1982). Be'eri-Shlevin et al. (2009) reported intrusion ages for the granitoids at 85.3 ± 2.7 Ma (U–Pb on zircon; ID-TIMS) and Rb–Sr ages on biotite and plagioclase at 63.4 ± 0.4 Ma and 48.2 ± 0.3 Ma, respectively. They attributed the Rb–Sr ages to deformation of the granitoids and related partial resetting of the Rb–Sr isotopic system. Both the geochemical and the mineralogical composition of the Anafi plutonic rocks reveal that the latter have been involved in subduction processes (Koutsovitis et al. 2012). Serpentinite within the tectonic mélange was also affected by HT–LP metamorphism as indicated by spinel chemistry analyses (Be'eri-Shlevin et al. 2009).

The *molasse-like (Late) Miocene to Pleistocene sedimentary deposits* (termed '*Theologou beds*' according to Philippson 1901) unconformably overlie all other units and consist of fluvio-lacustrine limy to marly clastic sediments with intercalations of brackish marls. Pre-Neogene components within the Theologou beds could not be correlated with any of the underlying units. Böger (1983) discussed the possibility that the Theologou beds are allochthonous.

Reinecke et al. (1982; their fig. 2) regarded the contacts of the four main units as thrusts, while strike-slip faults are partly present between the Theologou beds and the underlying units. However, structural and kinematic data for the inferred thrusting and strike-slip movements are entirely lacking. Soukis and Papanikolaou (2004) suggested three deformation phases for the evolution of Anafi: (a) Oligocene to Early Miocene SSW-directed brittle thrusting of the crystalline rocks on top of the flysch; (b) Middle to Late Miocene low-angle normal faulting that caused the emplacement of the Theologou beds onto the other units; and (c) Late Miocene to Pliocene high-angle normal faulting that affected all units of Anafi.

Four islands south of Anafi consist of sediments assigned to the Theologou beds (Pachia; Melidonis 1963); marble (Ftena islets; Melidonis 1963); and various micaschists and amphibolite interbedded with thin marble (Makra; Melidonis 1963). Granitoids occur in south-western Makra (Elsner 1981). Based on thin section analyses, Thorbecke (1987) assigned the crystalline rocks of Makra to the Asterousia Crystalline Complex.

2.3.2 HT–LP metamorphic and igneous rocks in the southern Aegean domain

The *Upper Unit* of the Attic–Cycladic Complex crops out as klippen and consists of HT–LP (P = 6.5–7.5 kbar, T = 530–610 °C; Patzak et al. 1994 for Tinos) paragneiss, micaschist, calcsilicate rock, interlayered with (para) amphibolite, serpentinite and unmetamorphosed granitoids in association with marble (e.g. Bonneau et al. 1980; Reinecke et al. 1982). Rocks of the Upper Unit are exposed on the islands of Anafi (Reinecke et al. 1982), Donousa (Altherr et al. 1980), Gramvonisi (Dürr 1985), Ikaria (Altherr et al. 1994), Makra (Thorbecke 1987), Nikouria (Dürr et al. 1978b), Syros (Bonneau et al.

1980) and Tinos (Patzak et al. 1994). Rocks of the Makrotantalon Unit in northern Andros, previously correlated with the Upper Unit (Bröcker and Franz 2006), show evidence for HP–LT metamorphism (Huyskens and Bröcker 2014). In turn, the Upper Unit escaped Eocene HP–LT metamorphism that affected the Cycladic Blueschist Unit underneath.

The *Cycladic Blueschist Unit* consists of metasediments, metavolcanics and metaophiolite (Okrusch and Bröcker 1990), which display evidence for at least two metamorphic events: (1) an Eocene blueschist to eclogite facies event (P = 12–20 kbar, T = 450–500 °C; Okrusch and Bröcker 1990), and (2) a Late Oligocene to Early Miocene retrograde overprint under greenschist to amphibolite facies conditions (P = 4–7 kbar, T = 400 ± 50 °C; Altherr et al. 1979; Wijbrans and McDougall 1986). Pre-Alpine rocks at the base of the Blueschist Unit are referred to as Chora Unit (Bonneau 1984). The Blueschist Unit has been thrust on top of the Basal Unit (Fig. 2.1). The Basal Unit consists of marble with schist intercalations and an Eocene metafl affected by blueschist facies metamorphism (P = 8–10 kbar, T ~ 350 °C; Shaked et al. 2000).

On Crete, HT–LP metamorphic and associated plutonic rocks are present in the Asterousia Crystalline Complex, which represents a subunit of the Uppermost Unit of the Cretan nappe stack. The Uppermost Unit rests on top of the Pindos Unit or the Tripolitsa Unit. All these units occupy the upper system of the Cretan nappe pile. The *Uppermost Unit* consists of several low-grade metamorphic subunits and one high-grade metamorphic subunit (=Asterousia Crystalline Complex).

The *Asterousia Crystalline Complex* of central and eastern Crete consists of amphibolite, calcsilicate rock, gneiss, metabasite, (partly metamorphosed) plutonic rocks, metapelite, quartzite, (mica)schist and slices of serpentinized ophiolite (Bonneau 1972). Seidel et al. (1981) determined upper amphibolite facies conditions (P = 4–5 kbar; T ≈ 700 °C) and obtained Latest Cretaceous K–Ar biotite, hornblende and muscovite cooling ages. Evidence for an igneous event during the Latest Cretaceous in rocks of the Asterousia Crystalline Complex has been reported from eastern Crete (e.g. Baranyi et al. 1975; Kneuker et al. 2015). Kneuker et al. (2015) showed that the melt in eastern Crete should have intruded and cooled down at upper structural levels.

A profile through the Asterousia Crystalline Complex in the type section in the western Asterousia Mountains between Lendas and Miamou (Fig. 2.1) shows orthoamphibolite at the base, overlain by metasedimentary rocks with intercalations of serpentinized mafic rocks in the upper parts (Koepke and Seidel 1984). There are striking differences compared with a profile section of the Upper Unit on Tinos (Fig. 2.1). Several *low-grade metamorphic subunits* have been proposed for the Uppermost Unit. Serpentinite intruded by gabbroic to plagiogranitic dykes during the Middle Jurassic (Seidel et al. 1981; Koepke et al. 2002) are usually considered as the structurally highest subunit (the '*nappe des serpen-*

tines' sensu Bonneau 1972). Krahl et al. (1982) distinguished three 'ophiolite'-bearing subunits (including the above-mentioned serpentinite) consisting of weakly metamorphosed limestone, cherty limestone, radiolarite, fl sediments and serpentinite (Vatos Unit), serpentinite containing gabbroic dykes and slices of amphibolite (Spili Unit), and blueschist facies metasediments and marble (Preveli Unit). The Kalypso Unit (Seidel et al. 1977) on Gavdos and the Miamou Unit (Bonneau et al. 1974) in the northern Asterousia Mountains were correlated with the Preveli Unit and the Vatos Unit, respectively (Krahl et al. 1982). A fourth low-grade metamorphic subunit, the Arvi Unit, consists of LT–LP-metamorphosed red pelagic limestone, basalt and fl sediments (Bonneau 1973; Robert and Bonneau 1982). Tortorici et al. (2012) regarded the ophiolite-bearing units as a wedge at the base of the Asterousia Crystalline Complex, which should have been accreted to the base of the upper plate (Pelagonian continental margin) during Palaeogene subduction.

2.4 Material and methods

2.4.1 Sampling, structural analyses, microfabrics, and XRD analyses

For field survey, we used the geological map provided by Reinecke et al. (1982). Geographic details given herein are based on the 1:15 000 Terrain hiking map of Michos et al. (2010). In order to date the timing of granitoid intrusions and detrital zircon and titanite, we collected seven samples for U-Pb age dating on zircon, all of which are from the Chalepa Group and each about five to ten kilograms (Fig. 2.2, Table 2.1). U-Pb age dating on three samples failed because one sample of anorthosite from a dyke cutting serpentinite in southeastern Anafi (Af161) and samples of calcsilicate rock (Af002) and impure quartzite (Af030), both collected from the amphibolite facies metasediments, did not contain (enough) zircon. U-Pb dating on titanite of sample Af002 failed, because the content of radiogenic lead was too low. We therefore report only U-Pb zircon ages of three samples of granodiorite (Af016, Af021 and Af022) and one sample of monzogranite (Af023).

Table 2.1 Geographic details for samples used for U-Pb age dating. No results were obtained for samples in italics.

Sample tag	Rock type	Location	Coordinates	Ground level (m a.s.l.)
Af002	Calcsilicate rock	600 m NW of the Zoodochos Pigi Monastery	36° 21′ 39.75″ N; 25° 49′ 24.92″ E	112
Af016	Granodiorite	Klisidi Beach	36° 20′ 39.05″ N; 25° 46′ 41.88″ E	2
Af021	Granodiorite	400 m SW of the Agios Nikolaos chapel	36° 23′ 07.16″ N; 25° 46′ 27.85″ E	242
Af022	Granodiorite	N of the Vrysi Spring	36° 22′ 47.15″ N; 25° 47′ 01.46″ E	133
Af023	Monzogranitic dyke	300 m W of the Profitis Ilias chapel	36° 23′ 09.38″ N; 25° 47′ 18.82″ E	105
Af030	Quartzite	400 m SE of the Agios Efthymios chapel	36° 22′ 14.16″ N; 25° 47′ 49.03″ E	271
Af161	Anorthosite dyke	400 m NW of the Zoodochos Pigi Monastery	36° 21′ 40.24″ N; 25° 49′ 33.97″ E	115

Thin sections of selected samples were analysed using a petrographic microscope. For oriented samples, thin sections were produced parallel to the mineral/stretching lineation and perpendicular to

the foliation. Point counting was performed on thin sections of igneous rocks using a Prior J0415G point counter using the method described in Middleton et al. (1985) and counting 1,000 points per thin section. The 95 % confidence interval (2σ) calculated for any mineral phase is at maximum 1.6 % using the formula of van der Plas & Tobi (1965). Equal-area projections and contouring were produced using the open source software Stereonet 9.2.0 applying the algorithms described in Allmendinger et al. (2012) and Cardozo and Allmendinger (2013).

Apart from microscopic analyses, the mineral content of selected samples was additionally investigated using X-ray diffraction (XRD). The samples were powdered using a disc mill and an agate mortar. About 1 g per sample was measured using a Panalytical X'Pert Pro diffractometer. Data evaluation was performed using the software X'pert Highscore Plus and MacDiff to obtain semiquantitative mineral contents for studied samples. Detection limits vary between 0.5 to 2 % depending on the mineral in question. Results of XRD analyses are given with the relative intensity of Bragg reflexes and the weight-based reference intensity ratio (RIR) for each mineral phase (Table 2.2).

Table 2.2 Semiquantitative XRD analyses of intrusive rocks showing relative amounts including weight-based RIR correction.

	Mineral phase	**Horn-blende**	**Quartz**	**K-feld-spar**	**Albite/Plagio-clase**	**Musco-vite**	**Biotite**	**Chlorite**
	Bragg reflex (Å)	8.42	4.26	3.22	3.18/3.21	10	10.05	3.55
	RIR value	0.73	3.03	0.55	0.64	0.43	1.40	1.00
Sample	Rock type							
Af016	Granodiorite	—	17.6	10.9	62.1	—	7.9	1.6
Af021	Granodiorite	—	27.2	9.3	62.6	—	0.9	—
Af022	Granodiorite	—	19.9	18.5	52.8	—	7.4	—
Af023	Monzogranite	—	23.5	30.8	41.4	2.3	—	—
Af024	Quartzdiorite	15.2	8.6	—	73.8	—	1.6	0.8
Af161	Monzodiorite	—	—	21.9	65.6	7.2	—	5.3
Af173x	Diorite	40.1	—	—	57.3	—	1.3	1.3
Af173y	Diorite	45.6	—	—	49.9	—	1.1	2.4

2.4.2 Geochronological analyses

Four samples of granitoids from the Chalepa Group were analysed at the University of Frankfurt using laser ablation inductively coupled plasma mass spectrometry (LA-ICP-MS) and isotope dilution thermal ionization mass spectrometry (ID-TIMS). Samples were processed using standard mineral separation techniques including crushing, mineral separation with heavy liquids (bromoform, methylen iodide) and magnetic separation with a Frantz isodynamic separator. Zircon grains with the size of 80–180 µm were hand-picked from the >1.6 Ampere fraction of the heavy minerals for further analyses.

Zircon used for LA-ICP-MS was mounted in epoxy-filled blocks and subsequently sectioned and polished to about 50–75 % of their thickness. Prior to analyses, cathodoluminescence (CL) images of

zircon were made using a JEOL JSM 6490 scanning electron microscope (SEM) equipped with a GATAN MiniCL detector. Sample mounts were cleaned with ethanol and deionized water in an ultrasonic bath to remove surface lead contamination before introduction into the sample cell. Measurements, data processing and error propagation followed the techniques described by Gerdes and Zeh (2006) and Frei and Gerdes (2009) using a Thermo-Finnigan Element II sector field ICP-MS attached to a New Wave LUV213 laser ablation system (λ = 213 nm). Ablation was carried out in helium carrier gas in a low volume cell (2.5 cm^3).

Laser beam parameters used were 30 µm diameter; 5 Hz repetition rate; and 75 % power output. Isotope data were acquired in peak-jumping mode on eight masses; ^{202}Hg, ^{204}Pb, ^{206}Pb, ^{207}Pb, ^{208}Pb, ^{235}U and ^{238}U. Background and ablation data for each analysis were collected over 90 s, with background measurements (carrier gas, no ablation) being taken over the first 30 s prior to initiation of ablation. Data were collected at time-resolved mode allowing acquisition of the signal as a function of time (ablation depth) and subsequent recognition of isotopic heterogeneities within the ablated volume. Raw data were processed using an Excel® spreadsheet program (Frei and Gerdes 2009). Mass discrimination and elemental fractionation during laser ablation were corrected by calibration against standard zircon GJ-1 (Jackson et al. 2004), which was analysed routinely during analytical sessions (three analyses of GJ-1 at the beginning and at the end of every session of 33 unknown analyses and two analyses of GJ-1 every 10 unknown analyses). Prior to this correction, the change of elemental fractionation (e.g. Pb/U and Pb/Th ratios as function of ablation time and thus depth) was corrected for each set of isotope ratios by applying a linear regression through all measured ratios versus time, excluding some outliers (>2 s.e.) and taking the intercept t = 0 as the correct ratio. Changes in isotopic ratios arising from laser drilling into domains of distinct Pb/U ratio (core/rim), mineral inclusions and zones affected by lead loss (metamictization, cracks) can usually be detected by careful monitoring of the time-resolved signal. Such analyses are usually rejected. Common lead correction was applied only when the interference- and background-corrected ^{204}Pb signal was significantly higher than the detection limit of about 20 cps. The latter is limited by the amount of mercury (Hg) in the carrier gas and the accuracy to which the ^{202}Hg and thus the interfering ^{204}Hg can be monitored. Corrections were based on common lead composition given by the second stage growth curve of Stacey and Kramers (1975) for Neoproterozoic age (600 Ma).

Zircon used for ID-TIMS was washed with 6 N hydrochloric acid (HCl) and acetone (C3H6O), and zircon grains were weighted, transferred to small Savillex beakers (Parrish 1987) and put with 24 N hydrofluoric acid (HF) for 6 h on the hotplate at 90 °C. HF was decanted and the vials loaded again with 24 N HF and a mixed $^{205}Pb/^{235}U$-spike. The Savillex vials were then placed into a Parr bomb. After dissolution at 180 °C for 96 h and subsequent evaporation to dryness at ca. 80 °C on a hotplate,

the samples were converted into chloride by adding 0.2 ml 3 N HCl. Chemical separation of lead (Pb) and uranium (U) on 200 µl columns (ion-exchange resin AG 1 × 8, 100–200 mesh) followed the method of Krogh (1973). U and Pb isotope ratios of zircon were obtained using a Finnigan MAT 261 mass spectrometer in static multicollector mode with simultaneous ion counting of ^{204}Pb (Dörr et al. 2002). All isotopic ratios were corrected for mass fractionation (1.0 ± 0.3 ‰/a.m.u), blank (appx. 3 pg) and initial lead using the Stacey and Kramers (1975) model lead composition. Zircon standard GJ-1 (Jackson et al. 2004) was repeatedly analysed under the same conditions as the samples in order to monitor the reproducibility and accuracy of our analyses. It yielded a concordia age at 607 ± 2 Ma (Fig. 2.3).

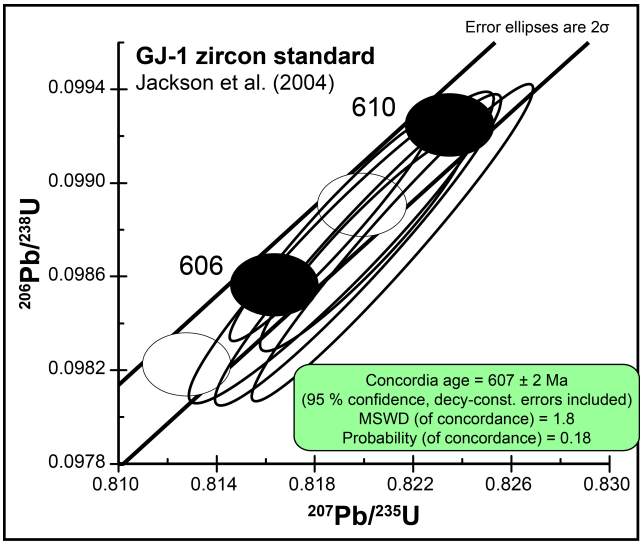

Fig. 2.3 Zircon standard GJ-1 (Jackson et al. 2004), which was measured in order to monitor the reproducibility and accuracy of our U-Pb (ID-TIMS) analyses.

U–Pb data were calculated using the programme PBDAT (Ludwig 1980) and isotope ratios were plotted using Isoplot (Ludwig 2012), with error ellipses reflecting 2σ uncertainties. ^{206}Pb/^{238}U median ages with (asymmetric) 95 % confidence intervals of the median age were obtained using the TuffZirc age extractor based on an algorithm as described in Ludwig and Mundil (2002), which is insensitive to lead loss and inheritance (Ludwig and Mundil 2002).

2.5 Results

2.5.1 Field relationships and tectonic contacts

Eocene flysch sediments form the parautochthonous base of the tectonostratigraphic column on Anafi (Fig. 2.2). They are overlain by crystalline rocks that comprise three main tectonic units, which are from bottom to top: (1) greenschist facies metamorphosed rocks (called hereinafter Anafi Greenschist); (2) orthoamphibolite with intercalations of quartzite, micaschist, and calcsilicate rock in the lower parts (called hereinafter Anafi Amphibolite Group); (3) amphibolite facies metasediments with slices of serpentinite and marble intruded by granitoids and younger dykes (called hereinafter Chalepa Group). The amphibolite facies rocks and the igneous rocks can be correlated with the Asterousia Crystalline Complex of Crete. This correlation is supported by the new results presented below.

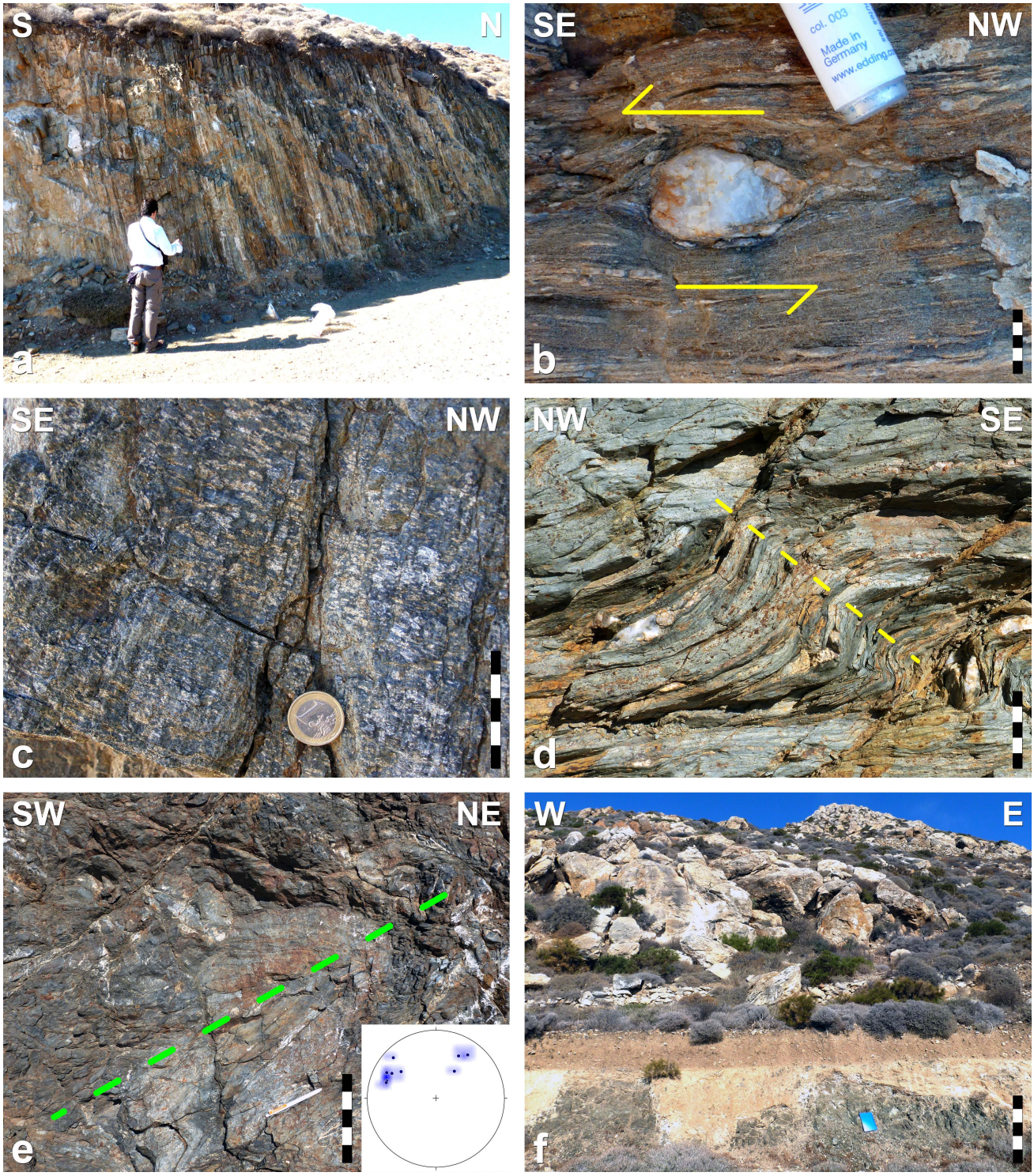

Fig. 2.4 Photographs of medium- to high-grade metamorphic rocks. (a) Mylonitic contact between the Anafi Greenschist (brown) and the Anafi Amphibolite Group (dark grey) showing repetition of greenschist and orthoamphibolite layers. Location: Road cut 200 m SW of Agios Mamas (36° 21′ 45.14″ N; 25° 48′ 07.33″ E). Scale bar: 1 m. (b) Sigmoidal quartz lens indicating top-to-the SE sense of shear in orthoamphibolite at the base of the Anafi Amphibolite Group. Location: As for Fig. 2.4a. Scale bar: 1 cm. (c) Foliation parallel view showing a well-developed NW–SE-trending mineral/stretching lineation and a weakly developed NE–SW-trending crenulation lineation in orthoamphibolite from the upper parts of the Anafi Amphibolite Group. Location: Road cut 400 m N of the Panagia ton Axinon chapel (36° 22′ 18.00″ N; 25° 47′ 09.50″ E). Scale bar: 5 cm. (d) NW-vergent open fold within the Anafi Greenschist. The fold axial plane (yellow dashed line) dips 164/35. Location: Road cut 500 m E of the gas station (36° 21′ 06.27″ N; 25° 46′ 41.87″ E). Scale bar: 5 cm. (e) NE-vergent fold within orthoamphibolite with the fold axial plane dipping 018/50. Inset showing equal area, lower hemisphere stereoplot summarizing the orientation of 9 fold axes measured at the base of the Anafi Amphibolite Group. Location: Road cut 850 m NW of the Megas Potamos bus station (36° 21′ 26.94″ N; 25° 48′ 26.41″ E). Scale bar: 20 cm. (f) Cataclastic contact between the ortho-amphibolite of the Anafi Amphibolite Group and overlying marbles of the Chalepa Group. Location: Road cut between Panagia ton Axinon and Agios Mamas; 800 m ESE of Panagia ton Axinon (36° 21′ 58.20″ N; 25° 47′ 39.03″ E). Scale bar: 1 m.

The contact between the Anafi Greenschist and the underlying flysch sediments is a brittle thrust marked by a cataclastic zone, which contains components derived from both units (Soukis and Papanikolaou 2004; their fig. 2a, b). Slickenside striation reveals a NW–SE tectonic transport, which is consistent with a top-to-the SE sense of shear indicated by SE-vergent folds affecting the flysch sediments.

The mylonitic contact between the Anafi Greenschist and the overlying Anafi Amphibolite Group is characterized by a ca. 50 m thick zone of tectonic repetition of orthoamphibolite and greenschist layers, which are orientated parallel to the main foliation of both units (Fig. 2.4a). Kinematic indicators such as sigmoidal quartz-rich lenses indicate a consistent top-to-the SE sense of shear (Fig. 2.4b). Both the rocks of the Anafi Greenschist and the Anafi Amphibolite Group show a pervasive foliation associated with a pronounced mineral/stretching lineation (Fig. 2.4c). Folding frequently occurs near the

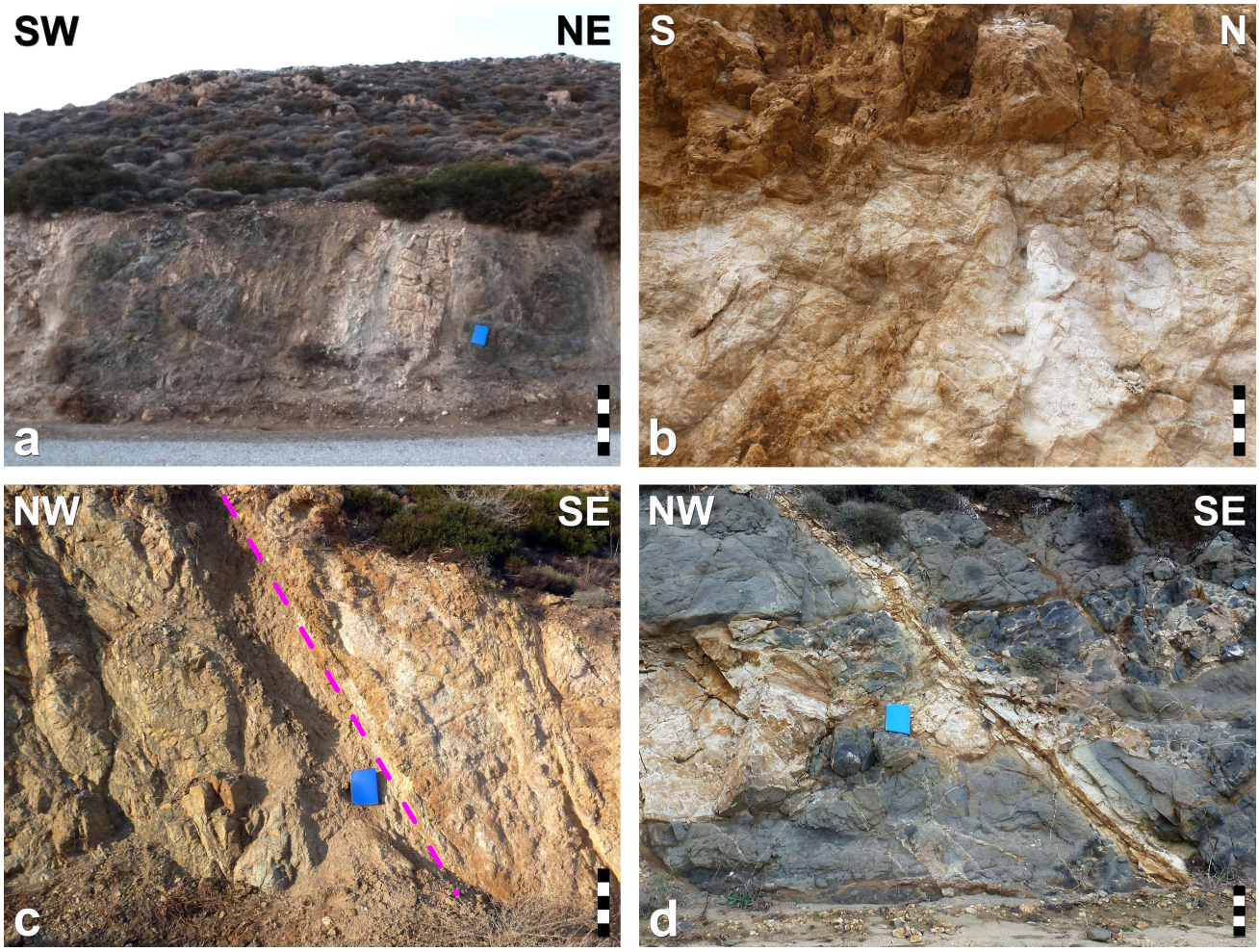

Fig. 2.5 Photographs of intrusive rocks and marble from Anafi. (a) Steep ESE-dipping layers of hornblende diorite (dark colours) and marble (bright colours) of the Chalepa Group as result of tectonic duplication in a cataclastic zone directly above the Anafi Amphibolite Group. Location: Road cut 100 m E of the Monastiri bus station (36° 21′ 20.68″ N; 25° 49′ 23.98″ E). Scale bar: 1 m. (b) Intrusive contact between granodiorite (light colour) and overlying marbles (brown). Marble fragments are present inside the granodiorite. Location: Road cut 250 m S of the dam (36° 21′ 04.87″ N; 25° 47′ 07.75″ E). Scale bar: 50 cm. (c) E-dipping thrust plane between the Anafi Greenschist (left of pink dashed line) and overlying granodiorite of the Chalepa Group. Location: Road cut 400 m NE of the Klisidi Beach (36° 20′ 52.23″ N; 25° 46′ 48.50″ E). (d) Granodiorite (light colours) forming enclaves in quartzdiorite (dark colours) indicating magma mingling. Both are cut by several faults. The large fault dips with 45° to the SE. Location: Road cut 200 m SW of Stavros (36° 22′ 08.19″ N; 25° 45′ 45.35″ E). Scale bar: 50 cm.

contact zone of the two units with folds affecting the foliation. Folds are either NW- (Fig. 2.4d) or NE-vergent (Fig. 2.4e). In southwestern Anafi, marble of the Chalepa Group rests tectonically on top of orthoamphibolite from the Anafi Amphibolite Group. Here, the contact is cataclastic (Fig. 2.4f).

A system of cataclastic NE-dipping thrust faults that caused tectonic alternation as well as tectonic duplication is observed within marble and hornblende diorite at the base of the Chalepa Group in southeastern Anafi (Fig. 2.5a). The contact between marble and granitoids is intrusive (Fig. 2.5b). In southwestern Anafi diorite and granodiorite of the Chalepa Group have been emplaced on top of the flysch sediments (see Soukis and Papanikolaou 2004; their fig. 5a) and on top of the Anafi Greenschist (Fig. 2.5c) via brittle thrust faults with slickenside striation indicating N–S-trending movements. The plutonic rocks in central and northeastern Anafi show felsic enclaves inside dark matrix or vice versa, which is interpreted to result from magma mingling (Fig. 2.5d). Bright plutonic rocks are granodiorite, whereas the dark variety is quartzdiorite.

2.5.2 Petrography, structural record and microfabrics

2.5.2.1 Anafi Greenschist

The fine-grained greenschist is characterized by a planar fabric that varies in intensity from a spaced cleavage to a pervasive, locally mylonitic foliation, the latter being defined by the shape-preferred orientation of actinolite and chlorite (Fig. 2.6a). Other constituents of the greenschist, which often occur in clusters or ribbons aligned parallel to the main foliation, are albite, epidote, and opaque phases. Pyrite, (clino-)zoisite, white mica and few amounts of calcite have been observed only in some samples.

The dominant foliation dips with varying degree either towards the NE or towards the SW (Fig. 2.7a). The foliation planes display a NW–SE-trending mineral/stretching lineation (Fig. 2.7b) defined by the shape-preferred orientation of actinolite and feldspar. Local variation in orientation of both foliation and lineation is present in northwestern Anafi. Here, the foliation dips moderately to the SE, while the lineation plunges gently to the SSW. In some outcrops, sigmoidally shaped quartz lenses indicate a top-to-the SE sense of shear. In thin sections, quartz of these lenses shows undulatory extinction and chessboard-type subgrains (Fig. 2.6b). A top-to-the SE sense of shear is also indicated by asymmetric pressure shadows of chlorite behind euhedral pyrite (Fig. 2.6b).

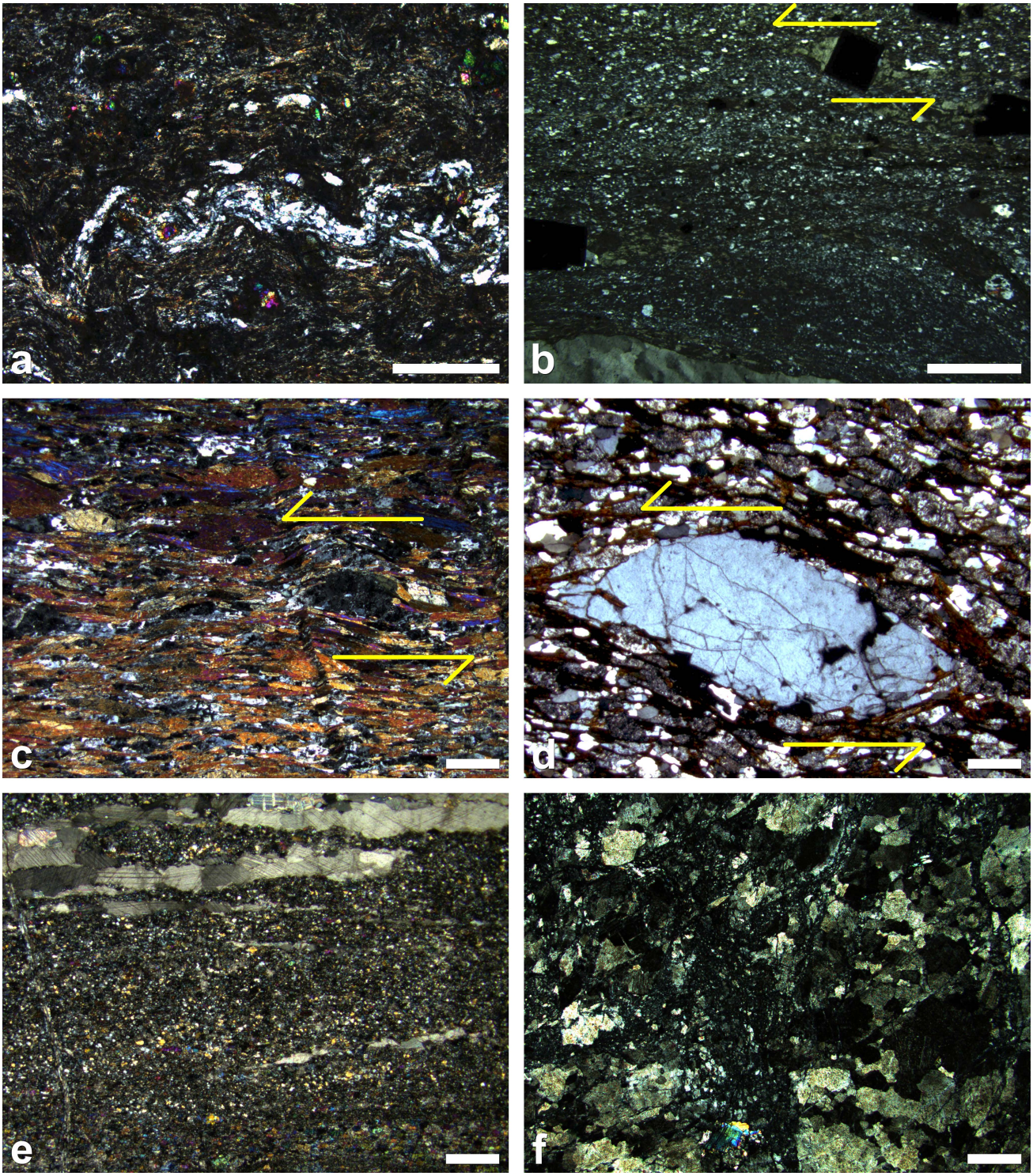

Fig. 2.6 Microphotographs of medium- to high-grade metamorphic rocks from Anafi (crossed polarizers). (a) Slaty (S_1) and crenulation (S_2) cleavage of very fine-grained actinolite and chlorite. K-feldspar has been folded, while epidote forms small microlithons. Sample Af092. Location: Along the paved road 1 km W of the Anafi Chora (36° 21′ 09.03″ N; 25° 45′ 17.05″ E). Scale bar: 500 µm. (b) Asymmetric pressure shadows of chlorite behind euhedral pyrite grains indicate top-to-the SE sense of shear in greenschist. One large quartz xenolith, which is partly visible at the bottom left, shows strong undulatory extinction and chessboard-type subgrains due to crystal dislocation. Sample Af064. Cutting section: 326/05. Location: 500 m E of the gas station (36° 21′ 02.87″ N; 25° 46′ 48.34″ E). Scale bar: 2 mm. (c) Shape-preferred orientation of hornblende and plagioclase forming the dominant foliation of orthoamphibolite. Sigmoidal plagioclase lenses indicate top-to-the SE sense of shear. Sample Af011. Cutting section: 122/30. Location: Along the paved road 1 km NW of the Megas Potamos bus station (36° 21′ 26.94″ N; 25° 48′ 26.41″ E). Scale bar: 1 mm. (d) Sigma clast of vein quartz with asymmetric pressure shadows of small quartz grains indicates top-to-the SE movement in quartzite at the base of the Anafi Amphibolite Group. Sample Af008. Cutting section: 112/20. Location: Along the paved road 200 m W of the Mega Potamos bus station (36° 21′ 17.99″ N; 25° 48′ 53.71″ E). Scale bar: 500 µm. (e) Fine-grained calcsilicate rock of the Chalepa Group. Thin layers of coarse-grained calcite with type II calcite twins according to the classification of Burkhard (1993) are oriented parallel to the main foliation. Sample Af002. Location: SE slope of the Chalepa, 700 m NW of the Zoodochos Pigi Monastery (36° 21′ 39.75″ N; 25° 49′ 24.92″ E). Scale bar: 1 mm. (f) Anorthosite from dyke cutting serpentinite in SE Anafi. It consists mostly of fine- to medium-grained, strongly fractured plagioclase indicating brittle deformation. Sample Af161. Location: 500 m NW of the Zoodochos Pigi Monastery (36° 21′ 40.24″ N; 25° 49′ 33.97″ E). Scale bar: 1 mm.

2.5.2.2 Anafi Amphibolite Group

The rocks above the Anafi Greenschist consists of thick layers of dark, monotonous orthoamphibolite with minor intercalations of calcsilicate rock, quartzite and micaschist in its lower part. Orthoamphibolite is fine- to medium-grained and consists of hornblende and plagioclase. It varies from strongly foliated to massive. Accessory minerals are quartz, calcite, and opaque phases. In massive samples, hornblende is often subhedral and plagioclase lacks preferred orientation. In high-strain domains, the cleavage of a spaced foliation is defined by the shape-preferred orientation of hornblende, while plagioclase with preferred orientation forms the microlithons (Fig. 2.6c).

Quartzite, micaschist and calcsilicate rock at the base of the Anafi Amphibolite Group comprise several decametres thick layers. Calcsilicate rock is very fine-grained and mainly consists of calcite, pyroxene (presumably diopside), hornblende, K-feldspar, plagioclase, and quartz. Impure quartzite consists of K-feldspar (up to 30 %), plagioclase, biotite, hornblende, and other phases. Quartz shows serrated grain boundaries, subgrains and undulatory extinction. Sigmoidally shaped large quartz aggregates indicate a top-to-the SE sense of shear (Fig. 2.6d). This sense of shear is also indicated by truncated fish of plagioclase inside orthoamphibolite (Fig. 2.6c).

The tightness of the foliation in the Amphibolite Group decreases structurally upwards. Orthoamphibolite and metasedimentary intercalations at the base exhibit a penetrative, often mylonitic foliation, while orthoamphibolite at middle and upper structural levels is massive. However, foliated orthoamphibolite is present close to the contact with the overlying Chalepa Group. The foliation in the Anafi Amphibolite Group dips moderately to steeply towards the NE and in some outcrops towards the SW (Fig. 2.7c). NW–SE-trending mineral/stretching lineation (Fig. 2.7d), defined by the alignment of stretched plagioclase and/or hornblende aggregates, is observed in orthoamphibolite situated at the lower structural levels. The foliation and the mineral/stretching lineation in quartzite, micaschist and calcsilicate rock show the same orientation. The intensity of the mineral/stretching lineation faints progressively structurally upwards. However, close to the contact with the overlying marble two lineations occur. The dominant lineation has a NW–SE trend, as observed at lower structural levels, but sometimes, a secondary, ill-defined NE–SW-trending lineation occurs, which partly is developed as mineral lineation and partly as crenulation lineation (Fig. 2.4c). Folds in the lower parts of the Anafi Amphibolite Group show a vergence towards NW, while some of the folds have a vergence towards the NE instead (Fig. 2.4e).

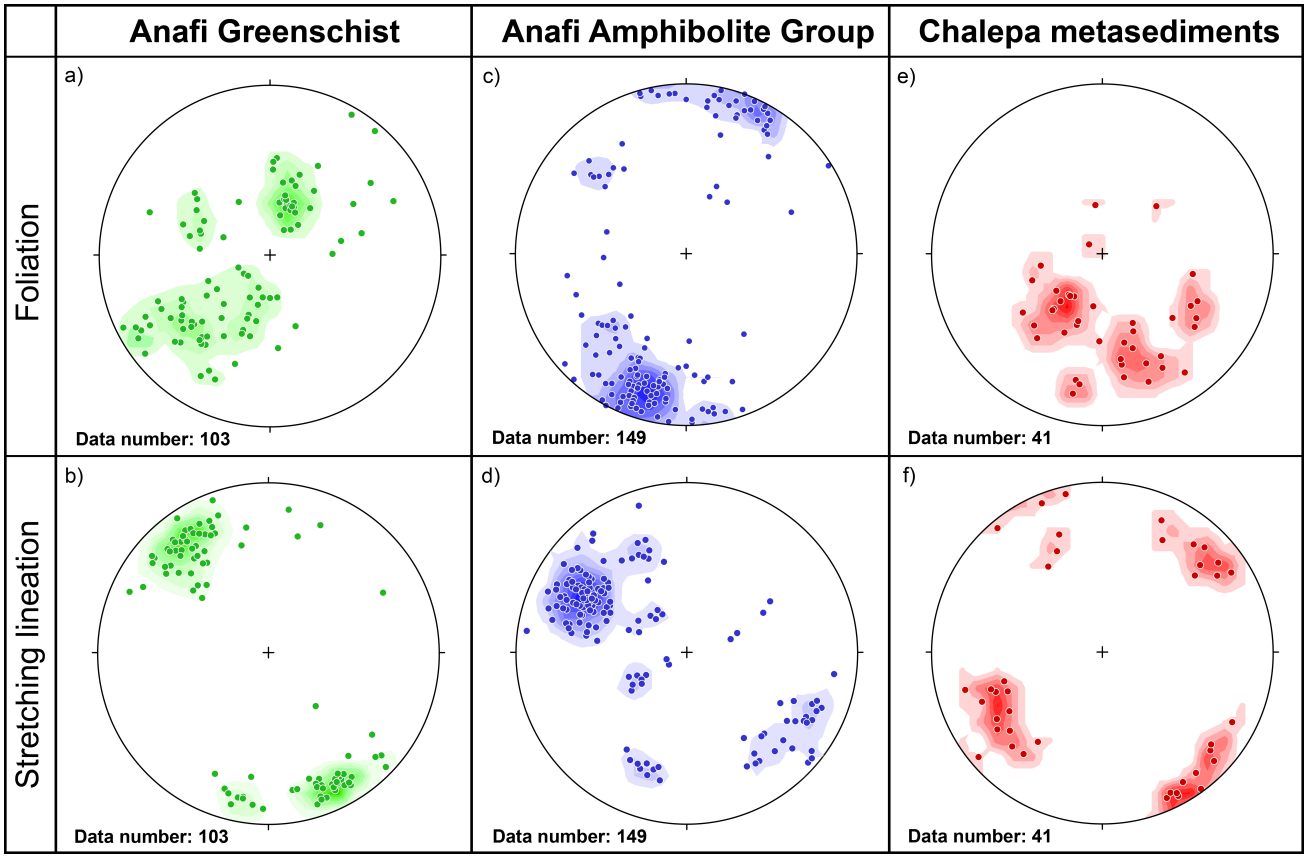

Fig. 2.7 Equal area, lower hemisphere stereoplots of structural data (mineral/stretching lineation and poles to main foliation) obtained from crystalline units of Anafi. Statistical analyses using the 1 % area contouring method are indicated.

2.5.2.3 Chalepa Group

2.5.2.3.1 Metasedimentary rocks and serpentinite

Metasedimentary rocks of the Chalepa Group comprise calcsilicate rock, micaschist, paragneiss, quartzite and banded amphibolite. As calcsilicate rock is very fine-grained, it has been analysed not only under the microscope, but also using XRD. It consists of hornblende (in one case anthophyllite), diopside, calcite, quartz, epidote group minerals (clinozoisite, epidote and zoisite), K-feldspar, plagioclase, muscovite, chlorite, clay minerals, garnet, and opaque phases (ilmenite and others). Calcsilicate rock of the Chalepa Group shows a much broader variability in composition than the homogeneous calcsilicate rock at the base of the Anafi Amphibolite Group. The foliation is defined by a shape-preferred orientation of very fine-grained amphibole, diopside and epidote group minerals. K-feldspar, plagioclase and quartz generally co-exist in large clusters or in form of foliation-parallel bands. Quartz shows strong undulatory extinction. Layers of fine- to medium-grained calcite with tabular twin lamellae are usually present (Fig. 2.6e). Calcite layers contain inclusions of diopside and zoisite.

Quartz of fine- to medium-grained quartzite shows evidence for dynamic recrystallization mainly by serrated grain boundaries, the latter pointing to grain boundary migration. The quartz grains exhibit well-developed shape-preferred orientation. Clusters of clay minerals, K-feldspar, plagioclase, zoisite,

mica, amphibole, opaque phases, or calcite are widespread. K-feldspar shows strain-induced replacement by myrmekite.

The metasedimentary rocks dip mainly to the NE or to the NW (Fig. 2.7e). We observed two mineral lineations within the banded paraamphibolite, calcsilicate rock, and micaschist. The prevailing lineation is trending NE–SW. A second, NW–SE-oriented lineation is less distinct (Fig. 2.7f). Both lineations are defined by the shape-preferred orientation of stretched quartz and/or amphibole, depending on the lithology. Unequivocal shear sense indicators, however, have not been found. Thus, a coaxial deformation cannot be excluded.

Slices of massive serpentinite are present on top of the metasedimentary rocks and on top and at the base of marble and plutonic rocks. They consist of lizardite (>75 %) and few amounts of magnetite and chlorite.

2.5.2.3.2 Igneous rocks

Igneous rocks are present in form of plutons and dykes. The 'hornblende diorite' sensu Reinecke et al. (1982) does not form a separate (sub)unit, but is described herein as part of other plutonic rocks. The structure of the plutonic rocks is inequigranular.

We conducted XRD measurements for all igneous rocks to determine their composition (Table 2). In order to distinguish between alkali feldspar and plagioclase, we measured the distances between different powder diffraction peaks of albite to determine the composition and structural phases applying the method of Chen (1977) for two samples (Af016 and Af023). The results show that albite tends to oligoclase composition. Furthermore, there is only few evidence for perthitic exsolution of feldspar in thin sections. This is why albite is counted as plagioclase. In addition to XRD analyses, we performed point counting on thin sections of the igneous rocks. Results are comparable to XRD analyses (Table 2.3). Except for sample Af161 (monzodiorite according to XRD analyses but anorthosite according to point counting analyses), there is no disagreement regarding the rock type. Samples of igneous rock types were plotted into a QAP diagram based on the composition obtained from point counting analyses (Fig. 2.8).

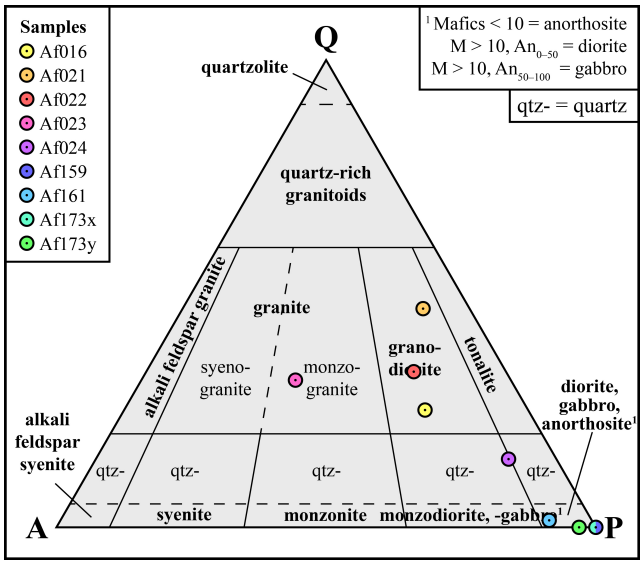

Fig. 2.8 Classification of igneous rocks from the Chalepa Group of Anafi in a QAP diagram after Streckeisen (1974). Mol-% were calculated for alkali feldspar, plagioclase and quartz based on point counting analyses (Table 2.3). Distinction of anorthosite, diorite, and gabbro after Le Maitre et al. (2002).

Table 2.3 Modal composition in volume per cent of igneous rocks from the Chalepa Group of Anafi based on point counting analyses. 1000 points were counted per thin section. 2σ errors are below 1.6 % for each mineral phase (van der Plas and Tobi 1965).

Sample	Biotite	Horn-blende	K-feld-spar	Plagio-clase	Quartz	White mica	Ore min-erals	Others	Rock type
Af016	9.1	—	17.0	49.8	22.4	1.3	0.4	—	Granodiorite
Af021	1.2	—	8.3	43.0	45.1	1.9	0.1	0.4	Granodiorite
Af022	6.5	—	16.3	47.4	27.1	1.1	0.8	0.8	Granodiorite
Af023	0.6	—	39.0	27.9	30.7	1.0	0.4	0.4	Monzogranite
Af024	3.8	27.5	6.3	51.0	9.8	—	0.4	0.8	Quartzdiorite
Af159	5.9	45.9	—	47.0	—	—	0.2	1.0	Diorite
Af161	—	—	6.7	86.2	1.4	3.6	—	2.1	Anorthosite
Af173x	1.3	31.9	—	63.3	—	1.0	1.7	0.8	Diorite
Af173y	1.6	31.7	1.9	59.4	—	1.9	2.4	1.1	Diorite

Granodiorite (samples Af016, Af021, and Af022) contains 18 to 30 % quartz, which shows undulatory extinction and chessboard-type subgrains (Fig. 2.9a). Grain boundaries between quartz and feldspar are often lobate. K-feldspar shows Karlsbad twins, while twinning is only poorly developed in plagioclase. K-feldspar is sometimes myrmekitic and plagioclase partly albitized. Oscillatory zoning is well-pronounced in many feldspar grains (Fig. 2.9a). Granodiorite contains few amounts (<7.5 %) of biotite and/or hornblende.

Quartzdiorite (sample Af024) consists of plagioclase, hornblende, biotite and quartz. Magmatic andesine to labradorite are frequently altered to albite/oligoclase. Grain boundaries between different phases are lobate.

Diorite (samples Af173x and Af173y) is more strongly weathered than other plutonic rocks and more fine-grained. The main constituents are hornblende and plagioclase (Table 2). The anorthite content of plagioclase was estimated at 56 % (XRD analyses) making the rock rather a gabbro than a diorite. This is further corroborated by the high content (> 40 %) of mafic phases. However, Reinecke et al. (1982) obtained lower anorthite contents of 32–45 %. 'Cognate' inclusions within the diorite were regarded by Reinecke et al. (1982) as the main criterion to establish the 'hornblende diorite' as a separate subunit. However, such elliptical to subroundish inclusions of more mafic magma engulfed by magma during emplacement can be found also elsewhere within the plutonic rocks, e.g. in granodiorite at the beach near the Agios Georgios sti Vrysi chapel.

Fine-grained *monzogranitic and anorthosite dykes* cut serpentinite, metasedimentary and plutonic rocks in northeastern and southeastern Anafi. Monzogranitic dykes within granodiorite (sample Af023) consist of plagioclase, quartz, and K-feldspar with few amounts of biotite (XRD detected muscovite instead) and hornblende (Fig. 2.8). Small needles of rutile are enclosed in quartz. Quartz shows weak undulatory extinction, fluid inclusions and deformation lamellae (Fig. 2.9b). Quartz and feldspar grains are angular with strongly varying grain sizes. K-feldspar is sometimes perthitic, which indicates

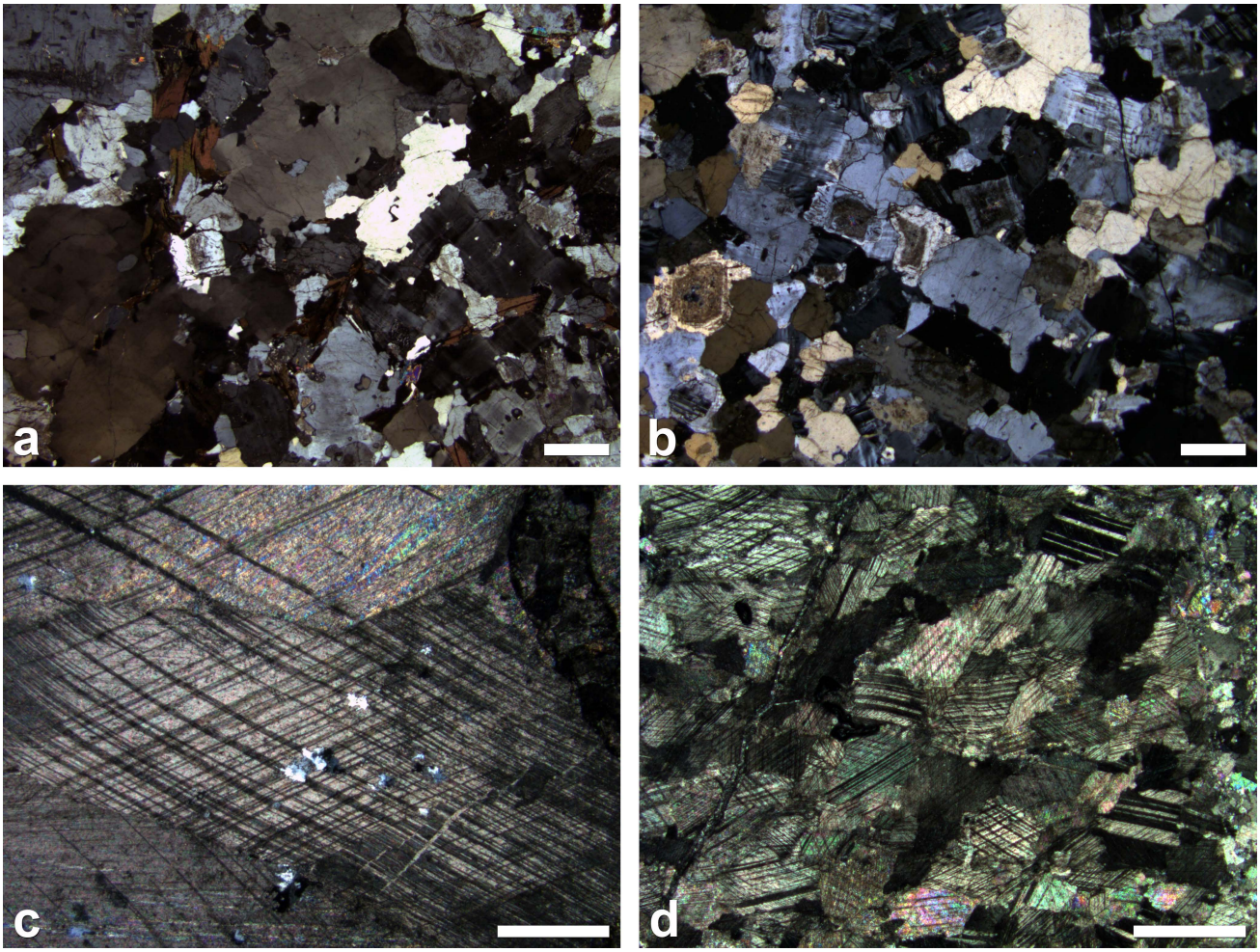

Fig. 2.9 Microphotographs of intrusive rocks and marble from Anafi (crossed polarizers). (a) Granodiorite showing weak zoning in K-feldspar. Feldspar is moderately sericitized. Quartz shows moderate undulatory extinction and weak chessboard-type subgrains. Grain boundaries are irregular and lobate. These features indicate high temperature deformation. Sample Af022. Location: Vrysi Spring (36° 22′ 47.15″ N; 25° 47′ 01.46″ E). Scale bar: 1 mm. (b) Monzogranitic dyke cutting the granodiorite in northeastern Anafi. The rock has a similar composition as sample Af022 (Fig. 2.9a). Quartz, however, showing fluid inclusions, deformation lamellae, only weak undulatory extinction and no chessboard-type subgrains. K-feldspar is largely monocline and sometimes Karlsbad twins and zoning are present (large grain in the middle bottom). Grain boundaries are straight. Sample Af023. Location: 300 m W of the Profitis Ilias chapel (36° 23′ 09.38″ N; 25° 47′ 18.82″ E). Scale bar: 1 mm. (c) Coarse-grained marble with thick, tabular calcite twins of type II according to the classification of Burkhard (1993). The marble is highly impure with many inclusions of quartz clusters. Sample Af020. Location: SW slope of the Toubaria, 1.25 km NW of the Anafi Chora (36° 21′ 14.91″ N; 25° 45′ 16.86″ E). Scale bar: 1 mm. (d) Marble from the monolithic Rock of Kalamos for comparison with Fig. 2.9c. Calcite grains are only medium-sized and twin lamellae thicker and sometimes slightly curved (image centre) belonging to the types II and III according to the classification of Burkhard (1993). Grain boundaries are partly curved indicating grain boundary migration. Sample Af156. Location: Drakondospilo cave on the Kalamos Peninsula (36° 21′ 17.18″ N; 25° 50′ 28.65″ E). Scale bar: 1 mm.

exsolution. Anorthosite dykes within metasedimentary rocks and serpentinite (sample Af161) are several decametres thick. These dykes (not to be confused with premetamorphic ‘plagiogranitic dykes’ sensu Reinecke et al. 1982 cutting the serpentinite NE of the Chora) consist mainly of plagioclase and K-feldspar with few amounts of white mica and clay minerals (Table 2). Mafic phases are completely absent. Grain boundaries between different phases are straight and angular, while mineral grains are fractured (Fig. 2.6f).

2.5.2.3.3 Marble

The plutonic rocks mentioned above intruded into marble. This is obvious by slices of marble having been incorporated into granodiorite and by intrusion contacts (Fig. 2.5b). Marble in northeastern and central Anafi is granoblastic, coarse-grained (up to 3.5 cm grain size), and consists of > 95 % calcite. Calcite shows mainly tabular, thick type II twins (according to Burkhard 1993) indicating deformation at T = 150–300 °C (Fig. 2.9c). Clusters of polycrystalline quartz within calcite grains or thin bands of quartz cutting calcite grains are very widespread. A comparison with marble from the monolithic rock of Kalamos revealed significant differences. The Kalamos marble is much more fine-grained (<1.5 mm grain size; Fig. 2.9d). Type II and III calcite twins suggest deformation temperatures > 200 °C.

2.5.3 U-Pb geochronological analyses

Zircon of three samples of granodiorite and of one sample of monzogranite from a dyke cutting through the granodiorite were analysed applying both LA-ICP-MS and ID-TIMS. Zircon separated from granodiorite of southern (Af016) and northeastern (Af021, Af022) Anafi are euhedral, pristine, pink-coloured with fine or coarse oscillatory zoning (Fig. 2.10a, b, c). The zircon grains are classified as types P_1, P_2 and G_1 according to the classification of Pupin (1980). Zircon of monzogranite is euhedral and classified as type S_9 and P_2 (Fig. 2.10d).

For calculation of $^{238}U/^{206}Pb$ median ages from LA-ICP-MS analyses, only $^{238}U/^{206}Pb$ ages of analyses with a concordance of 97–103 % were plotted. It was tested, whether all LA-ICP-MS analyses of one sample define a concordia. Probability curves of each sample (not shown in this publication) were created for LA-ICP-MS analyses of each sample to determine the most likely zircon population(s). The $^{238}U/^{206}Pb$ median age(s) of the most coherent zircon population(s) were calculated using the zircon age extractor of Isoplot (Ludwig 2012).

The uranium content of zircons separated from *granodiorite Af016* at the Klisidi Beach for LA-ICP-MS analyses is very high (397–5641 ppm). The amount of common lead (Pbc) is usually < 3 % (Table 2.4) and the influence of Pbc on the concordance is negligible for most analyses. Twelve analyses, yielding $^{238}U/^{206}Pb$ ages between 30.6 ± 0.9 Ma and 68.0 ± 1.2 Ma, show the lowest concordances and generally higher contents of Pbc (Table 2.4) compared to thirty analyses yielding $^{238}U/^{206}Pb$ ages ranging from 68.5 ± 1.0 Ma to 77.5 ± 1.1 Ma (Fig. 2.11a) with one concordant age at 83.9 ± 1.2 Ma. The $^{238}U/^{206}Pb$ median age calculated from a coherent group of fourteen analyses is 74.0 +0.8/–0.5 Ma (Fig. 2.11a). The zircons used for ID-TIMS analyses have a high uranium content of 1982–4563 ppm (Table 2.5). The $^{238}U/^{206}Pb$ ages of eight analyses plot between 60.50 ± 0.17 Ma and 72.65 ± 0.13 Ma.

Table 2.4 LA-ICP-MS data of zircons from granodiorite (samples Af016, Af021 and Af022) and monzogranite from a dyke cutting through granodiorite (sample Af023) of the Asterousia Crystalline Complex on Anafi. Errors are quoted at 2σ level.

[a]Within-run background-corrected mean ^{207}Pb signal. [b]Calculated relative to standard zircon GJ-1. [c]Corrected for background and within-run Pb/U or Pb/Th fractionation and normalised to GJ-1 (ID-TIMS value/measured value); $^{207}Pb/^{235}U$ calculated using $(^{207}Pb/^{206}Pb)/(^{238}U/^{206}Pb \times 1/137.88)$. [d]Mass bias corrected by normalising to GJ-1 (ca. 0.5 % per a.m.u.). [e]Error correlation defined as $err(^{206}Pb/^{238}U)/err(^{207}Pb/^{235}U)$. [f]Degree of concordance = $((^{238}U/^{206}Pb \text{ age} \times 100)/(^{207}Pb/^{206}Pb \text{ age}))$.

	^{207}Pb[a] [cps]	U[b] [ppm]	Pb[b] [ppm]	Th/U[b]	$^{206}Pb_c$[c] [%]	$^{206}Pb/^{238}U$[d]	±2σ [%]	$^{207}Pb/^{235}U$[d]	±2σ [%]	$^{207}Pb/^{206}Pb$[d]	±2σ [%]	ρ[e]	$^{206}Pb/^{238}U$	±2σ [Ma]	$^{207}Pb/^{235}U$	±2σ [Ma]	$^{207}Pb/^{206}Pb$	±2σ [Ma]	Conc.[f] [%]
Sample Af016																			
A468	60524	5641	41	1.04	13.0	0.00476	3.1	0.03112	10.3	0.04741	9.8	0.30	30.6	0.9	31.1	3.2	70	233	44
A431	16533	1729	12	1.28	4.1	0.00496	2.2	0.03366	4.4	0.04919	3.8	0.50	31.9	0.7	33.6	1.5	157	89	20
A425	32024	3673	31	0.86	3.7	0.00658	2.2	0.0446	4.2	0.04914	3.6	0.51	42.3	0.9	44.3	1.8	154	85	27
A424	19212	2367	20	0.80	2.7	0.00671	3.0	0.04489	4.3	0.04855	3.1	0.69	43.1	1.3	44.6	1.9	126	73	34
A458	22618	3078	35	0.93	1.9	0.00974	1.7	0.06371	5.5	0.04745	5.2	0.32	62.5	1.1	62.7	3.3	72	124	87
A463	17123	1917	23	0.84	2.1	0.01011	1.4	0.06785	3.0	0.04867	2.7	0.47	64.9	0.9	66.7	2.0	132	63	49
A465	14684	2193	26	0.83	0.6	0.01027	1.5	0.06728	2.9	0.04752	2.5	0.51	65.9	1.0	66.1	1.8	75	58	87
A429	13409	1915	21	0.44	1.5	0.01029	1.5	0.06788	3.3	0.04782	3.0	0.44	66.0	1.0	66.7	2.1	91	71	73
A437	20792	2586	31	0.88	1.1	0.01039	1.7	0.06909	2.7	0.04822	2.1	0.63	66.7	1.2	67.8	1.8	110	50	61
A461	6152	982	11	0.51	0.5	0.01051	1.4	0.06883	2.9	0.04752	2.6	0.49	67.4	1.0	67.6	1.9	75	61	90
A434	2616	421	4	0.24	0.0	0.01057	1.7	0.06949	2.6	0.04769	2.0	0.65	67.8	1.2	68.2	1.7	84	48	81
A466	20802	2080	26	0.83	2.7	0.01061	1.7	0.07184	3.7	0.04912	3.3	0.46	68.0	1.2	70.4	2.5	154	77	44
A470	12718	2117	25	0.80	0.4	0.01069	1.4	0.06984	2.2	0.04739	1.7	0.63	68.5	1.0	68.5	1.5	69	41	99
A455	4906	794	9	0.33	0.0	0.01079	1.8	0.07052	2.7	0.0474	2.0	0.67	69.2	1.2	69.2	1.8	69	47	100
A432	11756	1544	18	0.66	2.8	0.01080	1.6	0.07124	5.2	0.04783	5.0	0.31	69.3	1.1	69.9	3.5	91	118	76
A457	11374	1886	22	0.58	0.0	0.01090	1.4	0.07148	2.1	0.04756	1.6	0.65	69.9	1.0	70.1	1.4	77	38	90
A438	3948	397	5	0.27	3.0	0.01101	1.7	0.07219	6.1	0.04754	5.9	0.28	70.6	1.2	70.8	4.2	76	140	93
A427	10497	1585	19	0.58	0.8	0.01105	1.4	0.07279	3.0	0.04776	2.7	0.47	70.9	1.0	71.3	2.1	88	63	81
A451	22082	3033	35	0.43	0.6	0.01116	1.5	0.07324	2.4	0.04761	1.8	0.63	71.5	1.1	71.8	1.6	80	44	89
A435	8985	1464	17	0.53	0.0	0.01118	1.4	0.0735	2.1	0.0477	1.6	0.67	71.6	1.0	72.0	1.5	84	37	85
A436	4162	688	8	0.25	0.1	0.01120	1.5	0.07336	2.4	0.0475	1.8	0.65	71.8	1.1	71.9	1.7	75	43	96
A430	10692	1615	19	0.58	0.0	0.01121	1.7	0.07418	2.4	0.04799	1.7	0.72	71.9	1.2	72.7	1.7	99	39	73
A456	12297	1603	19	0.43	1.7	0.01140	1.4	0.07464	3.4	0.04747	3.1	0.42	73.1	1.0	73.1	2.4	73	74	100
A460	7403	1193	14	0.52	0.4	0.01142	1.4	0.07468	2.2	0.04742	1.7	0.64	73.2	1.0	73.1	1.6	70	41	104
A433	12607	1866	22	0.35	0.7	0.01146	1.4	0.0755	2.4	0.04776	2.0	0.57	73.5	1.0	73.9	1.7	87	48	84
A448	9536	1607	19	0.47	0.0	0.01146	1.5	0.07505	2.2	0.04747	1.6	0.67	73.5	1.1	73.5	1.6	73	39	100
A446	7552	1250	16	0.87	0.2	0.01148	1.4	0.07483	2.5	0.04728	2.1	0.56	73.6	1.0	73.3	1.8	64	50	116
A449	9839	1708	20	0.32	0.6	0.01155	1.5	0.07585	2.7	0.04765	2.2	0.57	74.0	1.1	74.2	1.9	82	52	90
A467	5503	665	8	0.29	1.7	0.01155	1.5	0.07563	4.9	0.04749	4.6	0.31	74.0	1.1	74.0	3.5	74	110	100
A428	6498	955	12	0.50	1.1	0.01155	1.9	0.07597	4.3	0.0477	3.9	0.43	74.0	1.4	74.3	3.1	85	92	88
A462	14874	1937	25	0.65	2.1	0.01158	1.5	0.07585	4.3	0.04751	4.0	0.35	74.2	1.1	74.2	3.0	75	95	99
A426	9410	1446	17	0.49	0.0	0.01164	1.5	0.07628	2.1	0.04752	1.5	0.70	74.6	1.1	74.6	1.5	75	36	99
A453	8010	1302	16	0.41	0.3	0.01168	1.4	0.07658	2.3	0.04756	1.7	0.64	74.8	1.1	74.9	1.6	77	41	97
A454	7645	1219	15	0.56	2.9	0.01171	1.5	0.07658	6.0	0.04743	5.8	0.25	75.1	1.1	74.9	4.4	71	139	106

A452	5334	831	10	0.28	0.1	0.01173	1.5	0.07682	2.3	0.04748	1.8	0.63	75.2	1.1	75.2	1.7	74	44	102
A450	6865	1049	12	0.34	0.1	0.01177	1.8	0.07724	2.4	0.04759	1.6	0.75	75.4	1.4	75.5	1.8	79	38	95
A445	12924	2061	25	0.45	0.1	0.01180	1.4	0.07725	2.1	0.04747	1.5	0.69	75.6	1.1	75.6	1.5	73	35	104
A464	7362	1011	12	0.44	0.8	0.01185	1.6	0.07748	3.5	0.04741	3.2	0.44	76.0	1.2	75.8	2.6	70	75	108
A444	9023	1391	17	0.36	1.5	0.01185	1.5	0.07771	3.5	0.04755	3.2	0.44	76.0	1.2	76.0	2.6	77	75	99
A459	10257	1272	16	0.60	1.4	0.01186	1.5	0.07763	3.7	0.04749	3.4	0.41	76.0	1.2	75.9	2.7	74	80	103
A469	8921	1369	17	0.39	0.0	0.01210	1.4	0.07953	2.4	0.04767	1.9	0.59	77.5	1.1	77.7	1.8	83	45	93
A447	23479	3343	47	0.74	0.5	0.01310	1.4	0.08607	3.5	0.04766	3.2	0.40	83.9	1.2	83.8	2.8	83	77	102
Sample Af021																			
A492	20457	2968	37	0.95	0.8	0.01070	1.4	0.06988	3.0	0.04737	2.6	0.47	68.6	1.0	68.6	2.0	68	62	101
A483	9547	1482	16	0.37	0.5	0.01086	1.5	0.07106	2.7	0.04744	2.2	0.55	69.7	1.0	69.7	1.8	71	53	98
A512	16869	2631	31	0.71	0.0	0.01090	1.4	0.07131	1.8	0.04744	1.1	0.78	69.9	1.0	69.9	1.2	72	27	98
A475	6943	1209	12	0.13	0.3	0.01096	1.4	0.07174	2.1	0.04747	1.6	0.67	70.3	1.0	70.3	1.4	73	37	97
A486	14513	1920	22	0.44	0.6	0.01097	1.4	0.07198	2.4	0.04758	2.0	0.58	70.3	1.0	70.6	1.7	78	47	90
A478	6373	1062	11	0.03	0.0	0.01109	1.4	0.07245	2.5	0.04739	2.0	0.57	71.1	1.0	71.0	1.7	69	48	103
A510	19491	3199	38	0.56	0.0	0.01116	1.4	0.07308	1.7	0.0475	1.0	0.82	71.5	1.0	71.6	1.2	75	23	96
A513	14545	2097	24	0.38	0.6	0.01121	1.4	0.07325	2.7	0.04741	2.3	0.53	71.8	1.0	71.8	1.9	70	55	103
A490	8582	1263	14	0.37	0.5	0.01122	1.5	0.07344	3.0	0.04746	2.6	0.50	71.9	1.1	72.0	2.1	72	62	99
A511	13414	2216	26	0.46	0.0	0.01129	1.5	0.07388	2.0	0.04748	1.3	0.74	72.3	1.0	72.4	1.4	73	31	98
A481	16716	2444	28	0.42	0.0	0.01129	1.4	0.07384	1.8	0.04743	1.1	0.79	72.4	1.0	72.3	1.2	71	25	102
A473	18362	2902	34	0.52	2.5	0.01131	1.4	0.07398	5.1	0.04744	4.9	0.28	72.5	1.0	72.5	3.6	72	116	101
A487	18524	3003	37	0.68	0.0	0.01132	1.4	0.07423	1.8	0.04758	1.0	0.80	72.5	1.0	72.7	1.2	78	25	93
A505	15461	1917	23	0.62	0.4	0.01132	1.5	0.07397	2.2	0.04739	1.6	0.67	72.6	1.1	72.5	1.5	69	39	105
A485	7566	1201	14	0.33	0.0	0.01134	1.6	0.07423	2.4	0.04746	1.8	0.65	72.7	1.1	72.7	1.7	73	44	100
A477	2412	376	4	0.32	0.0	0.01139	1.5	0.07446	3.2	0.0474	2.8	0.47	73.0	1.1	72.9	2.3	70	67	105
A509	22533	2511	31	0.51	2.5	0.01144	1.6	0.07499	8.1	0.04753	7.9	0.20	73.3	1.2	73.4	5.7	76	188	96
A508	81180	5984	84	0.82	6.3	0.01144	1.9	0.07511	7.3	0.04761	7.0	0.27	73.3	1.4	73.5	5.2	80	167	92
A500	5218	721	8	0.35	0.8	0.01147	1.5	0.07523	3.0	0.04755	2.6	0.52	73.5	1.1	73.6	2.1	77	61	95
A472	3484	425	5	0.22	1.0	0.01153	1.7	0.07555	3.7	0.04753	3.3	0.45	73.9	1.2	74.0	2.6	76	78	97
A489	12216	2047	24	0.34	0.6	0.01159	1.4	0.07588	2.3	0.04747	1.8	0.62	74.3	1.1	74.3	1.7	73	44	102
A488	1559	215	2	0.32	1.3	0.01162	1.6	0.07616	4.7	0.04753	4.4	0.35	74.5	1.2	74.5	3.4	76	104	98
A484	13821	2429	29	0.34	0.0	0.01173	1.8	0.07682	2.2	0.04748	1.3	0.81	75.2	1.3	75.2	1.6	74	31	102
A493	8647	1730	20	0.27	0.1	0.01177	1.7	0.07713	2.4	0.04752	1.7	0.71	75.4	1.3	75.4	1.7	76	40	100
A501	5737	879	10	0.35	1.5	0.01178	1.5	0.07723	3.9	0.04755	3.5	0.39	75.5	1.1	75.5	2.8	77	84	98
A479	15811	2277	28	0.46	0.7	0.01179	1.5	0.07738	2.3	0.0476	1.7	0.67	75.6	1.2	75.7	1.7	79	41	95
A504	15744	2308	29	0.48	0.0	0.01182	1.7	0.07759	2.0	0.04762	1.1	0.84	75.7	1.3	75.9	1.5	80	26	94
A503	5671	911	11	0.44	0.9	0.01184	1.4	0.07748	2.9	0.04748	2.5	0.50	75.8	1.1	75.8	2.1	73	60	103
A471	7850	1048	12	0.28	1.4	0.01186	1.4	0.0777	3.3	0.04753	3.0	0.43	76.0	1.1	76.0	2.4	76	71	100
A491	8544	1055	13	0.31	1.8	0.01187	1.6	0.07774	4.0	0.04752	3.6	0.41	76.0	1.2	76.0	2.9	75	86	101
A499	6908	652	8	0.37	3.3	0.01187	1.8	0.07766	5.2	0.04746	4.9	0.34	76.1	1.3	75.9	3.8	73	117	105
A507	7816	1208	14	0.37	0.0	0.01187	1.4	0.07794	1.9	0.04762	1.2	0.77	76.1	1.1	76.2	1.4	80	28	95
A502	18723	3049	37	0.41	0.3	0.01190	1.4	0.07797	1.9	0.04752	1.2	0.75	76.3	1.1	76.2	1.4	75	30	101
A476	16947	2566	32	0.49	0.5	0.01213	1.5	0.07946	2.8	0.04753	2.4	0.53	77.7	1.2	77.6	2.1	76	57	103

A506	6120	979	12	0.38	0.0	0.01215	1.5	0.07982	2.3	0.04767	1.7	0.66	77.8	1.2	78.0	1.7	83	41	94
A474	8708	1199	17	0.82	1.4	0.01223	1.5	0.08005	4.3	0.04748	4.1	0.36	78.3	1.2	78.2	3.3	74	96	106
A480	6479	1002	13	0.55	0.5	0.01230	1.6	0.08082	2.6	0.04764	2.1	0.61	78.8	1.2	78.9	2.0	82	49	97
Sample Af022																			
A525	32894	5340	57	0.40	0.4	0.01050	1.4	0.06865	1.9	0.04741	1.2	0.77	67.3	1.0	67.4	1.2	70	28	96
A535	9778	1589	17	0.40	0.7	0.01087	1.5	0.07114	2.6	0.04744	2.1	0.58	69.7	1.1	69.8	1.8	72	50	97
A518	8158	1349	15	0.34	0.0	0.01103	1.4	0.07203	2.6	0.04738	2.2	0.54	70.7	1.0	70.6	1.8	69	53	103
A526	5415	939	11	0.56	0.0	0.01106	1.5	0.07237	2.5	0.04747	2.1	0.58	70.9	1.0	71.0	1.7	73	49	98
A536	15854	2621	29	0.38	1.7	0.01109	1.4	0.07256	3.7	0.04745	3.5	0.37	71.1	1.0	71.1	2.6	72	83	99
A514	6797	1114	12	0.27	1.8	0.01112	1.5	0.07271	4.1	0.04743	3.9	0.36	71.3	1.1	71.3	2.8	71	92	101
A537	16654	2819	33	0.54	0.0	0.01113	1.5	0.07278	1.8	0.04742	1.0	0.84	71.4	1.0	71.3	1.2	70	23	101
A538	5265	872	10	0.27	0.0	0.01118	1.7	0.07314	2.6	0.04743	1.9	0.66	71.7	1.2	71.7	1.8	71	46	101
A516	23884	3155	36	0.33	2.3	0.01119	1.5	0.07311	4.0	0.04739	3.7	0.37	71.7	1.1	71.6	2.8	69	88	104
A531	15102	2538	29	0.34	0.0	0.01124	1.5	0.07357	1.8	0.04748	1.1	0.80	72.0	1.1	72.1	1.3	73	26	98
A539	8391	1311	15	0.34	0.0	0.01124	1.5	0.07354	2.4	0.04745	1.9	0.61	72.1	1.1	72.1	1.7	72	46	100
A532	14131	2378	27	0.38	0.0	0.01129	1.4	0.07394	1.7	0.04748	1.0	0.81	72.4	1.0	72.4	1.2	74	24	98
A524	21986	3555	42	0.54	0.2	0.01134	1.4	0.07417	2.2	0.04745	1.6	0.65	72.7	1.0	72.6	1.5	72	39	101
A522	10291	1698	20	0.50	0.0	0.01136	1.4	0.07437	1.8	0.04749	1.2	0.76	72.8	1.0	72.8	1.3	74	28	99
A527	14045	2379	27	0.40	0.3	0.01142	1.4	0.07473	1.9	0.04745	1.2	0.76	73.2	1.0	73.2	1.3	72	29	102
A517	14271	2362	27	0.34	0.0	0.01143	1.4	0.07487	1.9	0.0475	1.3	0.74	73.3	1.0	73.3	1.3	74	30	99
A515	11050	1693	20	0.43	2.2	0.01145	1.4	0.07494	4.7	0.04746	4.5	0.31	73.4	1.1	73.4	3.3	72	106	101
A540	18990	2451	29	0.49	0.8	0.01146	1.5	0.07489	2.3	0.04739	1.7	0.65	73.5	1.1	73.3	1.6	69	41	107
A519	4463	732	9	0.41	0.0	0.01152	1.4	0.07536	2.8	0.04746	2.4	0.52	73.8	1.1	73.8	2.0	73	57	102
A534	31051	4588	62	1.05	0.9	0.01152	1.6	0.07544	3.8	0.04749	3.5	0.42	73.8	1.2	73.8	2.7	74	83	100
A520	3126	476	5	0.23	0.0	0.01152	1.6	0.07541	2.9	0.04746	2.4	0.56	73.9	1.2	73.8	2.1	73	57	102
A529	12661	2029	24	0.42	0.5	0.01161	1.5	0.07602	2.3	0.04748	1.8	0.64	74.4	1.1	74.4	1.7	73	42	101
A530	9404	1564	19	0.46	0.0	0.01167	1.5	0.07639	1.9	0.04747	1.1	0.79	74.8	1.1	74.7	1.3	73	27	103
A542	7430	1141	13	0.34	0.0	0.01175	1.5	0.07696	2.3	0.0475	1.7	0.68	75.3	1.1	75.3	1.6	75	39	101
A521	15231	2493	30	0.46	0.0	0.01176	1.4	0.07702	1.9	0.0475	1.3	0.74	75.4	1.1	75.3	1.4	74	31	102
A528	10935	1791	21	0.33	0.0	0.01181	1.4	0.07747	2.0	0.04758	1.4	0.72	75.7	1.1	75.8	1.5	78	33	96
A533	9704	1569	19	0.37	0.6	0.01184	1.5	0.07754	2.3	0.04749	1.7	0.68	75.9	1.2	75.8	1.7	74	39	102
A541	20609	3053	39	0.57	0.0	0.01204	1.5	0.07888	2.2	0.04752	1.5	0.70	77.1	1.2	77.1	1.6	76	36	102
A523	9164	1432	17	0.31	1.5	0.01211	1.6	0.07948	3.6	0.0476	3.3	0.43	77.6	1.2	77.7	2.7	79	78	98
Sample Af023																			
A547	3518	679	7	0.84	2.3	0.00934	1.4	0.06077	5.1	0.04717	4.9	0.28	60.0	0.9	59.9	3.0	58	116	104
A559	4125	857	10	0.77	0.0	0.00974	1.6	0.06344	2.7	0.04726	2.2	0.60	62.5	1.0	62.5	1.6	62	52	100
A573	3011	543	6	0.65	0.1	0.00988	1.5	0.06435	3.3	0.04723	2.9	0.46	63.4	1.0	63.3	2.0	61	69	104
A545	3380	563	6	0.58	2.7	0.01028	1.5	0.06706	5.7	0.04731	5.5	0.26	65.9	1.0	65.9	3.7	65	131	102
A555	4491	757	9	0.71	0.4	0.01031	1.6	0.0681	2.8	0.04788	2.3	0.58	66.2	1.1	66.9	1.8	93	54	71
A572	4468	791	10	0.90	0.9	0.01053	1.4	0.06876	3.1	0.04735	2.7	0.47	67.5	1.0	67.5	2.0	67	65	101
A569	5015	904	11	0.91	0.0	0.01073	1.4	0.07013	2.8	0.04741	2.4	0.50	68.8	1.0	68.8	1.9	70	58	98
A570	17770	2802	30	0.36	0.3	0.01075	1.6	0.07011	2.7	0.04731	2.3	0.57	68.9	1.1	68.8	1.8	65	54	107
A574	2131	350	4	0.66	0.0	0.01080	1.6	0.07063	3.3	0.04741	2.9	0.48	69.3	1.1	69.3	2.2	70	69	99

A562	26965	3901	46	0.64	0.7	0.01084	1.4	0.07075	2.6	0.04733	2.1	0.56	69.5	1.0	69.4	1.7	66	51	106
A544	13488	2205	27	0.85	0.0	0.01086	1.6	0.07098	2.1	0.0474	1.3	0.76	69.6	1.1	69.6	1.4	69	32	101
A558	11473	1969	22	0.38	0.0	0.01087	1.4	0.07103	1.9	0.0474	1.3	0.73	69.7	0.9	69.7	1.3	69	30	100
A563	3637	601	7	0.79	0.0	0.01096	1.5	0.07172	3.0	0.04746	2.6	0.50	70.3	1.0	70.3	2.0	72	61	97
A556	8128	1398	17	0.77	0.8	0.01097	1.5	0.07177	2.6	0.04745	2.1	0.59	70.3	1.1	70.4	1.8	72	51	97
A546	2024	345	4	0.70	0.1	0.01108	1.6	0.07241	3.7	0.04741	3.4	0.42	71.0	1.1	71.0	2.5	70	80	102
A554	3100	541	7	0.81	2.8	0.01109	1.5	0.07252	6.0	0.04744	5.8	0.26	71.1	1.1	71.1	4.1	71	137	99
A575	16395	2545	30	0.55	0.6	0.01115	1.5	0.07284	2.3	0.04739	1.8	0.63	71.5	1.0	71.4	1.6	69	43	103
A543	7987	1355	18	1.06	1.6	0.01122	1.4	0.0734	3.8	0.04745	3.5	0.37	71.9	1.0	71.9	2.6	72	84	100
A564	21586	3520	42	0.59	0.2	0.01132	1.4	0.07404	1.8	0.04744	1.1	0.78	72.6	1.0	72.5	1.3	71	27	102
A565	2122	344	5	1.17	0.0	0.01136	1.5	0.07425	2.9	0.04742	2.5	0.51	72.8	1.1	72.7	2.1	70	60	103
A568	12101	2064	24	0.39	0.0	0.01144	1.4	0.07492	1.8	0.04749	1.0	0.81	73.3	1.1	73.4	1.3	74	25	99
A557	11326	1797	24	1.04	0.1	0.01153	1.6	0.07542	2.0	0.04744	1.2	0.78	73.9	1.1	73.8	1.4	71	30	104
A548	1581	248	3	0.45	1.5	0.01187	1.8	0.07777	4.6	0.0475	4.2	0.39	76.1	1.3	76.0	3.3	75	100	102
A561	25466	3416	46	0.83	0.6	0.01192	1.4	0.07796	2.4	0.04744	1.9	0.60	76.4	1.1	76.2	1.7	72	45	107

Table 2.5 ID-TIMS data of zircons from granodiorite (samples Af016, Af021 and Af022) and monzogranite from a dyke cutting through granodiorite (sample Af023) of the Asterousia Crystalline Complex on Anafi. Errors are quoted at 2σ-level. * = corrected for mass fractionation (1.12 ± 0.18 ‰ per a.m.u.), ^{205}Pb-spike contribution and analytical blank of 2 pg. Cor. = correlation coefficient of ^{207}Pb/^{235}U to ^{206}Pb/^{238}U errors.

Sample Analyses	Weight [µg]	U [ppm]	Pb [ppm]	^{206}Pb/^{204}Pb*	^{206}Pb/^{238}U	± 2σ [%]	^{207}Pb/^{235}U	± 2σ [%]	^{207}Pb/^{206}Pb	± 2σ [%]	Cor.	Apparent ages [Ma] ^{206}Pb/^{238}U	± 2σ	^{207}Pb/^{235}U	± 2σ	^{207}Pb/^{206}Pb	± 2σ
Sample Af016																	
4511	10	3737	44.25	1328	0.01133	0.18	0.07422	0.63	0.04750	0.59	0.34	72.65	0.13	72.70	0.46	74.20	14
4506	10	3222	38.98	1017	0.01133	0.34	0.07421	0.84	0.04751	0.73	0.51	72.63	0.24	72.69	0.61	74.69	17
4512	20	1982	24.73	628	0.01129	0.21	0.07397	0.70	0.04750	0.64	0.43	72.40	0.15	72.46	0.51	74.62	15
4509	10	3269	40.45	554	0.01123	0.26	0.07359	1.38	0.04751	1.29	0.45	72.02	0.19	72.10	1.00	74.88	31
4510	10	2492	31.70	440	0.01115	0.44	0.07305	3.51	0.04750	3.29	0.52	71.50	0.32	71.59	2.51	74.38	78
4508	10	4563	62.59	348	0.01109	0.46	0.07259	1.13	0.04748	1.01	0.45	71.08	0.33	71.15	0.80	73.49	24
4505	10	2079	25.11	435	0.01069	0.38	0.06998	0.83	0.04749	0.71	0.53	68.53	0.26	68.68	0.57	73.93	17
4507	10	1988	23.08	285	0.00943	0.28	0.06168	1.41	0.04744	1.29	0.45	60.50	0.17	60.77	0.78	71.55	31
Sample Af021																	
4517	21	2729	32.75	1656	0.01167	0.37	0.07629	0.76	0.04741	0.66	0.51	74.79	0.28	74.65	0.56	70.18	16
4513	14	3865	47.54	818	0.01157	0.60	0.07577	1.10	0.04751	0.88	0.61	74.14	0.45	74.17	0.82	75.08	21
4520	19	3230	39.65	1094	0.01156	0.13	0.07553	0.45	0.04740	0.43	0.32	74.08	0.10	73.93	0.33	69.09	10
4515	15	2688	33.53	708	0.01156	0.51	0.07576	1.23	0.04755	1.07	0.51	74.07	0.38	74.15	0.91	76.82	25
4516	16	2382	28.67	1228	0.01155	0.16	0.07556	0.51	0.04743	0.48	0.33	74.06	0.12	73.97	0.38	70.80	11
4514	16	2454	30.27	870	0.01155	0.38	0.07588	0.97	0.04766	0.85	0.51	74.02	0.28	74.27	0.72	82.38	20
Sample Af022																	
4526	25	3646	44.79	1103	0.01178	0.52	0.07724	0.86	0.04752	0.66	0.65	75.55	0.39	75.54	0.65	75.23	16
4528	32	4204	51.33	1387	0.01171	0.38	0.07687	1.60	0.04761	1.48	0.43	75.06	0.28	75.20	1.20	79.76	35
4521	28	2224	27.50	966	0.01168	0.84	0.07624	1.10	0.04736	0.71	0.76	74.84	0.62	74.60	0.75	66.96	17
4524	27	4097	48.16	1623	0.01151	0.37	0.07557	1.04	0.04762	0.92	0.46	73.77	0.28	73.97	0.77	80.34	22
4523	24	2807	32.79	1904	0.01151	0.14	0.07550	0.50	0.04759	0.49	0.28	73.75	0.10	73.91	0.37	79.02	12
4522	22	3166	39.96	1566	0.01150	0.26	0.07568	0.43	0.04771	0.34	0.63	73.73	0.19	74.08	0.32	85.16	7.9
4527	25	1980	25.67	672	0.01150	0.60	0.07556	2.75	0.04765	2.54	0.45	73.72	0.44	73.96	2.03	81.99	60
Sample Af023																	
4539	10	1906	38.45	180	0.00983	1.22	0.06429	9.38	0.04741	8.85	0.49	63.09	0.77	63.26	5.93	69.79	210
4543	10	2016	39.44	222	0.00982	1.02	0.06404	4.59	0.04728	4.32	0.37	63.01	0.64	63.03	2.89	63.51	100
4544	10	2794	71.25	73	0.00982	0.89	0.01881	44.4	0.01389	43.8	0.75	62.98	0.56	18.92	8.40	N/A	N/A
4541	10	1993	39.09	159	0.00937	0.86	0.06120	3.41	0.04739	3.18	0.37	60.10	0.52	60.31	2.05	68.79	76
4546	10	3429	65.68	171	0.00924	1.02	0.06297	9.24	0.04943	8.72	0.55	59.29	0.60	62.01	5.73	168.06	200
4545	10	1472	29.55	101	0.00864	1.48	0.05646	21.4	0.04739	20.2	0.81	55.46	0.82	55.77	11.93	68.90	480

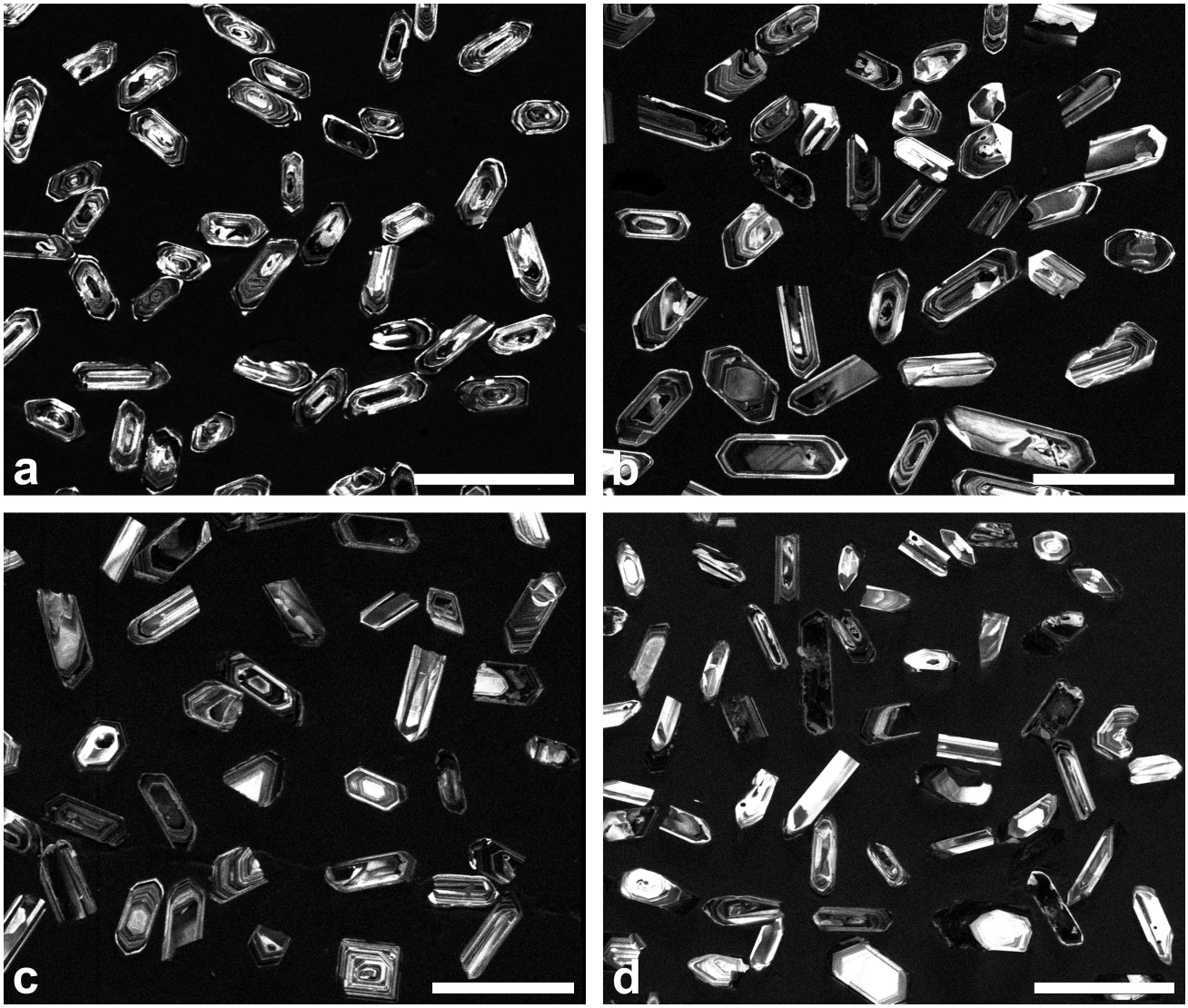

Fig. 2.10 Cathodoluminescence images of zircon for LA-ICP-MS analyses from (a) granodiorite Af016, (b) granodiorite Af021, (c) granodiorite Af022, and (d) monzogranite Af023. The zircons of all four samples are euhedral, prismatic, pristine and show regular growth zoning without textural discontinuities. Some grains show dark cores. Scale bars: 250 µm.

The $^{238}U/^{206}Pb$ median age calculated from three analyses is 72.6 +0.1/–0.2 Ma (Fig. 2.11a). Four analyses (4505, 4509, 4510, and 4508) are slightly discordant, whereas analysis 4507 yielding the youngest age (not shown in Fig. 2.11a) is highly discordant. The three analyses with the highest $^{206}Pb/^{204}Pb$ ratios define a concordia age of 72.5 ± 0.1 Ma with a mean standard weighted deviation (MSWD) of concordance of 0.34 and a probability (P) of 0.56 (Fig. 2.11b). The discordia calculated for ID-TIMS analyses of granodiorite Af016 intercepts at 0 ± 5 and 74.8 ± 7 Ma with a MSWD of 0.013 (Fig. 2.12).

Zircons for LA-ICP-MS analyses from *granodiorite Af021* near the Agios Nikolaos chapel have a similar uranium content as those of the granodiorite Af016 but a higher variability, ranging from 215 to 5984 ppm. The amount of Pbc is usually lower than in analyses of granodiorite Af016 (Table 2.4) and the influence of Pbc therefore completely negligible. Thirty-seven analyses yield $^{238}U/^{206}Pb$ ages of 68.6 ± 1.0 Ma to 78.8 ± 1.2 Ma. Two zircon populations, each defined by a coherent group of

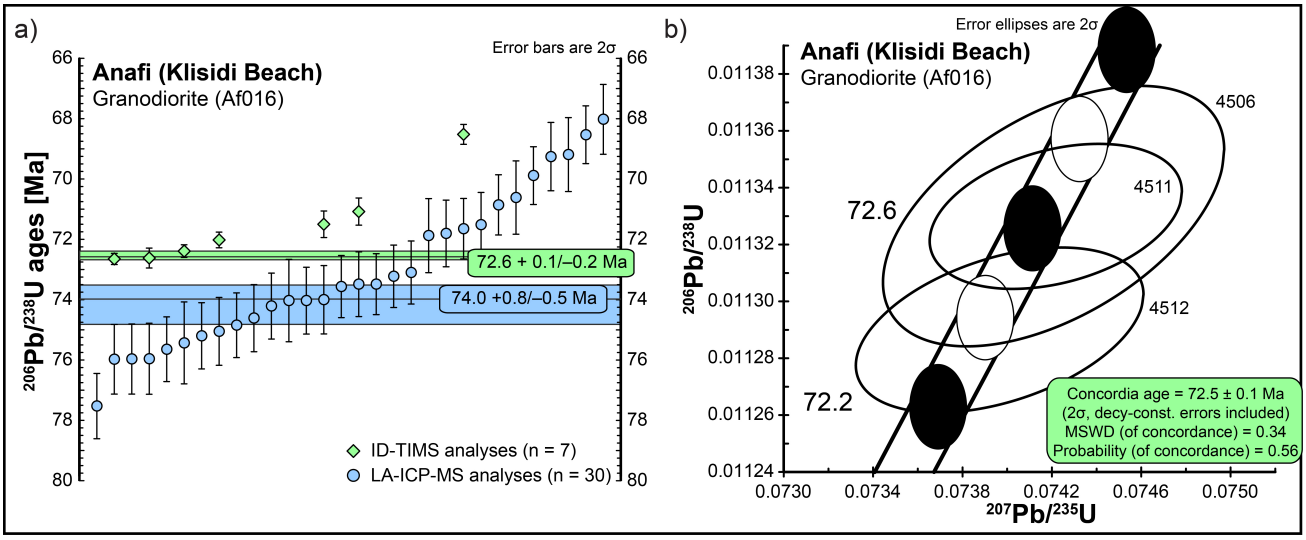

Fig. 2.11 LA-ICP-MS (blue) and ID-TIMS (green) $^{238}U/^{206}Pb$ zircon ages of granodiorite Af016 from the Klisidi Beach; (a) scatter plot with 95 % confidence interval of the median age; (b) U-Pb concordia diagram calculated from three ID-TIMS analyses; numbering and error of the ellipses are given in Table 2.5.

fourteen analyses, have an equal likelihood according to the probability curve. The older zircon population yields a $^{238}U/^{206}Pb$ median age of 75.7 ± 0.4 Ma, while the $^{238}U/^{206}Pb$ median age of the younger zircon populations is 72.55 +0.8/–0.2 Ma (Fig. 2.13a). The uranium content of zircon for ID-TIMS analyses ranges from 2382 to 3865 ppm (Table 2.5). The $^{238}U/^{206}Pb$ ages of five analyses plot close to 74 Ma and yield a $^{238}U/^{206}Pb$ median age of 74.1 +0.1/–0.1 Ma (Fig. 2.13a). These analyses define a concordia age of 74.0 ± 0.1 Ma with a MSWD of 0.25 and a probability of 0.62 (Fig. 2.13b). Analysis 4517 yields a slightly older $^{238}U/^{206}Pb$ age of 74.79 ± 0.28 Ma. Overall, at least three zircon populations at around 75.7 Ma, 74.1 Ma and the youngest at 72.5 Ma can be assumed for granodiorite Af021 (Fig. 2.13a).

The uranium content of zircons separated for LA-ICP-MS analyses from *granodiorite Af022* near the Vrysi Spring does not differ from the previous samples and ranges from 476 to 5340 ppm (Table 2.4). The amount of Pbc is always < 2.3 %. All twenty-nine analyses yield concordant $^{238}U/^{206}Pb$ ages ranging from 67.3 ± 1.0 Ma to 77.6 ± 1.2 Ma. The $^{238}U/^{206}Pb$ median age calculated from a coherent group of thirteen analyses is 73.2 +0.6/–1.2 Ma (Fig. 2.14a). Uranium content of zircons used for ID-TIMS analyses ranges from 1980 to 4204 ppm (Table 2.5). Three analyses plot at ca. 75 Ma (Fig. 2.14a), whereas four analyses with significantly younger $^{238}U/^{206}Pb$ ages define a $^{238}U/^{206}Pb$

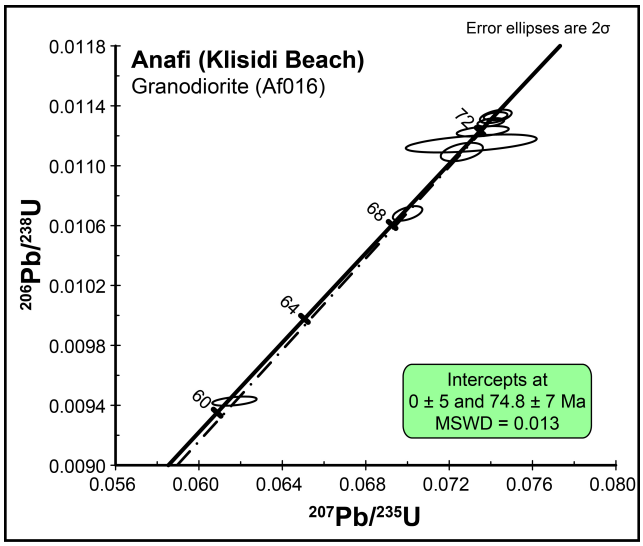

Fig. 2.12 U-Pb discordia diagram calculated from ID-TIMS analyses of granodiorite Af016; numbering and error of the ellipses are given in Table 2.5.

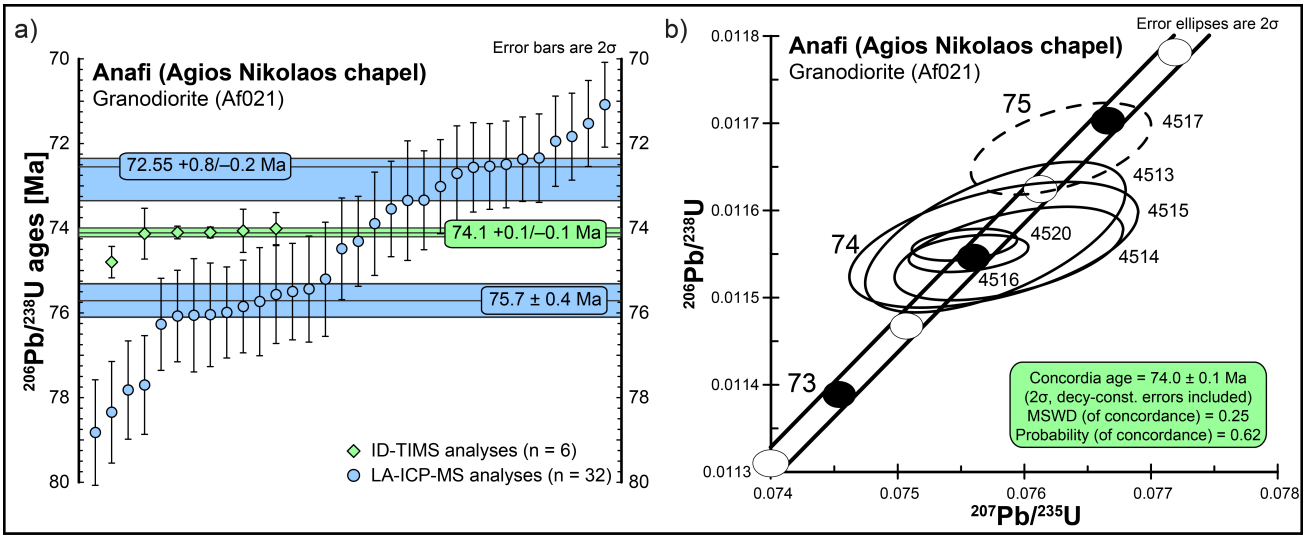

Fig. 2.13 LA-ICP-MS (blue) and ID-TIMS (green) $^{238}U/^{206}Pb$ zircon ages of granodiorite Af021 400 m SW of the Agios Nikolaos chapel; (a) scatter plot with 95 % confidence interval of the median age; (b) U-Pb concordia diagram calculated from six ID-TIMS analyses; numbering and error of the ellipses are given in Table 2.5.

median age of 73.8 +0.1/–0.1 Ma (Fig. 2.14a). The two zircon population yield ID-TIMS concordia ages at 75.2 ± 0.2 Ma (MSWD = 0.14; P = 0.71) and at 73.8 ± 0.1 Ma (MSWD = 0.87; P = 0.35), respectively (Fig. 2.14b). These ages could also be reproduced from LA-ICP-MS analyses; six LA-ICP-MS analyses define a concordia age of 75.2 ± 0.5 Ma (MSWD = 0.0052; P = 0.94), while twelve LA-ICP-MS yield a concordia age at 73.2 ± 0.3 Ma (MSWD = 0.001; P = 0.999).

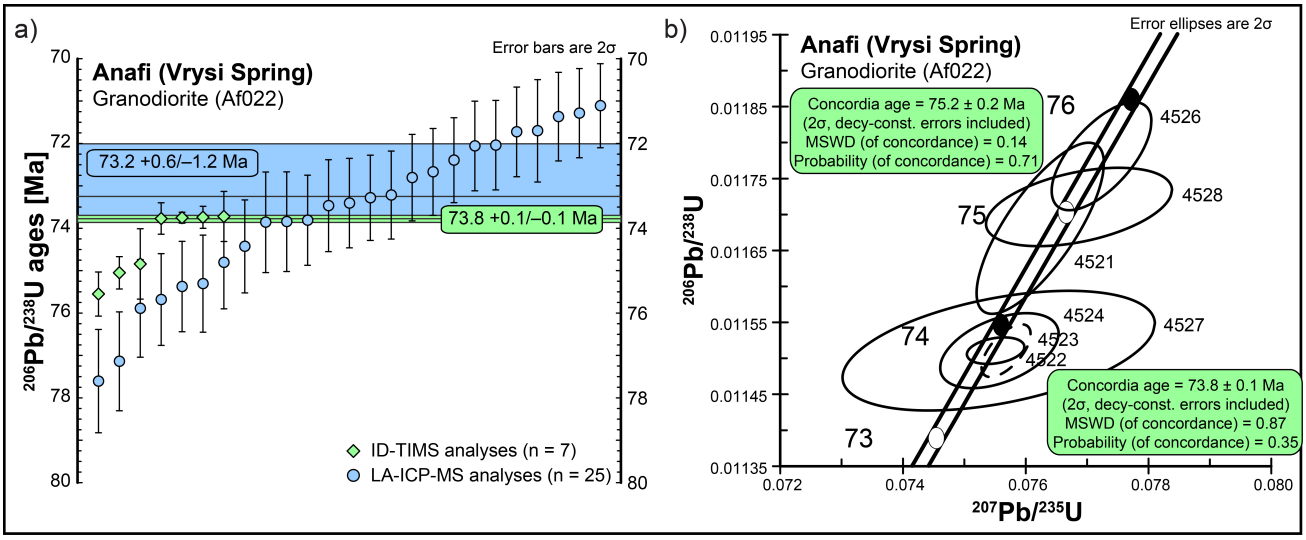

Fig. 2.14 LA-ICP-MS (blue) and ID-TIMS (green) $^{238}U/^{206}Pb$ zircon ages of granodiorite Af022 near the Vrysi Spring; (a) scatter plot with 95 % confidence interval of the median age; (b) U-Pb concordia diagram calculated from seven ID-TIMS analyses yielding two possible ages; numbering and error of the ellipses are given in Table 2.5.

Zircons separated from a *monzogranite dyke (Af023)* near the Profitis Ilias chapel for LA-ICP-MS analyses have a lower uranium content than zircons from granodiorite samples, ranging from 248 to 3901 ppm, but the amount of Pbc is still low (Table 2.4). Twenty-four analyses yield concordant $^{238}U/^{206}Pb$ ages ranging from 60.0 ± 0.9 Ma to 76.4 ± 1.1 Ma and the $^{238}U/^{206}Pb$ median age calculated

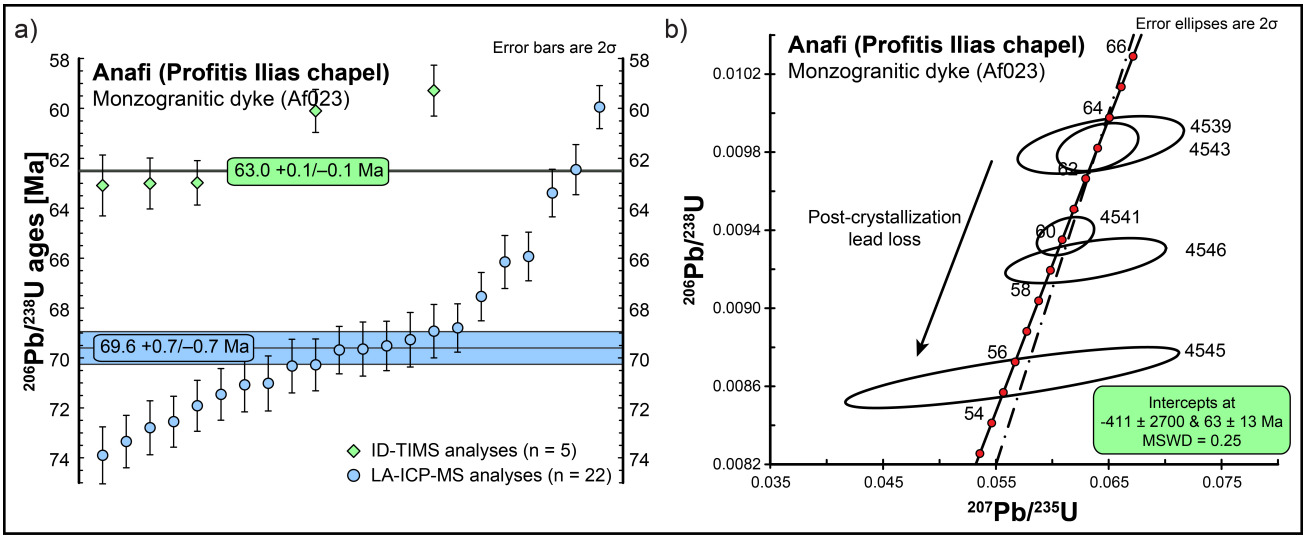

Fig. 2.15 LA-ICP-MS (blue) and ID-TIMS (green) $^{238}U/^{206}Pb$ zircon ages of monzogranite Af023 300 m W of the Profitis Ilias chapel; (a) scatter plot with 95 % confidence interval of the median age; (b) U-Pb discordia diagram calculated from ID-TIMS analyses; numbering and error of the ellipses are given in Table 2.5.

from nine analyses is 69.6 +0.7/–0.7 Ma (Fig. 2.15a). ID-TIMS was performed on small zircon fractions (three to ten grains per analysis). The uranium content was lower than in zircon from granodiorite used for ID-TIMS analyses (1472 to 3429 ppm; Table 2.5). In addition, the content of common lead is significantly higher. $^{238}U/^{206}Pb$ ages plot from 55.46 ± 0.82 to 63.09 ± 0.77 Ma with three analyses yielding a $^{238}U/^{206}Pb$ median age of 63.0 +0.1/–0.1 Ma (Fig. 2.15a). Despite its low $^{206}Pb/^{204}Pb$ ratio, analysis 4544 has a similar $^{238}U/^{206}Pb$ age as the oldest concordant analyses (4539 and 4543). Fig. 2.15b shows the influence of post-crystallization lead loss on ID-TIMS analyses.

2.6 Discussion

2.6.1 Implications for the magmatic evolution

Magmatic zircons of three samples of granodiorite, which intruded into Asterousia-type marble in northeastern and southern Anafi, analysed with LA-ICP-MS yielded concordant $^{238}U/^{206}Pb$ ages ranging from 67.3 ± 1.0 Ma to 78.8 ± 1.2 Ma (middle Campanian to Maastrichtian) and one significantly older concordant age of 83.9 ± 1.2 Ma (late Santonian). By interpreting the $^{238}U/^{206}Pb$ ages as crystallization ages of zircon, the data suggest several zircon populations in each sample (Fig. 2.11a, 12a, 13a). $^{238}U/^{206}Pb$ median ages calculated for the zircon populations considered most probable are 72.55 +0.8/–0.2 Ma (Af021), 73.2 +0.6/–1.2 Ma (Af022), 74.0 +0.8/–0.5 Ma (Af016), and 75.7 ± 0.4 Ma (Af021). Since zircon of each of these zircon populations is present in all three samples, a joint evolution of the three granodiorite samples is implied.

The $^{238}U/^{206}Pb$ median age calculated from 41 analyses of the combined dataset is 73.3 ± 0.3 Ma (Fig. 2.16). Nonetheless, it is also obvious from Fig. 2.16 that the precision of the LA-ICP-MS analyses

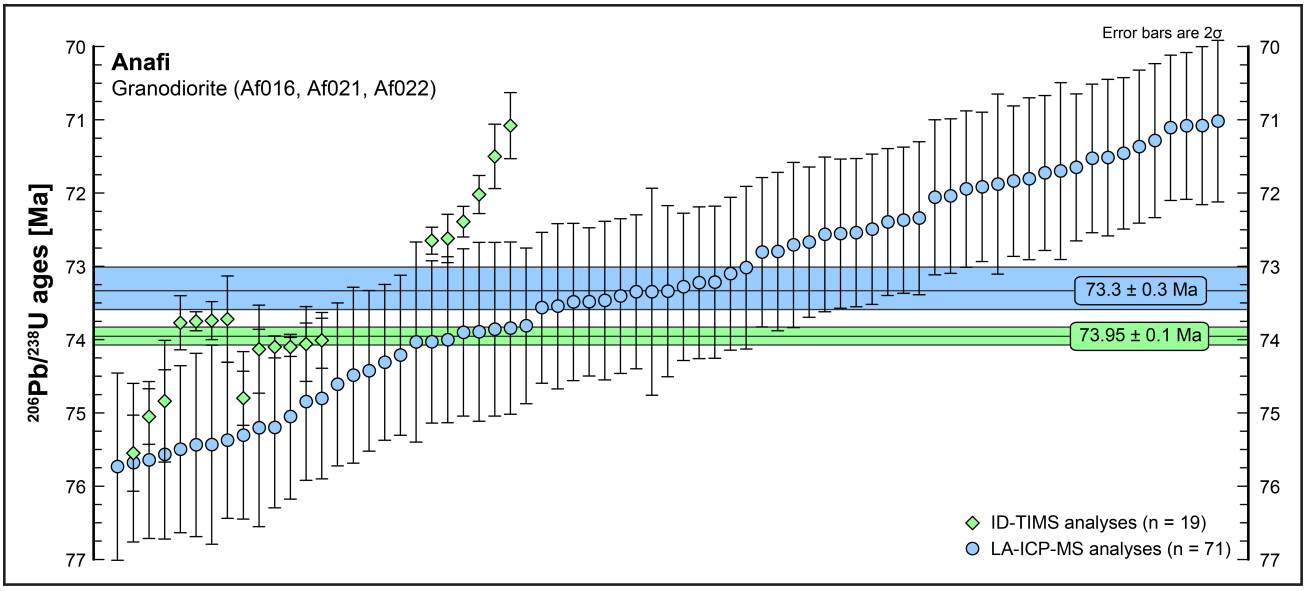

Fig. 2.16 Scatter plot showing a compilation of LA-ICP-MS (blue) and ID-TIMS (green) $^{238}U/^{206}Pb$ zircon ages of three granodiorite samples (Af016, Af021 and Af022) from Anafi with 95 % confidence interval of the median age. Analyses with $^{238}U/^{206}Pb$ ages ranging from 70 to 76 Ma only were considered.

does not allow distinguishing the different zircon populations in the combined dataset, despite 2σ uncertainties being 1.3 to 2.0 % of the $^{238}U/^{206}Pb$ age and thus lower than the uncertainties usually obtained for LA-ICP-MS data, which is 2–8 % (Peytcheva and von Quadt 2011). The $^{238}U/^{206}Pb$ median ages of the youngest (72.55 +0.8/–0.2 Ma) and the oldest (75.7 ± 0.4 Ma) zircon population are considered as the minimum and the maximum emplacement age of granodiorite. Younger $^{238}U/^{206}Pb$ ages point to post-crystallization lead loss, while $^{238}U/^{206}Pb$ ages older than 75.7 ± 0.4 Ma might indicate that magmatic activity has already been active during the middle Campanian and probably already during the late Santonian.

ID-TIMS analyses of zircon from the same samples corroborate a late Campanian age of zircon from the Anafi granodiorite. Granodiorite samples collected from northeastern Anafi yielded concordia U-Pb zircon ages at 74.0 ± 0.1 Ma (Af021) and 73.8 ± 0.1 Ma (Af022), while sample Af022 yielded also a second concordia age at 75.2 ± 0.2 Ma (Figs. 2.13b, 2.14b). Although the lower MSWD and the higher probability favour the older concordia age for granodiorite Af022, three of the four zircons defining the younger concordia age have the highest $^{206}Pb/^{204}Pb$ ratio (Table 2.5). Granodiorite from southern Anafi (Af016) yielded a younger concordia age at 72.5 ± 0.1 Ma (Fig. 2.11b). However, the probability of this concordia age is low (0.56) and the MSWD is high (0.34). The discordia line for zircon of granodiorite Af016 intercepts at 74.8 ± 7 Ma and has a lower MSWD of 0.013. The ID-TIMS concordia ages overlap with $^{238}U/^{206}Pb$ median ages of LA-ICP-MS analyses. The ID-TIMS concordia ages of granodiorite Af021 (74.0 ± 0.1 Ma) and of granodiorite Af022 (73.8 ± 0.1 Ma) are identical with the LA-ICP-MS $^{238}U/^{206}Pb$ median age of granodiorite Af016 (74.0 +0.8/–0.5 Ma), while the older ID-TIMS concordia age of granodiorite Af022 (75.2 ± 0.2 Ma) is identical with the LA-ICP-MS

$^{238}U/^{206}Pb$ median age of granodiorite Af021 (75.7 ± 0.4 Ma). Furthermore, the ID-TIMS concordia age of granodiorite Af016 (72.5 ± 0.1 Ma) is identical with the LA-ICP-MS $^{238}U/^{206}Pb$ median age of granodiorite Af021 (72.55 +0.8/–0.2 Ma).

Be'eri-Shlevin et al. (2009) reported an older Coniacian to Santonian intrusion age for the Anafi granodiorite (which they termed 'biotite granite'). They analysed samples from northeastern Anafi (close to the Vrysi Spring) and from southern Anafi (ca. 1 km NE of the Klisidi Beach) using ID-TIMS and obtained two $^{238}U/^{206}Pb$ ages overlapping the concordia at 75 Ma (NE Anafi) and ca. 72 Ma (S Anafi), respectively. However, Be'eri-Shlevin et al. (2009) calculated a discordia line using analyses of both samples and interpreted the upper intercept (85.3 ± 2.7 Ma) as the crystallization age of zircon. We combined $^{238}U/^{206}Pb$ zircon ages from ID-TIMS analyses of the Anafi granodiorite from this study and from Be'eri-Shlevin et al. (2009) in one boxplot diagram (Fig. 2.17). At least three zircon populations can be observed. Granodiorite from northeastern Anafi define $^{238}U/^{206}Pb$ median ages of 73.95 ± 0.1 Ma (ten analyses) and of 74.8 +0.2/–0.1 Ma (four analyses), while samples from southern Anafi define a younger $^{238}U/^{206}Pb$ median age of 72.6 +0.1/–0.2 Ma (three analyses). However, it is considered statistically more likely to argue that zircon from older populations at ~74 Ma in granodiorite from southern Anafi has not been measured with ID-TIMS in both studies than assuming a distinct evolution of granodiorite from southern Anafi and from northeastern Anafi, which is not supported by the LA-ICP-MS data. Two ID-TIMS analyses yielded slightly older $^{238}U/^{206}Pb$ ages at 75.5 Ma, while the oldest $^{238}U/^{206}Pb$ ages obtained are from granodiorite of southern Anafi (77.3 ± 0.3 Ma and 79.4 ± 0.3 Ma, Be'eri-Shlevin et al. 2009). Different younger ages are discordant and interpreted to result from post-crystallization lead loss.

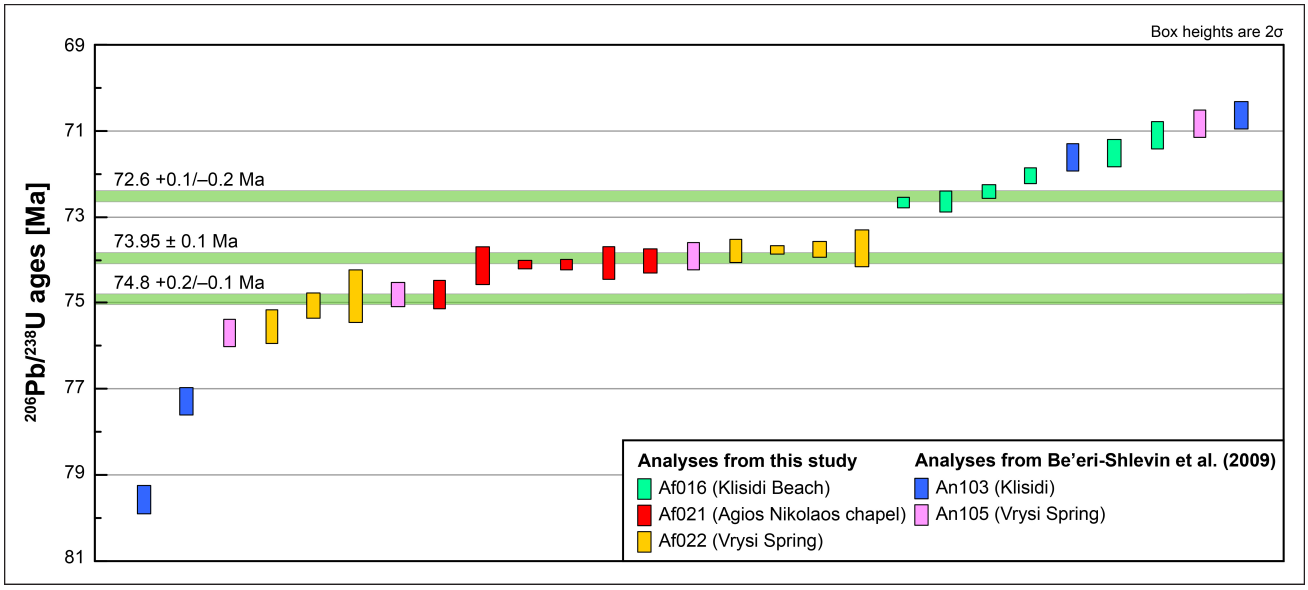

Fig. 2.17 Boxplots summarizing 27 ID-TIMS $^{238}U/^{206}Pb$ zircon ages of analyses on granodiorite from Anafi from this study and from Be'eri-Shlevin et al. (2009). Three $^{238}U/^{206}Pb$ median ages (given with the 95 % confidence intervals of the median age) were calculated for the combined dataset.

Taken together, both LA-ICP-MS and ID-TIMS analyses of zircons from granodiorite of Anafi suggest that granodiorite contains several zircon populations, which can be reproduced by both methods. The most likely $^{238}U/^{206}Pb$ ages interpreted as crystallization ages of different zircon populations from the Anafi granodiorite are 72.6 +0.1/–0.2 Ma, 73.95 ± 0.1 Ma, and 74.8 +0.2/–0.1 Ma ($^{238}U/^{206}Pb$ median ages of ID-TIMS analyses). These ages are within the error uncertainties of the $^{238}U/^{206}Pb$ median ages calculated from LA-ICP-MS analyses. Zircon populations yielding $^{238}U/^{206}Pb$ ages older than the $^{238}U/^{206}Pb$ median ages of these zircon populations suggest continuous magmatic activity inside the Asterousia realm during the middle to late Campanian. The minimum emplacement age of granodioritic magma inside the Asterousia-type marble of Anafi is 72.6 +0.1/–0.2 Ma. A late Campanian emplacement of granodiorite inside Asterousia-type marble on Anafi is also supported by the U-Pb zircon age (74.5 ± 0.25 Ma) obtained from quartzdiorite intruded into Asterousia-type marble near Pachia Ammos in eastern Crete (Kneuker et al. 2015).

Most U-Pb analyses of zircon from monzogranite Af023 yielded younger $^{238}U/^{206}Pb$ ages compared with the ages of the Anafi granodiorite (Fig. 2.15a). A younger intrusion of monzogranite is in line with monzogranite dykes cutting through granodiorite in northeastern Anafi. The $^{238}U/^{206}Pb$ median age calculated from ten analyses point to a crystallization of zircon at 69.9 +0.7/–0.7 Ma (Maastrichtian). LA-ICP-MS analyses of zircon yielding older $^{238}U/^{206}Pb$ ages at 72 to 74 Ma might be inherited from granodiorite. ID-TIMS analyses suggest a younger crystallization of zircon at ~63 Ma (middle Danian). However, the results are from zircon fractions of several small grains with a high specific surface and the content of common lead is high for these analyses. The impact of the common lead correction on the $^{238}U/^{206}Pb$ ages and their uncertainties is therefore larger than for other analyses. The precision suggested by the small uncertainties of the calculated $^{238}U/^{206}Pb$ median age is ambiguous and the ID-TIMS $^{238}U/^{206}Pb$ ages of zircons is believed to reflect post-crystallization lead loss (Fig. 2.15b). LA-ICP-MS data is not or less influenced by lead loss, because of the much smaller volume of zircon analysed and the careful monitoring of the measured oscillatory zoned domains by cathodoluminescence images during laser ablation. We therefore believe that the $^{238}U/^{206}Pb$ median age of 69.9 +0.7/–0.7 Ma calculated from LA-ICP-MS better reflects the true crystallization age of zircon from monzogranite Af023. Emplacement of monzogranitic dykes inside granodiorite of northeastern Anafi should be therefore Maastrichtian in age. Younger $^{238}U/^{206}Pb$ ages, including the ages obtained from ID-TIMS analyses, may reflect post-crystallization lead loss.

It is noteworthy that both the granodiorite samples and the monzogranite sample contain no zircon yielding $^{238}U/^{206}Pb$ ages older than late Santonian. This means that inherited zircon from reworked continental crust lacks. Therefore, the data suggest that the reworked magma might be derived from subducted oceanic crust.

2.6.2 Implications for the tectonometamorphic evolution of the Anafi nappe stack

Apart from north-western Anafi, the mineral/stretching lineation of the Anafi Greenschist shows a consistent NW–SE orientation (Fig. 2.7b). Asymmetric fabrics in the Anafi Greenschist displaying the NW–SE-trending mineral/stretching lineation indicate a top-to-the SE sense of shear (Fig. 2.6b). The mineral assemblage (actinolite, albite, epidote-group minerals) as well as the deformation microfabrics (spaced cleavage, shape-preferred orientation of minerals) observed imply metamorphic conditions as high as upper greenschist facies. However, quartz lenses show undulatory extinction and chessboard-type subgrains in thin section, which reflects deformation at T > 600 °C instead (e.g. Kruhl 1996). As the Anafi Greenschist is almost free from quartz, except for these lenses, and further evidence for high-temperature deformation lacks, we regard these high-temperature deformation structures as inherited. Taking into consideration that the protolith of the greenschist is basalt (Reinecke et al. 1982), quartz lenses might have been engulfed as xenoliths by the protolithic basaltic magma during rise from lower structural levels.

The brittle thrust between the Anafi Greenschist and the underlying flysch sediments is associated with SE-directed transport, which is corroborated by the vergence of folds within the flysch sediments. In contrast, the contact between the Anafi Greenschist and the overlying Anafi Amphibolite Group is mylonitic (Fig. 2.4a). Close to the contact zone with the Anafi Greenschist, the mineral/ stretching lineation is trending NW–SE (Fig. 2.7d) in all rock types of the Anafi Amphibolite Group (orthoamphibolite and metasedimentary intercalations) and truncated fish and sigmoidally shaped quartz grains indicate top-to-the SE tectonic transport (Figs. 2.4b, 2.6c, d). Folds within the orthoamphibolite indicate both a NE- and a NW-oriented vergence (Fig. 2.4e). Both fold types affect the foliation and should therefore be younger than the mylonitic top-to-the SE shearing.

K-Ar hornblende ages of the orthoamphibolite yielded 68.9 ± 0.8 Ma and 69.3 ± 2.2 Ma, respectively (Reinecke et al. 1982). The closure temperature for the K-Ar system of hornblende has been assessed at 530 ± 40 °C (Harrison 1981). Be'eri-Shlevin et al. (2009) estimated peak temperatures of 677–726 ºC for amphibolite facies metamorphism of orthoamphibolite using the edenite-tremolite geothermometer for hornblende assemblages of Holland and Blundy (1994) on results from electron microprobe analysis. This means that the peak of amphibolite facies metamorphism could be significantly older than the K-Ar hornblende ages.

Amphibolite facies metasedimentary rocks, serpentinite and igneous rocks, which form the Chalepa Group, are separated from the underlying units by brittle thrusts (Fig. 2.5c) with slickenside striation indicating N–S-trending movements. Metasediments of this unit are foliated. As for the upper parts of the Anafi Amphibolite Group, two mineral lineations, one NE–SW-oriented and another NW–SE-

oriented, can rarely be observed within these rocks (Fig. 2.7f). However, no reliable shear sense indicators associated with either of the two motions could be found. Since the NE–SW-oriented mineral/stretching lineation is found subordinate only in the upper parts of the Anafi Amphibolite Group, i.e. remote from the mylonitic thrust between Anafi Greenschist and Anafi Amphibolite Group, and within the Chalepa Group, it is believed that this lineation is older than the dominant NW–SE-oriented mineral/stretching lineation.

Serpentinite, although showing evidence of having been affected by HT–LP metamorphism (spinel chemistry analyses in Be'eri-Shlevin et al. 2009), which means that serpentinite slices must have been incorporated within the Anafi metasediments before HT–LP metamorphism, is not foliated. From the amphibolite facies metasediments only one K-Ar biotite age of paragneiss (63.5 ± 0.5 Ma) has been reported (Reinecke et al. 1982). The closure temperature for the K-Ar system of biotite has been constrained at 310 ± 30 °C (Harrison et al. 1985).

Plutonic rocks are free from a grain-shape fabric, whereas chessboard-type subgrains in quartz of granodiorite samples (Fig. 2.9a), as well as strain-induced myrmekite suggest low subsolidus strain accommodated at high temperature (> ca. 650 °C, Vernon 1991). High temperature deformation of the granodiorite is further corroborated by strongly curved and lobate grain boundaries between quartz and feldspar indicating solid-state diffusion creep (Gower and Simpson 1992), which is possible only under upper amphibolite to granulite facies conditions. High-temperature deformation fabrics in plutonic rocks could be interpreted that the plutonic rocks underwent HT–LP metamorphism along with the surrounding high-grade metamorphic rocks. This is further suggested by K-Ar ages of hornblende of the plutonic rocks (Reinecke et al. 1982), which are identical with the K-Ar hornblende ages of orthoamphibolite from the Anafi Amphibolite Group when considering the 2σ uncertainties (Fig. 2.18). K-Ar dating of biotite and Rb-Sr analyses of biotite-plagioclase of the granodiorite yielded early Danian ages (63.6 ± 0.6 to 65.1 ± 0.6 Ma and 63.4 ± 0.4 Ma, respectively; Reinecke et al. 1982; Be'eri-Shlevin et al. 2009), which are compatible with the K-Ar age of biotite from paragneiss (63.5 ± 0.5 Ma; Reinecke et al. 1982) of the metasediments (Fig. 2.18). Thus, the plutonic rocks should have cooled down coevally with the other Asterousia-type crystalline rocks below the closure temperatures of hornblende and biotite, respectively.

The development of a pervasive foliation in granitoids is strongly influenced by the amount of mechanically weak phases, particularly of quartz. Given that granitoids with high amounts of quartz and phyllosilicates are deformed under greenschist or amphibolite facies conditions, they are in most cases foliated due to pervasive viscous strain of the weak phases. Granitoids, which are poor in quartz and phyllosilicates, however, largely remain unfoliated (e.g. Vernon and Flood 1988). In the granitoids examined in the present study, the amount of weak minerals ranges between 24 to 47 % (Table 2.3),

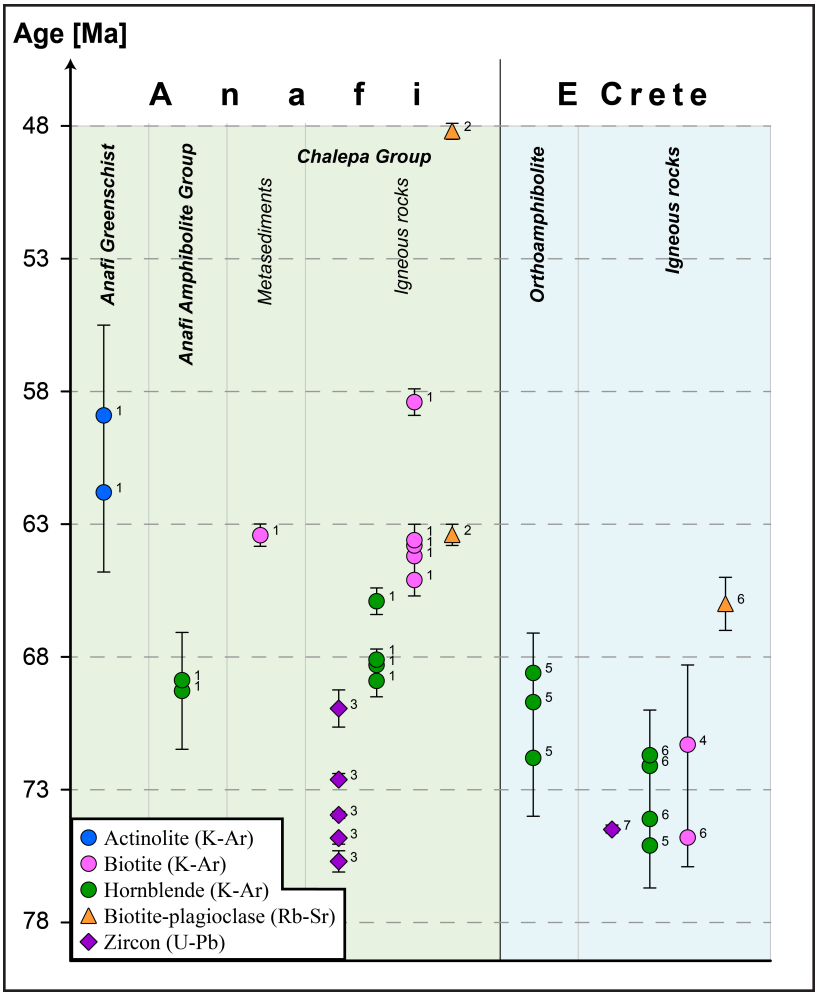

Fig. 2.18 Scatter plot summarizing geochronological data from Anafi and the areas of Pachia Ammos and Kritsa in eastern Crete. U-Pb ages from Anafi are $^{238}U/^{206}Pb$ median ages of the most probable zircon populations from this study. Data of Anafi are sorted for tectonic units. Data sources: *Anafi* [1]Reinecke et al. (1982), [2]Be'eri-Shlevin et al. (2009), and [3]this study; *Eastern Crete* [4]Lippolt and Baranyi (1976), [5]Seidel et al. (1981), [6]Langosch et al. (2000), and [7]Kneuker et al. (2015). Data from Lippolt and Baranyi (1976) was recalculated in Seidel et al. (1981).

thus implying that they should be foliated if they had faced amphibolite facies metamorphic conditions. As the granitoids are unfoliated, it is rather assumed that they intruded into Asterousia-type marble late- or post-kinematically with respect to the metamorphic rocks, and that weak deformation under high temperature was active during the initial cooling phase of the plutons.

Compared to the plutonic rocks, the microstructures of the igneous dykes cutting through the Chalepa Group in northeastern and southeastern Anafi reveal different structures. Samples from monzogranitic dykes cutting through granodiorite and from anorthosite dykes cutting through serpentinite are entirely free from a grain-shape fabric and from high-temperature deformation. Instead, weak undulatory extinction, fluid inclusions and deformation lamellae in quartz of the monzogranite as well as fracturing of feldspar in anorthosite indicate deformation under brittle conditions. Intrusion of monzogranitic and anorthosite dykes should therefore be post-metamorphic.

2.6.3 Provenance of the Anafi tectonic units

The protoliths of the Chalepa Group metasediments (calcsilicate rock, micaschist, marble, paraamphibolite, and quartzite) are interpreted as a variegated series (for example limestone and marl) deposited on a continental platform. The protolith of the orthoamphibolite from the Anafi Amphibolite Group is basalt with geochemical signature of back-arc basin tholeiites (Reinecke et al. 1982). The orthoamphibolite must therefore have been formed in the back-arc basin of a former subduction zone in the upper plate. The metasediments situated at the base of the Anafi Amphibolite Group (calcsilicate

rock, micaschist, and quartzite) are regarded as sedimentary deposits during short interruption of basaltic magmatism.

More divisive is the provenance of the Anafi Greenschist, which differs from the Asterousia-type crystalline rocks concerning both the metamorphic grade and the cooling history. Reinecke et al. (1982) determined Middle to Late Palaeocene K-Ar cooling ages of actinolite (Fig. 2.18). As the closure temperature of the K-Ar system of actinolite (470 ± 25 °C; Dahl 1996) is close to the peak of greenschist facies metamorphism, this age should approximately reflect the age of the greenschist facies metamorphism. In contrast to the greenschist, the Asterousia-type crystalline rocks had already cooled down below the closure temperature of biotite during the Early Palaeocene (Fig. 2.18).

Greenschist facies metamorphism in the Cyclades is usually associated with Oligocene to Miocene retrograde overprint of Cycladic blueschists (e.g. Altherr et al. 1982; Schliestedt et al. 1987). K-Ar ages of the Anafi Greenschist, however, exclude such a correlation. Furthermore, the rocks of the Cycladic Blueschist Unit have been affected by Eocene blueschist to eclogite facies metamorphism (Okrusch and Bröcker 1990), which is younger than the greenschist facies metamorphism of the Anafi Greenschist.

Greenschist facies metabasite in northeastern Mykonos does not show blueschist facies fabrics and has therefore not been attributed to the Cycladic Blueschist Unit but related to the Upper Unit (Dürr and Altherr 1979). This metabasite is cut by dykes in the lower part and intruded by Miocene granite, which forms the base (Dürr et al. 1978a; Lecomte et al. 2010). It is overlain by Miocene molasse sediments (Dürr and Altherr 1979). The metabasite is strongly deformed. However, greenschist facies metamorphism on Mykonos has not been dated yet, nor are geochemical analyses available allowing a comparison with the Anafi Greenschist. A correlation of the Mykonos Greenschist with the Anafi Greenschist, as already implied in Reinecke et al. (1982), is therefore tempting but needs further studies.

Taking into consideration the metamorphic grade of the Anafi Greenschist, a correlation with the low-grade metamorphic subunits of the Uppermost Unit on Crete is likely. This would be the only known exposure of the low-grade metamorphic subunits of the Uppermost Unit in the Cyclades. Indeed, Bonneau (1984) suggested a correlation of the Anafi Greenschist with the Arvi Unit. The Arvi Unit is exposed in the southern Dikti Mountains near Arvi and in the western Asterousia Mountains (e.g. Robert and Bonneau 1982) and probably also in the area of Anogia–Gonies (Thorbecke 1973, 1987; Bonneau et al. 1977). However, the Arvi Unit is anchimetamorphic (Robert and Bonneau 1982), the age of anchimetamorphism being unknown. Basaltic pillow lavas, which could be considered as protoliths of the Anafi Greenschist occur at the base of the Arvi Unit (Palamakumbura et al. 2013).

Geochemical patterns of the Arvi basalt show ocean island basalt (OIB) characteristics (Palamakumbura et al. 2013) in contrast to the MORB patterns of the Anafi Greenschist (Reinecke et al. 1982). A relationship of the Anafi Greenschist with the Arvi basalt is therefore unlikely. The protolith of the Arvi Unit, as exposed in the southern Dikti Mountains, are interpreted to result from a Late Cretaceous seamount that formed in the northern domain of the Pindos Ocean (Palamakumbura et al. 2013).

New findings of greenschist facies rocks in the area of Melambes in central Crete demand further studies, but preliminary results show that greenschist facies rocks at the base of the Asterousia Crystalline Complex might have been more widespread than previously believed (Wiesenbach et al. 2014). A correlation of the Anafi Greenschist with low-grade metamorphic subunits of the Uppermost Unit (i.e. Preveli, Spili, and Vatos Units, respectively) is unlikely. Greenschist facies rocks were recorded only from the Spili Unit, but K-Ar ages of hornblende yielded Jurassic ages (Seidel et al. 1981; Krahl et al. 1982). The Preveli Unit shows blueschist facies metamorphic overprint and the Vatos Unit consists of low-grade metamorphic sediments and ophiolite pebbles (Krahl et al. 1982).

Thus, the affinity of the Anafi Greenschist remains enigmatic with three possible equivalents in the southern Aegean region. Greenschist facies rocks might represent a higher metamorphosed part of the Arvi Unit to the north if the basic volcanics at the base of the Arvi Unit prove to be the protolith of the Anafi and Mykonos Greenschists or we might deal with remnants of a Palaeocene Greenschist Unit at the base of the Asterousia Crystalline Complex. However, other scenarios are also possible. The limited data from all three equivalents do not allow a conclusive statement, but encourage further studies to unravel the story behind Middle to Late Palaeocene greenschist facies metamorphism in the southern Aegean.

2.6.4 Regional tectonic implications

Serpentinite inside the Asterousia-type rocks is not compatible with the surrounding rocks and is therefore interpreted as tectonic slices, which should have been obducted and accreted to the upper plate (the Asterousia-type rocks) during northward subduction of Neotethys lithosphere. For this reason, the incorporation of serpentinite within the Asterousia-type rocks predates amphibolite facies metamorphism affecting the Asterousia-type rocks.

The new U-Pb zircon ages suggest that plutonic rocks intruded into the Chalepa Group during the middle to late Campanian from ca. 72.5 to 79 Ma. Published REE patterns suggest the Anafi plutonics to plot in the volcanic-arc field (Koutsovitis et al. 2012), which is consistent with plutonic magmatism in the magmatic arc of a subduction zone. This is further corroborated by high $^{87}Sr/^{86}Sr$ initial isotope ratios (0.706167 to 0.706752; Be'eri-Shlevin et al. 2009) implying a crustal signature of reworked subducted crust. Thus, the igneous rocks investigated in the present study should have intruded inside

a Campanian magmatic arc that was affected by high heat flow and related HT–LP metamorphism responsible for pervasive deformation of both the Anafi Amphibolite Group and the metasediments and serpentinite slices of the Chalepa Group. Both the metamorphic and the plutonic rocks cooled down collectively as suggested by the published K-Ar cooling ages (Fig. 2.18).

U-Pb ages and K-Ar ages of the crystalline rocks on Anafi indicate very slow cooling of the Asterousia-type crystalline rocks. The plutonic rocks of Anafi are therefore believed to have intruded at deep structural levels, where the temperature of the country rock was high. During slow cooling the time for high-temperature deformation in intrusive rocks was sufficient. This situation is in striking contrast to the situation in eastern Crete, where dioritic rocks intruded into marble at the same time, but at upper structural levels as is indicated by rock fabrics and by similar U-Pb zircon and K-Ar cooling ages (Fig. 2.18; Kneuker et al. 2015).

Magmatic arc settings with similar intrusion ages like those obtained in the present study are known from at least two adjacent regions. A magmatic belt of Late Cretaceous age is present in south-eastern Europe and northern Anatolia. The Pontide magmatic belt runs along the southern Black Sea coast from Georgia to the Marmara Sea. It is generally interpreted as the zone, where the Neotethyan lithosphere was subducted underneath the Pontides (e.g. Okay 2008 and references therein). Andesitic dykes in the Strandja Massif (north-western Turkey) revealed ages of 78 Ma (Moore et al. 1980), while granitoid intrusions in the Beypazarı region of the Sakarya Zone yielded ages of 72.5 ± 12.6 to 78.6 ± 4.7 Ma (Helvacı et al. 2014). Çinku et al. (2010) assumed southward migration of arc magmatism during the Turonian to Maastrichtian of up to 450 km in the Sakarya Zone. In south-eastern Europe, the western Black Sea Fault separates the Pontide magmatic belt from the Banatitic Magmatic and Metallogenetic Belt (or Apuseni–Banat–Timok–Srednogorie Belt), which runs from the Bulgarian Black Sea coast south of the Balkan Mountains, through eastern Serbia and south-western Romania. The Banatitic Belt contains calc-alkaline rocks of gabbroic to granitic composition. U–Pb zircon ages of ca. 92 to 78 Ma (ID-TIMS) were obtained for subvolcanic and plutonic rocks from the central Srednogorie Zone (von Quadt et al. 2005) in western Bulgaria and similar ages (ID-TIMS and LA-ICP-MS) also from the western Srednogorie (Georgiev et al. 2012). U–Pb ages (SIMS on zircon) from granodiorite of the Banat Region in Romania yielded 79.6 ± 2.5 Ma and 75.5 ± 1.6 Ma (Nicolescu et al. 1999). For a summary of geochronological data from the Banatitic Belt, see von Quadt et al. (2007; fig. 1). Late Cretaceous HT–LP metamorphism, however, is unknown from this magmatic belt.Another region, which has been interpreted as a magmatic arc is the Central Anatolian Crystalline Complex in central Turkey (Lefebvre 2011). It consists of metasedimentary (amphibolite, calcsilicate rock, marble, micaschist, paragneiss, and quartzite; e.g. Seymen 1983) and plutonic (mainly granite, gran-

odiorite, quartz-monzonite, and quartz-monzodiorite; Akıman et al. 1993) rocks. HT–LP metamorphism (greenschist to granulite facies) occurred during the middle Turonian to early Santonian with U-Pb ages (SHRIMP) on monazite yielding ca. 91–85 Ma (Whitney et al. 2003). Intrusion of plutonic rocks is dated at 71 ± 2 Ma to 78 ± 3 Ma (U-Pb on zircon; LA-ICP-MS; Köksal et al. 2013), thus perfectly correlating with the plutonic activity determined for the Asterousia Crystalline Complex. $^{87}Sr/^{86}Sr$ initial isotope ratios (0.70826–0.70917) are higher than those of the Anafi granodiorite implying also a crustal signature (Köksal et al. 2013). HT–LP metamorphism being older than intrusive magmatism is another striking similarity between the Central Anatolian Crystalline Complex and the Asterousia-type crystalline rocks on Anafi.

Stacking of the Anafi crystalline units was related to ductile SE-directed thrusting that carried the Anafi Amphibolite Group on top of the Anafi Greenschist at deep structural levels (Fig. 2.19). Based on the K-Ar actinolite ages of the Anafi Greenschist, this event is constrained as Palaeocene. The NW–SE-oriented mineral/stretching lineation and the top-to-the SE shear sense indicators are associated with this event. An ill-defined, inherited NE–SW-oriented mineral/stretching lineation has been largely overprinted and erased during greenschist facies thrusting but is better defined within the amphibolite facies rocks further off the mylonitic thrust contact.

Thus, Palaeocene greenschist facies metamorphism of the Anafi Greenschist is synchronous with the early nappe stacking. Progressive shortening resulted in brittle SE-directed thrusting of both the Anafi Greenschist and the Anafi Amphibolite Group on top of the Eocene flysch at upper structural levels (Fig. 2.19) and SE-vergent folds observed within all three units. Due to the age of the flysch sediments, this event is late or post Eocene in age. Meanwhile, the metasediments, igneous rocks and serpentinite of the Chalepa Group must have been internally stacked under brittle conditions. Prolonged shortening of the lithosphere and clockwise rotation caused southward brittle thrusting of the Chalepa Group on top of all units underneath (Fig. 2.19). This event should have occurred during the (Early) Oligocene. Ongoing clockwise rotation of the Aegean block lead to NE–SW-oriented compression being the dominant transport direction during the Oligocene to Early Miocene. NE-vergent

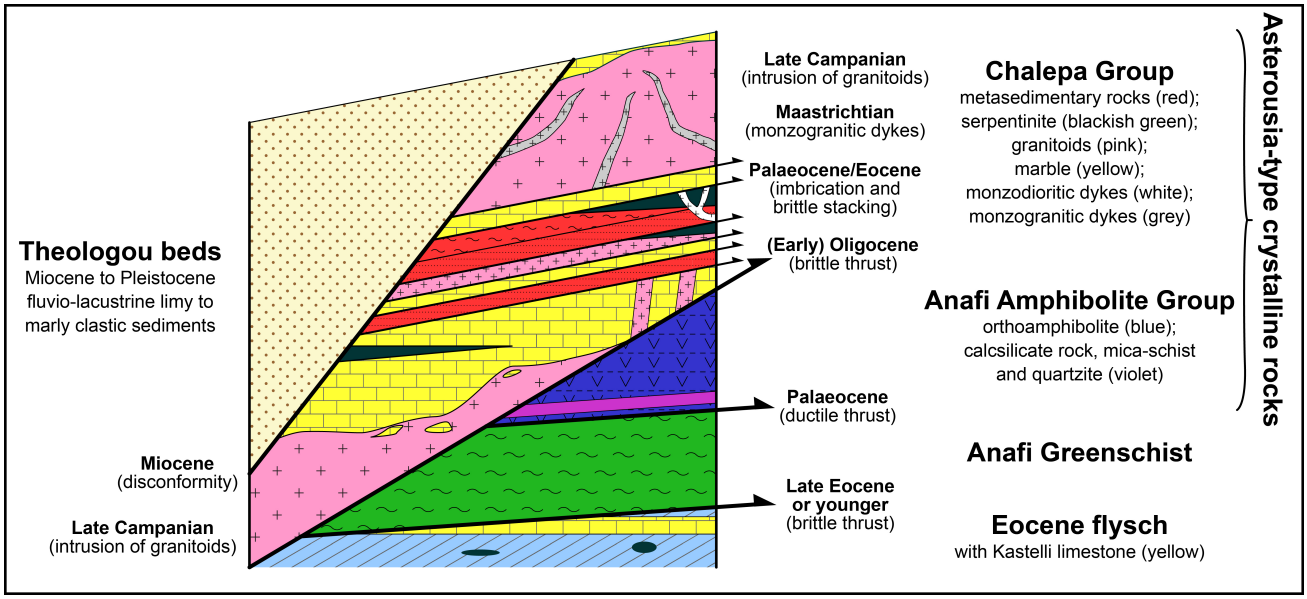

Fig. 2.19 Simplified, not to scale tectonostratigraphic column for Anafi showing the succession of tectonic units and indicating the age of tectonic contacts. Based on findings of Reinecke (1978), Reinecke et al. (1982) and own observations.

folds should have developed during this period. The Theologou Beds, which rest unconformably on top of all crystalline units and the Eocene flysch are Miocene to Pleistocene in age.

The implications for the tectonometamorphic and magmatic evolution of the crystalline rocks of Anafi presented above are not in line with published models (Soukis and Papanikolaou 2004; see chapter 2.3.1 for a summary of their model). The new data presented herein, combined with published data, revealed that the nappe emplacement on Anafi started with SE-directed ductile thrusting at lower structural levels followed by SE- and S-directed brittle thrusting at higher structural levels rather than SSW-directed brittle thrusting of the crystalline rocks on top of the flysch as previously suggested by Soukis and Papanikolaou (2004).

2.7 Conclusions

The following conclusions can be drawn based on the new data presented above:

(1) LA-ICP-MS and ID-TIMS analyses of zircon from granitoids intruded into Asterousia-type marble of the Chalepa Group on Anafi reproduced similar zircon populations of middle to late Campanian age. The $^{238}U/^{206}Pb$ median age of the youngest zircon population (72.6 +0.1/–0.2 Ma) is considered as the minimum emplacement age of granodiorite, while the main popolation at 74 Ma and older $^{238}U/^{206}Pb$ ages represent inherited zircons from older intrusive events. Zircon with older, inherited ages of continental crust were not found.

(2) Zircon from monzogranite records a separate intrusive event at 69.9 +0.7/–0.7 Ma unreported so far from the southern Aegean region.

(3) Intrusive magmatism is associated with partial melting of subducted crust and continuous intrusion of the reworked magma inside a volcanic arc situated on continental crust, where large amounts of marble occupied both the lower and the upper crust. Similarities in the metamorphic and magmatic evolution of the Asterousia Crystalline Complex and the Central Anatolian Crystalline complex demand further studies.

(4) The Asterousia-type crystalline rocks on Anafi (Anafi Amphibolite Group and Chalepa Group) represent a deep, ductile structural level of this unit, where plutonic rocks faced late- to post-intrusive high-temperature deformation. Comparison of U-Pb and K-Ar ages indicates very slow cooling of the Asterousia-type crystalline rocks on Anafi.

(5) Palaeocene greenschist facies metamorphism as observed within the Anafi Greenschist at the base of the Asterousia-type crystalline rocks is unique in the Internal Hellenides domain.

(6) The stacking of the different nappes on Anafi occurred during a period of continuous shortening and steady exhumation and uplift from lower to higher structural levels in a NW-dipping subduction/accretion complex during the Early to Middle Palaeogene. Prolonged compression and clockwise rotation of the complex is responsible for southward stacking during the Late Palaeogene and concluded with NE–SW compression during the Early Neogene.

2.8 Acknowledgements

We would like to thank Maria Bladt and Nils Prawitz for help with thin section production and Linda Marko for help with LA-ICP-MS analyses. We further would like to thank Tilo Dirk Kneuker for fruitful discussions regarding exposures of the Asterousia Crystalline Complex in the northern Ierapetra Graben and Joachim Krahl is thanked for valuable information on the stratigraphy of the Uppermost Unit. Eberhard Gischler and Anja Isaack are thanked for providing a point counter and introducing the first author to this method. Klaus Gessner, Petek Ayda Ustaömer and an anonymous reviewer are thanked for helpful reviews on the manuscript and Timur Ustaömer is thanked for editing our manuscript. The first author gratefully acknowledges financial support for fieldwork by the Hermann-Willkomm-Stiftung and by ERASMUS (Leonardo-da-Vinci programme; Grant Agreement no. 2013-1-DE2-LEO02-16568).

2.9 References

Akıman, O., Erler, A., Göncüoğlu, M.C., Güleç, N., Geven, A., Türeli, T.K. & Kadioğlu, Y.K. (1993): Geochemical characteristics of granitoids along the western margin of the Central Anatolian Crystalline Complex and their tectonic implications. – *Geological Journal*, **28** (3–4): pp. 371–382. DOI: 10.1002/gj.3350280315.

Allmendinger, R.W., Cardozo, N. & Fisher, D.M. (2012): *Structural geology algorithms: vectors and tensors*. – Cambridge University Press, 289 p.; Cambridge.

Altherr, R., Kreuzer, H., Lenz, H., Wendt, I., Harre, W. & Dürr, S. (1994): Further evidence for a Late-Cretaceous low pressure/high-temperature terrane in the Cyclades, Greece. Petrology and geochronology of crystalline rocks from the islands of Donoussa and Ikaria. – *Chemie der Erde*, **54**: pp. 319–328.

Altherr, R., Kreuzer, H., Wendt, I., Lenz, H., Wagner, G.A., Keller, J., Harre, W. & Höhndorf, A. (1982): A Late Oligocene/Early Miocene high temperature belt in the Attic-Cycladic Crystalline Complex (SE Pelagonian, Greece). – *Geologisches Jahrbuch, Reihe E*, **23**: pp. 97–164.

Altherr, R., Schliestedt, M., Okrusch, M., Seidel, E., Kreuzer, H., Harre, W., Lenz, H., Wendt, I. & Wagner, G.A. (1979): Geochronology of high-pressure rocks on Sifnos (Cyclades, Greece). – *Contributions to Mineralogy and Petrology*, **70** (3): pp. 245–255. DOI: 10.1007/BF00375354.

Altherr, R., Seidel, E., Okrusch, M., Schliestedt, M., Reinecke, T., Kreuzer, H., Harre, W., Klein, H. & Dürr, S. (1980): Metamorphic rocks associated with ophiolites in Greece: petrology and geochronology. – In: Panayiotou, A. (ed.) *International Ophiolite Symposium, Nicosia - Cyprus, 1–8 April, 1979. Abstracts of papers submitted*. Τμήμα Γεωλογικής Επισκόπησης [Geological Survey Department], pp. 9–10; Λευκωσία [Nicosia].

Aubouin, J. & Dercourt, J. (1965): Sur la géologie de l'Égée: regard sur la Crète (Grèce). – *Bulletin de la Société Géologique de France, série 7*, **7**: pp. 787–821.

Avigad, D. & Garfunkel, Z. (1989): Low-angle faults above and below a blueschist belt–Tinos Island, Cyclades, Greece. – *Terra Nova*, **1** (2): pp. 182–187. DOI: 10.1111/j.1365-3121.1989.tb00350.x.

Avigad, D., Garfunkel, Z., Jolivet, L. & Azañón, J.M. (1997): Back arc extension and denudation of Mediterranean eclogites. – *Tectonics*, **16** (6): pp. 924–941. DOI: 10.1029/97TC02003.

Baranyi, I., Lippolt, H.J. & Todt, W. (1975): Kalium-Argon-Datierungen an zwei Magmatiten von Kalo Chorio, Nord-Ost-Kreta. – *Neues Jahrbuch für Geologie und Paläontologie, Monatshefte*, **5**: pp. 257–262.

Be'eri-Shlevin, Y., Avigad, D. & Matthews, A. (2009): Granitoid intrusion and high temperature metamorphism in the Asteroussia Unit, Anafi Island (Greece): petrology and geochronology. – *Israel Journal of Earth Sciences*, **58** (1): pp. 13–27. DOI: 10.1560/IJES.58.1.13.

Böger, H. (1983): Stratigraphische und tektonische Verknüpfungen kontinentaler Sedimente des Neogens im Ägäis-Raum. – *Geologische Rundschau*, **72** (3): pp. 771–813. DOI: 10.1007/BF01848344.

Bonneau, M. (1972): La nappe métamorphique de l'Asteroussia, lambeau d'affinités pélagoniennes charrié jusque sur la zone de Tripolitza de la Crète moyenne (Grèce). – *Comptes Rendus de l'Académie des Sciences, série D*, **275**: pp. 2303–2306.

Bonneau, M. (1973): Les différentes «séries ophiolitifères» de la Crète: une mise au point. – *Comptes Rendus de l'Académie des Sciences, série D*, **276**: pp. 1249–1252.

Bonneau, M. (1984): Correlation of the Hellenide nappes in the south-east Aegean and their tectonic reconstruction. – *Geological Society, London, Special Publications*, **17**: pp. 517–527. DOI: 10.1144/GSL.SP.1984.017.01.38.

Bonneau, M., Angelier, J. & Epting, M. (1977): Réunion extraordinaire de la Société Géologique de France en Crète. – *Bulletin de la Société Géologique de France, série 7*, **19** (1): pp. 87–102. DOI: 10.2113/gssgfbull.S7-XIX.1.87.

Bonneau, M., Beauvais, L. & Middlemiss, F.A. (1974): L'unité de Miamou (Crète - Grèce) et sa macrofaune d'âge Jurassique supérieur (Brachiopodes. Madreporaires). – *Annales de la Société Géologique du Nord*, **94** (2): pp. 71–85.

Bonneau, M., Blake Jr., M.C., Geyssant, J., Kienast, J.-R., Lepvrier, C., Maluski, H. & Papanikolaou, D.J. (1980): Sur la signification des séries métamorphiques (schistes bleus) des Cyclades (Hellénides, Grèce). L'exemple de l'île de Syros. – *Comptes Rendus de l'Académie des Sciences, série D*, **29**: pp. 1463–1467.

Bröcker, M. & Franz, L. (2006): Dating metamorphism and tectonic juxtaposition on Andros Island (Cyclades, Greece): results of a Rb-Sr study. – *Geological Magazine*, **143** (5): pp. 609. DOI: 10.1017/S001675680600241X.

Burkhard, M. (1993): Calcite twins, their geometry, appearance and significance as stress-strain markers and indicators of tectonic regime: a review. – *Journal of Structural Geology*, **15** (3–5): pp. 351–368. DOI: 10.1016/0191-8141(93)90132-T.

Cardozo, N. & Allmendinger, R.W. (2013): Spherical projections with OSXStereonet. – *Computers & Geosciences*, **51**: pp. 193–205. DOI: 10.1016/j.cageo.2012.07.021.

Chatzaras, V., Xypolias, P., Kokkalas, S. & Koukouvelas, I.K. (2011): Oligocene-Miocene thrusting in central Aegean: insights from the Cycladic island of Amorgos. – *Geological Journal*, **46** (6): pp. 619–636. DOI: 10.1002/gj.1304.

Chen, P.-Y. (1977): *Table of key lines in X-ray powder diffraction patterns of minerals in clays and associated rocks*. – State of Indiana, Department of Natural Resources, Geological Survey, 67 p.; Bloomington, Indiana.

Çinku, M.C., Ustaömer, T., Hirt, A.M., Hisarlı, Z.M., Heller, F. & Orbay, N. (2010): Southward migration of arc magmatism during latest Cretaceous associated with slab steepening, East Pontides, N Turkey: new paleomagnetic data from the Amasya region. – *Physics of the Earth and Planetary Interiors*, **182** (1–2): pp. 18–29. DOI: 10.1016/j.pepi.2010.06.003.

Dahl, P.S. (1996): The effects of composition on retentivity of argon and oxygen in hornblende and related amphiboles: a field-tested empirical model. – *Geochimica et Cosmochimica Acta*, **60** (19): pp. 3687–3700. DOI: 10.1016/0016-7037(96)00170-6.

Dörr, W., Belka, Z., Marheine, D., Schastok, J., Valverde-Vaquero, P. & Wiszniewska, J. (2002): U–Pb and Ar–Ar geochronology of anorogenic granite magmatism of the Mazury complex, NE Poland. – *Precambrian Research*, **119** (1–4): pp. 101–120. DOI: 10.1016/S0301-9268(02)00119-5.

Dürr, S. (1985): *Γεωλογικός χάρτης της Ελλάδος 1:50.000. Φύλλο Αμοργός–Δονούσα [Geological map of Greece 1:50,000. Amorgos–Donoussa sheet]*. – Geological map, Ινστιτούτο γεωλογικών και μεταλλεύτικων έρευνων [Institute of Geology and Mineral Exploration]; Αθήνα [Athens].

Dürr, S. & Altherr, R. (1979): Existence de klippes d'une nappe composite néogène dans l'île de Mykonos/Cyclades. – *Rapports et Procès-verbaux des Réunions / Commission Internationale pour l'Exploration Scientifique de la Mer Méditerranée*, **25/26** (2a): pp. 33–34.

Dürr, S., Altherr, R., Keller, J., Okrusch, M. & Seidel, E. (1978a): The Median Aegean Crystalline Belt: stratigraphy, structure, metamorphism, magmatism. – In: Closs, H., Roeder, D., Schmidt, K. (eds.) *Alps, Apennines, Hellenides: geodynamic investigation along geotraverses by an Internat. group of geoscientists*. Schweizerbart, pp. 455–478; Stuttgart.

Dürr, S., Seidel, E., Kreuzer, H. & Harre, W. (1978b): Témoins d'un métamorphisme d'âge crétacé supérieur dans l'Égéide: datations radiométriques de minéraux provenant de l'île de Nikouriá (Cyclades, Grèce). – *Bulletin de la Société Géologique de France, série 7*, **20** (2): pp. 209–213.

Elsner, A.E. (1981): Gliederung der "Theologus-Schichten" im Westteil der Insel Anaphi, Kykladen, Griechenland. – Diploma thesis, University of Kiel, 146 p. (unpubl.); Kiel.

Frei, D. & Gerdes, A. (2009): Precise and accurate in situ U-Pb dating of zircon with high sample throughput by automated LA-SF-ICP-MS. – *Chemical Geology*, **261** (3–4): pp. 261–270. DOI: 10.1016/j.chemgeo.2008.07.025.

Georgiev, S., von Quadt, A., Heinrich, C.A., Peytcheva, I. & Marchev, P. (2012): Time evolution of a rifted continental arc: integrated ID-TIMS and LA-ICPMS study of magmatic zircons from the Eastern Srednogorie, Bulgaria. – *Lithos*, **154**: pp. 53–67. DOI: 10.1016/j.lithos.2012.06.020.

Gerdes, A. & Zeh, A. (2006): Combined U–Pb and Hf isotope LA-(MC-)ICP-MS analyses of detrital zircons: comparison with SHRIMP and new constraints for the provenance and age of an Armorican metasediment in central Germany. – *Earth and Planetary Science Letters*, **249** (1–2): pp. 47–61. DOI: 10.1016/j.epsl.2006.06.039.

Gower, R.J.. & Simpson, C. (1992): Phase boundary mobility in naturally deformed, high-grade quartzofeldspathic rocks: evidence for diffusional creep. – *Journal of Structural Geology*, **14** (3): pp. 301–313. DOI: 10.1016/0191-8141(92)90088-E.

Harrison, T.M. (1981): Diffusion of 40Ar in hornblende. – *Contributions to Mineralogy and Petrology*, **78** (3): pp. 324–331. DOI: 10.1007/BF00398927.

Harrison, T.M., Duncan, I. & McDougall, I. (1985): Diffusion of 40Ar in biotite: temperature, pressure and compositional effects. – *Geochimica et Cosmochimica Acta*, **49** (11): pp. 2461–2468. DOI: 10.1016/0016-7037(85)90246-7.

Helvacı, C., Yücel Öztürk, Y., Satır, M. & Shang, C.K. (2014): U-Pb zircon and K-Ar geochronology reveal the emplacement and cooling history of the Late Cretaceous Beypazarı granitoid, central Anatolia, Turkey. – *International Geology Review*, **56** (9): pp. 1138–1155. DOI: 10.1080/00206814.2014.921795.

Holland, T. & Blundy, J. (1994): Non-ideal interactions in calcic amphiboles and their bearing on amphibole-plagioclase thermometry. – *Contributions to Mineralogy and Petrology*, **116** (4): pp. 433–447. DOI: 10.1007/BF00310910.

Huyskens, M.H. & Bröcker, M. (2014): The status of the Makrotantalon Unit (Andros, Greece) within the structural framework of the Attic-Cycladic Crystalline Belt. – *Geological Magazine*, **151** (3): pp. 430–446. DOI: 10.1017/S0016756813000307.

Jackson, S.E., Pearson, N.J., Griffin, W.L. & Belousova, E.A. (2004): The application of laser ablation-inductively coupled plasma-mass spectrometry to in situ U-Pb zircon geochronology. – *Chemical Geology*, **211** (1–2): pp. 47–69. DOI: 10.1016/j.chemgeo.2004.06.017.

Jolivet, L. & Brun, J.-P. (2010): Cenozoic geodynamic evolution of the Aegean. – *International Journal of Earth Sciences*, **99** (1): pp. 109–138. DOI: 10.1007/s00531-008-0366-4.

Katzir, Y., Matthews, A., Garfunkel, Z., Schliestedt, M. & Avigad, D. (1996): The tectono-metamorphic evolution of a dismembered ophiolite (Tinos, Cyclades, Greece). – *Geological Magazine*, **133** (3): pp. 237–254.

Kneuker, T., Dörr, W., Petschick, R. & Zulauf, G. (2015): Upper crustal emplacement and deformation of granitoids inside the Uppermost Unit of the Cretan nappe stack: constraints from U-Pb zircon dating, microfabrics and paleostress analyses. – *International Journal of Earth Sciences*, **104** (2): pp. 351–367. DOI: 10.1007/s00531-014-1088-4.

Koepke, J. & Seidel, E. (1984): Oberkretazisches Kristallin an der Basis von Ophiolithen der Südägäis: Charakterisierung der Metamorphose-Fazies. – *Tschermaks Mineralogische und Petrographische Mitteilungen*, **33** (4): pp. 263–286. DOI: 10.1007/BF01082673.

Koepke, J., Seidel, E. & Kreuzer, H. (2002): Ophiolites on the southern Aegean islands Crete, Karpathos and Rhodes: composition, geochronology and position within the ophiolite belts of the Eastern Mediterranean. – *Lithos*, **65** (1–2): pp. 183–203. DOI: 10.1016/S0024-4937(02)00165-2.

Köksal, S., Toksoy-Köksal, F., Göncüoğlu, M.C., Möller, A., Gerdes, A. & Frei, D. (2013): Crustal source of the Late Cretaceous Satansarı monzonite stock (central Anatolia – Turkey) and its significance for the Alpine geodynamic evolution. – *Journal of Geodynamics*, **65**: pp. 82–93. DOI: 10.1016/j.jog.2012.06.003.

Koutsovitis, P., Soukis, K.I. & Lozios, S. (2012): Implications for the Upper Cycladic Unit: petrological, mineralogical and structural study of intrusive rocks from the Late-Cretaceous volcanic-arc in Anafi Island, Cyclades, Greece. – In: *EGU General Assembly Conference Abstracts*. p. 13303; Wien.

Krahl, J., Herbart, H. & Katzenberger, S. (1982): Subdivision of the allochthonous “Ophiolites”-bearing formation upon the Pindos group, southwestern part of central Crete, Greece. – In: *International Symposium on the Hellenic Arc and Trench (H.E.A.T.). April 8–10. 1981, Athens. Proceedings. Volume 1*. Εθνικό Μετσόβιο Πολυτεχνείο [Ethnikó Metsóvio Polytechneío], pp. 324–341; Αθήνα [Athens].

Krogh, T.E. (1973): A low-contamination method for hydrothermal decomposition of zircon and extraction of U and Pb for isotopic age determinations. – *Geochimica et Cosmochimica Acta*, **37** (3): pp. 485–494. DOI: 10.1016/0016-7037(73)90213-5.

Kruhl, J.H. (1996): Prism- and basal-plane parallel subgrain boundaries in quartz: a microstructural geothermobarometer. – *Journal of Metamorphic Geology*, **14** (5): pp. 581–589. DOI: 10.1046/j.1525-1314.1996.00413.x.

Langosch, A., Seidel, E., Stosch, H.-G. & Okrusch, M. (2000): Intrusive rocks in the ophiolitic mélange of Crete – Witnesses to a Late Cretaceous thermal event of enigmatic geological position. – *Contributions to Mineralogy and Petrology*, **139** (3): pp. 339–355. DOI: 10.1007/s004100000136.

Le Maitre, R.W., Streckeisen, A., Zanettin, B., Le Bas, M.J., Bonin, B. & Bateman, P. (2002): *Igneous rocks: a classification and glossary of terms*. – Cambridge University Press, 252 p.; Cambridge.

Lecomte, E., Jolivet, L., Lacombe, O., Denèle, Y., Labrousse, L. & Le Pourhiet, L. (2010): Geometry and kinematics of Mykonos detachment, Cyclades, Greece: evidence for slip at shallow dip. – *Tectonics*, **29** (5): pp. 1–22. DOI: 10.1029/2009TC002564.

Lefebvre, C.J.C. (2011): The tectonics of the Central Anatolian Crystalline Complex: a structural, metamorphic and paleomagnetic study. – PhD thesis, Universiteit Utrecht, 139 p. (unpubl.); Utrecht.

Lippolt, H.J. & Baranyi, I. (1976): Oberkretazische Biotit- und Gesteinsalter aus Kreta. – *Neues Jahrbuch für Geologie und Paläontologie, Monatshefte*, **7**: pp. 405–414.

Ludwig, K.R. (1980): Calculation of uncertainties of U-Pb isotope data. – *Earth and Planetary Science Letters*, **46** (2): pp. 212–220. DOI: 10.1016/0012-821X(80)90007-2.

Ludwig, K.R. (2012): User's manual for Isoplot 3.75. A geochronological toolkit for Microsoft Excel. – *Berkeley Geochronology Center Special Publication*, **5**: pp. 1–75.

Ludwig, K.R. & Mundil, R. (2002): Extracting reliable U-Pb ages and errors from complex populations of zircons from Phanerozoic tuffs. – *Geochimica et Cosmochimica Acta*, **66**: pp. 463. DOI: 10.1016/S0016-7037(02)01011-6.

Maluski, H., Bonneau, M. & Kienast, J.-R. (1987): Dating the metamorphic events in the Cycladic area: $^{39}Ar/^{40}Ar$ data from metamorphic rocks of the island of Syros (Greece). – *Bulletin de la Société Géologique de France, série 8*, **3** (5): pp. 833–842.

Melidonis, N.G. (1963): Η γεωλογία της νήσου Ανάφης (Στρωματογραφία – Τεκτονική – Πετρολογία – Κοιτασματολογία) [The geology of Anafi Island (Stratigraphy – Tectonics – Petrology – Economic geology)]. – *Γεωλογικές και γεωφυσικές μελέτες [Geological and Geophysical Research]*, **8**: pp. 61–308.

Michos, A., Vradelis, I. & Psimenos, S. (2010): *318 Anafi. 1:15000*. – Hiking map, Terrain; Athens.

Middleton, A.P., Freestone, I.C. & Leese, M.N. (1985): Textural analysis of ceramic thin sections: Evaluation of grain sampling procedures. – *Archaeometry*, **27** (1): pp. 64–74. DOI: 10.1111/j.1475-4754.1985.tb00348.x.

Moore, W., McKee, E. & Akinci, Ö. (1980): Chemistry and chronology of plutonic rocks in the Pontide mountains, northern Turkey. – In: Janović, S., Sillitoe, R.H. (eds.) *European Copper Deposits. Proceedings of an International Symposium held at Bor, Yugoslavia, 18–22 September 1979*. Univerzitet u Beogradu, pp. 209–216; Beograd.

Nicolescu, Ș, Cornell, D.H. & Bojar, A.-V. (1999): Age and tectonic setting of Bocșa and Ocna de Fier - Dognecea granodiorites (southwest Romania) and of associated skarn mineralisation. – *Mineralium Deposita*, **34** (8): pp. 743–753. DOI: 10.1007/s001260050235.

Okay, A.I. (2008): Geology of Turkey: a synopsis. – *Anschnitt*, **21**: pp. 19–42.

Okrusch, M. & Bröcker, M. (1990): Eclogites associated with high-grade blueschists in the Cyclades archipelago, Greece: a review. – *European Journal of Mineralogy*, **2** (4): pp. 451–478. DOI: 10.1127/ejm/2/4/0451.

Palamakumbura, R.N., Robertson, A.H.F. & Dixon, J.E. (2013): Geochemical, sedimentary and micropaleontological evidence for a Late Maastrichtian oceanic seamount within the Pindos ocean (Arvi Unit, S Crete, Greece). – *Tectonophysics*, **595–596**: pp. 250–262. DOI: 10.1016/j.tecto.2012.04.019.

Parrish, R.R. (1987): An improved micro-capsule for zircon dissolution in U–Pb geochronology. – *Chemical Geology: Isotope Geoscience section*, **66** (1–2): pp. 99–102. DOI: 10.1016/0168-9622(87)90032-7.

Patzak, M., Okrusch, M. & Kreuzer, H. (1994): The Akrotiri unit on the island of Tinos, Cyclades, Greece: witness to a lost terrane of Late Cretaceous age. – *Neues Jahrbuch für Geologie und Paläontologie, Abhandlungen*, **194**: pp. 211–252.

Pe-Piper, G. & Photiades, A. (2006): Geochemical characteristics of the Cretaceous ophiolitic rocks of Ikaria island, Greece. – *Geological Magazine*, **143** (4): pp. 417–429. DOI: 10.1017/S0016756806002081.

Peytcheva, I. & von Quadt, A. (2011): Advantages and disadvantages of LA-ICP-MS and ID-TIMS U-Pb dating of complex zircons: a case study of Lutzkan and Ruy granitoids in W Bulgaria. – In: *Geosciences 2011. Proceedings of the national Conference with international participation*. pp. 69–70; Sofia.

Philippson, A. (1901): *Beiträge zur Kenntnis der griechischen Inselwelt*. – Justus Perthes, 172 p.; Gotha.

van der Plas, L. & Tobi, A.C. (1965): A chart for judging the reliability of point counting results. – *American Journal of Science*, **263** (1): pp. 87–90. DOI: 10.2475/ajs.263.1.87.

Pupin, J.P. (1980): Zircon and granite petrology. – *Contributions to Mineralogy and Petrology*, **73** (3): pp. 207–220. DOI: 10.1007/BF00381441.

von Quadt, A., Moritz, R., Peytcheva, I. & Heinrich, C.A. (2005): 3: Geochronology and geodynamics of Late Cretaceous magmatism and Cu–Au mineralization in the Panagyurishte region of the Apuseni–Banat–Timok–Srednogorie belt, Bulgaria. – *Ore Geology Reviews*, **27** (1–4): pp. 95–126. DOI: 10.1016/j.oregeorev.2005.07.024.

von Quadt, A., Peytcheva, I., Heinrich, C.A., Cvetković, V. & Banjesević, M. (2007): Upper Cretaceous magmatic evolution and related Cu–Au mineralization in Bulgaria and Serbia. – In: Andrew, C.J. (ed.) *Digging deeper. Proceedings of the Ninth Biennial SGA Meeting, Dublin 2007*. Irish Association for Economic Geology, pp. 861–864; Dublin.

Reinecke, T. (1978): Petrographie und Tektonik des Präneogens im östlichen Teil der Insel Anaphi, Kykladen, Griechenland. – Diploma thesis, University of Kiel, 105 p. (unpubl.); Kiel.

Reinecke, T., Altherr, R., Hartung, B., Hatzipanagiotou, K., Kreuzer, H., Harre, W., Klein, H., Keller, J., Geenen, E. & Böger, H. (1982): Remnants of a Late Cretaceous high temperature belt on the island of Anafi (Cyclades, Greece). – *Neues Jahrbuch für Mineralogie, Abhandlungen*, **145** (2): pp. 157–182.

Robert, U. & Bonneau, M. (1982): Les basalts des nappes du Pinde et d'Arvi et leur signification dans l'évolution géodynamique de la Méditerrannée orientale. – *Annales Géologiques des Pays Helléniques*, **31**: pp. 373–408.

Schliestedt, M., Altherr, R. & Matthews, A. (1987): Evolution of the Cycladic Crystalline Complex: petrology, isotope geochemistry and geochronology. – In: Helgeson, H.C. (ed.) Chemical Transport in Metasomatic Processes. – *NATO ASI Series. C: Mathematical and Physical Sciences*, **218**: pp. 389–428.

Seidel, E., Okrusch, M., Kreuzer, H., Raschka, H. & Harre, W. (1981): Eo-Alpine metamorphism in the Uppermost Unit of the Cretan nappe system – petrology and geochronology. Part 2. Synopsis of high-temperature metamorphics and associated ophiolites. – *Contributions to Mineralogy and Petrology*, **76** (3): pp. 351–361. DOI: 10.1007/BF00375462.

Seidel, E., Schliestedt, M., Kreuzer, H. & Harre, W. (1977): Metamorphic rocks of Late Jurassic age as components of the ophiolitic mélange on Gavdos and Crete (Greece). – *Geologisches Jahrbuch, Reihe B*, **28**: pp. 3–21.

Seymen, I. (1983): Tamadağ (Kaman-Kırşehir) çevresinde Kaman grubunun ve onunla sınırdaş oluşukların karşılaştırılmalı tektonik özellikler. – *Türkiye Jeoloji Kurumu Bülteni*, **26**: pp. 89–98.

Shaked, Y., Avigad, D. & Garfunkel, Z. (2000): Alpine high-pressure metamorphism at the Almyropotamos window (southern Evia, Greece). – *Geological Magazine*, **137** (4): pp. 367–380. DOI: 10.1017/S001675680000426X.

Soukis, K.I. & Papanikolaou, D.J. (2004): Contrasting geometry between Alpine and Late- to Post-Alpine tectonic structures in Anafi island (Cyclades). – *Bulletin of the Geological Society of Greece*, **36** (Proceedings of the 10th International Congress, Thessaloniki, April 2004): pp. 1688–1696.

Stacey, J.S. & Kramers, J.D. (1975): Approximation of terrestrial lead isotope evolution by a two-stage model. – *Earth and Planetary Science Letters*, **26** (2): pp. 207–221. DOI: 10.1016/0012-821X(75)90088-6.

Streckeisen, A. (1974): Classification and nomenclature of plutonic rocks recommendations of the IUGS subcommission on the systematics of igneous rocks. – *Geologische Rundschau*, **63** (2): pp. 773–786. DOI: 10.1007/BF01820841.

Thorbecke, G. (1973): Die Gesteine der Ophiolith-Decke von Anoja/Mittelkreta. – *Berichte der Naturforschenden Gesellschaft zu Freiburg i. Br.*, **63**: pp. 81–92.

Thorbecke, G. (1987): *Die Zonengliederung der ägäischen Helleniden und westlichen Tauriden*. – Gesellschaft der Geologie- und Bergbaustudenten in Österreich, 161 p.; Wien.

Tortorici, L., Catalano, S., Cirrincione, R. & Tortorici, G. (2012): The Cretan ophiolite-bearing mélange (Greece): a remnant of Alpine accretionary wedge. – *Tectonophysics*, **568–569**: pp. 320–334. DOI: 10.1016/j.tecto.2011.08.022.

Vernon, R.H. (1991): Questions about myrmekite in deformed rocks. – *Journal of Structural Geology*, **13** (9): pp. 979–985. DOI: 10.1016/0191-8141(91)90050-S.

Vernon, R.H. & Flood, R.H. (1988): Contrasting deformation of S- and I-type granitoids in the Lachlan Fold Belt, eastern Australia. – *Tectonophysics*, **147** (1–2): pp. 127–143. DOI: 10.1016/0040-1951(88)90152-7.

Whitney, D.L., Teyssier, C., Fayon, A.K., Hamilton, M.A. & Heizler, M. (2003): Tectonic controls on metamorphism, partial melting, and intrusion: timing and duration of regional metamorphism and magmatism in the Niğde Massif, Turkey. – *Tectonophysics*, **376** (1–2): pp. 37–60. DOI: 10.1016/j.tecto.2003.08.009.

Wiesenbach, B., Martha, S.O., Dörr, W., Petschick, R., Xypolias, P. & Zulauf, G. (2014): Structural evolution and kinematics of Pelagonian-type crystalline rocks of central Crete and Anafi island. – In: *Deutsche Gesellschaft für Geowissenschaften (ed.) GeoFrankfurt 2014 – Dynamik des Systems Erde / Earth System Dynamics. Abstract Volume. Deutsche Gesellschaft für Geowissenschaften*, p. 592; Frankfurt am Main. DOI: 10.13140/2.1.1133.3448.

Wijbrans, J.R. & McDougall, I. (1986): 40Ar/39Ar dating of white micas from an Alpine high-pressure metamorphic belt on Naxos (Greece): the resetting of the argon isotopic system. – *Contributions to Mineralogy and Petrology*, **93** (2): pp. 187–194. DOI: 10.1007/BF00371320.

3 The tectonometamorphic and magmatic evolution of the Uppermost Unit in central Crete (Melambes area): constraints on a Late Cretaceous magmatic arc in the Internal Hellenides (Greece)

Silviu O. Martha[1], Wolfgang Dörr[1], Axel Gerdes[1], Jochen Krahl[1], Jolien Linckens[1], Gernold Zulauf[1]

[1]Institut für Geowissenschaften, Goethe-Universität Frankfurt, Altenhöferallee 1, 60438 Frankfurt am Main, Germany. E-mail: s.martha@em.uni-frankfurt.de, w.doerr@em.uni-frankfurt.de, gerdes@em.uni-frankfurt.de, krahl@em.uni-frankfurt.de, linckens@em.uni-frankfurt.de, g.zulauf@em.uni-frankfurt.de

Keywords: Hellenides • Ductile deformation • Magmatic arc • U-Pb dating • Greenschist

Published in: *Gondwana Research*, **48**: pp. 50–71. DOI: 10.1016/j.gr.2017.04.004.

3.1 Abstract

Crete consists of a nappe pile that formed during Alpine subduction and collision. The lower nappes belong to the External Hellenides, whereas the uppermost nappe is ascribed to the Pelagonian Zone of the Internal Hellenides. The Uppermost Unit consists of several subunits including the Asterousia Crystalline Complex (ACC), which comprises metasedimentary rocks, (meta)granitoids and serpentinite, the protolith age and the tectonometamorphic evolution of which are largely unknown. In the present study, we present new structural, microfabric and geochronological data from the Uppermost Unit in the Melambes area (central Crete). $^{206}Pb/^{238}U$ zircon ages (LA-ICP-MS and ID-TIMS) indicate granitic and dioritic intrusions between 71.9 ± 0.6 and 76.9 ± 0.3 Ma. Identical ages have previously been obtained from comparable intrusions in eastern Crete and on Anafi. The composition and geochemical signature suggest an extended magmatic arc along the southern active margin of the Pelagonian-Lycian Block. Post-intrusive shearing transformed granite into orthogneiss, whereas diorite remained free from foliation, because of the lower amount of mechanically weak phases. Deformation microfabrics suggest top-to-the SE shearing under amphibolite facies conditions of the ACC and at greenschist facies conditions of rocks at the base of the ACC referred to as Akoumianos Greenschist. The Akoumianos Greenschist is considered as the northern part of the Pindos realm that was subducted underneath the Pelagonian-Lycian active margin. Based on our new and on published data, the following orogenic stages are suggested to have contributed to the evolution of the Hellenides during the Late Cretaceous to Eocene: (1) pre-middle Campanian collision and subduction of the Pindos lithosphere underneath the southern margin of the Pelagonian-Lycian terrane led to obduction and offscraping of serpentinized ocean floor and stacking of the ACC during amphibolite facies top-to-the SE thrusting, (2) formation of a Campanian magmatic arc along the Pelagonian-Lycian active margin; (3) Maastrichtian collision and stacking of the magmatic arc during top-to-the SE mylonitic shearing; (4) Palaeocene top-to-the SE greenschist-facies shearing of the ACC on top of the Akoumianos Greenschist; (5) Late Eocene thrusting of the Uppermost Unit on top of the Arvi and Pindos units. Thus, top-to the SE was the dominant shear sense in the southern Aegean from at least the mid-Late Cretaceous until the Eocene.

3.2 Introduction

The island of Crete consists of a nappe pile composed of several metamorphic and non-metamorphic nappes that have been stacked during Eocene to Early Miocene progressive convergence of the African and Eurasian plates. This phase of Alpine orogeny is related to the closure of the Pindos Ocean and the subsequent subduction of Apulia underneath the Pelagonian-Lycian Block (e.g. Seidel et al.

1982; Doutsos et al. 1993; Zulauf et al. 2008). Most of the units of the Cretan nappe pile are ascribed to the External Hellenides. The Uppermost Unit, however, is usually attributed to the Pelagonian Zone of the Internal Hellenides (e.g. Aubouin and Dercourt 1965; Bonneau 1972a). It consists of several subunits metamorphosed under different metamorphic conditions with one subunit comprising rocks that underwent high temperature (HT) – low pressure (LP) amphibolite facies metamorphism supposedly during the Latest Cretaceous (Seidel et al. 1976, 1981). This high-grade metamorphic subunit is usually referred to as the Asterousia Crystalline Complex (Bonneau 1972a). Igneous intrusions inside the Asterousia Crystalline Complex (ACC) are largely Campanian in age (Kneuker et al. 2015; Martha et al. 2016). Rocks of the ACC are exposed on Crete and on several Cycladic islands (Martha et al. 2016 and references therein).

The Uppermost Unit is supposed to have formed a once widespread terrane in the southern Aegean realm that due to erosion is now only scarcely preserved (Creutzburg and Seidel 1975). On Crete, rocks of the Uppermost Unit are usually restricted to graben structures (Creutzburg and Seidel 1975). The Uppermost Unit and the underlying non-metamorphic Pindos Unit share a common tectonic history since at least the Late Eocene and have remained in the upper 4–7 km of the crust (Thomson et al. 1999). Thus, unravelling the tectonometamorphic evolution of the Uppermost Unit has to consider that this unit escaped the Oligocene to Miocene tectonometamorphic events affecting most of the nappes of the Cretan nappe pile underneath (e.g. Altherr et al. 1994).

Martha et al. (2016) showed that structural data and microfabrics of Asterousia-type and greenschist facies metamorphic rocks from Anafi (southern Cyclades) preserve information on the pre-Eocene tectonometamorphic evolution of the Hellenides in the southern Aegean realm. The Uppermost Unit is therefore considered as a key in understanding the early Alpine tectonic evolution of the Hellenides. In the present contribution, we present new data obtained from field studies and from detailed analyses of the Uppermost Unit exposed in central Crete west of the village Melambes. We present (1) new kinematic and (micro)structural data from low-grade- and high-grade metamorphic rocks; (2) petrographic data of crystalline rocks; (3) electron backscatter diffraction (EBSD) analyses of quartz from quartzite to reveal the textures and possible slip systems; (4) electron microprobe (EMP) analysis on greenschist; and (5) laser ablation inductively coupled plasma mass spectrometry (LA-ICP-MS) and isotope dilution thermal ionisation mass spectrometry (ID-TIMS) $^{206}Pb/^{238}U$ zircon ages obtained from granitoids, which intruded into the Asterousia-type metasedimentary sequence. The new results will be combined with published data to develop a new geodynamic model for the early Alpine evolution of the Uppermost Unit and adjacent domains.

3.3 Regional geology

3.3.1 The Uppermost Unit of the Cretan nappe pile

The Cretan nappe pile results from Alpine stacking of rocks that were previously situated side by side in the Neotethys realm (Fig. 3.1). Several lithotectonic units assembling the Cretan nappe pile are subdivided into a lower and an upper nappe system (e.g. Fassoulas 1998). Late Oligocene to Early Miocene subduction-related LT–HP-metamorphism affected the units of the lower nappe system (Seidel et al. 1982), which consists of at least five units (i.e. Plattenkalk Unit, Trypali Unit, Phyllite-Quartzite Unit s.str., Pre-Alpine Basement Unit, Tyros Unit and Tripolitsa Unit; e.g. Dornsiepen and Manutsoglu 1994; Zulauf et al. 2008; Klein et al. 2013). The upper nappe system was situated at upper crustal levels since at least the Eocene (Thomson et al. 1999) and escaped Oligocene to Miocene LT–HP-metamorphism. It can be subdivided into the Pindos and the Uppermost units. The Pindos Unit consists of non-metamorphic Triassic to Jurassic deep-water sediments overlain by Late Cretaceous flysch, pelagic limestone and Early Palaeogene flysch (e.g. Bonneau and Fleury 1971).

The Uppermost Unit on top includes several subunits that differ in composition and metamorphic grade. While all other units of the Cretan nappe pile are considered as part of the External Hellenides, the Uppermost Unit is usually assigned to the Pelagonian Zone of the Internal Hellenides (e.g. Bonneau 1972a, 1984; Tortorici et al. 2012). However, this assignment was founded mainly on the structural position of the unit and on the presence of Late Jurassic ophiolitic bodies within the Uppermost Unit.

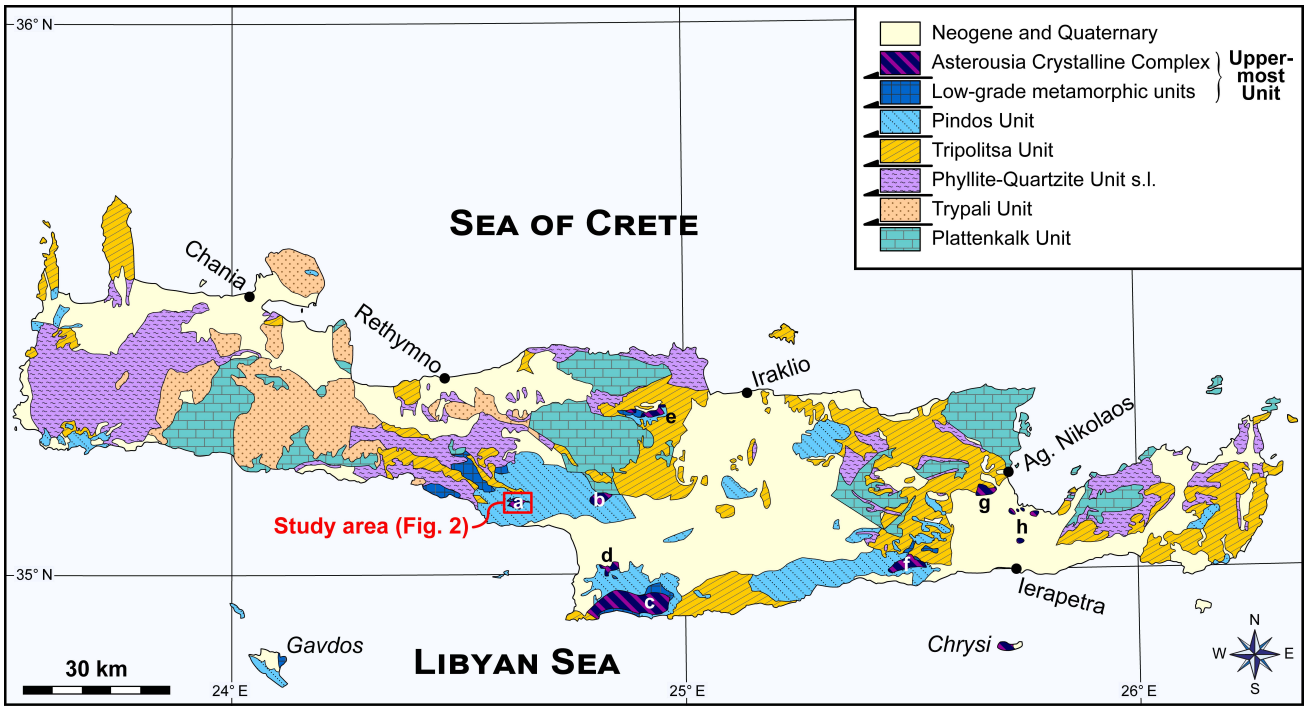

Fig. 3.1 Geological map of Crete showing the pre-Neogene units (modified after Creutzburg and Seidel 1975). Occurrences of the Asterousia Crystalline Complex on Crete: (a) west of Melambes (study area); (b) between Kamares and Magarikari; (c) western Asterousia Mountains between Kali Limenes and Lendas; (d) Messara Plain between Petrokefali and Kouses; (e) north of Anogia and Gonies; (f) south of the Dikti Mountains in the area of Pefkos, Kalami and Sykologos; (g) Kritsa; (h) northern Ierapetra Graben between Kalo Chorio and Pachia Ammos and near Stavros.

The Pelagonian Zone was correlated with the Lycian nappes in western Anatolia (e.g. Robertson et al. 1996) and the two are supposed to have formed a microcontinent during the Cretaceous, the Pelagonian-Lycian Block (e.g. Ring and Layer 2003; Gessner et al. 2011).

The subdivision of the Uppermost Unit is controversial with at least five to six subunits separated by thrust planes. The very low- to low-grade metamorphic subunits of the Uppermost Unit are (1) anchimetamorphic pelagic limestone, terrigeneous turbidites and basalt referred to as Arvi Unit; (Bonneau 1973; Robert and Bonneau 1982; Palamakumbura et al. 2013); (2) blueschist facies metamorphic sedimentary rocks and volcanics referred to as Preveli Unit (Krahl et al. 1982); (3) serpentinite comprising gabbroic dykes and slices of amphibolite referred to as Spili Unit (Krahl et al. 1982); and (4) greenschist facies sediments and serpentinite referred to as Vatos Unit (e.g. Aubouin and Dercourt 1965; Krahl et al. 1982). Other subunits, i.e. the Miamou and Kalypso units (Bonneau et al. 1974; Schliestedt and Seidel 1976) are probably correlated with the Vatos and Preveli units, respectively (Bonneau and Lys 1978; Krahl et al. 1982). The existence of an independent topmost "*nappe des serpentines*" that faced low-grade metamorphism during the Late Jurassic (Seidel et al. 1977) is controversially discussed (e.g. Bonneau 1972a; Seidel et al. 1981; Krahl et al. 1982). A consensus on the subdivision of the low-grade metamorphic subunits of the Uppermost Unit is far from being reached.

High-grade metamorphic rocks and late- or post-metamorphic intrusions of granitoids form the Asterousia Crystalline Complex (ACC). Asterousia-type rocks are known in central and eastern Crete from at least eight localities (Fig. 3.1). Further occurrences of Asterousia-type rocks are reported from the Cycladic islands of Anafi (Reinecke et al. 1982), Donousa (Altherr et al. 1980), Ikaria (Altherr et al. 1994), Makra (Thorbecke 1987), Nikouria (Dürr et al. 1978), Syros (Bonneau et al. 1980) and Tinos (Patzak et al. 1994). Metamorphic rocks of the ACC comprise calcsilicate rock, metabasite, metapelite, orthoamphibolite, orthogneiss, paraamphibolite, paragneiss, quartzite and micaschist (Bonneau 1972a). Slices of serpentinite inside the HT–LP metamorphic rocks are usually present. Granitoid rocks range from granite and granodiorite to (hornblende) diorite and quartzdiorite (e.g. Davis 1967; Wachendorf et al. 1980; Langosch et al. 2000). Metamorphic conditions for the ACC on Crete have been constrained as upper amphibolite facies with P = 400–500 MPa and $T_{max} \approx 700$ °C (Seidel et al. 1976, 1981). K-Ar ages of metamorphic rocks indicate Late Cretaceous cooling with biotite ages ranging from 66.1 ± 0.9 to 72.4 ± 0.7 Ma and hornblende ages ranging from 66.3 ± 2.9 to 75.6 ± 1.2 Ma (Seidel et al. 1976, 1981; Koepke and Seidel 1984; Langosch et al. 2000). $^{206}Pb/^{238}U$ zircon ages from quartzdiorite in the northern Ierapetra Graben near Pachia Ammos indicate granitoid emplacement at 74.5 ± 0.25 Ma (Kneuker et al. 2015). Similar $^{206}Pb/^{238}U$ zircon ages were obtained from granodiorite intruded into Asterousia-type marble on Anafi (Martha et al. 2016), the minimum emplacement age of

which was constrained at 72.6 +0.1/–0.2 Ma, while the largest zircon population yielded ages at 74 Ma. Older $^{206}Pb/^{238}U$ ages suggest continuous emplacement of granitoids from ca. 72.5–79 Ma (Martha et al. 2016). REE patterns (Koutsovitis et al. 2012) and $^{87}Sr/^{86}Sr$ initial isotope ratios (Be'eri-Shlevin et al. 2009) of the Anafi granodiorite are consistent with magmatism inside a continental magmatic arc setting.

A recent approach for a subdivision of the Uppermost Unit has been made by Tortorici et al. (2012). These authors considered the Uppermost Unit as an "ophiolite-bearing mélange" and distinguished three tectonic subunits, which they regarded as the toe (Lower Unit) and the innermost and deeper subducted parts (Intermediate and Upper units) of an accretionary wedge. The non- to weakly-metamorphic Lower Unit comprises parts of the Pindos and Tripolitsa flysch and turbiditic sequences of the Vatos Unit. The Intermediate Unit on top consists of greenschist to HP-greenschist facies metamorphic ocean-derived sediments and exotic continental basement derived blocks with associated Late Cretaceous intrusive granitoids (i.e. the ACC). The Upper Unit is the topmost unit of the sequence comprising blueschist facies metamorphic rocks and compares to the Preveli Unit and in part to the Vatos Unit. All three units are associated with 'ophiolitic rocks' and the Upper Unit was correlated with the Cycladic Blueschist Unit (Fassoulas 1998; Tortorici et al. 2012).

The provenance of the Uppermost Unit is ambiguous. Hall et al. (1984) suggested all subunits to be a large olistostrome within the Late Cretaceous to Eocene Pindos flysch. The prevalent view, however, regards the ACC to be a remnant of the Pelagonian Zone, which has been thrust on top of the Cretan nappe pile and on top of the Cycladic Blueschist Unit (e.g. Bonneau 1972a, 1982; Reinecke et al. 1982). Tortorici et al. (2012) considered the Uppermost Unit as a remnant of an accretionary wedge complex to the south of the Pelagonian Zone and emplaced onto the Cretan nappe pile during the Late Oligocene to Early Miocene. Apatite fission track ages reported by Thomson et al. (1998, 1999) from the ACC, the Pindos flysch (described as 'Uppermost Unit (undifferentiated)' by the authors) and from the low-grade metamorphic units in central Crete yielded ages at ca. 15 Ma and at ca. 30 Ma. This indicates that the Uppermost Unit and the Pindos Unit remained within or below the apatite annealing zone from the Eocene/Oligocene to the Middle Miocene and thus at upper structural levels (Thomson et al. 1998, 1999). Be'eri-Shlevin et al. (2009) suggested a correlation of the Uppermost Unit with the Pontides and Sakarya volcanic arcs in western Turkey, while Martha et al. (2016) pointed to similarities in the magmatic and metamorphic evolution with the Central Anatolian Crystalline Complex.

3.3.2 The Asterousia Crystalline Complex west of Melambes

The study area between the villages Melambes, Nea Krya Vrysi, Ano Saktouria and Kato Saktouria (Fig. 3.2) is largely composed of HT–LP metamorphic rocks that have been studied by Bonneau (1972b). Geological maps of the area have been published by Krahl et al. (1982), Bonneau (1985) and Tortorici et al. (2012). It is the westernmost occurrence of the ACC on Crete (Bonneau 1972a) and comprises amphibolite facies metamorphic rocks (amphibolite, calcsilicate rock, marble, paragneiss and quartzite) cut by intrusive rocks (biotite granite, leucogranite and granodiorite) and slices of serpentinite and metagabbro (Bonneau 1972b; Krahl et al. 1982). The metamorphic rocks west of Melambes are intercalated between flysch sediments of the Pindos Unit and Neogene sediments (Bonneau 1972b). The Pindos flysch has been dated as Ypresian (Early Eocene) based on foraminifer findings (Bonneau 1972b), whereas the Neogene sediments are of middle Tortonian (Late Miocene) age based on findings of fresh-water molluscs (Meulenkamp 1969).

Although Bonneau (1972b) found no contact with the Pindos Unit, he placed the high-grade metamorphic rocks on top of the latter and below the Vatos Unit, which is exposed further northwest in the Spili-Ardaktos Graben. Bonneau et al. (1977), Seidel et al. (1981) and Bonneau (1985) placed the low-grade metamorphic units of the Uppermost Unit at the base of the ACC, but a "nappe de serpentines" on top. Krahl et al. (1982) placed the ACC at the base of the Uppermost Unit, whereas Tortorici et al. (2012) included the ACC as exotic blocks in their Intermediate Unit. The controversial position of the ACC in the Melambes area results from no evident contact with any other unit having been reported.

K-Ar hornblende ages of paraamphibolite (67.0 ± 1.5 Ma) and K-Ar biotite ages of micaschist (66.1 ± 0.9 Ma and 69.9 ± 0.9 Ma) are interpreted as cooling of the metasedimentary rocks, supposedly from amphibolite facies metamorphism (Seidel et al. 1976, 1981). Geochemical analyses of metagranite from the area west of Melambes and of granitic and dioritic rocks from the ACC yielded A-type signature (Langosch 1999). Granitic and dioritic rocks of the ACC are believed to have formed in a supra-subduction zone setting from a depleted mantle source (Langosch et al. 2000).

3.4 Material and methods

3.4.1 Sampling and microfabric analyses

Geological mapping of the Uppermost Unit was conducted using topographic maps at a scale of 1:5000 obtained from the Hellenic Military Geographical Service (http://www.gys.gr/) and produced in the 1980s as well as the newest Google Earth™ satellite images from the study area (Wiesenbach 2014. For U-Pb age dating, we collected six samples of metadiorite, orthogneiss and monzogranite from a dyke, each about ten kilograms, geographical details of which are summarized in Table 3.1.

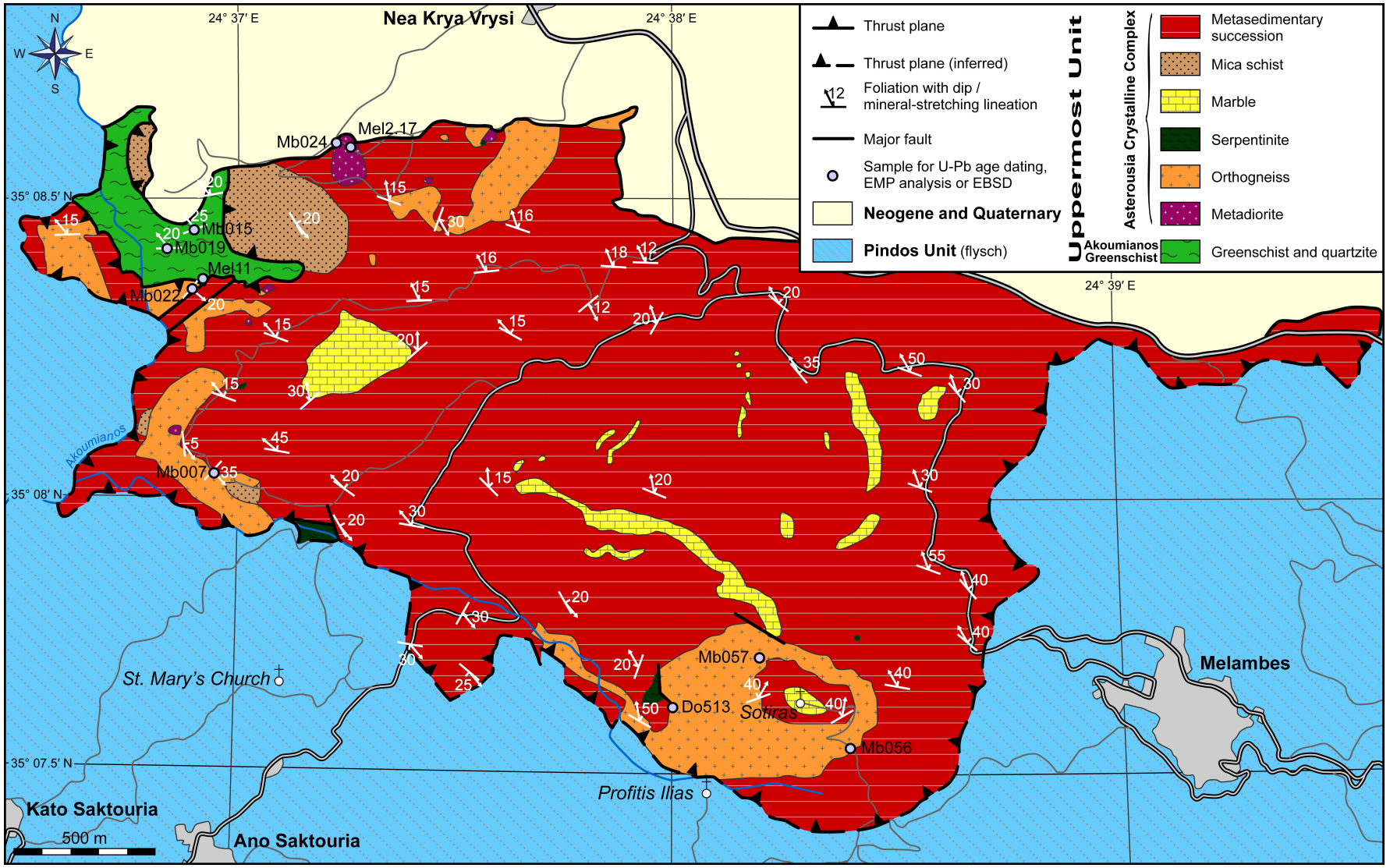

Fig. 3.2 Geological map of the Uppermost Unit in the area of Melambes, Nea Krya Vrysi and Saktouria (modified after Wiesenbach 2014). Structural data and locations of samples collected for geochronological, EMP and EBSD analyses are shown.

Statistical analyses of structural data obtained in the study area were carried out using the open source software Stereonet 9.2.0 applying the algorithms described in Allmendinger et al. (2012) and Cardozo and Allmendinger (2013).

Thin sections of oriented samples, cut parallel to the stretching lineation and perpendicular to the foliation, were analysed using a petrographic microscope focusing on mineral content and deformation microfabrics. For igneous rocks, point counting was performed using a Prior J0415G point counter applying the method described in Middleton et al. (1985). 1,000 points were counted per thin section. The 95 % confidence interval (2σ) calculated for any mineral phase is at maximum 1.6 % using the formula of van der Plas and Tobi (1965).

Table 3.1 Geographic details for samples used for U-Pb age dating.

Sample tag	Rock type	Location	Coordinates	Ground level (m a.s.l.)
Do513	Orthogneiss	450 m W of the Sotiras chapel	35° 07′ 39.30″ N; 24° 37′ 59.30″ E	563
Mb022	Orthogneiss	900 m NE of St Mary's Church	35° 08′ 26.46″ N; 24° 36′ 51.84″ E	237
Mb024	Metadiorite	750 m SW of Nea Krya Vrysi	35° 08′ 42.62″ N; 24° 37′ 13.26″ E	372
Mb056	Monzogranitic dyke	225 m SE of the Sotiras chapel	35° 07′ 35.93″ N; 24° 38′ 23.10″ E	726
Mb057	Orthogneiss	200 m NW of the Sotiras chapel	35° 07′ 45.58″ N; 24° 38′ 11.48″ E	728
Mel2.17*	Metadiorite	750 m SW of Nea Krya Vrysi	35° 08′ 41.46″ N; 24° 37′ 13.02″ E	380

*Thin sections of this sample are labelled Mel19.

3.4.2 Electron backscatter diffraction analyses

Two samples of quartzite from the low-grade (Mel11) and the high-grade metamorphic rocks (Mb007b) were examined using electron backscatter diffraction (EBSD). After performing petrographic analyses, thin sections were embedded in epoxy resin and then polished with diamond solution for several hours until the surface was plane and free of scratches. Finally, thin sections were polished with colloidal silica on a vibratory polisher for half an hour (SYTON method of Fynn and Powell 1979). Thin sections were coated with a thin layer of carbon and surrounded from one side with a thin copper band in order to minimize ionic charging. EBSD analyses were performed using a JEOL JSM 6490 scanning electron microscope equipped with a HKL Nordlys EBSD detector. Acceleration voltage for the measurements was 15 kV, beam current was 8 nA and the working distance varied between 18 and 20 mm. EBSD patterns were indexed using the HKL Technology CHANNEL 5 software (Schmidt and Olesen 1989). Only EBSD measurements with a mean angular deviation (MAD) < 1.3 were accepted and recorded. For the pole figure, one point per grain was plotted. For the pole figure of sample Mb007b, 150 grains were manually measured and saved. Pole figures showing the geometry of c-axis crystallographic-preferred orientation (CPO) of quartz were produced as lower hemisphere, equal area projections.

3.4.3 Electron microprobe analysis

Two samples of greenschist (samples Mb015 and Mb019) were chosen for quantitative mineral analysis using the electron microprobe (EMP) analyser JEOL JXA-8900. Thin sections were embedded in epoxy resin and polished with diamond solution for several hours. Thin sections were coated with carbon and surrounded from one side with a thin copper band in order to minimize ionic charging. 12 major elements were measured simultaneously using a wavelength dispersive spectrometer and reported as oxides (SiO_2, TiO_2, Al_2O_3, Cr_2O_3, FeO, MnO, MgO, CaO, NiO, Na_2O, K_2O, P_2O_5). Analysis parameters were 15 kV and 20 nA and the spot size was 3 µm. Peak integration times were 20 s (Na), 30 s (K, Mn, Ca, P and Ni), 40 s (Al, Ti, Si, Mg and Cr) and 60 s (Fe), while the background was measured at integration times ranging from 15 to 40 s. Several mineral (anorthite, hornblende and plagioclase) and oxide standards were analysed at the beginning and at the end of the analytical session under the same conditions to verify the accuracy of our measurements. Backscattered electron (BSE) images were produced in order to distinguish mineral phases before selecting grains to be measured. Amphibole grains were measured one-by-one due to their small grain size. Calculation of the structural formulae was conducted using the worksheets provided online by Andy Tindle (http://www.open.ac.uk/earth-research/tindle/AGTHome.html).

3.4.4 LA-ICP-MS and ID-TIMS analyses

Samples for laser ablation inductively coupled plasma mass spectrometry (LA-ICP-MS) and isotope dilution thermal ionisation mass spectrometry (ID-TIMS) were treated using the same procedure as described in Martha et al. (2016). Cathodoluminescence images of zircon for LA-ICP-MS were made prior to LA-ICP-MS analyses, but after polishing, using a JEOL JSM 6490 scanning electron microscope equipped with a Gatan MiniCL detector. Laser-induced elemental fractionation and instrumental mass discrimination in LA-ICP-MS analyses were corrected by normalisation to standard zircon GJ-1 (Jackson et al. 2004), which was analysed during the analytical session under the same conditions as the samples. U-Pb data was calculated using the programme PBDAT (Ludwig 1980) and isotope ratios were plotted using Isoplot (Ludwig 2012), with error ellipses reflecting 2σ uncertainties. TuffZirc $^{206}Pb/^{238}U$ ages with (asymmetric) 95 % confidence intervals of the median age were obtained using an algorithm insensitive to Pb loss and inheritance (Ludwig and Mundil 2002).

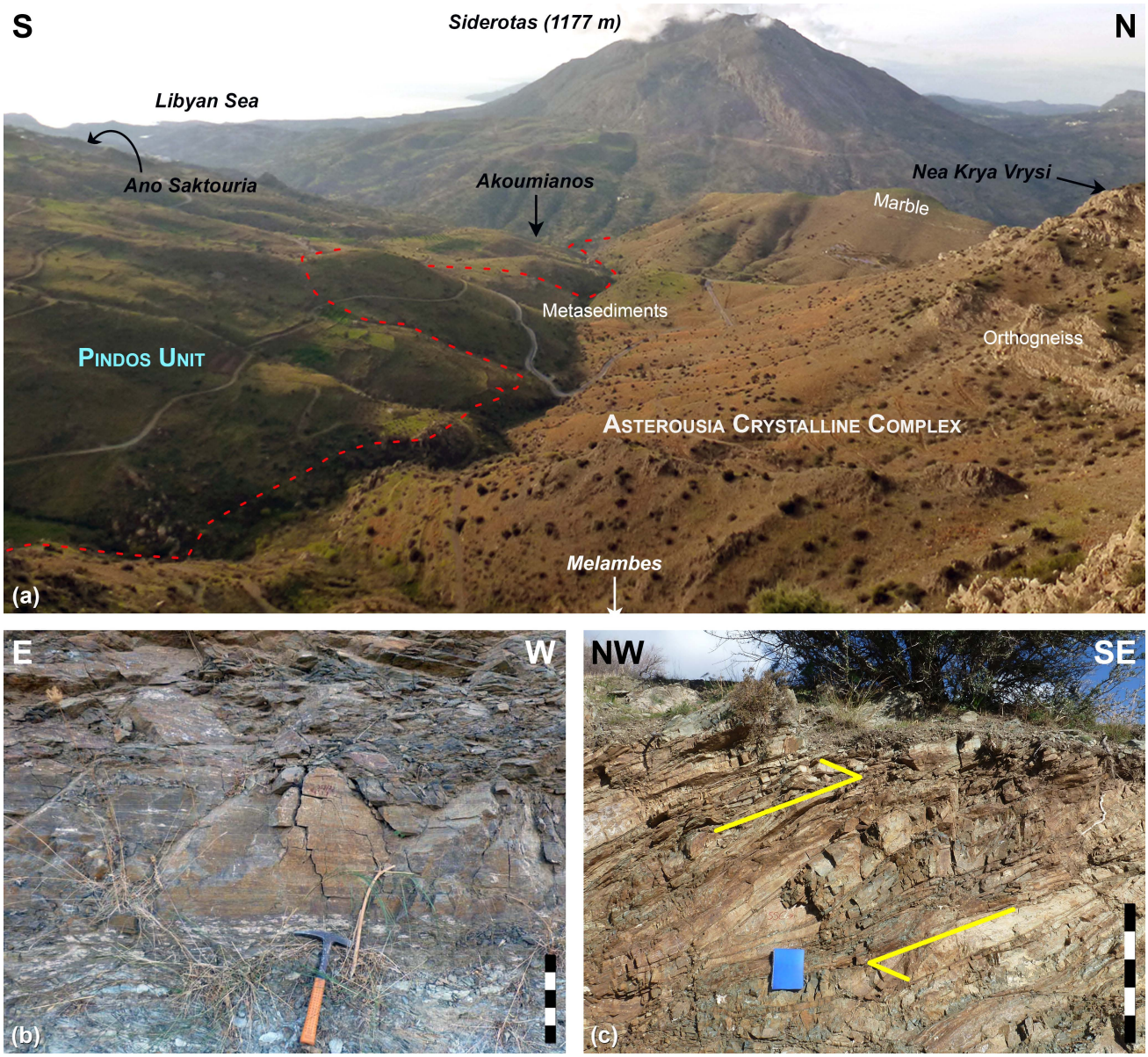

Fig. 3.3 Photographs from the Uppermost Unit west of Melambes. (a) View from near the Sotiras chapel (35° 07′ 41.70″ N; 24° 38′ 11.84″ E) towards the west showing the southern part of the study area. The marble exposure in the background is the occurrence in the western part of the mapped area (cf. Fig. 3.2). The contact between Pindos Unit and ACC is indicated by the red dashed line. (b) Layer of low-grade metamorphic quartzite. Location: Valley of an ephemeral stream 1.5 km SW of Nea Krya Vrysi (35° 08′ 26.52″ N; 24° 36′ 53.40″ E). Scale bar: 25 cm. Photo: Courtesy of Bastian Wiesenbach. (c) Duplex of greenschist in greenschist of the Akoumianos Greenschist indicating a top-to-the SE sense of shear. Location: Valley of an ephemeral stream 1.5 km SW of Nea Krya Vrysi (35° 08′ 29.52″ N; 24° 36′ 50.95″ E). Scale bar: 1 m.

3.5 Results

3.5.1 Field observations and structural record

The metamorphic succession that had previously been mapped as ACC (Krahl et al. 1982; Bonneau 1985; Tortorici et al. 2012) in the area west of Melambes has been re-mapped at a scale of 1:5,000 (Wiesenbach 2014; our Fig. 3.2). It was found that the metamorphic sequence differs in grade of metamorphic overprint and can thus be subdivided into two groups; (1) low-grade metamorphic rocks, referred to as Akoumianos Greenschist and (2) high-grade metamorphic rocks, referred to as Asterousia Crystalline Complex. The contact between the Akoumianos Greenschist and the overlying ACC

is a badly exposed thrust sheet dipping moderately (~30°) towards the west (Wiesenbach 2014). A clear contact with the supposedly underlying Pindos flysch could not be observed in field (Fig. 3.3a). Neogene marls and siltstones unconformably overlie the metamorphic rocks.

Low-grade metamorphic rocks are found in a valley of the ephemeral Akoumianos River at the lowest point of the study area. They comprise greenschist and minor occurrences of micaschist and fractured quartzite on top (Fig. 3.3b), the latter being separated from the greenschist by normal faults. All low-grade metamorphic rocks exhibit a well-pronounced stretching lineation on the foliation planes, which is defined by the alignment of actinolite, hornblende and feldspar (greenschist and micaschist) and quartz (quartzite). The foliation dips shallowly to the NW (Fig. 3.4a), whereas the mineral/stretching lineation is NW–SE-oriented (Fig. 3.4b). Asymmetric structures in the upper part of the sequence, such as shear bands and duplex structures suggest a top-to-the SE sense of shear (Fig. 3.3c).

The high-grade metamorphic sequence consists of metasedimentary rocks, (meta)igneous rocks and slices of serpentinite. The metasedimentary rocks (calsilicate rock, marble, metapelite, micaschist, paraamphibolite, paragneiss and quartzite) are usually found in the field as alternating thin layers of only several centimetres to decametres in thickness. Thick layers of micaschist are found at the base of the high-grade metamorphic sequence in the western part of the study area, while thick, massive layers of pure marble occur in the topmost position, usually forming the hilltops. A general increase of carbonate-dominated rocks (calcsilicate rock and marble) can be observed within the metasedimentary succession structurally upwards. Igneous intrusions are found in the lower parts of the metasedimentary succession. They comprise orthogneiss and small bodies of dark, unfoliated metadiorite. Monzogranitic and pegmatitic dykes cut through the metasedimentary succession. Metadiorite occurs only in the westernmost part of the study area and intrudes both the metasedimentary succession and the orthogneiss. The contact between granitoids and country rock is sharp and irregular. A contact aureole was generally not observed but small apophyses extend into the country rock (Fig. 3.5a). Small slices of serpentinite intercalated within the lower parts of the metasedimentary succession are usually associated with faults.

Both metasedimentary rocks and orthogneiss show a pervasive foliation that usually dips at low to medium angles to the NE or to the SW (Fig. 3.4c). Local variation in the orientation of the foliation was observed in few outcrops in the southeastern and western part of the mapped area, where the foliation dips at low to medium angles to the NW or to the SE. This may result from local displacement.

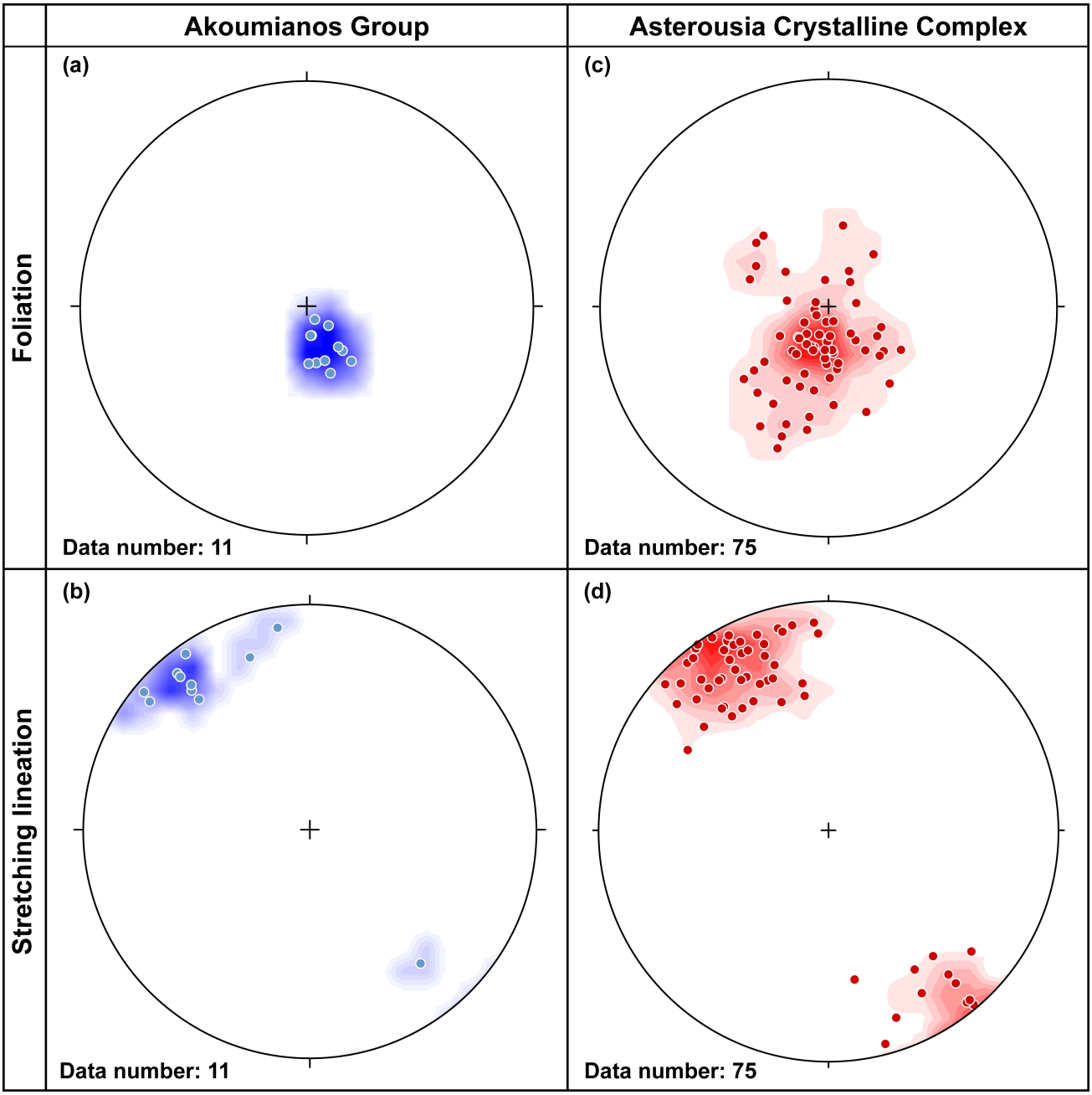

Fig. 3.4 Equal area, lower hemisphere stereoplots of structural data (stretching/mineral lineation and poles to main foliation) from low-grade metamorphic rocks of the Akoumianos Greenschist and high-grade metamorphic rocks of the Asterousia Crystalline Complex in the area west of Melambes. Statistical analyses using the 1 % area contouring method are indicated.

A mineral/stretching lineation consistently trending NNW–SSE to NW–SE (Fig. 3.4d) is most pronounced on the foliation planes of calcsilicate rock, orthogneiss and quartzite and is defined by the shape-preferred orientation of hornblende and pyroxene (calcsilicate rock), quartz and feldspar (orthogneiss) and quartz (quartzite).

The high-grade metamorphic rocks display manifold structures. Boudinage is frequently observed in the inhomogeneous metasedimentary succession, where thin layers of different rock types with a high competence contrast occur. Boudinage includes symmetric pinch and swell structures (necked boudins) and tapering boudins, as well as asymmetric boudins according to the classification of

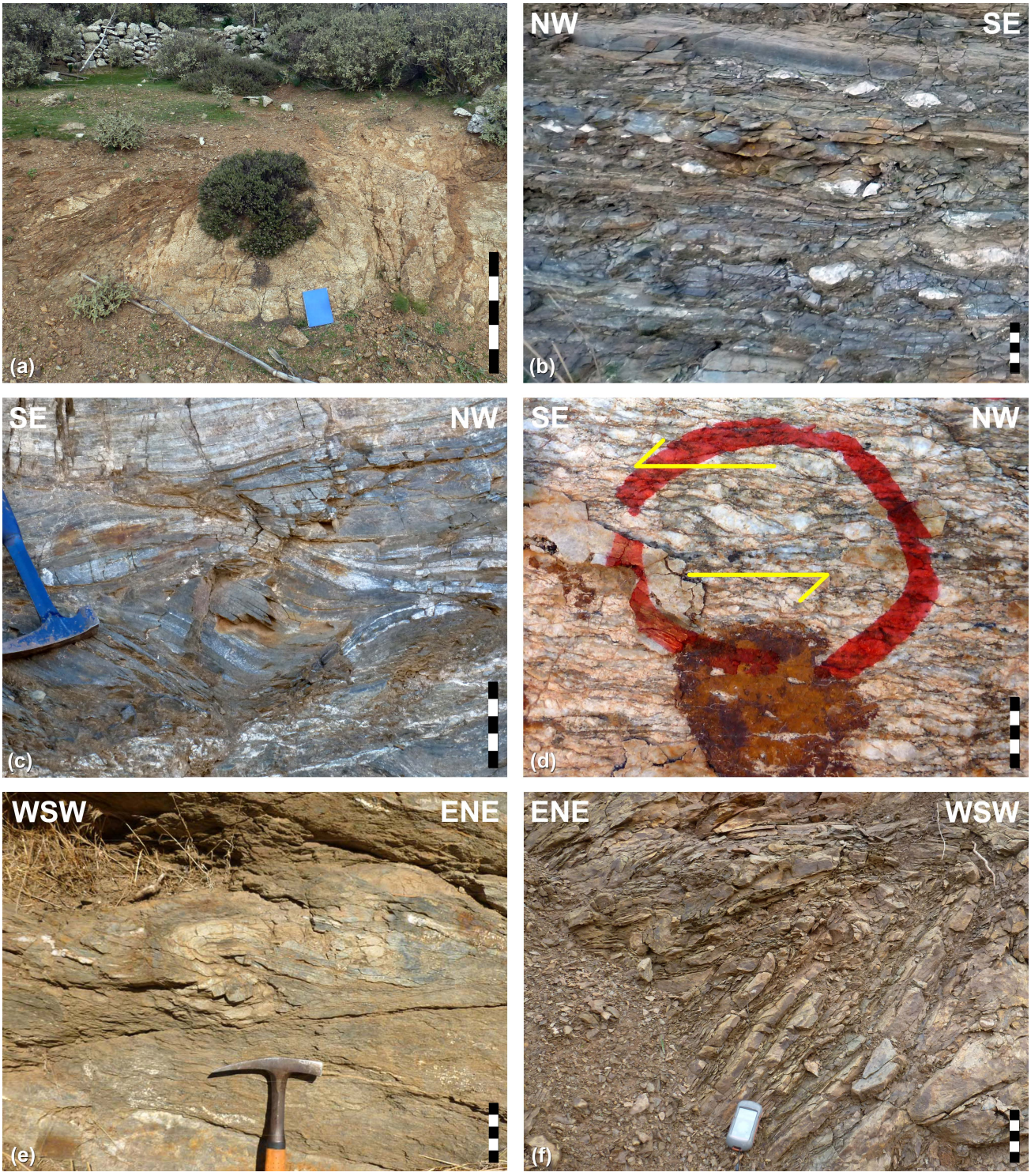

Fig. 3.5 Photographs of high-grade metamorphic rocks from the ACC west of Melambes. (a) Fragment of metagranite inside Asterousia-type metapelite. 200 m SW of the Sotiras chapel (35° 07′ 35.93″ N; 24° 38′ 23.10″ E). Scale bar = 1 m. (b) Boudinaged vein quartz in metapelitic rocks. Most quartz boudins are symmetric tapering boudins according to the classification of Goscombe et al. (2004), while some are slightly asymmetric indicating a top-to-the SE sense of shear. Road cut 1 km NW of Melambes (35° 08′ 24.59″ N; 24° 38′ 14.46″ E). Scale bar = 10 cm. (c) Asymmetric boudin of calcsilicate rock in less competent quartzite indicating top-to-the SE sense of shear. Road cut 1 km SSE of Nea Krya Vrysi (35° 08′ 24.18″ N; 24° 37′ 48.54″ E). Scale bar = 10 cm. (d) Sigmoidal clast of vein quartz in orthogneiss indicating a top-to-the SE sense of shear. Road cut 850 m SW of Nea Krya Vrysi (35° 08′ 36.32″ N; 24° 37′ 20.25″ E). Scale bar: 0.5 cm. (e) Drag folds within micaschist indicating a top-to-the WSW sense of shear. Road cut 1 km SW of Nea Krya Vrysi (35° 08′ 41.46″ N; 24° 37′ 13.02″ E). Scale bar = 10 cm. Photo: Courtesy of Bastian Wiesenbach. (f) WSW-vergent fold in Pindos flysch close to the contact with the overlying ACC. Road cut 700 m WNW of the Profitis Ilias chapel (35° 07′ 39.28″ N; 24° 37′ 39.97″ E). Scale bar = 10 cm.

Goscombe et al. (2004). Quartz veins in metapelite result usually in symmetric tapering boudins or sometimes slightly sigmoidal lenses (Fig. 3.5b). The average aspect ratio calculated for quartz boudins is 3.2 ± 0.1 (Table 3.2). Asymmetric boudins often originate from boudinage of calcsilicate rock in less competent rock types (Fig. 3.5c) and indicate a top-to-the SE sense of shear. Other shear sense indicators observed include C-type shear bands, asymmetrically shaped duplex structures, sigmoidal clasts (Fig. 3.5d) and asymmetric folds, all of which imply a dominant top-to-the SE transport. Some asymmetric folds and drag folds display a WSW-vergence instead (Fig. 3.5e), which is also found in folds affecting the Pindos flysch as well (Fig. 3.5f). Chevron folds in alternating layers of Pindos chert and limestone near Agios Pavlos about 7 km SW from the study area also show a W-vergence (e.g. Klein et al. 2013). At the southwestern margin of the study area along the dirt road 1.3 km N of Ano Saktouria, a succession of calcsilicate rock and marble developed drag folds (Fig. 3.6a) indicating a top-to-the SE sense of shear (Fig. 3.6b). Fold axes plunge at moderate angles to the NNW. Shear folding at the base of this succession also indicates a top-to-the SE sense of shear (Fig. 3.6c), while unfolded calcsilicate rock at the base of the folded sequence forms slightly asymmetric boudins (Fig. 3.6d).

Table 3.2 Summary of measurements on tapering quartz boudins within metapelite of the Asterousia Crystalline Complex west of Melambes and calculation of the aspect ratio. The arithmetic mean is given with the standard error.

	Range [cm]	Median [cm]	Arithmetic mean [cm]	Standard deviation	Measurements
Boudin length (L)	1.0–57.2	4.9	6.1 ± 0.5	5.8	119
Boudin width (W)	0.4–15.2	1.6	2.0 ± 0.1	1.6	119
Aspect ratio (L/W)	1.8–6.7	3.2	3.2 ± 0.1	0.9	119

A system of small-scale normal faults and reverse faults displacing the metasedimentary succession is observed throughout the whole succession. Normal faults within the metasedimentary succession and displacing also the marble exposure in the western part of the mapped area are N–S-oriented.

3.5.2 Petrography and microfabrics

3.5.2.1 Akoumianos Greenschist

Low grade metamorphic schists are very fine-grained and comprise two types: (1) *micaschist* consisting of K-feldspar, plagioclase, quartz, white mica and biotite (sample Mb017) and (2) *greenschist* consisting of epidote, actinolite, hornblende, chlorite, titanite and plagioclase (samples Mb015 and Mb019). Both types of schists show a pervasive foliation defined by shape-preferred orientation of either biotite and white mica or chlorite and amphibole (actinolite and hornblende), respectively. Despite the very fine grain size, shear sense indicators were frequently observed in thin sections. We observed S-C fabrics (Fig. 3.7a), sigmoidally shaped K-feldspar and epidote (Fig. 3.7a, b) and asymmetric pressure shadows of chlorite behind epidote and other clasts. All these indicate a consistent top-

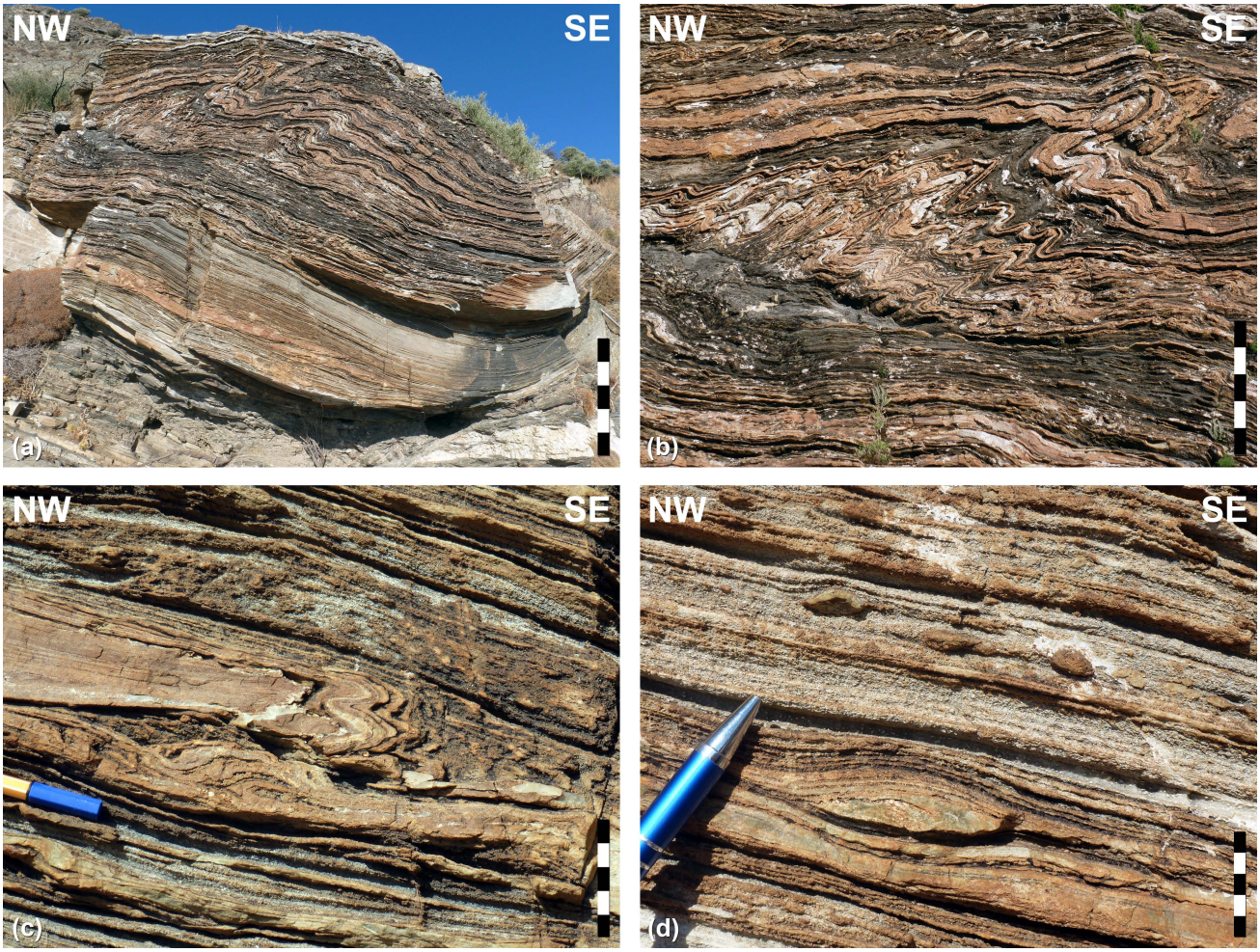

Fig. 3.6 Photographs of high-grade metamorphic rocks from the ACC west of Melambes. (a) SE-vergent drag folds in calcsilicate rock and marble above a mylonitic thrust, with the fold axes perpendicular to the mylonitic stretching lineation, indicating top-to-the SE sense of shear. Road cut 900 m SSW of Nea Krya Vrysi (35° 08′ 07.00″ N; 24° 36′ 55.23″ E). Scale bar = 1 m. (b) Close-up view of drag folds shown in (a). Scale bar = 50 cm. (c) Intrafolial fold of calcsilicate rock in a mylonitic shear zone at the base of the folded sequence. Fold axes plunge at moderate angles to the SE. Asymmetric fabrics below the fold indicate a top-to-the SE sense of shear. Scale bar = 5 cm. (d) Asymmetric boudins of calcsilicate rock inside mylonitic marble showing top-to-the SE sense of shear at the base of the folded sequence shown in (a). Scale bar = 3 cm.

to-the SE transport during ductile shearing. The thin section of sample Mb007b was also used for EMP analysis (see below).

Impure *quartzite* (sample Mel11) consists of ca. 75 % quartz with garnet, K-feldspar, plagioclase, white mica, clay minerals and accessories. Quartz is very fine-grained and dynamically recrystallized. Relics of small, elongate older grains with weak undulatory extinction are rare but usually old grains are affected by subgrains. (Sub)grain boundaries are sharp and straight or only weakly lobate. Quartz shows a weak grain shape-preferred orientation. White mica and clay minerals display shape-preferred orientation as well. Irregularly shaped syn-tectonic porphyroblasts of garnet show slightly asymmetric quartz-rich pressure shadows (Fig. 3.7c). In most cases, garnet was replaced by other phases, largely

chlorite, which forms pseudomorphs after garnet (Fig. 3.7d). The thin section of sample Mel11 was also used for EBSD analysis of quartz grains (see below).

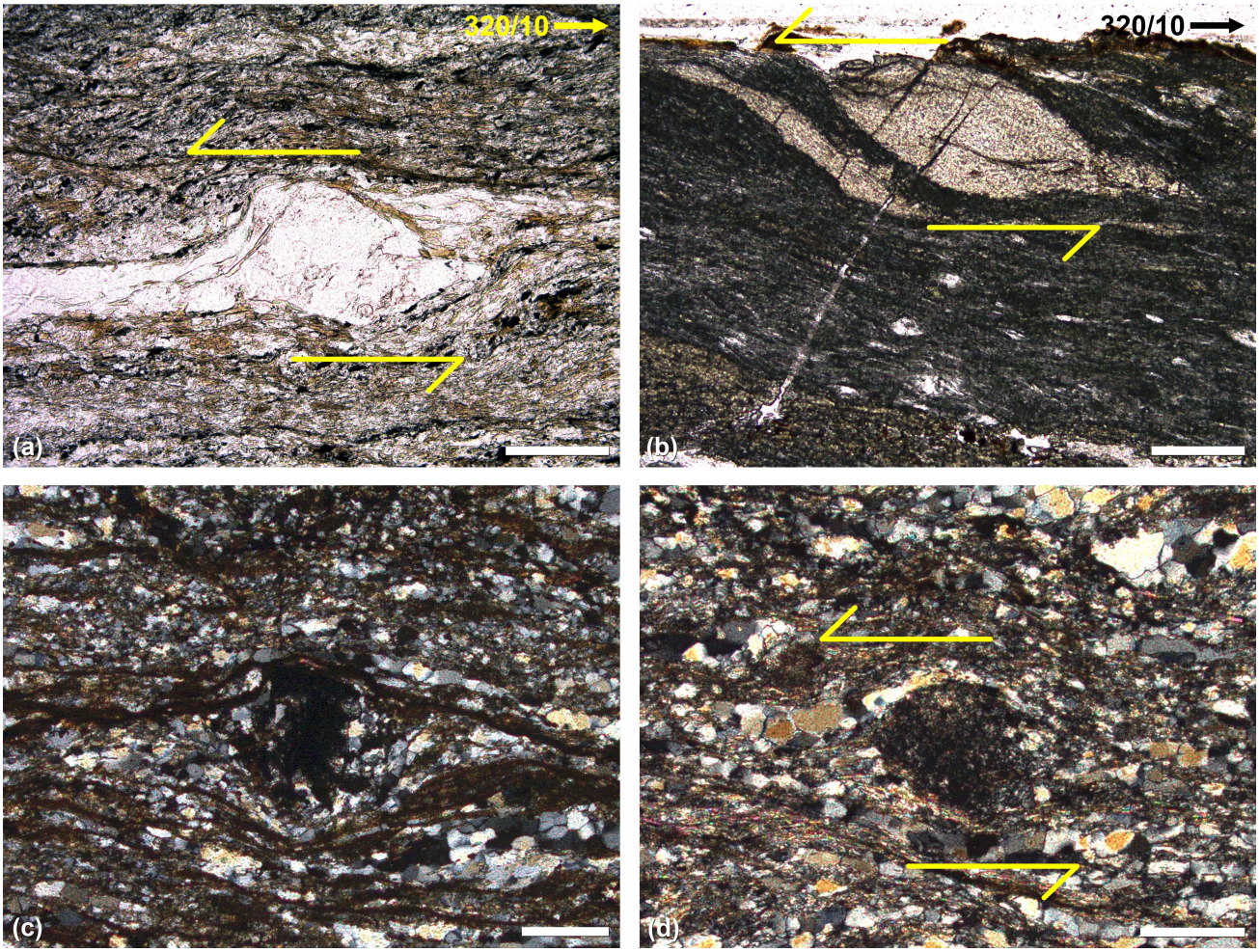

Fig. 3.7 Microphotographs of low-grade metamorphic rocks from the Akoumianos Greenschist south of Nea Krya Vrysi (cross-polarized light). (a) Micaschist showing sigmoidally shaped K-feldspar indicating a top-to-the SE tectonic transport. Road cut 1.3 km SW of Nea Krya Vrysi (35° 08′ 37.45″ N; 24° 36′ 54.22″ E). Sample: Mb017. Scale bar: 2 mm. (b) Sigmoidal epidote clast in greenschist indicating a top-to-the SE sense of shear. Road cut 1.5 km SW of Nea Krya Vrysi (35° 08′ 31.34″ N; 24° 36′ 49.17″ E). Sample: Mb019 (see also Fig. 12). Scale bar = 200 µm. (c) Syn-tectonic garnet porphyroblast with asymmetric pressure shadow of quartz in impure quartzite indicating a top-to-the SE sense of shear. Valley 1.5 km SW of Nea Krya Vrysi (35° 08′ 26.52″ N; 24° 36′ 53.40″ E). Sample: Mel11. Scale bar = 250 µm. (d) Pseudomorph of chlorite after garnet with an asymmetric pressure shadow indicating a top-to-the SE sense of shear. Same sample as in (c). Scale bar = 250 µm.

3.5.2.2 Asterousia Crystalline Complex

3.5.2.2.1 High-grade metasedimentary rocks

Quartzite (samples Mb007b, Mb012 and Mel51) consists of quartz, K-feldspar, plagioclase, garnet, biotite, epidote, white mica and chlorite, with quartz always making up more than two thirds of the constituents. The fabric of quartzite is mylonitic with ribbons of quartz and mineral clasts in a fine-grained, dynamically recrystallized matrix consisting mostly of quartz. Almost pure layers of recrystallized quartz occur in alternation with highly impure layers. Quartz shows serrated grain boundaries and undulatory extinction but lacks chessboard type subgrains. Relics of older grains are absent. White

mica is acicular and shows grain shape-preferred orientation. Unrecrystallized relics of feldspar are sometimes preserved. Mineral clasts consisting of K-feldspar, plagioclase or garnet (Fig. 3.8a) are very abundant and, if elongated, can be either symmetric or asymmetric, in the latter case indicating consistently a top-to-the SE sense of shear sense. This sense of shear is also indicated by S-C fabrics and mica fish (Fig. 3.8b). The thin section of sample Mb007b was also used for EBSD analysis on quartz (see below).

Calcsilicate rock (samples Mb007a, Mb029) is very inhomogeneous in composition and consists of varying amounts of calcite, clinopyroxene (presumably diopside), amphibole (presumably hornblende), K-feldspar, opaque phases, plagioclase and quartz, all of which are found in a fine-grained matrix. Clinopyroxene and K-feldspar show grain shape-preferred orientation. Some samples of calcsilicate rock contain also garnet, which is never found as porphyroblasts but only xenomorphic and concentrated in layers within the matrix (Fig. 3.8c). Calcite usually occurs recrystallized in veins but may also be found within the matrix. Feldspar (both K-feldspar and plagioclase) and quartz are dynamically recrystallized and show undulatory extinction. Shear-sense indicators were not observed in calcsilicate rock.

The lower part of the high-grade metasedimentary sequence west of Melambes is characterized by alternating layers of thin-bedded marble and paraamphibolite. *Paraamphibolite* (samples Mb026, Mb033 and Mb038) usually consists of > 50 % green amphibole (hornblende) with varying amounts of calcite, chlorite, clinopyroxene (presumably diopside) and plagioclase. A foliation is defined by the shape-preferred orientation of hornblende grains. Calcite is medium-grained (0.4–4 mm) and frequently found recrystallized in veins reaching a length of up to 5 cm and subparallel to the main foliation. Small inclusions of diopside and hornblende are usually present inside these veins. Calcite shows thick, tabular twins of type II (Fig. 3.8d) according to the classification of Burkhard (1993). Shear sense indicators are almost absent. In one case, a small porphyroblast of plagioclase with an asymmetric pressure shadow indicating a top-to-the SE sense of shear was observed.

Paragneiss (sample Mb041) is made of biotite, K-feldspar, plagioclase, quartz (> 50 %), staurolite and white mica. Grain shape-preferred orientation is obvious by acicular biotite (Fig. 3.8e). Both feldspar and quartz are recrystallized. White mica is of secondary origin and only infrequently aligned parallel to the main foliation. Staurolite is found as poikiloblasts within a fine-grained matrix made of the other constituents and shows slightly asymmetric pressure shadows of biotite indicating a top-to-the SE sense of shear (Fig. 3.8f).

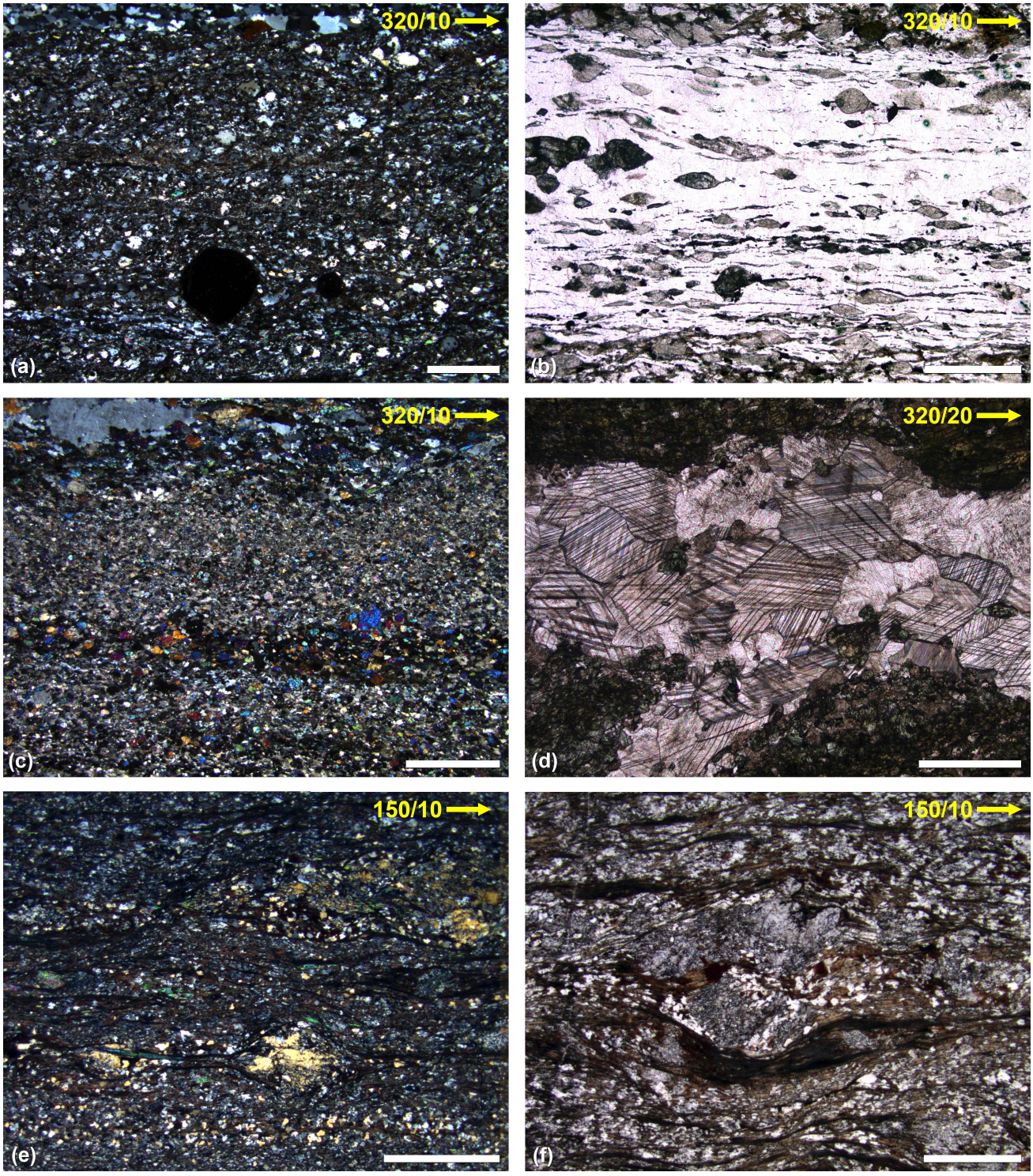

Fig. 3.8 Microphotographs of high-grade metamorphic rocks from the ACC west of Melambes. (a) Garnet clasts in impure quartzite. Cross-polarized light. Sample: Mb007b. Road cut 825 m NW of St Mary's church (35° 08′ 07.00″ N; 24° 36′ 55.23″ E). Scale bar = 1 mm. (b) Numerous mica fishes indicating a top-to-the SE sense of shear in matrix of quartz. Plane-polarized light. Same sample as in (a). Scale bar: 500 µm. (c) Fine-grained calcsilicate rock with dark layers rich in garnet. Cross-polarized light. Sample: Mb007a. Location: See Fig. 8a. Scale bar: 2 mm. (d) Calcite vein in paraamphibolite with type II twins according to the classification of Burkhard (1993). Plane-polarized light. Sample: Mb026. Location: On the hill 800 m N of St Mary's church (35° 08′ 07.53″ N; 24° 37′ 05.25″ E). Scale bar: 500 µm. (e) Paragneiss consisting of several staurolite poikiloblasts in fine-grained matrix of K-feldspar, plagioclase and quartz with biotite and white mica showing shape-preferred orientation. Cross-polarized light. Sample: Mb041. Location: Road cut 600 m W of Melambes (35° 07′ 46.69″ N; 24° 38′ 40.43″ E). Scale bar: 2 mm. (f) Staurolite porphyroblast with asymmetric pressure shadows indicating a top-to-the SE sense of shear. Plane-polarized light. Same sample as in (e). Scale bar: 1 mm.

3.5.2.2.2 Igneous rocks

The main constituents of *orthogneiss/metagranite* (samples Do513a, Do513b, Mb008, Mb022, Mb022q, Mb023, Mb024, Mb028 and Mb057) are K-feldspar, quartz, plagioclase, hornblende, biotite, white mica and opaque phases. Modal abundances were determined by point counting (Table 3.3). Since no growth of new minerals was observed, the mineral composition of orthogneiss is believed to represent the original composition of the igneous rocks before deformation and metamorphism. Thus, the modal abundances of quartz, alkali feldspar and plagioclase were recalculated and plotted in a QAP diagram. Orthogneiss samples plot in the syeno- and monzogranite fields (Fig. 3.9). Deformation of granite was ductile and penetrative. A pervasive mylonitic foliation is defined by grain shape-preferred orientation of biotite, white mica and hornblende (Fig. 3.10a). Recrystallization of mica was not observed. Feldspar is sometimes recrystallized. K-feldspar is usually microcline, which is indicated by cross-hatched twinning. It is sometimes perthitic and myrmekite growth is common. Plagioclase is often strongly albitized and sericitized. Grains of K-feldspar, not recrystallized, show rare Karlsbad twinning, while very rare primary zoning has been preserved in plagioclase. Quartz is usually dynamically recrystallized and large grains show undulatory extinction and weakly developed chessboard-type subgrains. Serrated boundaries between feldspar and quartz are the rule. Sigmoidally shaped K-feldspar and quartz as well as S-C fabrics in sections cut perpendicular to the foliation and parallel to the stretching lineation indicate a top-to-the SE sense of shear (Fig. 3.10a, b).

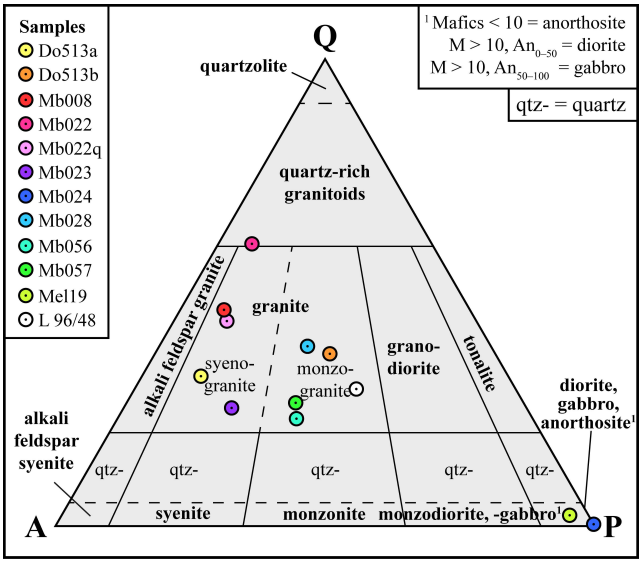

Fig. 3.9 Composition of igneous rocks from the study area plotted in a QAP diagram (Streckeisen 1974). Modal amount of alkali feldspar, plagioclase and quartz are recalculated from results of point counting analyses (Table 3.3). Distinction of anorthosite, diorite and gabbro after Le Maitre et al. (2002). The composition of sample L 96/48 from Langosch (1999) was determined using the CIPW norm for geochemical analyses.

Monzogranite (sample Mb056) from a dyke cutting through metapelite SE of the Sotiras chapel and close to the intrusive contact of orthogneiss with metapelite consists of K-feldspar, quartz, plagioclase, hornblende, biotite, white mica and opaque phases. The amount of quartz (20.4 %) and mica (4.2 %) is lower than in any of the metagranite samples. Furthermore, mica shows no shape-preferred orientation. Quartz and feldspar are partly recrystallized and boundaries between the two phases are usually angular (Fig. 3.10c). Grain size is strongly variable. Quartz shows weak undulatory extinction and deformation lamellae. K-feldspar is often perthitic indicating exsolution.

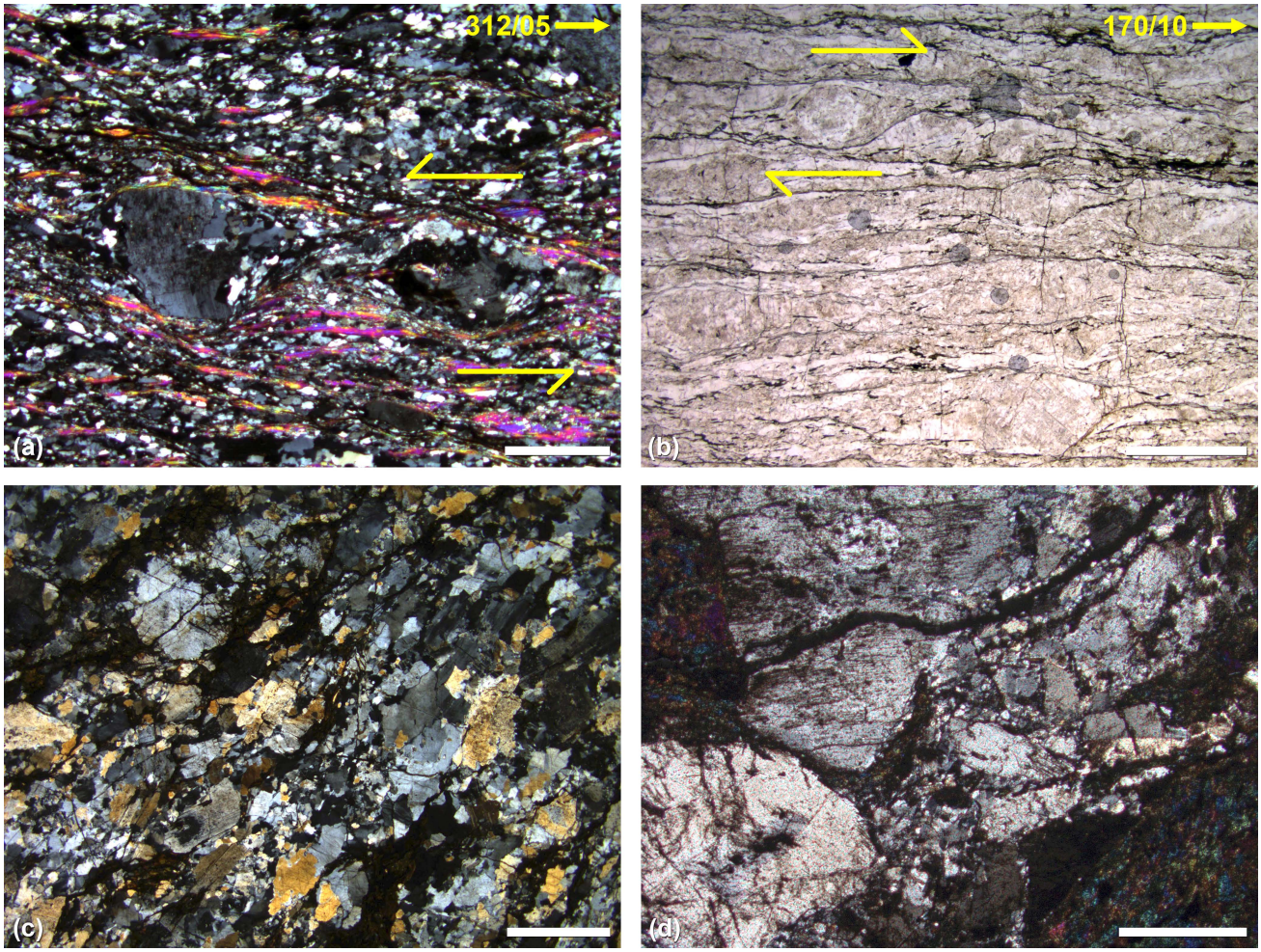

Fig. 3.10 Microphotographs of (meta)igneous rocks from the ACC west of Melambes. (a) Orthogneiss showing shape-preferred orientation of white mica and two porphyroclasts of K-feldspar with asymmetric pressure shadows consisting of quartz. Cross-polarized light. Sample: Mb008. Location: Road cut 750 m NW of St Mary's church (35° 08′ 04.98″ N; 24° 36′ 56.16″ E). Scale bar: 2 mm. (b) σ-clasts of K-feldspar in orthogneiss indicating a top-to-the SE sense of shear. Plane-polarized light. Sample: Mb023. Road cut 800 m SSW of Nea Krya Vrysi (35° 08′ 36.32″ N; 24° 37′ 20.25″ E). Scale bar: 2 mm. (c) Monzogranite from a dyke cutting through metapelite. Cross-polarized light. Sample: Mb056. Location: Road cut 225 m SE of the Sotiras chapel (35° 07′ 35.93″ N; 24° 38′ 23.10″ E). Scale bar: 2 mm. (d) Partly recrystallized plagioclase in metadiorite. Cross-polarized light. Sample: Mel19. Location: Road cut 750 m SW of Nea Krya Vrysi (35° 08′ 41.46″ N; 24° 37′ 13.02″ E). Scale bar: 1 mm.

Table 3.3 Modal composition in volume percent of igneous rocks from the Asterousia Crystalline Complex west of Melambes. 1,000 points were counted per thin section. 2σ errors are below 1.6 % for each mineral phase (van der Plas and Tobi 1965).

Sample	Biotite	Chlorite	Horn-blende	K-feld-spar	Plagio-clase	Quartz	White mica	Ore minerals	Others	Rock type
Do513a	3.7	—	—	51.6*	10.1	29.6	3.3	0.4	0.3	Syenogranite
Do513b	8.2	—	0.1	27.7*	29.3	31.4	2.9	0.3	0.1	Monzogranite
Mb008	5.0	—	—	34.9	6.2	35.4	16.4	2.1	—	Syenogranite
Mb022	7.7	—	1.9	28.7*	5.4	53.3	1.9	0.6	0.5	Syenogranite
Mb022q	4.3	—	0.8	41.9*	8.9	39.7	3.4	0.6	0.4	Syenogranite
Mb023	4.1	—	—	48.1*	17.6	22.2	6.6	1.1	0.3	Syenogranite
Mb024	4.0	0.3	48.7	—	42.9	0.4	—	3.6	0.1	Diorite
Mb028	21.0	—	1.9	23.9	19.3	27.1	5.2	1.2	0.4	Monzogranite
Mb056	3.9	—	3.9	38.9*	29.5	20.4	0.3	2.6	0.5	Monzogranite
Mb057	6.5	—	3.0	37.8*	28.1	23.6	0.3	0.3	0.4	Monzogranite
Mel19	3.6	—	51.6	1.5	40.6	1.0	—	1.1	0.4	Diorite

* K-feldspar is partly perthitic.

Metadiorite (samples Mb024 and Mel19) is very fine-grained and consists of green hornblende and plagioclase, with biotite, chlorite, K-feldspar, opaque phases and quartz occurring as accessory minerals (Table 3.3). The content of mafic phases (biotite, chlorite and hornblende) is > 50 vol%. Although the anorthite content in plagioclase was not determined, the complete absence of clinopyroxene justifies the classification as diorite. Shape-preferred orientation of mineral phases was not observed. Plagioclase shows only rare twinning and is strongly albitized. Dynamic recrystallization of plagioclase is rare (Fig. 3.10d). Very few amounts of recrystallized quartz are usually present.

3.5.3 EBSD analyses

The contoured pole diagrams of quartz c-axes orientations show elongated, asymmetric and single girdles. The girdle of quartz c-axes orientations in quartzite from the low-grade metamorphic rocks (Mel11) is broad (Fig. 3.11a). However, quartz c-axes orientations for quartzite from the high-grade metamorphic rocks (Mb007b) show a small girdle (Fig. 3.11b). Both CPO patterns are typical for quartz developed by non-coaxial deformation. The dominant slip systems during crystal plastic deformation of quartz in sample Mel11 were rhomb <a> slip and subordinate prism <a> slip (Passchier and Trouw 2005 and references therein). The CPO patterns of sample Mb007b, on the other hand, indicate prism <a> slip and, to a lesser extent, rhomb <a> slip to be the dominant slip systems during deformation. This corresponds to deformation temperatures of ca. 500 °C for the Akoumianos-type quartzite and slightly higher deformation temperatures for the Asterousia-type quartzite (Lister and Dornsiepen 1982; Stipp et al. 2002). The asymmetry of both textures is consistent with a top-to-the SE sense of shear.

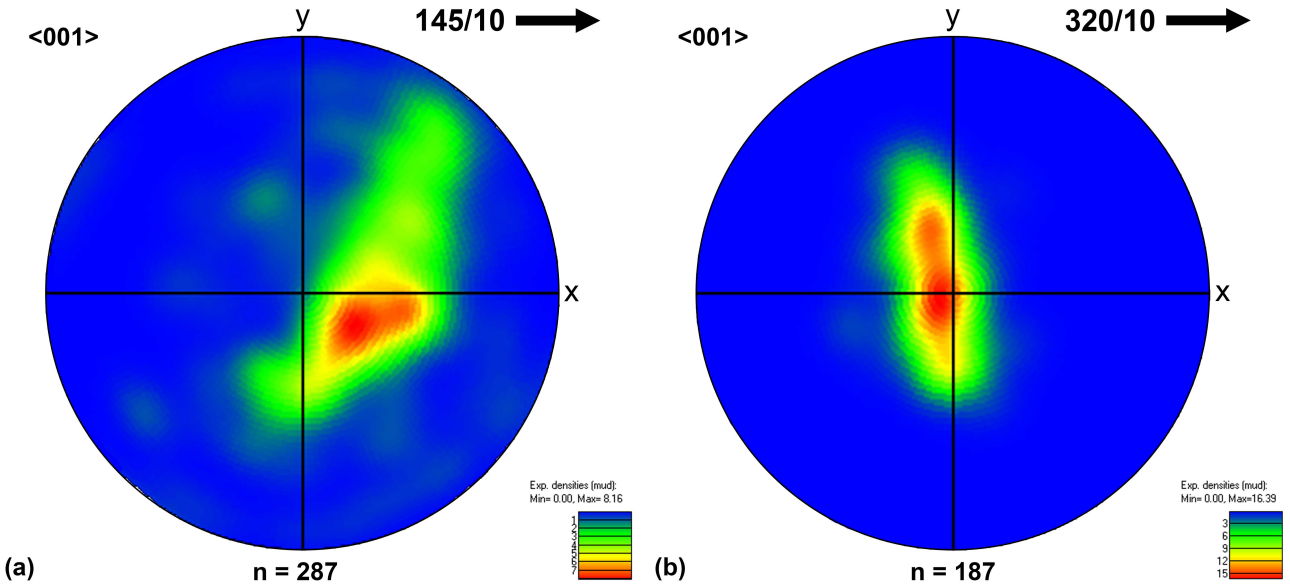

Fig. 3.11 Equal area, lower hemisphere pole diagrams of contoured CPO patterns of quartz c-axes in impure quartzite of a) sample Mel11 (cf. Fig. 7d) from the Akoumianos Greenschist and (b) sample Mb007b (cf. Fig. 8a, b) from the ACC. Note that sample Mel11 was cut subparallel to the stretching lineation, resulting in slightly shifted CPO patterns.

3.5.4 EMP analysis

Results of representative chemical analyses applying EMP analysis on two samples of greenschist (samples Mb015 and Mb019) from the Akoumianos Greenschist are presented in Tables 3.4 and 3.5. Structural formulae calculated from the chemical analyses revealed the following phases: albite, actinolite, actinolitic hornblende, chlorite, magnesio-hornblende, microcline, oligoclase and richterite. Titanite is visible as euhedral, rhombic grains on BSE images (Fig. 3.12a). Three types of Ca-amphiboles (actinolite, actinolitic hornblende and magnesio-hornblende) and one Na-Ca amphibole (richterite) are suggested from the structural formulae calculated (Fig. 3.12b). Plagioclase has anorthite contents ranging from 0.64 to 15.71 % and can be classified as albite to Ca-poor oligoclase. Microcline occurs as accessory mineral.

Table 3.4 Representative chemical analyses on greenschist Mb015 from the Akoumianos valley and calculation of structural formulae. [1]Chemical composition of oxides in weight percent; [2]For epidote all iron is converted to Fe^{3+}; Fe^{2+}/Fe^{3+} estimations for amphiboles are made by assuming 13 total cations excluding Ca, Na and K (Leake 1978); [3]An content = anorthite content of plagioclase [Ca/(Na+K+Ca)]; [4]Mineral abbreviations: acthbl = actinolitic hornblende, chl = chlorite; epd = epidote; hbl = magnesio-hornblende, olg = oligoclase, rct = richterite, wmc = white mica.

Analysis	**p1**	**p4**	**p7**	**p9**	**p11**	**p16**	**p17**	**p21**
SiO_2	47.88	49.88	58.31	51.76	38.70	65.69	65.97	29.86
TiO_2	0.04	0.18	0.10	0.30	0.11	—	—	0.06
Al_2O_3	32.57	7.07	19.15	6.03	25.76	20.87	20.62	21.16
Cr_2O_3	0.01	0.22	0.02	0.15	0.05	—	0.01	0.01
FeO	1.26	12.46	3.92	11.42	8.89	0.08	0.12	18.02
MnO	0.01	0.22	0.10	0.25	0.12	0.01	0.02	0.25
MgO	1.18	14.39	3.17	14.93	0.03	0.01	0.01	17.62
CaO	—	12.20	6.57	12.00	23.45	2.53	2.34	0.56
NiO	—	0.04	0.02	0.02	—	—	0.02	0.06
Na_2O	0.19	1.06	7.12	0.79	0.15	10.35	10.53	0.73
K_2O	10.86	0.18	0.15	0.18	—	0.13	0.09	0.01
P_2O_5	0.01	—	0.01	0.03	0.03	—	—	0.01
Total	94.00	97.90	98.62	97.84	97.29	99.67	99.72	88.35
	O = 11	O = 23	O = 23	O = 23	O = 12.5	O = 8	O = 8	O = 28
Si	3.225	7.172	7.764	7.386	3.030	2.900	2.911	5.902
Ti	0.002	0.020	0.010	0.032	0.006	—	—	0.008
$^{[4]}Al$	0.775	0.828	0.236	0.614	—	1.086	1.072	2.098
$^{[6]}Al$	1.810	0.370	2.769	0.400	2.377	—	—	2.885
Fe^{3+}	—	0.331	—	0.232	0.582	0.003	0.004	0.320
Fe^{2+}	0.071	1.167	0.436	1.131	—			2.659
Mn	0.000	0.027	0.011	0.030	0.008	0.001	0.001	0.042
Mg	0.118	3.085	0.629	3.176	0.004	0.001	0.001	5.191
Ca	—	1.879	0.937	1.835	1.967	0.120	0.111	0.119
Na	0.025	0.295	1.838	0.217	0.022	0.886	0.901	0.562
K	0.933	0.034	0.025	0.032	—	0.007	0.005	0.006
∑ cations	6.959	15.208	14.655	15.084	7.996	5.003	5.006	19.802
An content[3]	—	—	—	—	—	11.817	10.886	—
Mineral phase[4]	wmc	hbl	rct	acthbl	epd	olg	olg	chl

Due to the amphibole-plagioclase mineral assemblage, the geothermometer of Holland and Blundy (1994) was applied for different mineral pairs of plagioclase and amphibole (Table 3.6). This geothermometer needs an estimation for pressure conditions. Low pressure during metamorphism is indicated by the aluminium content in hornblende being low (6.53–7.07 %). Therefore, only pressures of 200,

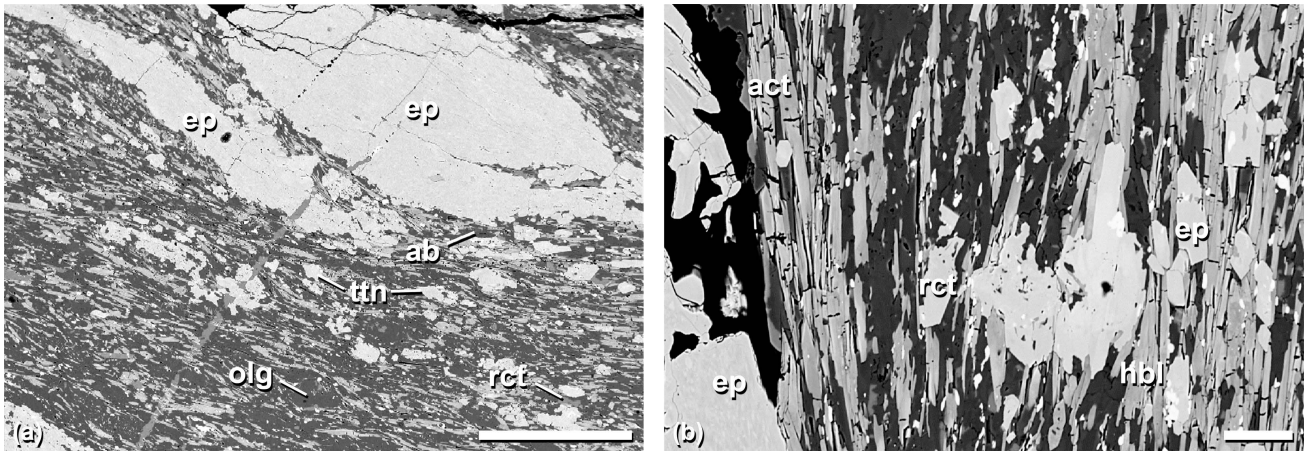

Fig. 3.12 Backscattered electron images of greenschist (sample Mb019; cf. Fig. 3.7b). (a) Sigmoidal epidote lens and euhedral, rhombic titanite grains in fine-grained matrix. Scale bar: 200 µm. (b) Fine-grained matrix consisting of acicular actinolite, epidote, richterite and hornblende. Scale bar: 30 µm.

300 and 400 MPa, respectively, have been considered in Table 3.6. Calculated temperatures of metamorphism scatter between 394 °C for the mineral pairs low-Ca albite and actinolite (P = 200 MPa) to 564 °C for the mineral pairs low-Ca oligoclase and magnesio-hornblende (P = 400 MPa). Estimations of the metamorphic conditions applying the hornblende-plagioclase geothermobarometer of Plyusnina (1982) yielded P = 250–400 MPa and T = 500 +15/–30 °C.

Table 3.5 Representative chemical analyses on greenschist Mb019 from the Akoumianos valley and calculation of structural formulae. [1]Chemical composition of oxides in weight percent; [2]For epidote all iron is converted to Fe^{3+}; Fe^{2+}/Fe^{3+} estimations for amphiboles are made by assuming 13 total cations excluding Ca, Na and K (Leake 1978); [3]An content = anorthite content of plagioclase [Ca/(Na+K+Ca)]; [4]Mineral abbreviations: alb = albite, act = actinolite, acthbl = actinolitic hornblende, epd = epidote, hbl = magnesio-hornblende, mcl = microcline, olg = oligoclase, rct = richterite, ttn = titanite.

Analysis	**p15**	**p17**	**p29**	**p30**	**p40**	**p41**	**p59**	**p60**	**p62**	**p63**	**p68**
SiO_2	66.07	69.58	42.43	65.61	68.59	38.75	54.84	51.80	54.52	49.89	58.56
TiO_2	—	0.02	26.62	—	0.02	0.06	0.12	0.18	0.09	0.20	0.10
Al_2O_3	21.50	19.38	6.46	21.62	19.91	24.24	2.67	5.19	2.67	6.53	12.77
Cr_2O_3	0.02	—	0.09	—	—	0.02	0.06	0.09	0.09	—	0
FeO	0.01	0.13	0.56	0.09	0.33	11.03	10.30	11.97	10.86	14.63	5.70
MnO	—	—	0.03	0.02	—	0.20	0.28	0.27	0.29	0.26	0.17
MgO	0.01	0.05	—	0.11	0.04	0.06	17.46	16.01	17.22	13.63	7.30
CaO	2.68	0.22	19.96	0.09	1.24	23.41	12.69	12.34	12.48	12.03	7.29
NiO	0.02	0.02	—	—	—	0.03	0.02	—	0.03	0.01	0.01
Na_2O	10.53	11.37	3.40	0.17	11.39	0.02	0.44	0.83	0.44	0.99	6.27
K_2O	0.08	0.78	0.05	14.92	0.06	—	0.06	0.10	0.07	0.13	0.30
P_2O_5	0.02	—	—	—	0.01	—	0.07	—	—	—	—
Total	100.94	101.54		102.62	101.60	97.81	99.00	98.78	98.38	98.76	98.48
	O = 8	O = 8	—	O = 8	O = 8	O = 12.5	O = 23	O = 23	O = 23	O = 23	O = 23
Si	2.883	3.002	—	2.925	2.963	3.034	7.665	7.301	7.635	7.165	7.935
Ti	—	0.001	—	—	0.001	0.004	0.012	0.019	0.010	0.022	0.010
$^{[4]}Al$	1.106	0.986	—	1.075	1.014	—	0.335	0.699	0.365	0.835	0.065
$^{[6]}Al$	—	—	—	0.061	—	2.237	0.104	0.164	0.076	0.270	1.975
Fe^{3+}	0.000	0.005	—	0.003	0.012	0.722	0.270	0.514	0.384	0.519	—
Fe^{2+}			—			—	0.934	0.897	0.888	1.238	0.646
Mn	—	—	—	0.001	—	0.013	0.033	0.032	0.034	0.032	0.020
Mg	0.001	0.003	—	0.007	0.003	0.006	3.638	3.364	3.595	2.918	1.475
Ca	0.125	0.010	—	0.004	0.057	1.964	1.900	1.864	1.873	1.851	1.058
Na	0.891	0.951	—	0.014	0.954	0.003	0.118	0.226	0.118	0.277	1.647
K	0.005	0.043	—	0.848	0.003	—	0.010	0.019	0.012	0.023	0.052
∑ cations	5.012	5.001	—	4.939	5.007	7.984	15.029	15.108	15.003	15.151	14.885
An content[3]	12.274	1.004	—	0.485	5.645	—	—	—	—	—	—
Mineral phase[4]	olg	alb	alb + ttn	mcl	alb	epd	act	acthbl	act	hbl	rct

Table 3.6 Geothermometry calculations for several amphibole-plagioclase pairs from greenschist samples Mb015 and Mb019 using the representative chemical analyses (Tables 3.4 and 3.5).

Sample	Mb015								Mb019							
Pairs*	p4/p16	p4/p17	p9/p16	p9/p17	p15/p59	p15/p60	p15/p62	p15/p63	p17/p59	p17/p60	p17/p62	p17/p63	p40/p59	p40/p60	p40/p62	p40/p63
Estimated pressure P = 200 MPa																
T [°C]**	530.2	499.8	524.5	494.0	532.6	562.7	532.4	556.3	393.6	421.5	394.3	416.8	480.8	510.3	481.0	504.5
Estimated pressure P = 300 MPa																
T [°C]**	535.2	505.6	529.5	499.8	534.5	565.2	534.1	560.1	395.1	423.6	395.7	420.0	482.5	512.6	482.6	508.1
Estimated pressure P = 400 MPa																
T [°C]**	540.2	511.4	534.5	505.5	536.3	567.8	535.8	564.0	396.6	425.7	397.1	423.3	484.2	515.0	484.2	511.7

*Mineral pairs of plagioclase + amphibole using the analysis numbers indicated in Tables 3.4 and 3.5; **Temperature calculations using the edenite-richterite geothermometer for hornblende assemblages lacking quartz (Holland and Blundy 1994).

3.5.5 Geochronological analyses

Six samples of igneous rocks intruded into the high-grade metasedimentary succession west of Melambes were selected for U-Pb age dating on zircon. Zircons of metadiorite samples Mb024 and Mel2.17, orthogneiss samples Do513, Mb022 and Mb057 and monzogranite sample Mb057 were analysed with LA-ICP-MS, while zircons of samples Do 513 and Mel2.17 were also analysed with ID-TIMS. ID-TIMS analyses on Do513 failed due to the low content of radiogenic lead within single zircons.

3.5.5.1 Metadiorite (samples Mb024 and Mel2.17)

Zircons from metadiorite are heteromorphic, most zircon grains being colourless and having a homogeneous core with a narrow overgrowth rim showing fine oscillatory zoning (Fig. 3.13a). Some zircon grains lack a homogeneous core but show coarse oscillatory zoning throughout and sometimes faint sector zoning. Small inclusions may occur in these zircons.

Zircons of metadiorite samples Mb024 and Mel2.17 analysed with LA-ICP-MS have low uranium contents ranging from 29 to 359 ppm

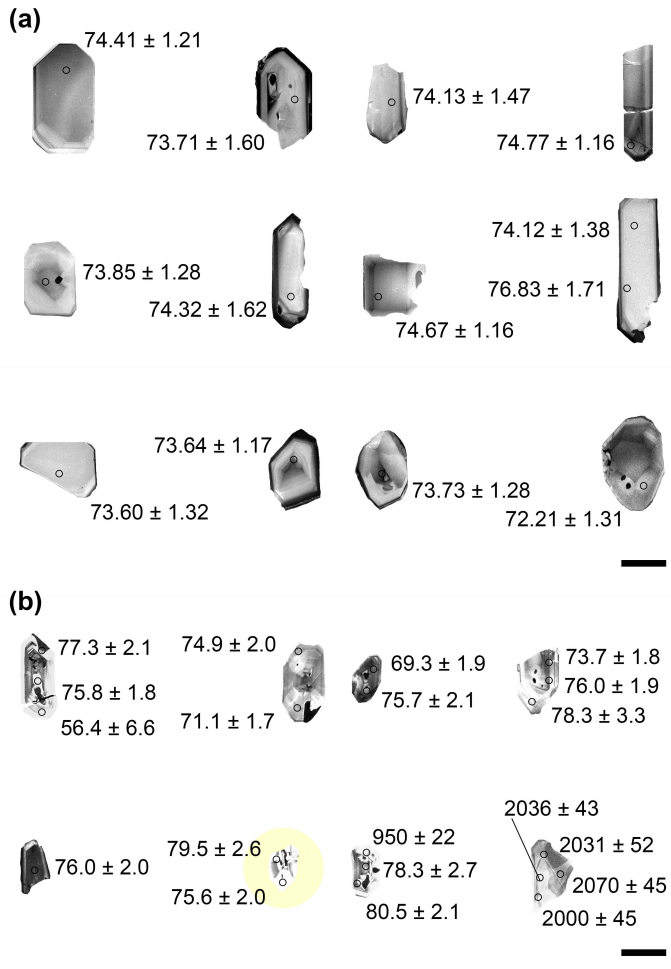

Fig. 3.13 Representative cathodoluminescence images of zircons from metadiorite Mel2.17 (a) and orthogneiss Do513 (b). Zircons are euhedral, prismatic and pristine. Small inclusions are common. Zircons from orthogneiss show regular growth zoning, while zircons from metadiorite lack growth zoning. One amorphous and pristine zircon grain from orthogneiss Do513 yielding Palaeoproterozoic ages lacks growth zoning and inclusions. Scale bars: 100 µm.

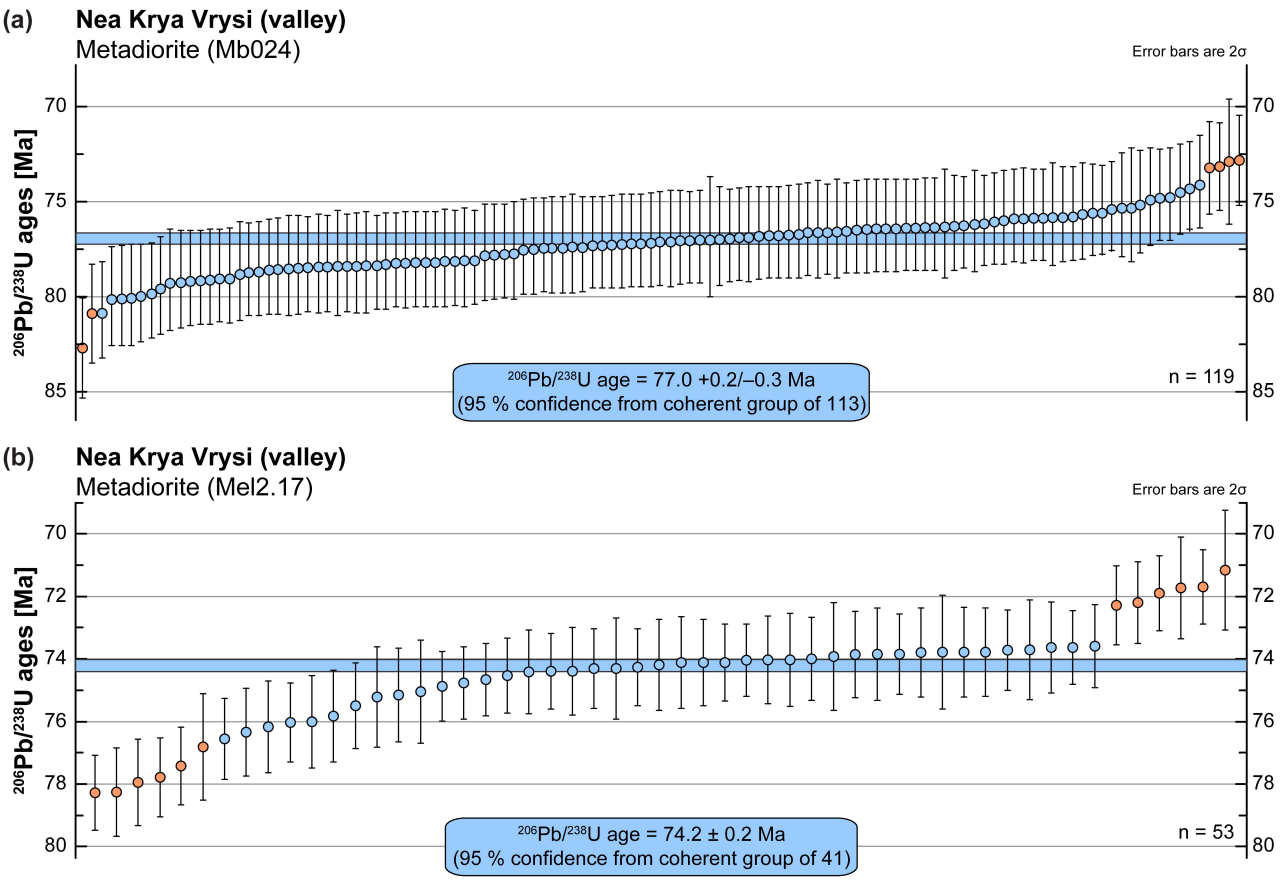

Fig. 3.14 Scatter plots summarizing $^{238}U/^{206}Pb$ zircon ages obtained from LA-ICP-MS analyses on metadiorite samples Mel2.17 (a) and Mb024 (b) from the ACC SW of Nea Krya Vrysi. Error bars represent the 95 % confidence interval of the median age.

(Table 3.7). Th/U ratios usually range between ~0.5 and ~1.5. The amount of common lead (Pbc) is low and except for analysis A40 (Pbc = 19.6) yielding the youngest age obtained, the influence of Pbc on the concordance is negligible. LA-ICP-MS analyses resulted in $^{206}Pb/^{238}U$ concordant ages at 82.7 ± 2.6 to 72.3 ± 1.3 Ma. The $^{206}Pb/^{238}U$ median age calculated from 113 analyses on zircons from Mb024 is 77.0 +0.2/–0.3 Ma (Fig. 3.14a), while 41 analyses on zircons from Mel2.17 yielded a $^{206}Pb/^{238}U$ median age at 74.2 ± 0.2 Ma (Fig. 3.14b). Ninety-two analyses on zircons from metadiorite Mb024 resulted in a concordia age at 76.9 ± 0.3 with a mean standard weighted deviation (MSWD) of 0.43 and a probability of concordance (P) of 0.51 (Fig. 3.15a), while thirty-one analyses on zircons from metadiorite Mel2.17 yielded a concordia age at 74.1 ± 0.3 Ma (MSWD = 0.082; P = 0.77; Fig. 3.15b). Six analyses with the youngest $^{206}Pb/^{238}U$ ages obtained for metadiorite Mel2.17 result in a concordia age at 71.9 ± 0.6 Ma (MSWD = 0.26; P = 0.61; Fig. 3.15a). There was no correlation observed between the shape of zircon grains and the U-Pb ages.

Zircons from metadiorite Mel2.17 analysed using ID-TIMS have a moderate uranium content ranging from 342 to 1296 ppm (Table 3.8). $^{206}Pb/^{238}U$ ages range from 72.0 ± 1.0 Ma to 74.8 ± 0.6 Ma. Three analyses, including the analyses with the lowest and the highest uranium contents, define a

concordia age at 72.2 ± 0.4 Ma (MSWD = 0.01; P = 0.92; Fig. 3.15d), while the other three analyses define a concordia age at 74.3 ± 0.4 Ma (MSWD = 0.14; P = 0.71; Fig. 3.15d).

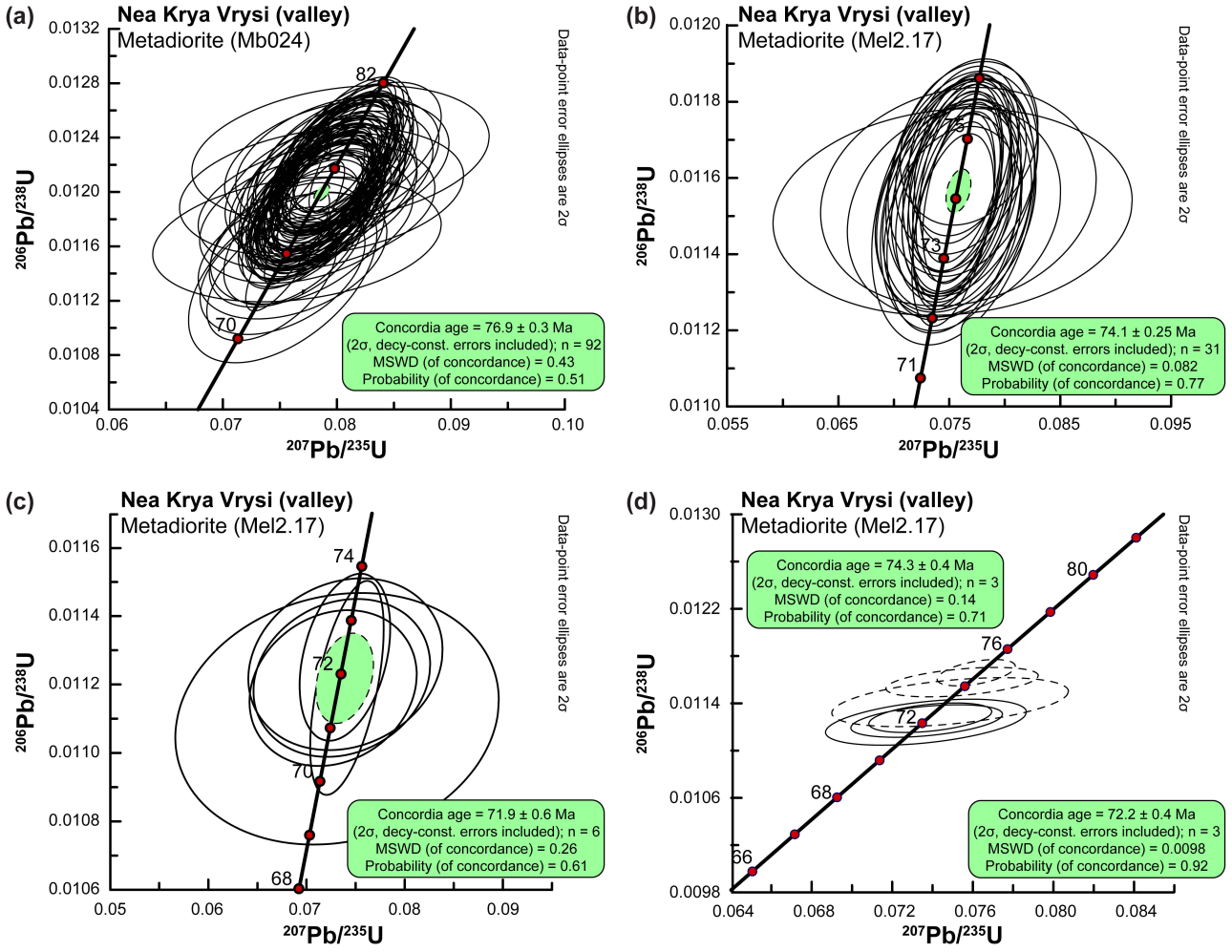

Fig. 3.15 U-Pb concordia diagrams of LA-ICP-MS (a, b, d) and ID-TIMS (c) analyses on zircon from metadiorite samples Mel2.17 (a–c) and Mb024 (d) from the ACC SW of Nea Krya Vrysi. Numbering and error of the ellipses are given in Table 3.8 for ID-TIMS analyses and in Table 3.7 for LA-ICP-MS analyses.

3.5.5.2 Orthogneiss (samples Do513, Mb022 and Mb057)

Zircons from orthogneiss are small, euhedral and show pronounced fine oscillatory zoning but lack structural discontinuities and microfractures (Fig. 3.13b). Small inclusions (presumably of apatite) are frequent. The most concordant analyses (97–103 % concordance) with Late Cretaceous ages yielded $^{206}Pb/^{238}U$ ages of 77.8 ± 1.9 to 67.4 ± 1.7 Ma. The uranium content for these analyses ranges from 122 to 1480 ppm, while the Th/U ratio ranges between 0.16 and 1.65 (Table 3.7). Analyses revealing ages > 78 Ma have high amounts of Pbc and a very low concordance. Fourteen analyses of zircons from orthogneiss Do513 resulted in a $^{206}Pb/^{238}U$ median age at 76.0 +2.3/–0.4 Ma (Fig. 3.16a), while ten analyses on zircons from sample Mb022 yielded a $^{206}Pb/^{238}U$ median age at 74.2 +2.0/–1.5 Ma (Fig. 3.16b) and twenty-eight analyses on zircons from orthogneiss Mb057 yielded a $^{206}Pb/^{238}U$ median

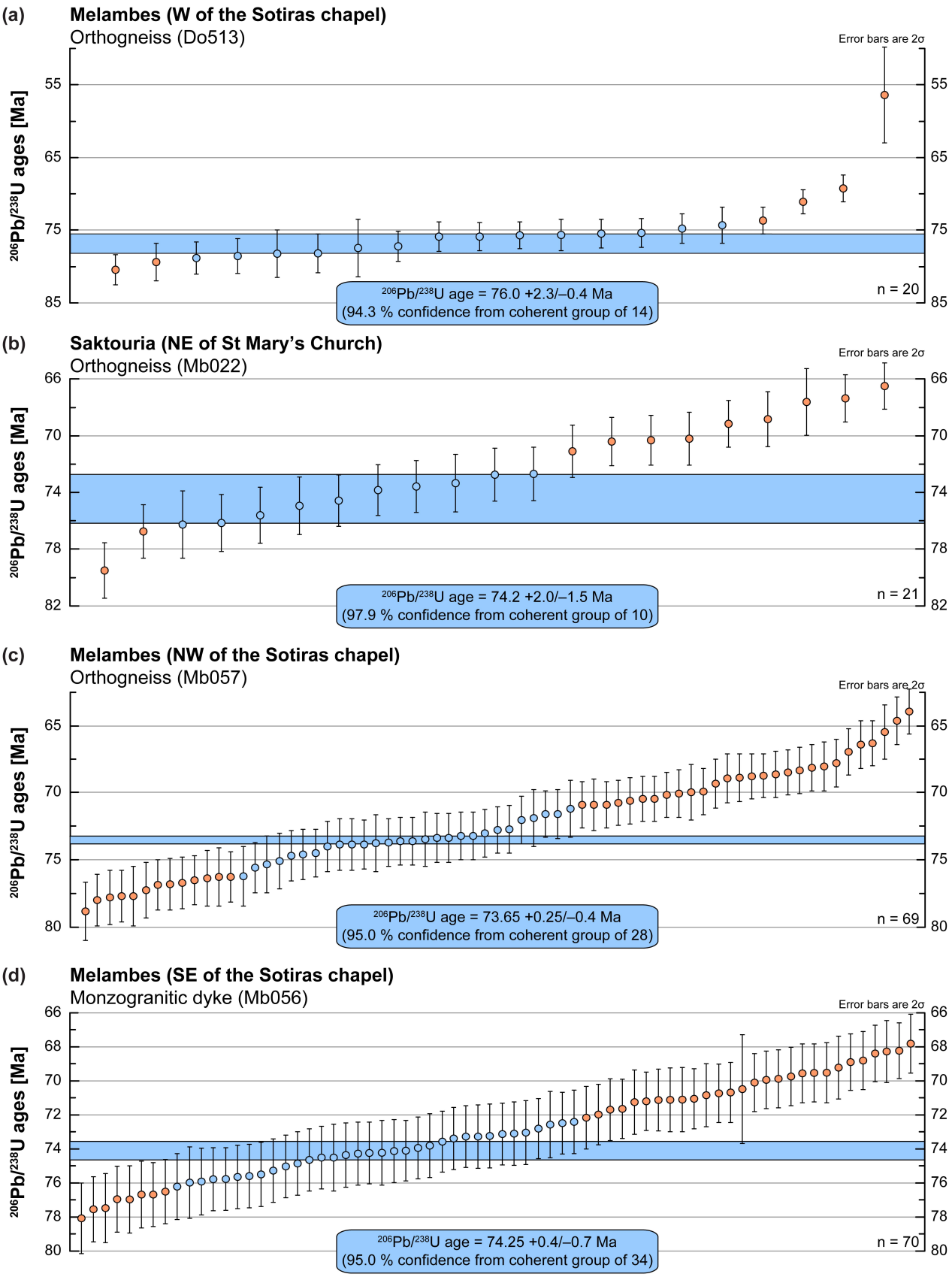

Fig. 3.16 Scatter plots summarizing $^{238}U/^{206}Pb$ zircon ages obtained from LA-ICP-MS analyses on orthogneiss samples (a) Do513, (b) Mb022 and (c) Mb057 and (d) on monzogranite sample Mb056. Error bars represent the 95 % confidence interval of the median age.

Table 3.7 Pb, U and Th LA-ICP-MS results for zircons of orthogneiss Do513, Mb022, Mb056 and Mb057 and metadiorite Mb024 and Mel2.17 from the Asterousia Crystalline Complex west of Melambes. Spot size = 30 µm, depth of crater ca. 15 µm. $^{206}Pb/^{238}U$ error is the quadratic additions of the within run precision (2 standard errors) and the external reproducibility (2 standard deviations) of the reference zircon. $^{207}Pb/^{206}Pb$ error propagation (^{207}Pb signal dependent) following Gerdes and Zeh (2009). $^{207}Pb/^{235}U$ error is the quadratic addition of the $^{207}Pb/^{206}Pb$ and $^{206}Pb/^{238}U$ uncertainty. Errors of the mean values are given at 2σ level.

	^{207}Pb[a] [cps]	U[b] [ppm]	Pb[b] [ppm]	Th/U[b]	^{206}Pbc[c] [%]	$^{206}Pb/^{238}U$[d]	±2σ [%]	$^{207}Pb/^{235}U$[d]	±2σ [%]	$^{207}Pb/^{206}Pb$[d]	±2σ [%]	ρ[e]	$^{206}Pb/^{238}U$	±2σ [Ma]	$^{207}Pb/^{235}U$	±2σ [Ma]	$^{207}Pb/^{206}Pb$	±2σ [Ma]	Conc.[f] [%]
Sample Do513 (orthogneiss 450 m W of the Sotiras chapel)																			
A1427	2802	101	2	0.76	22.6	0.00878	11.8	0.06392	25.0	0.05279	22.1	0.47	56.4	6.6	62.9	15.4	320	501	18
A1434	1990	375	5	1.21	2.8	0.01080	2.7	0.06999	9.1	0.04699	8.7	0.30	69.3	1.9	68.7	6.0	49	207	143
A1451	5475	1098	16	1.38	2.0	0.01109	2.4	0.07207	8.1	0.04712	7.8	0.29	71.1	1.7	70.7	5.6	55	185	129
A1428	1013	218	3	1.12	1.6	0.01150	2.5	0.07480	8.7	0.04715	8.4	0.29	73.7	1.8	73.2	6.2	57	200	130
A1448	1917	135	2	0.66	0.5	0.01160	3.4	0.07496	11.1	0.04685	10.5	0.31	74.4	2.5	73.4	7.9	42	251	179
A1436	5966	613	10	1.06	4.5	0.01168	2.7	0.07585	9.1	0.04710	8.7	0.29	74.9	2.0	74.2	6.6	54	209	138
A1449	1215	243	3	1.04	2.0	0.01177	2.6	0.07605	8.8	0.04685	8.4	0.30	75.5	2.0	74.4	6.3	41	201	182
A1453	1790	285	4	0.30	2.5	0.01179	2.6	0.07761	9.2	0.04774	8.8	0.29	75.6	2.0	75.9	6.7	86	208	88
A1435	2076	244	4	1.09	4.1	0.01182	2.8	0.07743	13.4	0.04751	13.1	0.21	75.7	2.1	75.7	9.9	75	312	101
A1425	2863	388	7	1.40	2.8	0.01183	2.4	0.07883	4.1	0.04834	3.3	0.60	75.8	1.8	77.0	3.1	116	78	65
A1444	4918	437	7	1.17	8.1	0.01185	2.6	0.07688	10.9	0.04704	10.6	0.24	76.0	1.9	75.2	7.9	51	253	148
A1452	942	168	2	0.71	2.2	0.01186	2.7	0.07709	9.4	0.04716	9.0	0.28	76.0	2.0	75.4	6.8	57	214	132
A1426	2621	659	11	1.65	0.2	0.01206	2.7	0.07917	4.8	0.04761	4.0	0.57	77.3	2.1	77.4	3.6	80	94	97
A1455	24241	352	13	0.79	34.1	0.01211	5.2	0.08050	24.7	0.04821	24.1	0.21	77.6	4.0	78.6	18.8	110	570	71
A1445	11583	442	10	1.22	13.4	0.01221	3.5	0.07963	16.6	0.04728	16.3	0.21	78.3	2.7	77.8	12.5	64	387	123
A1429	353	64	1	0.58	2.2	0.01223	4.3	0.07924	13.4	0.04700	12.7	0.32	78.3	3.3	77.4	10.0	49	303	160
A1456	4487	347	6	0.87	12.1	0.01228	3.0	0.07986	13.1	0.04719	12.7	0.23	78.6	2.4	78.0	9.9	59	304	134
A1443	892	176	3	1.03	1.6	0.01232	2.8	0.07969	9.7	0.04691	9.3	0.29	78.9	2.2	77.8	7.3	45	222	176
A1454	6928	453	8	0.54	13.9	0.01240	3.3	0.08010	18.5	0.04684	18.2	0.18	79.5	2.6	78.2	14.1	41	436	194
A1446	3781	446	7	0.99	4.4	0.01257	2.6	0.08117	8.4	0.04683	8.0	0.31	80.5	2.1	79.2	6.4	41	191	198
A1447	3579	42	8	0.83	0.2	0.15880	2.5	1.60400	4.6	0.07325	3.9	0.55	950	22	972	29	1021	79	93
A1430	9327	27	12	0.74	0.4	0.36380	2.6	6.32700	3.4	0.12610	2.2	0.77	2000	45	2022	30	2045	38	98
A1431	7412	21	9	0.61	0.3	0.37140	2.5	6.55100	3.7	0.12790	2.8	0.66	2036	43	2053	33	2070	49	98
A1432	11877	34	15	0.91	0.4	0.37040	3.0	6.50600	3.7	0.12740	2.2	0.80	2031	52	2047	33	2062	39	98
A1433	14938	43	20	1.05	0.2	0.37860	2.5	6.77100	3.4	0.12970	2.3	0.74	2070	45	2082	31	2094	41	99
Sample Mb022 (orthogneiss 900 m NE of St Mary's Church)																			
A371	4015	418	5	0.36	1.4	0.01037	2.5	0.06949	3.4	0.04861	2.4	0.72	66.5	1.6	68.2	2.3	129	56	52
A374	2016	266	3	0.16	0.9	0.01051	2.5	0.06858	4.1	0.04734	3.2	0.62	67.4	1.7	67.4	2.6	67	76	101
A361	1115	85	1	0.53	3.8	0.01055	3.5	0.06909	9.8	0.04751	9.1	0.36	67.6	2.4	67.8	6.4	75	216	90
A367	14945	654	9	0.48	11.8	0.01073	2.8	0.07009	9.0	0.04736	8.5	0.32	68.8	1.9	68.8	6.0	67	202	102
A380	16406	1731	27	0.00	1.7	0.01079	2.4	0.07214	4.0	0.04850	3.2	0.60	69.2	1.7	70.7	2.7	124	76	56
A372	6652	289	4	0.51	9.1	0.01095	2.7	0.07170	9.1	0.04748	8.7	0.29	70.2	1.9	70.3	6.2	73	207	96
A381	17060	1480	22	0.00	3.9	0.01097	2.5	0.07169	11.3	0.04739	11.1	0.22	70.3	1.8	70.3	7.7	69	263	102
A366	3932	515	7	0.08	0.4	0.01098	2.4	0.07260	3.3	0.04794	2.3	0.73	70.4	1.7	71.2	2.3	96	53	73
A379	9162	897	13	0.00	2.4	0.01109	2.6	0.07285	7.8	0.04762	7.4	0.34	71.1	1.9	71.4	5.4	80	175	88

A368	5688	285	4	0.93	7.5	0.01134	2.6	0.07423	7.5	0.04747	7.1	0.34	72.7	1.9	72.7	5.3	73	168	100
A364	5640	499	7	0.01	2.3	0.01135	2.6	0.07652	4.0	0.04889	3.1	0.65	72.8	1.9	74.9	2.9	143	72	51
A363	3071	139	2	0.33	10.4	0.01144	2.8	0.07494	12.9	0.04749	12.6	0.22	73.4	2.0	73.4	9.2	74	299	99
A376	1686	217	3	1.35	0.3	0.01148	2.5	0.07496	4.5	0.04735	3.7	0.56	73.6	1.8	73.4	3.2	67	88	110
A375	1323	171	2	0.98	0.2	0.01152	2.5	0.07543	5.4	0.04748	4.9	0.45	73.9	1.8	73.8	3.9	73	116	101
A377	1426	191	3	1.07	0.6	0.01164	2.4	0.07620	3.7	0.04748	2.8	0.66	74.6	1.8	74.6	2.7	74	66	101
A378	2357	158	2	0.91	7.3	0.01180	2.6	0.07745	11.8	0.04760	11.5	0.22	75.6	2.0	75.7	8.6	79	273	95
A362	989	79	1	0.56	3.7	0.01189	2.7	0.07767	9.1	0.04739	8.7	0.29	76.2	2.0	75.9	6.7	69	207	111
A369	3001	330	5	1.10	1.2	0.01198	2.5	0.07851	5.7	0.04752	5.2	0.43	76.8	1.9	76.7	4.2	76	123	101
A365	3785	439	7	0.03	0.9	0.01241	2.5	0.08273	3.2	0.04833	2.0	0.78	79.5	2.0	80.7	2.4	116	46	69
A373	4327	240	3	0.23	6.1	0.01190	3.1	0.08444	6.1	0.05145	5.3	0.51	76.3	2.4	82.3	4.9	261	121	29
A390	24719	792	15	0.00	11.6	0.01170	2.7	0.08839	6.4	0.05481	5.8	0.43	75.0	2.0	86.0	5.3	405	129	19
Sample Mb024 (metadiorite 750 m SW of Nea Krya Vrysi)																			
A343	1272	107	1	1.01	1.4	0.01136	3.3	0.07434	6.3	0.04744	5.4	0.52	72.8	2.4	72.8	4.4	71	127	102
A426	736	83	1	0.81	0.8	0.01137	4.5	0.07531	9.0	0.04802	7.7	0.50	72.9	3.3	73.7	6.4	100	183	73
A438	1049	99	1	0.68	1.1	0.01142	3.4	0.07530	7.9	0.04781	7.1	0.43	73.2	2.5	73.7	5.6	90	168	82
A344	493	44	1	0.64	0.7	0.01153	3.3	0.07618	8.9	0.04790	8.2	0.37	73.9	2.4	74.6	6.4	94	195	78
A350	5090	361	5	0.00	b.d.	0.01157	3.1	0.07573	4.0	0.04747	2.4	0.79	74.2	2.3	74.1	2.8	73	57	102
A408	532	72	1	0.81	0.6	0.01161	3.2	0.07565	7.4	0.04727	6.6	0.44	74.4	2.4	74.0	5.3	63	158	118
A407	1674	122	2	0.54	4.8	0.01164	3.3	0.07661	8.1	0.04772	7.5	0.40	74.6	2.4	75.0	5.9	85	177	87
A364	2509	340	5	0.70	6.6	0.01165	3.2	0.07655	13.5	0.04766	13.1	0.24	74.7	2.4	74.9	9.8	83	311	90
A466	639	81	1	0.81	0.6	0.01166	3.5	0.07639	6.7	0.04751	5.7	0.52	74.7	2.6	74.7	4.8	75	136	100
A419	970	123	2	0.95	0.2	0.01174	3.2	0.07689	5.5	0.04750	4.5	0.58	75.2	2.4	75.2	4.0	74	107	101
A366	4059	520	8	0.24	b.d.	0.01177	3.1	0.07722	3.7	0.04758	2.0	0.84	75.4	2.4	75.5	2.7	78	47	96
A356	704	34	0	0.86	0.3	0.01177	3.2	0.07723	6.2	0.04757	5.2	0.53	75.5	2.4	75.5	4.5	78	124	97
A352	3878	136	2	1.14	6.4	0.01180	3.3	0.07736	9.9	0.04755	9.3	0.33	75.6	2.5	75.7	7.2	77	222	98
A435	759	94	1	0.87	0.4	0.01181	3.2	0.07782	5.9	0.04779	5.0	0.55	75.7	2.4	76.1	4.3	89	117	85
A418	868	115	2	0.94	0.1	0.01181	3.2	0.07757	5.4	0.04762	4.4	0.58	75.7	2.4	75.9	4.0	80	105	94
A355	541	29	0	0.82	0.0	0.01182	3.3	0.07745	5.2	0.04752	3.9	0.64	75.8	2.5	75.7	3.8	75	94	100
A427	1383	176	2	1.02	0.3	0.01182	3.2	0.07751	5.8	0.04755	4.8	0.56	75.8	2.4	75.8	4.2	77	114	98
A429	839	91	1	0.72	1.0	0.01183	3.2	0.07771	6.6	0.04763	5.8	0.49	75.8	2.4	76.0	4.9	81	138	94
A388	1124	140	2	0.90	0.3	0.01184	3.2	0.07816	5.7	0.04786	4.7	0.56	75.9	2.4	76.4	4.2	92	112	82
A382	2976	281	4	1.09	2.2	0.01186	3.1	0.07861	5.9	0.04808	5.0	0.54	76.0	2.4	76.8	4.4	103	117	74
A391	812	107	1	0.89	0.2	0.01188	3.3	0.07855	5.1	0.04796	3.9	0.65	76.1	2.5	76.8	3.8	97	93	78
A462	1671	213	3	1.09	1.2	0.01189	3.2	0.07827	10.8	0.04775	10.3	0.30	76.2	2.4	76.5	8.0	87	245	88
A428	1210	127	2	0.78	1.4	0.01189	3.2	0.07822	6.9	0.04771	6.1	0.47	76.2	2.5	76.5	5.1	85	144	90
A457	1134	153	2	0.27	0.0	0.01189	3.2	0.07810	5.9	0.04763	4.9	0.54	76.2	2.4	76.4	4.3	81	117	94
A354	1621	71	1	1.05	1.6	0.01190	3.2	0.07773	6.3	0.04739	5.4	0.50	76.2	2.4	76.0	4.6	69	130	111
A455	899	113	2	0.89	0.3	0.01190	3.2	0.07860	5.9	0.04791	4.9	0.54	76.2	2.4	76.8	4.4	95	117	80
A423	654	71	1	0.72	0.8	0.01190	3.2	0.07800	5.7	0.04754	4.7	0.57	76.3	2.5	76.3	4.2	77	112	100
A453	707	87	1	0.85	0.4	0.01190	3.2	0.07790	5.8	0.04748	4.8	0.56	76.3	2.5	76.2	4.3	73	114	104
A470	754	94	1	0.83	0.4	0.01191	3.3	0.07823	6.4	0.04765	5.5	0.51	76.3	2.5	76.5	4.7	82	131	93
A465	1335	165	2	0.97	0.5	0.01192	3.2	0.07844	5.7	0.04774	4.7	0.57	76.4	2.4	76.7	4.2	87	111	88

A346	1778	154	2	1.06	0.2	0.01192	3.2	0.07826	4.8	0.04762	3.5	0.67	76.4	2.4	76.5	3.5	80	84	95
A471	502	68	1	0.83	0.6	0.01192	3.4	0.07823	5.9	0.04758	4.9	0.57	76.4	2.6	76.5	4.4	79	116	97
A394	820	104	1	0.90	0.3	0.01193	3.1	0.07812	5.3	0.04749	4.2	0.60	76.5	2.4	76.4	3.9	74	100	103
A369	566	62	1	0.83	0.9	0.01193	3.4	0.07850	7.3	0.04772	6.5	0.46	76.5	2.5	76.7	5.4	85	155	90
A454	797	101	1	0.86	0.3	0.01194	3.2	0.07824	4.4	0.04754	3.1	0.72	76.5	2.4	76.5	3.3	76	73	100
A345	1074	85	1	0.86	1.1	0.01195	3.2	0.07821	6.2	0.04746	5.3	0.52	76.6	2.4	76.5	4.6	73	125	106
A416	1208	163	2	0.93	0.2	0.01195	3.2	0.07837	5.8	0.04756	4.8	0.55	76.6	2.4	76.6	4.3	77	115	99
A420	1174	150	2	0.99	0.2	0.01196	3.2	0.07818	5.2	0.04743	4.2	0.61	76.6	2.4	76.4	3.9	71	99	108
A404	949	119	2	0.80	0.3	0.01196	3.2	0.07821	5.2	0.04744	4.1	0.62	76.6	2.4	76.5	3.8	71	97	107
A377	818	109	1	0.89	3.6	0.01196	3.2	0.07885	8.5	0.04780	7.9	0.38	76.7	2.5	77.1	6.3	89	187	86
A446	683	91	1	0.87	0.4	0.01197	3.3	0.07852	5.4	0.04758	4.4	0.60	76.7	2.5	76.8	4.0	79	103	98
A445	1016	132	2	0.84	0.2	0.01197	3.2	0.07859	5.4	0.04761	4.3	0.60	76.7	2.5	76.8	4.0	80	102	96
A461	1390	184	3	0.98	0.2	0.01198	3.2	0.07875	4.9	0.04767	3.6	0.66	76.8	2.4	77.0	3.6	83	87	92
A409	560	69	1	0.84	0.3	0.01199	3.4	0.07855	7.8	0.04752	7.0	0.44	76.8	2.6	76.8	5.8	76	166	102
A412	1126	149	2	0.98	0.2	0.01199	3.2	0.07844	5.0	0.04743	3.9	0.63	76.9	2.4	76.7	3.7	71	93	108
A358	2764	354	5	0.98	0.1	0.01200	3.2	0.07890	4.5	0.04769	3.2	0.70	76.9	2.4	77.1	3.3	84	76	91
A351	2760	179	3	0.51	6.2	0.01200	3.2	0.07871	12.9	0.04757	12.5	0.25	76.9	2.5	76.9	9.6	78	297	99
A389	988	128	2	0.50	0.1	0.01201	3.2	0.07896	5.5	0.04768	4.5	0.58	77.0	2.4	77.2	4.1	83	107	92
A458	853	82	1	0.52	3.2	0.01202	3.3	0.07868	8.7	0.04747	8.1	0.37	77.0	2.5	76.9	6.5	73	193	106
A398	1613	199	3	0.86	0.4	0.01202	3.2	0.07902	4.3	0.04767	2.9	0.74	77.0	2.4	77.2	3.2	83	69	93
A431	881	111	1	0.85	0.3	0.01203	3.2	0.07908	5.5	0.04768	4.5	0.58	77.1	2.5	77.3	4.1	83	106	93
A447	926	123	2	0.91	0.1	0.01203	3.2	0.07911	5.0	0.04768	3.8	0.64	77.1	2.4	77.3	3.7	83	90	92
A434	1287	162	2	0.89	0.3	0.01204	3.1	0.07873	4.6	0.04743	3.4	0.68	77.1	2.4	76.9	3.4	71	81	109
A400	1380	159	2	0.87	1.1	0.01204	3.2	0.07895	6.0	0.04756	5.1	0.53	77.1	2.4	77.2	4.5	78	121	99
A361	940	102	1	0.97	0.7	0.01205	3.3	0.07945	6.4	0.04781	5.5	0.51	77.2	2.5	77.6	4.8	90	130	86
A392	746	95	1	0.86	0.3	0.01206	3.3	0.07884	7.5	0.04742	6.8	0.44	77.3	2.5	77.1	5.6	70	161	110
A357	793	98	1	0.60	0.2	0.01206	3.3	0.07903	5.8	0.04753	4.8	0.57	77.3	2.5	77.2	4.3	76	113	102
A371	1189	158	2	0.96	0.1	0.01207	3.2	0.07902	4.8	0.04750	3.5	0.67	77.3	2.5	77.2	3.6	75	84	104
A436	841	110	1	0.56	0.2	0.01207	3.3	0.07943	5.4	0.04771	4.2	0.61	77.4	2.5	77.6	4.0	85	101	91
A437	870	110	2	1.03	0.4	0.01208	3.3	0.07931	7.1	0.04763	6.3	0.46	77.4	2.5	77.5	5.3	81	148	95
A469	716	95	1	0.75	0.8	0.01211	3.3	0.07955	5.8	0.04765	4.8	0.57	77.6	2.5	77.7	4.3	82	113	95
A397	1568	201	3	0.68	0.2	0.01211	3.2	0.07944	4.7	0.04756	3.4	0.68	77.6	2.5	77.6	3.5	77	81	100
A381	2304	187	3	1.19	3.2	0.01211	3.3	0.08034	8.3	0.04810	7.6	0.40	77.6	2.5	78.5	6.3	104	180	75
A432	857	114	2	0.84	0.5	0.01216	3.2	0.07991	5.4	0.04765	4.3	0.59	77.9	2.5	78.1	4.0	82	102	95
A449	560	74	1	0.57	0.3	0.01216	3.4	0.07989	5.7	0.04763	4.6	0.59	77.9	2.6	78.0	4.3	81	110	96
A417	875	117	2	0.91	0.1	0.01217	3.2	0.07973	5.2	0.04752	4.1	0.61	78.0	2.5	77.9	3.9	75	98	104
A421	688	84	1	0.83	0.5	0.01217	3.3	0.07997	5.9	0.04765	4.9	0.56	78.0	2.6	78.1	4.5	82	117	95
A467	1526	186	3	0.97	0.5	0.01218	3.2	0.07971	7.2	0.04748	6.4	0.45	78.0	2.5	77.9	5.4	73	152	107
A402	1210	153	2	0.99	0.2	0.01218	3.2	0.08022	4.4	0.04778	3.0	0.73	78.0	2.5	78.4	3.3	88	70	88
A362	832	102	1	0.87	0.3	0.01218	3.2	0.07992	5.3	0.04757	4.1	0.62	78.1	2.5	78.1	4.0	78	98	100
A363	992	121	2	0.45	0.3	0.01219	3.2	0.07977	4.9	0.04747	3.7	0.66	78.1	2.5	77.9	3.7	73	88	107
A393	1159	152	2	0.98	0.9	0.01219	3.2	0.07998	5.5	0.04760	4.5	0.59	78.1	2.5	78.1	4.1	79	106	98
A401	797	104	1	0.87	4.5	0.01219	3.3	0.08007	10.0	0.04763	9.5	0.33	78.1	2.6	78.2	7.6	81	225	97

A399	1428	184	3	0.87	0.2	0.01220	3.2	0.08022	4.8	0.04768	3.5	0.67	78.2	2.5	78.4	3.6	83	84	94
A406	521	63	1	0.54	0.5	0.01220	3.4	0.08036	5.6	0.04776	4.4	0.61	78.2	2.7	78.5	4.2	87	105	89
A360	723	94	1	0.85	0.0	0.01221	3.4	0.08030	6.3	0.04769	5.3	0.54	78.2	2.6	78.4	4.7	84	125	93
A411	933	101	1	0.66	1.5	0.01221	3.3	0.08004	7.3	0.04754	6.5	0.46	78.2	2.6	78.2	5.5	76	154	102
A390	1309	172	2	0.94	3.7	0.01222	3.2	0.08009	9.1	0.04755	8.5	0.35	78.3	2.5	78.2	6.9	77	202	102
A448	695	85	1	0.80	0.4	0.01222	3.3	0.08056	6.3	0.04783	5.3	0.53	78.3	2.6	78.7	4.8	91	127	86
A372	1285	164	2	0.97	0.1	0.01222	3.2	0.08015	4.9	0.04757	3.8	0.65	78.3	2.5	78.3	3.7	78	90	101
A415	895	109	2	1.03	0.3	0.01223	3.3	0.08026	5.1	0.04761	3.9	0.65	78.3	2.6	78.4	3.9	80	93	98
A460	712	94	1	0.90	0.7	0.01224	3.3	0.08060	6.3	0.04778	5.3	0.52	78.4	2.5	78.7	4.7	88	127	89
A395	893	120	2	0.93	b.d.	0.01224	3.2	0.08037	5.3	0.04762	4.3	0.60	78.4	2.5	78.5	4.0	80	101	97
A413	1610	215	3	1.12	0.1	0.01226	3.2	0.08018	5.0	0.04742	3.9	0.63	78.6	2.5	78.3	3.8	70	93	112
A367	1450	177	2	0.90	0.4	0.01227	3.2	0.08058	5.1	0.04765	4.0	0.62	78.6	2.5	78.7	3.9	82	96	96
A452	611	81	1	0.85	5.9	0.01228	3.3	0.08037	13.2	0.04749	12.8	0.25	78.6	2.6	78.5	10.1	74	305	107
A422	956	127	2	0.93	0.3	0.01231	3.2	0.08084	6.0	0.04762	5.0	0.54	78.9	2.5	78.9	4.6	80	120	98
A433	949	124	2	0.86	0.3	0.01232	3.1	0.08061	4.5	0.04746	3.2	0.70	78.9	2.5	78.7	3.4	73	76	109
A349	3086	217	3	0.72	0.1	0.01232	3.2	0.08140	3.8	0.04790	2.1	0.83	79.0	2.5	79.5	2.9	94	51	84
A444	763	124	2	0.91	b.d.	0.01233	3.2	0.08233	6.8	0.04842	6.1	0.46	79.0	2.5	80.3	5.3	120	143	66
A375	1292	170	2	1.06	0.2	0.01234	3.2	0.08111	4.9	0.04768	3.6	0.66	79.1	2.5	79.2	3.7	83	86	95
A424	793	104	1	0.88	0.0	0.01235	3.3	0.08101	5.4	0.04759	4.3	0.61	79.1	2.6	79.1	4.1	79	102	101
A370	1085	143	2	0.93	0.3	0.01244	3.2	0.08150	5.6	0.04752	4.7	0.56	79.7	2.5	79.6	4.3	76	111	105
A468	951	118	2	0.94	0.3	0.01246	3.2	0.08179	4.7	0.04761	3.4	0.69	79.8	2.6	79.8	3.6	80	82	100
A430	447	58	1	0.83	1.2	0.01247	3.3	0.08205	6.5	0.04770	5.5	0.51	79.9	2.6	80.1	5.0	85	132	94
A368	724	96	1	0.79	0.0	0.01248	3.3	0.08205	6.3	0.04769	5.3	0.52	79.9	2.6	80.1	4.8	84	127	95
A459	624	75	1	0.54	0.3	0.01249	3.3	0.08222	6.2	0.04776	5.2	0.53	80.0	2.6	80.2	4.8	87	123	92
A376	1065	132	2	0.96	0.2	0.01260	3.2	0.08291	5.4	0.04773	4.4	0.59	80.7	2.6	80.9	4.2	86	105	94
A425	789	93	1	0.89	0.2	0.01263	3.2	0.08285	7.0	0.04757	6.2	0.46	80.9	2.6	80.8	5.5	78	148	104
A347	1780	134	2	1.10	0.3	0.01291	3.2	0.08493	5.0	0.04771	3.8	0.64	82.7	2.6	82.8	4.0	85	91	98
Sample Mb056 (monzogranitic dyke 225 SE oft he Sotiras chapel)																			
A126	3090	372	5	0.31	0.5	0.00986	3.6	0.06507	4.3	0.04786	2.3	0.85	63.3	2.3	64.0	2.7	92	54	69
A135	1282	171	2	0.85	0.0	0.01038	5.3	0.06863	6.2	0.04798	3.4	0.84	66.5	3.5	67.4	4.1	98	80	68
A117	7083	866	11	0.00	0.4	0.01044	3.9	0.06946	11.8	0.04824	11.1	0.33	67.0	2.6	68.2	7.8	111	263	60
A162	3751	491	6	0.34	0.2	0.01058	2.6	0.06992	3.4	0.04794	2.3	0.75	67.8	1.7	68.6	2.3	96	53	71
A151	3640	504	7	0.19	0.1	0.01064	2.4	0.07002	3.4	0.04773	2.5	0.70	68.2	1.6	68.7	2.3	86	58	79
A127	3361	382	5	0.23	0.4	0.01065	2.7	0.07039	4.4	0.04795	3.4	0.61	68.3	1.8	69.1	2.9	97	82	70
A93	3011	434	5	0.40	b.d.	0.01067	2.4	0.06996	3.8	0.04756	3.0	0.63	68.4	1.6	68.7	2.6	78	71	88
A143	10209	1308	21	0.00	0.3	0.01073	2.5	0.07062	3.5	0.04772	2.4	0.72	68.8	1.7	69.3	2.3	86	58	80
A63	8298	975	13	0.00	0.7	0.01075	2.4	0.07141	3.9	0.04818	3.1	0.62	68.9	1.7	70.0	2.7	108	73	64
A169	4643	265	4	0.88	6.3	0.01080	2.7	0.07059	10.8	0.04740	10.5	0.25	69.3	1.8	69.3	7.3	70	250	100
A144	8007	988	14	0.00	0.7	0.01085	2.6	0.07075	13.8	0.04731	13.6	0.18	69.5	1.8	69.4	9.3	65	324	107
A98	7375	858	11	0.06	0.6	0.01085	2.5	0.07189	3.0	0.04806	1.7	0.82	69.6	1.7	70.5	2.1	102	41	68
A193	3521	449	5	0.40	0.3	0.01085	2.5	0.07191	3.9	0.04806	3.0	0.64	69.6	1.7	70.5	2.7	102	72	68
A156	2805	398	5	0.50	0.3	0.01088	2.5	0.07114	3.7	0.04742	2.8	0.66	69.8	1.7	69.8	2.5	71	67	99
A94	3656	514	6	0.46	0.0	0.01090	2.5	0.07127	3.7	0.04742	2.8	0.66	69.9	1.7	69.9	2.5	70	67	99

A145	4606	629	9	0.00	b.d.	0.01091	2.4	0.07145	3.3	0.04750	2.3	0.73	70.0	1.7	70.1	2.3	74	54	94
A154	5366	760	11	0.00	0.0	0.01094	2.4	0.07204	2.9	0.04777	1.6	0.84	70.1	1.7	70.6	2.0	88	38	80
A190	1635	152	2	0.81	2.8	0.01100	4.6	0.07198	9.1	0.04747	7.9	0.50	70.5	3.2	70.6	6.2	73	187	96
A101	4066	545	6	0.45	0.1	0.01103	2.5	0.07301	3.1	0.04802	1.9	0.80	70.7	1.8	71.6	2.2	100	44	70
A95	6126	708	10	0.00	0.7	0.01103	2.4	0.07328	3.3	0.04816	2.2	0.75	70.7	1.7	71.8	2.3	107	51	66
A179	9600	1038	14	0.00	1.6	0.01105	2.6	0.07244	8.9	0.04754	8.5	0.30	70.9	1.8	71.0	6.1	76	201	93
A155	4493	610	9	0.04	0.1	0.01108	2.5	0.07302	3.0	0.04778	1.6	0.84	71.1	1.8	71.6	2.1	88	38	81
A178	7924	879	11	0.00	1.8	0.01109	2.7	0.07247	15.3	0.04738	15.0	0.17	71.1	1.9	71.0	10.5	68	357	104
A188	4927	604	8	0.00	0.8	0.01110	2.7	0.07403	3.2	0.04839	1.8	0.83	71.1	1.9	72.5	2.2	118	42	60
A125	7377	391	6	0.73	7.0	0.01110	2.6	0.07266	8.0	0.04749	7.5	0.32	71.1	1.8	71.2	5.5	74	179	96
A163	6989	916	12	0.00	0.3	0.01111	2.4	0.07358	2.9	0.04804	1.6	0.83	71.2	1.7	72.1	2.0	101	38	70
A184	5087	657	9	0.00	0.7	0.01112	2.7	0.07300	9.2	0.04763	8.8	0.29	71.3	1.9	71.5	6.4	81	209	88
A121	4521	581	8	0.02	0.2	0.01118	2.4	0.07379	3.3	0.04788	2.3	0.73	71.7	1.7	72.3	2.3	94	53	77
A191	4673	496	8	0.11	1.0	0.01119	2.5	0.07451	4.3	0.04831	3.4	0.60	71.7	1.8	73.0	3.0	114	81	63
A83	2969	390	5	0.32	b.d.	0.01123	2.5	0.07424	4.2	0.04795	3.4	0.59	72.0	1.8	72.7	2.9	97	80	74
A100	2851	366	4	0.29	0.5	0.01126	2.6	0.07367	4.7	0.04746	4.0	0.54	72.2	1.8	72.2	3.3	72	94	100
A183	7129	859	11	0.00	0.4	0.01130	2.6	0.07502	3.7	0.04815	2.6	0.70	72.4	1.9	73.4	2.6	107	62	68
A176	1463	159	2	0.29	1.7	0.01131	2.5	0.07394	6.2	0.04741	5.7	0.41	72.5	1.8	72.4	4.4	70	135	103
A140	1109	139	2	0.79	0.7	0.01132	2.7	0.07399	4.9	0.04739	4.1	0.55	72.6	1.9	72.5	3.4	69	97	105
A76	7270	1004	14	0.00	b.d.	0.01136	2.4	0.07455	2.7	0.04759	1.2	0.90	72.8	1.8	73.0	1.9	79	28	92
A137	814	109	1	0.73	0.2	0.01140	2.6	0.07437	5.5	0.04733	4.8	0.47	73.0	1.9	72.8	3.8	66	114	111
A141	1536	169	2	0.76	1.2	0.01141	2.6	0.07465	5.6	0.04746	4.9	0.46	73.1	1.9	73.1	3.9	73	118	101
A65	2612	330	4	0.89	0.5	0.01141	2.5	0.07469	5.5	0.04747	4.9	0.45	73.1	1.8	73.1	3.9	73	117	100
A92	976	122	2	0.68	2.0	0.01143	2.6	0.07478	6.9	0.04745	6.4	0.37	73.3	1.9	73.2	4.9	72	152	102
A73	1610	178	2	0.80	1.8	0.01143	2.6	0.07469	8.0	0.04737	7.6	0.32	73.3	1.9	73.1	5.7	68	181	108
A89	6934	480	6	0.23	4.5	0.01144	2.5	0.07480	6.9	0.04744	6.4	0.36	73.3	1.8	73.2	4.9	72	152	102
A118	1844	239	3	1.05	0.3	0.01145	2.5	0.07591	4.3	0.04809	3.5	0.58	73.4	1.8	74.3	3.1	103	83	71
A120	5483	673	8	0.26	1.0	0.01148	2.5	0.07497	4.2	0.04736	3.4	0.58	73.6	1.8	73.4	3.0	67	82	109
A172	1334	182	2	0.92	0.4	0.01152	2.6	0.07542	4.5	0.04749	3.7	0.57	73.8	1.9	73.8	3.2	74	87	100
A160	2792	265	4	0.88	2.0	0.01154	2.5	0.07535	5.1	0.04737	4.5	0.49	73.9	1.8	73.8	3.6	68	106	109
A165	2426	260	4	1.11	1.2	0.01156	2.4	0.07568	5.5	0.04747	4.9	0.44	74.1	1.8	74.1	3.9	73	117	102
A81	1475	184	3	1.08	0.4	0.01157	2.5	0.07573	4.2	0.04748	3.4	0.60	74.1	1.9	74.1	3.0	73	81	101
A142	1423	161	2	0.63	1.0	0.01159	2.6	0.07594	6.3	0.04754	5.8	0.41	74.3	1.9	74.3	4.6	76	137	97
A157	2212	212	3	0.73	2.5	0.01159	2.5	0.07566	7.4	0.04737	7.0	0.33	74.3	1.8	74.1	5.3	68	167	110
A173	2238	302	4	1.30	1.3	0.01159	2.5	0.07599	4.6	0.04755	3.8	0.55	74.3	1.8	74.4	3.3	77	91	96
A132	8338	441	6	0.63	5.5	0.01160	2.6	0.07615	6.7	0.04759	6.2	0.38	74.4	1.9	74.5	4.8	79	147	94
A174	3880	194	3	0.92	8.5	0.01163	2.7	0.07616	10.6	0.04750	10.3	0.25	74.5	2.0	74.5	7.7	75	245	100
A166	2721	313	5	0.86	0.9	0.01163	2.5	0.07739	3.2	0.04826	1.9	0.79	74.5	1.8	75.7	2.3	112	46	66
A152	2011	222	3	0.85	1.4	0.01165	2.5	0.07630	4.6	0.04751	3.8	0.54	74.7	1.8	74.7	3.3	75	91	100
A136	1269	147	2	0.89	0.4	0.01168	2.5	0.07690	5.1	0.04774	4.5	0.49	74.9	1.9	75.2	3.7	86	106	87
A128	2326	296	4	0.99	0.1	0.01171	2.5	0.07676	3.5	0.04755	2.6	0.69	75.0	1.8	75.1	2.6	77	61	97
A161	1975	234	3	0.82	0.8	0.01175	2.5	0.07681	4.6	0.04742	3.8	0.55	75.3	1.9	75.1	3.3	70	91	107
A108	4473	336	4	0.51	4.1	0.01178	2.5	0.07704	6.0	0.04742	5.5	0.42	75.5	1.9	75.4	4.4	70	130	107

A84	2367	292	4	0.60	1.3	0.01180	2.5	0.07729	5.0	0.04751	4.4	0.49	75.6	1.9	75.6	3.7	75	104	101
A111	3264	449	6	0.24	0.0	0.01181	2.5	0.07736	3.3	0.04752	2.2	0.76	75.7	1.9	75.7	2.4	75	51	100
A74	1247	148	2	0.73	0.6	0.01183	2.4	0.07739	5.6	0.04746	5.0	0.44	75.8	1.8	75.7	4.1	73	120	104
A112	2830	343	4	0.44	0.8	0.01183	2.5	0.07758	3.8	0.04757	2.9	0.64	75.8	1.9	75.9	2.8	78	70	98
A187	3727	225	4	1.30	7.6	0.01185	2.6	0.07765	9.4	0.04752	9.0	0.28	75.9	2.0	75.9	6.9	76	214	100
A85	1525	78	1	0.73	7.6	0.01186	2.8	0.07752	10.1	0.04742	9.7	0.28	76.0	2.1	75.8	7.4	70	230	108
A88	2671	236	4	1.32	4.1	0.01189	2.6	0.07914	6.6	0.04826	6.0	0.39	76.2	1.9	77.3	4.9	112	143	68
A167	1771	161	2	0.81	2.7	0.01194	2.5	0.07788	7.6	0.04729	7.2	0.33	76.5	1.9	76.1	5.6	64	171	119
A129	3595	363	5	0.51	2.0	0.01196	2.5	0.07839	5.3	0.04755	4.7	0.46	76.6	1.9	76.6	3.9	77	112	99
A77	961	125	2	0.72	0.0	0.01197	2.6	0.07840	4.8	0.04750	4.1	0.54	76.7	2.0	76.6	3.6	75	96	103
A66	1715	203	3	0.89	0.3	0.01201	2.6	0.07867	5.1	0.04750	4.4	0.51	77.0	2.0	76.9	3.8	74	104	104
A159	2756	264	4	0.91	3.0	0.01201	2.5	0.07849	5.6	0.04738	5.0	0.45	77.0	1.9	76.7	4.1	69	119	112
A80	1527	157	2	0.52	2.2	0.01210	2.6	0.07907	6.8	0.04741	6.3	0.39	77.5	2.0	77.3	5.1	70	149	111
A091	3259	386	5	0.90	0.9	0.01211	2.5	0.07937	3.7	0.04755	2.7	0.67	77.6	1.9	77.6	2.7	77	65	101
A78	1331	79	1	0.69	7.5	0.01219	2.6	0.08023	9.4	0.04774	9.0	0.28	78.1	2.1	78.4	7.1	86	215	90
A170	2301	218	3	1.06	1.9	0.01236	2.4	0.08112	6.0	0.04759	5.5	0.40	79.2	1.9	79.2	4.6	79	130	100
A107	7877	698	9	0.36	2.1	0.01271	2.5	0.08524	5.2	0.04863	4.5	0.48	81.4	2.0	83.1	4.1	130	107	63
A90	7932	852	16	0.00	0.5	0.01509	2.8	0.10100	4.8	0.04855	3.9	0.58	96.5	2.7	97.7	4.5	126	93	76
A72	2469	129	4	0.60	1.2	0.03273	3.4	0.23310	4.6	0.05165	3.1	0.74	208	7	213	9	270	71	77
Sample Mb057 (orthogneiss 200 m NW of the Sotiras chapel)																			
A262	4079	444	5	0.32	0.9	0.00781	2.7	0.05116	5.3	0.04751	4.6	0.51	50.2	1.4	50.7	2.6	75	108	67
A225	3623	183	3	1.16	11.2	0.00919	3.4	0.06029	14.2	0.04757	13.7	0.24	59.0	2.0	59.4	8.2	78	326	76
A226	2754	158	2	0.42	7.6	0.00987	5.1	0.06446	10.5	0.04738	9.1	0.49	63.3	3.2	63.4	6.4	68	217	93
A276	11250	1072	14	0.00	3.1	0.00997	2.7	0.06518	13.3	0.04740	13.1	0.20	64.0	1.7	64.1	8.3	70	311	92
A327	12656	524	7	0.72	11.8	0.01008	2.8	0.06593	9.4	0.04744	8.9	0.30	64.7	1.8	64.8	5.9	71	212	91
A315	4853	388	5	0.72	6.9	0.01022	3.1	0.06690	11.2	0.04750	10.7	0.28	65.5	2.0	65.8	7.1	74	255	88
A274	10671	1231	16	0.00	1.5	0.01035	2.5	0.06750	12.4	0.04729	12.2	0.21	66.4	1.7	66.3	8.0	64	289	104
A227	19943	1334	16	0.11	5.5	0.01037	2.7	0.06787	10.8	0.04748	10.5	0.25	66.5	1.8	66.7	7.0	74	250	90
A268	4115	480	6	0.17	0.6	0.01045	2.6	0.06917	3.7	0.04800	2.6	0.71	67.0	1.7	67.9	2.4	99	61	67
A248	9892	582	7	0.37	9.0	0.01058	2.6	0.06919	9.3	0.04745	8.9	0.28	67.8	1.7	67.9	6.1	72	212	94
A341	14799	817	13	0.00	8.9	0.01061	2.7	0.06930	11.7	0.04736	11.4	0.23	68.0	1.8	68.0	7.8	68	272	101
A205	3157	419	5	0.52	1.0	0.01063	2.5	0.06943	5.0	0.04737	4.3	0.50	68.2	1.7	68.2	3.3	68	103	100
A342	4578	262	3	0.73	6.0	0.01067	2.5	0.06970	8.7	0.04738	8.3	0.29	68.4	1.7	68.4	5.7	69	197	100
A291	7873	849	13	0.00	1.2	0.01068	2.4	0.07112	4.9	0.04830	4.2	0.50	68.5	1.7	69.8	3.3	114	100	60
A213	3107	352	4	0.72	1.3	0.01071	2.6	0.07002	5.2	0.04740	4.5	0.49	68.7	1.7	68.7	3.5	69	108	99
A293	9921	1421	21	0.00	0.1	0.01072	2.4	0.07050	2.7	0.04769	1.3	0.88	68.8	1.6	69.2	1.8	84	31	82
A294	4157	505	7	0.04	0.6	0.01073	2.4	0.07130	3.5	0.04820	2.6	0.69	68.8	1.7	69.9	2.4	109	60	63
A310	6975	426	6	0.63	6.2	0.01074	2.6	0.07054	8.3	0.04763	7.9	0.31	68.9	1.8	69.2	5.6	81	188	85
A352	5909	122	2	0.85	7.4	0.01076	2.7	0.07043	7.3	0.04749	6.8	0.36	69.0	1.8	69.1	4.9	74	162	93
A290	6515	780	10	0.00	0.7	0.01082	2.7	0.07173	4.0	0.04809	3.0	0.67	69.4	1.8	70.3	2.7	104	71	67
A266	6979	819	10	0.01	0.7	0.01092	2.5	0.07265	3.3	0.04827	2.1	0.76	70.0	1.7	71.2	2.2	112	51	62
A322	23096	1537	25	0.00	6.1	0.01092	3.0	0.07184	9.0	0.04772	8.5	0.33	70.0	2.1	70.4	6.1	86	201	82
A260	4512	274	4	0.85	6.0	0.01093	2.6	0.07146	7.8	0.04742	7.4	0.33	70.1	1.8	70.1	5.3	70	176	100

A289	6054	824	11	0.00	0.4	0.01095	2.5	0.07244	3.6	0.04799	2.7	0.68	70.2	1.7	71.0	2.5	99	63	71
A288	6779	964	13	0.00	b.d.	0.01099	2.4	0.07242	2.7	0.04778	1.3	0.88	70.5	1.7	71.0	1.9	88	31	80
A254	8003	646	8	0.28	4.1	0.01100	2.5	0.07201	6.2	0.04750	5.7	0.40	70.5	1.7	70.6	4.2	74	135	95
A333	9292	1139	14	0.02	0.6	0.01102	2.4	0.07329	3.4	0.04825	2.4	0.70	70.6	1.7	71.8	2.4	112	58	63
A218	9198	1007	15	0.00	0.7	0.01104	2.4	0.07326	4.4	0.04812	3.6	0.55	70.8	1.7	71.8	3.0	105	86	67
A219	6279	753	10	0.00	0.8	0.01106	2.4	0.07355	3.4	0.04823	2.4	0.71	70.9	1.7	72.1	2.4	111	57	64
A295	7727	446	6	0.58	6.8	0.01106	2.7	0.07227	8.9	0.04737	8.5	0.31	70.9	1.9	70.8	6.1	68	203	104
A292	6270	781	12	0.00	0.5	0.01107	2.4	0.07330	3.1	0.04804	1.9	0.79	70.9	1.7	71.8	2.2	101	46	70
A324	4552	185	3	0.95	11.0	0.01111	3.1	0.07273	9.3	0.04746	8.8	0.33	71.3	2.2	71.3	6.4	72	209	98
A234	3146	236	3	0.83	4.8	0.01118	2.6	0.07298	8.9	0.04736	8.5	0.29	71.6	1.8	71.5	6.1	68	202	106
A311	6695	875	10	0.43	0.4	0.01118	2.4	0.07325	3.8	0.04751	2.9	0.64	71.7	1.7	71.8	2.6	75	69	95
A204	13793	956	11	0.20	4.9	0.01122	2.9	0.07350	10.5	0.04753	10.1	0.28	71.9	2.1	72.0	7.3	76	240	95
A223	4961	693	9	0.17	b.d.	0.01125	2.5	0.07424	3.1	0.04787	1.7	0.83	72.1	1.8	72.7	2.1	93	41	77
A350	2954	208	3	0.08	0.1	0.01135	2.5	0.07496	3.2	0.04789	2.0	0.77	72.8	1.8	73.4	2.3	94	48	77
A323	6672	681	8	0.24	2.0	0.01136	2.4	0.07439	5.3	0.04750	4.8	0.45	72.8	1.8	72.9	3.8	74	113	98
A233	2516	302	4	0.65	0.7	0.01140	2.4	0.07471	4.3	0.04754	3.5	0.57	73.1	1.8	73.2	3.0	76	84	96
A337	2907	223	3	0.94	4.5	0.01143	2.5	0.07470	9.3	0.04741	8.9	0.27	73.3	1.8	73.1	6.6	70	212	105
A231	2289	289	4	1.00	0.3	0.01143	2.5	0.07479	5.3	0.04745	4.7	0.47	73.3	1.8	73.2	3.7	72	111	102
A221	2087	178	2	0.87	3.0	0.01145	2.5	0.07496	6.9	0.04747	6.4	0.36	73.4	1.8	73.4	4.9	73	152	101
A263	1535	206	3	0.75	0.1	0.01146	2.5	0.07488	4.5	0.04739	3.8	0.55	73.5	1.8	73.3	3.2	69	90	107
A343	3783	123	2	0.41	11.7	0.01146	2.8	0.07508	12.4	0.04751	12.1	0.23	73.5	2.1	73.5	8.8	75	287	98
A265	2059	277	4	0.86	0.2	0.01149	2.5	0.07522	4.1	0.04748	3.2	0.60	73.6	1.8	73.6	2.9	74	77	100
A344	2598	254	3	0.83	0.0	0.01149	2.5	0.07606	3.1	0.04800	1.9	0.79	73.7	1.8	74.4	2.2	99	45	74
A209	2652	345	4	0.77	0.1	0.01151	2.5	0.07522	4.2	0.04739	3.4	0.59	73.8	1.8	73.6	3.0	69	80	107
A358	8108	292	5	0.91	12.8	0.01152	2.8	0.07570	11.6	0.04767	11.2	0.25	73.8	2.1	74.1	8.3	83	266	89
A201	4099	443	5	0.42	0.9	0.01152	2.5	0.07706	3.9	0.04851	3.0	0.63	73.9	1.8	75.4	2.8	124	71	60
A300	11148	598	8	0.60	8.1	0.01153	2.6	0.07599	7.8	0.04781	7.4	0.33	73.9	1.9	74.4	5.6	90	175	82
A199	12490	917	15	0.00	4.6	0.01153	2.6	0.07529	8.8	0.04736	8.4	0.30	73.9	1.9	73.7	6.3	67	200	110
A299	5082	417	5	0.21	3.2	0.01155	2.6	0.07572	5.6	0.04755	4.9	0.46	74.0	1.9	74.1	4.0	77	117	96
A232	1989	254	3	0.90	0.3	0.01163	2.4	0.07619	4.5	0.04750	3.8	0.54	74.6	1.8	74.6	3.3	75	90	100
A210	1993	218	3	0.94	2.0	0.01165	2.5	0.07654	6.0	0.04766	5.4	0.41	74.7	1.8	74.9	4.3	82	129	91
A222	1567	127	2	0.77	3.0	0.01166	2.5	0.07627	6.8	0.04743	6.3	0.38	74.7	1.9	74.6	4.9	71	149	105
A245	5826	228	3	0.33	13.0	0.01173	2.8	0.07695	10.2	0.04759	9.8	0.28	75.2	2.1	75.3	7.5	79	234	95
A267	8049	361	6	0.77	10.0	0.01176	2.9	0.07698	9.1	0.04748	8.6	0.32	75.4	2.2	75.3	6.6	73	205	103
A220	1412	178	2	0.83	0.4	0.01180	2.5	0.07723	4.9	0.04747	4.2	0.52	75.6	1.9	75.5	3.6	73	100	103
A271	52690	1726	33	0.00	11.6	0.01191	2.9	0.07776	10.2	0.04736	9.7	0.29	76.3	2.2	76.0	7.5	68	232	113
A215	1391	151	2	0.31	1.1	0.01191	2.5	0.07800	6.0	0.04749	5.5	0.41	76.3	1.9	76.3	4.4	74	131	103
A306	5123	289	4	0.62	9.5	0.01192	2.8	0.07813	10.6	0.04755	10.2	0.27	76.4	2.1	76.4	7.8	77	243	99
A251	8470	351	5	0.50	11.9	0.01192	2.7	0.07798	9.6	0.04744	9.2	0.29	76.4	2.1	76.2	7.1	71	219	107
A264	3971	484	6	0.55	0.7	0.01195	2.5	0.07837	4.5	0.04756	3.8	0.55	76.6	1.9	76.6	3.3	77	89	99
A318	2588	163	2	0.63	5.4	0.01198	2.6	0.07861	7.8	0.04759	7.4	0.33	76.8	2.0	76.8	5.8	79	175	97
A316	2289	284	4	0.76	0.4	0.01200	2.5	0.07859	4.7	0.04752	4.0	0.53	76.9	1.9	76.8	3.5	75	94	102
A224	6116	705	8	0.31	1.1	0.01200	2.5	0.07856	4.0	0.04747	3.2	0.61	76.9	1.9	76.8	3.0	73	75	105

A235	3095	152	2	0.76	7.3	0.01207	2.7	0.07931	8.6	0.04766	8.2	0.31	77.3	2.0	77.5	6.4	82	194	94
A203	3359	314	4	0.88	3.3	0.01213	2.9	0.07917	9.9	0.04734	9.5	0.29	77.7	2.2	77.4	7.4	66	225	117
A347	2142	122	2	0.28	2.8	0.01214	2.5	0.07963	6.8	0.04756	6.4	0.36	77.8	1.9	77.8	5.1	77	151	101
A257	1614	121	2	0.63	4.7	0.01214	2.6	0.07951	7.3	0.04748	6.8	0.36	77.8	2.0	77.7	5.5	74	162	106
A353	1891	99	1	0.94	0.9	0.01218	2.5	0.07977	6.2	0.04748	5.6	0.41	78.1	2.0	77.9	4.6	73	134	106
A351	1687	41	1	0.61	7.3	0.01231	2.7	0.08058	10.8	0.04746	10.4	0.25	78.9	2.2	78.7	8.2	72	248	109
A228	10169	988	13	0.27	1.4	0.01303	2.5	0.08590	3.4	0.04782	2.4	0.72	83.4	2.0	83.7	2.8	90	57	92
A216	1960	189	3	0.28	3.8	0.01398	2.7	0.09199	7.6	0.04774	7.1	0.36	89.5	2.4	89.4	6.5	86	167	104
A214	27932	82	25	0.87	0.3	0.26470	2.5	3.52400	2.7	0.09655	1.0	0.92	1514	33	1533	21	1558	19	97
Sample Mel2.17 (metadiorite 750 m SW of Nea Krya Vrysi)																			
A40	2103	60	1	0.97	19.6	0.01110	2.7	0.07310	18.4	0.04776	18.2	0.15	71.2	1.9	71.6	13	87	430	82
A19	275	65	1	0.90	b.d.	0.01119	1.7	0.07268	9.6	0.04713	9.4	0.17	71.7	1.2	71.2	7	56	224	129
A17	294	37	0	0.76	0.4	0.01119	2.3	0.07000	4.1	0.04801	3.4	0.55	71.7	1.6	72.6	3	100	82	72
A62	2085	281	4	1.29	4.9	0.01122	1.7	0.07358	10.0	0.04757	9.8	0.17	71.9	1.2	72.1	7	78	233	92
A21	969	116	2	1.08	1.5	0.01126	1.8	0.07396	10.9	0.04762	10.7	0.17	72.2	1.3	72.5	8	80	255	90
A20	985	147	2	1.21	1.2	0.01128	1.8	0.07387	5.1	0.04750	4.8	0.35	72.3	1.3	72.4	4	75	114	97
A41	411	61	1	0.97	1.2	0.01148	1.8	0.07534	6.7	0.04759	6.4	0.27	73.6	1.3	73.8	5	79	153	94
A47	1860	273	4	1.47	1.1	0.01149	1.6	0.07540	3.9	0.04760	3.6	0.41	73.6	1.2	73.8	3	79	86	93
A13	254	42	1	0.91	b.d.	0.01149	2.0	0.07540	4.1	0.04760	3.5	0.49	73.6	1.5	73.8	3	79	84	93
A55	247	37	0	0.83	0.5	0.01150	2.2	0.07544	6.6	0.04757	6.2	0.33	73.7	1.6	73.9	5	78	147	94
A42	2365	359	5	1.27	1.2	0.01150	1.8	0.07544	4.0	0.04757	3.6	0.44	73.7	1.3	73.9	3	78	85	95
A48	816	119	2	1.15	8.8	0.01151	1.9	0.07534	17.5	0.04746	17.4	0.11	73.8	1.4	73.8	13	72	413	102
A50	869	61	1	0.74	7.2	0.01151	2.0	0.07545	10.4	0.04753	10.2	0.19	73.8	1.4	73.9	7	76	243	97
A60	247	36	0	0.78	1.4	0.01151	2.5	0.07539	8.0	0.04749	7.6	0.31	73.8	1.8	73.8	6	74	180	100
A49	290	42	1	0.65	1.4	0.01152	1.9	0.07540	7.6	0.04749	7.4	0.25	73.8	1.4	73.8	5	74	175	100
A54	542	79	1	0.90	1.2	0.01152	1.7	0.07548	5.7	0.04751	5.4	0.31	73.9	1.3	73.9	4	75	129	98
A25	421	59	1	0.95	0.1	0.01152	2.0	0.07566	7.7	0.04762	7.5	0.26	73.9	1.5	74.1	6	80	177	92
A66	701	103	1	1.09	1.6	0.01152	1.9	0.07531	6.8	0.04740	6.6	0.28	73.9	1.4	73.7	5	69	156	107
A45	277	40	1	0.76	1.9	0.01153	2.3	0.07574	7.5	0.04762	7.1	0.31	73.9	1.7	74.1	5	80	168	92
A38	600	88	1	1.02	0.8	0.01155	1.8	0.07584	5.5	0.04763	5.2	0.33	74.0	1.3	74.2	4	81	123	91
A24	1484	149	2	0.94	7.1	0.01155	2.0	0.07583	13.4	0.04761	13.2	0.15	74.0	1.5	74.2	10	80	314	92
A09	641	92	1	1.00	0.0	0.01155	1.9	0.07570	4.4	0.04753	3.9	0.44	74.0	1.4	74.1	3	76	93	98
A11	644	94	1	1.04	0.0	0.01155	1.6	0.07589	4.2	0.04764	3.8	0.38	74.1	1.2	74.3	3	81	91	91
A59	1503	220	3	1.48	1.4	0.01156	1.7	0.07612	3.7	0.04774	3.3	0.45	74.1	1.2	74.5	3	86	79	86
A28	515	78	1	0.94	1.2	0.01156	1.9	0.07569	5.3	0.04747	5.0	0.35	74.1	1.4	74.1	4	73	119	102
A61	470	67	1	1.00	0.8	0.01157	2.0	0.07563	6.3	0.04743	6.0	0.31	74.1	1.5	74.0	5	71	143	104
A72	641	95	1	1.00	0.9	0.01158	2.0	0.07594	5.0	0.04757	4.6	0.39	74.2	1.5	74.3	4	78	110	95
A27	944	140	2	1.29	0.9	0.01159	1.7	0.07580	4.4	0.04744	4.1	0.38	74.3	1.2	74.2	3	71	97	104
A39	373	51	1	0.86	1.7	0.01160	2.2	0.07616	7.4	0.04763	7.0	0.30	74.3	1.6	74.5	5	81	167	92
A64	595	88	1	1.01	0.5	0.01160	1.7	0.07594	4.9	0.04749	4.6	0.35	74.3	1.3	74.3	4	74	109	101
A32	867	116	2	1.13	0.8	0.01161	1.9	0.07623	7.2	0.04763	7.0	0.26	74.4	1.4	74.6	5	81	165	92
A31	1101	151	2	1.02	0.6	0.01161	1.6	0.07606	4.0	0.04752	3.6	0.41	74.4	1.2	74.4	3	75	86	99
A65	750	112	2	1.08	1.0	0.01161	1.8	0.07604	5.6	0.04750	5.3	0.32	74.4	1.3	74.4	4	74	126	100

A26	784	113	2	1.08	1.8	0.01163	1.6	0.07608	6.3	0.04744	6.1	0.26	74.5	1.2	74.5	5	72	145	104
A51	919	134	2	1.20	1.3	0.01165	1.6	0.07624	4.7	0.04746	4.4	0.33	74.7	1.2	74.6	3	72	105	103
A63	2096	215	3	1.65	2.1	0.01167	1.6	0.07633	5.3	0.04746	5.1	0.29	74.8	1.2	74.7	4	72	121	104
A44	12875	1882	39	3.09	3.3	0.01169	1.5	0.07681	6.6	0.04767	6.4	0.23	74.9	1.1	75.1	5	83	152	90
A14	276	39	1	0.77	0.0	0.01171	2.2	0.07653	7.2	0.04740	6.9	0.31	75.1	1.7	74.9	5	69	163	108
A43	810	120	2	1.10	1.1	0.01173	2.0	0.07710	5.7	0.04769	5.4	0.35	75.2	1.5	75.4	4	84	128	90
A58	392	53	1	0.96	1.1	0.01174	2.2	0.07717	6.1	0.04768	5.7	0.35	75.2	1.6	75.5	4	83	135	90
A10	689	102	1	1.05	0.0	0.01178	1.8	0.07706	5.0	0.04744	4.6	0.37	75.5	1.4	75.4	4	71	110	106
A53	857	120	2	1.15	1.9	0.01183	1.9	0.07761	5.6	0.04756	5.3	0.35	75.8	1.5	75.9	4	78	125	98
A22	92	67	1	0.98	b.d.	0.01186	1.9	0.07581	21.2	0.04635	21.1	0.09	76.0	1.5	74.2	15	16	507	482
A46	412	60	1	0.95	1.3	0.01187	1.7	0.07778	5.2	0.04754	4.9	0.32	76.0	1.3	76.1	4	77	116	99
A30	316	49	1	0.82	0.8	0.01189	1.9	0.07808	7.1	0.04764	6.8	0.27	76.2	1.5	76.3	5	81	161	94
A52	407	60	1	0.94	1.1	0.01191	1.9	0.07804	5.6	0.04751	5.3	0.33	76.4	1.4	76.3	4	75	126	102
A16	439	62	1	0.76	0.1	0.01195	1.7	0.07850	4.9	0.04765	4.6	0.35	76.6	1.3	76.7	4	82	109	93
A29	424	62	1	0.93	0.8	0.01199	2.2	0.07888	6.0	0.04770	5.5	0.37	76.8	1.7	77.1	4	85	132	90
A15	1233	183	4	2.85	b.d.	0.01209	1.6	0.07857	3.9	0.04715	3.6	0.42	77.5	1.3	76.8	3	57	85	137
A18	376	59	1	0.95	b.d.	0.01214	1.6	0.07901	3.4	0.04719	3.0	0.48	77.8	1.3	77.2	3	59	71	132
A23	970	147	2	1.20	1.3	0.01217	1.8	0.07925	6.1	0.04724	5.8	0.29	78.0	1.4	77.4	5	61	139	127
A56	510	74	1	0.98	0.7	0.01222	1.8	0.08029	5.3	0.04767	5.0	0.34	78.3	1.4	78.4	4	83	119	94
A57	714	108	2	1.13	1.1	0.01222	1.5	0.08030	5.3	0.04767	5.1	0.29	78.3	1.2	78.4	4	83	121	95
A12	247	39	1	0.63	b.d.	0.01544	14.0	0.34840	66.1	0.16360	64.6	0.21	98.8	13.7	303.5	190	2494	1088	4

[a] Within-run background-corrected mean ^{207}Pb signal in cps (counts per second).
[b] U and Pb content and Th/U ratio were calculated relative to standard zircon GJ-1.
[c] Percentage oft he common lead on the ^{206}Pb. b.d. = below detection limit.
[d] Corrected for background, within-run Pb/U fractionation (in case of $^{206}Pb/^{238}U$) and common Pb using Stacey and Kramers (1975) model Pb composition and subsequently normalised to standard zircon GJ-1 (ID-TIMS value/measured value); $^{207}Pb/^{235}U$ calculated using $(^{207}Pb/^{206}Pb)/(^{238}U/^{206}Pb \times 1/137.88)$.
[e] Error correlation defined as $err(^{206}Pb/^{238}U)/err(^{207}Pb/^{235}U)$.
[f] Degree of concordance = $100 \times (^{238}U/^{206}Pb$ age$)/(^{207}Pb/^{206}Pb$ age).

Table 3.8 U-Pb analytical results for zircons of metadiorite Mel2.17 from the ACC SW of Nea Krya Vrysi. Errors are quoted at 2σ-level.

	Weight [µg]	**U [ppm]**	**Pb [ppm]**	**$^{206}Pb/^{204}Pb$***	**$^{206}Pb/^{238}U$**	**±2σ [%]**	**$^{207}Pb/^{235}U$**	**±2σ [%]**	**$^{207}Pb/^{206}Pb$**	**±2σ [%]**	**Cor.**	**Apparent ages [Ma]**					
Analyses												**$^{206}Pb/^{238}U$**	**±2σ**	**$^{207}Pb/^{235}U$**	**±2σ**	**$^{207}Pb/^{206}Pb$**	**±2σ**
4550	16	593	12.74	565	0.01166	0.78	0.07614	2.07	0.04735	1.82	0.49	74.8	0.6	74.5	1.5	66.8	43
4553	18	488	10.74	339	0.01158	0.89	0.07544	4.09	0.04725	3.78	0.44	74.2	0.7	73.9	3.0	62.0	90
4554	14	395	8.89	228	0.01141	1.48	0.07485	6.40	0.04756	5.90	0.44	73.2	1.1	73.3	4.7	77.7	140
4551	17	1296	25.06	729	0.01129	0.90	0.07387	3.37	0.04747	3.12	0.41	72.4	0.7	72.4	2.4	72.9	74
4549	22	425	9.06	355	0.01125	1.00	0.07368	4.17	0.04749	3.86	0.42	72.1	0.7	72.2	3.0	74.1	92
4548	2	342	7.48	262	0.01124	1.41	0.07365	5.52	0.04753	5.06	0.44	72.0	1.0	72.2	4.0	76.1	120

* = corrected for mass fractionation (1.12 ±0.18 ‰ per a.m.u.), ^{205}Pb-spike contribution and analytical blank of 2 pg. Cor. = correlation coefficient of $^{207}Pb/^{235}U$ to $^{206}Pb/^{238}U$ errors.

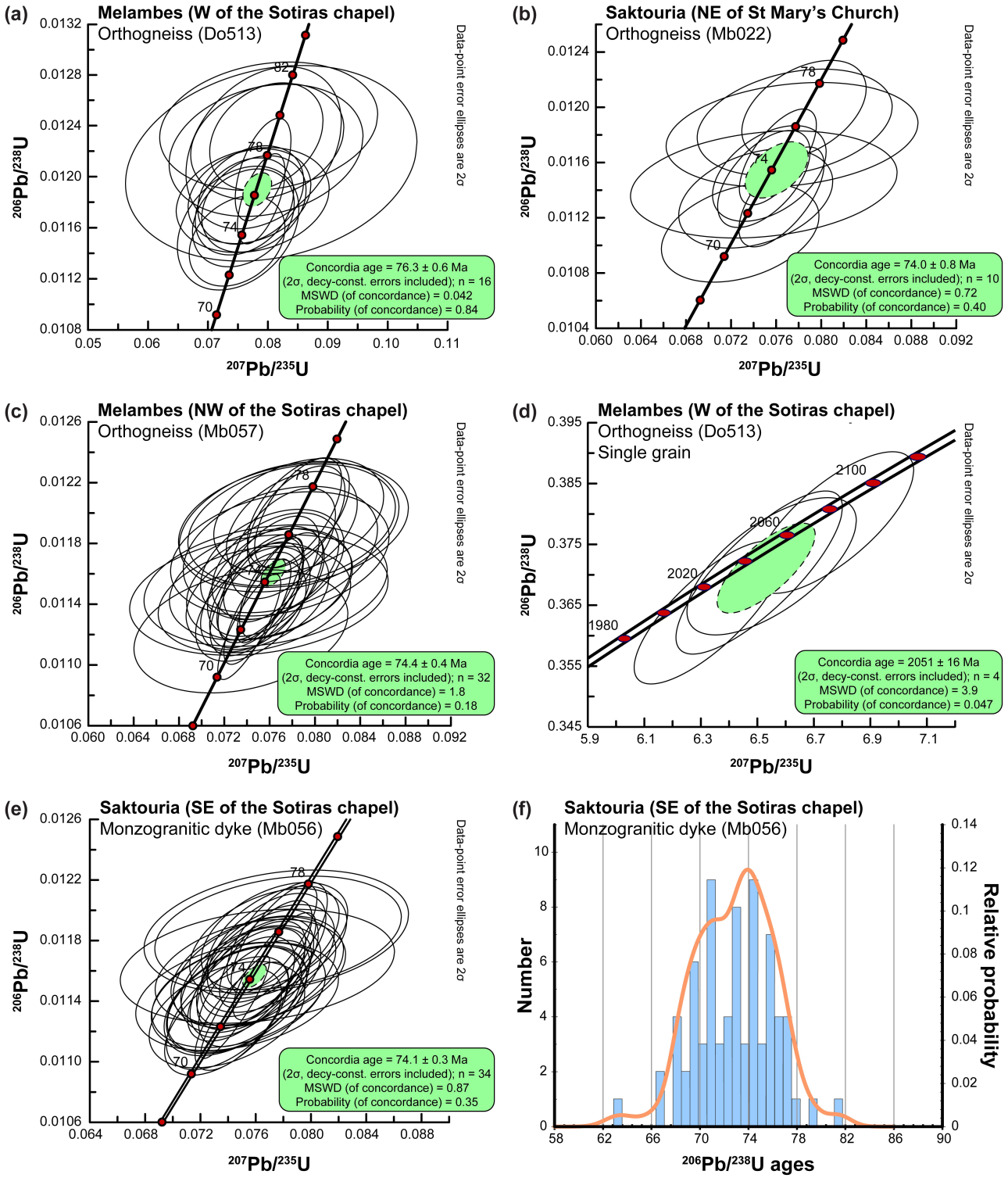

Fig. 3.17. U-Pb concordia diagrams of LA-ICP-MS analyses on zircon from orthogneiss samples (a, b) Do513, (c) Mb022 and (d) Mb057 and (e) from monzogranite sample Mb056. Numbering and error of the ellipses are given in Table 3.7. (f) Density plot of $^{238}U/^{206}Pb$ zircon ages obtained from LA-ICP-MS analyses on monzogranite Mb056.

age at 73.65 +0.25/–0.4 Ma (Fig. 3.16c). Three concordia ages were calculated for the orthogneiss samples at 76.3 ± 0.6 Ma (Do513; MSWD = 0.042; P = 0.84; Fig. 3.17a), 74.0 ± 0.8 Ma (Mb022; MSWD = 0.72; P = 0.40; Fig. 3.17b) and at 74.4 ± 0.4 Ma (Mb057; MSWD = 1.8; P = 0.18; Fig. 3.17c), respectively.

Considerably older concordant $^{206}Pb/^{238}U$ zircon ages are reported from only three zircon grains. One analysis (A1447) on one zircon grain from Do513 yielded a $^{206}Pb/^{238}U$ age at 950 ± 22 Ma, the concordance of which is 93 %. However, two analyses on the same grain yielded Campanian ages (Fig. 3.13b). Four analyses on one pristine zircon from Do513 with fine oscillatory zoning and a faint sector zoning (Fig. 3.13b) yielded concordant Palaeoproterozoic $^{206}Pb/^{238}U$ ages at 2000 ± 45 Ma to 2070 ± 45 Ma that define a concordia age at 2051 ± 16 Ma (Fig. 3.17d). Another concordant $^{206}Pb/^{238}U$ age was obtained on one zircon grain from orthogneiss sample Mb057 at 1514 ± 33 Ma.

3.5.5.3 Monzogranitic dyke (sample Mb056)

Zircons extracted from a monzogranitic dyke cutting through metapelite SE of the Sotiras chapel do not differ on cathodoluminescence images from orthogneiss zircons. Uranium contents range from 78 to 1308 ppm, while Th/U ratios are < 1.3 (Table 3.7). The influence of Pbc on the concordance is negligible. Thirty-four analyses yielded a $^{206}Pb/^{238}U$ median age of 74.25 +0.4/–0.7 Ma (Fig. 3.16d) and 34 analyses yielded a concordia age at 74.1 ± 0.3 Ma (MSWD = 0.87; P = 0.35; Fig. 3.17e). The $^{206}Pb/^{238}U$ ages obtained from monzogranite Mb056 are presented in a density plot indicating two zircon populations at ca. 71 Ma and at ca. 74 Ma for monzogranite (Fig. 3.17f). However, analyses from the younger zircon population usually have much lower concordances (Table 3.7).

3.6 Discussion

3.6.1 Igneous intrusions inside the Asterousia Crystalline Complex

3.6.1.1 Late Cretaceous igneous activity

LA-ICP-MS analyses of zircon extracted from metadiorite samples Mb024 and Mel2.17 in the valley south of Nea Krya Vrysi yielded concordant $^{206}Pb/^{238}U$ ages between ~72 and 80 Ma. Th/U ratios between 0.2 and 1.5 and cathodoluminescence images showing small, euhedral zircon with pronounced fine oscillatory zoning indicate a magmatic origin of these zircons (e.g. Vavra et al. 1999; Hoskin and Schaltegger 2003). Based on LA-ICP-MS analyses three concordia ages were calculated at 76.9 ± 0.3 Ma (Mb024), 74.1 ± 0.3 Ma (Mel2.17) and 71.9 ± 0.6 Ma (Mel2.17). The zircon populations at ~74 Ma and at ~72 Ma in Mel2.17 are confirmed by ID-TIMS analyses on zircon from the same sample yielding concordia ages at 74.3 ± 0.4 Ma and 72.2 ± 0.4 Ma. The age spectra of $^{206}Pb/^{238}U$ ages from LA-ICP-MS analyses on zircon from orthogneiss samples Do513, Mb022 and Mb056 are

identical with those found in metadiorite samples. However, the overall concordance of the analyses is lower. Three concordia ages were calculated for the three othogneiss samples at 76.3 ± 0.6 Ma (Do513), 74.4 ± 0.4 Ma (Mb057) and at 74.0 ± 0.8 Ma (Mb022), thus comparing well with the concordia ages of the two older zircon populations of metadiorite samples. A younger zircon population at ~72 Ma is indicated by some concordant analyses in samples Mb022 and Mb057, but is less evident than in metadiorite samples. $^{206}Pb/^{238}U$ zircon ages younger than 72 Ma are usually less concordant and are best explained by post-crystallization lead loss. Th/U ratios and cathodoluminescence images of orthogneiss zircons confirm a magmatic origin of these zircons as well. A sample of monzogranite (Mb056) from a dyke cutting through metapelite close to the intrusive contact of orthogneiss and metapelite near the Sotiras chapel yielded the same age spectra as observed in metadiorite and orthogneiss. The concordia age calculated for zircons from this sample is at 74.1 ± 0.3 Ma. A younger zircon population at ca. 71 Ma is suggested from the density plot of $^{206}Pb/^{238}U$ zircon ages. However, theses ages have significantly lower concordances compared to the 74 Ma zircon population. Thus, it cannot be ruled out that they result from lead loss. Overall, at least three zircon populations at 76.5 Ma, 74 Ma and 72 Ma are suggested from our data for the Asterousia-type (meta)granitoids exposed in the Melambes area.

Identical $^{206}Pb/^{238}U$ zircon age spectra were also reported from eastern Crete and from Anafi (Fig. 3.18), where Asterousia-type granitoids intruded into marble. The minimum crystallization age of granodiorite zircons from Anafi was constrained at 72.6 +0.1/–0.2 Ma, while the largest zircon population yielded an age of 74.0 ± 0.1 Ma (Martha et al. 2016). Older $^{206}Pb/^{238}U$ ages indicate older zircon populations meaning that intrusive magmatism should have commenced at ca. 80 Ma or even earlier. Zircons from quartzdiorite west of Pachia Ammos in eastern Crete yielded a crystallization age at 74.5 ± 0.25 Ma (Kneuker et al. 2015). Furthermore, Hinsken et al. (2016) reported U-Pb ages (sector field ICP-MS) of detrital zircon extracted from metasedimentary rocks of the Cycladic Blueschist Unit on Tinos, the youngest ages of which are 70–80 Ma, the Asterousia-type granitoids therefore being a possible source for these detrital zircons. Thus, the age spectra of the studied zircons from the Melambes granodiorite are compatible with those reported from at least three other localities in the southern Aegean confirming the presence of a middle to late Campanian magmatic arc. Monzogranite from dykes cutting through the Anafi granodiorite yielded $^{206}Pb/^{238}U$ median zircon ages at 69.9 ± 0.7 Ma (Martha et al. 2016) indicating that arc magmatism was also active during the early Maastrichtian.

The orthogneiss from the Melambes area is strongly foliated and shows evidence for high-temperature mylonitic top-to-the SE shearing. Deformation temperatures > 600 °C are indicated by dynamic

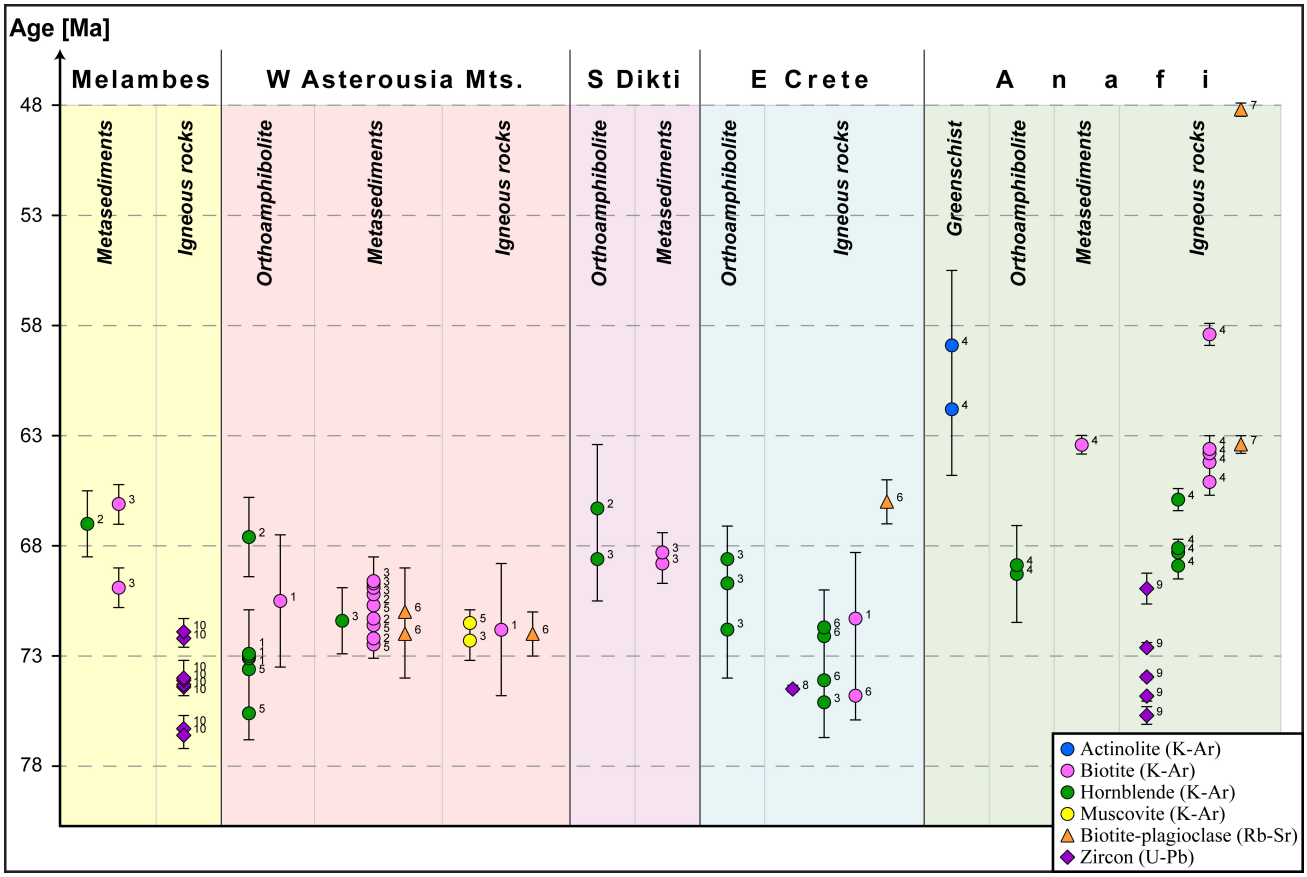

Fig. 3.18 Scatter chart summarizing geochronological data from the Melambes area, the western Asterousia Mountains between Kali Limenes and Lendas, south of the Dikti Mountains (Pefkos, Kalami and Sykologos area), eastern Crete (Kritsa area and northern Ierapetra Graben) and Anafi. Data sources: [1]Lippolt and Baranyi (1976), [2]Seidel et al. (1976), [3]Seidel et al. (1981), [4]Reinecke et al. (1982), [5]Koepke and Seidel (1984), [6]Langosch et al. (2000), [7]Be'eri-Shlevin et al. (2009), [8]Kneuker et al. (2015), [9]Martha et al. (2016), [10]this study. Data from Lippolt and Baranyi (1976) and Seidel et al. (1976) were recalculated in Seidel et al. (1981). For convenience, no analyses with error margins > 3.0 Ma are included, except for one value on the Anafi Greenschist from Reinecke et al. (1982).

recrystallization of quartz and feldspar, serrated boundaries between feldspar and quartz and strain-induced myrmekite. Micas (both biotite and white mica) show grain shape-preferred orientation. Since there is no evidence of quartz, plagioclase and K-feldspar to have been consumed and/or transformed during deformation, the modal composition of these phases is believed to represent the original composition of the protolithic magma, which can be classified as monzogranitic to syenogranitic. Unlike orthogneiss, metadiorite and the sample of monzogranite from a dyke are unfoliated. However, metadiorite shows evidence for crystal plastic deformation and although the primary magmatic fabrics are well preserved, dynamic recrystallization of plagioclase and quartz, the presence of chlorite and the albitization of plagioclase indicate that diorite should have faced high-temperature deformation. The microfabrics of feldspar and quartz observed in monzogranite bear evidence for brittle, low-grade deformation at T_{max} = 400 °C.

HT-deformation fabrics in granitoids are supposed to have developed during post-intrusive slow initial cooling and top-to-the SE shearing resulting in significant finite strain. The deformation fabrics of igneous rocks depend on the amount of mechanically weak phases, such as quartz and mica, which

is high in metagranite/orthogneiss (30.4–62.9 %) but low in metadiorite (~4.5 %) and monzogranite (24.6 %). Under the same deformation conditions, igneous rocks rich in weak phases develop pervasive foliation, while igneous rocks poor in these phases do not (e.g. Vernon and Flood 1988). The lack of foliation in metadiorite and monzogranite from a dyke can therefore be explained by the low amount of mechanically weak phases in contrast to metagranite (orthogneiss). Compared with the Melambes granitoids, the Anafi granodiorite and the Pachia Ammos quartzdiorite are both unfoliated. However, microfabrics of the Anafi granodiorite suggest high-temperature (T > 600 °C) deformation at low strain during the initial cooling phase of the plutons (Martha et al. 2016), while the Pachia Ammos quartzdiorite bares evidence for post-Oligocene brittle deformation only and must have cooled down rapidly (Kneuker et al. 2015).

3.6.1.2 Pre-Campanian zircon ages and magma source

Zircon grains yielding $^{206}Pb/^{238}U$ ages older than Campanian have not been found in Asterousia-type granitoids from Anafi (Be'eri-Shlevin et al. 2009; Martha et al. 2016) and eastern Crete (Kneuker et al. 2015) and also lack in metadiorite and monzogranite from a dyke of the present study. However, three zircon grains from orthogneiss samples Do513 and Mb057 yielded Proterozoic ages. Analysis A1447 of one zircon grain gives a Tonian age at 950 ± 22 Ma. However, this grain yielded also younger Campanian ages. Cathodoluminescence images do not allow deciding, if we deal with an inherited core surrounded by a younger overgrowth rim. More reliable are four analyses on one zircon grain yielding Palaeoproterozoic ages. These analyses define a concordia age at 2051 ± 6 Ma (Fig. 3.17b). Although CL images prove a faint sector zoning typical for metamorphic zircon (Fig. 3.13c), the Th/U ratios suggest rather a magmatic origin of the zircon. This holds also true for analysis A214 on one zircon grain of Mb057 yielding a concordant $^{206}Pb/^{238}U$ age at 1514 ± 33 Ma.

Similar $^{206}Pb/^{238}U$ ages of detrital zircon have been reported from the Pelagonian Zone in northwestern Greece, which is considered as the parent terrane of the ACC. Zircons separated from orthogneiss and granite in the area between Florina and Fotino yielded Tonian ages, the oldest of which are 966 ± 3 to 957 ± 9 Ma (TIMS; Anders et al. 2006). Detrital zircons of metalitharenite from the Pelagonian Zone in the eastern Aegean Sea (islands of Inousses and Psara near Chios) yielded pre-700 Ma age groups at 1050–900 Ma and 2040–1880 Ma (LA–SF–ICP–MS analyses; Meinhold and Frei 2008). Zlatkin et al. (2014) reported similar $^{206}Pb/^{238}U$ age spectra for metasedimentary rocks from the Pelagonian Zone in mainland Greece (areas of Deskati, Fotino and Livadi), but they also obtained zircon age peaks at ca. 1.7 Ga, 1.5 Ga and 1.3 Ga (U–Pb–Hf method). Taking into account the few inherited zircon ages obtained from the Asterousia-type granitoids, this comparison has to be considered very preliminary.

The almost complete absence of pre-Campanian zircon ages in Asterousia-type (meta)granitoids suggests a relatively young protolith to be the source of the granitoids. This corroborates previous assumptions of Langosch et al. (2000) using geochemical data from Asterousia-type granitoids on Crete. Langosch et al. (2000) assumed partial melting of an igneous continental crust and explained the igneous sequence with assimilation–fractional crystallization of dioritic magma and assimilation of sediments. However, this scenario assumes that diorite is older than granite, which is not supported by the U-Pb age data from the present study. Langosch et al. (2000) also reported that granitic rocks from central Crete (Melambes area and western Asterousia Mountains) have A-type signature, whereas diorite from eastern Crete (Kritsa, Kalo Chorio and Pachia Ammos areas) has I-type signature. This suggests a different evolution for granitic and dioritic magma. Assuming that granitic and dioritic magma have developed in different magma chambers or in different parts of the same magma chamber, as also discussed in Langosch et al. (2000), is therefore considered the most likely hypothesis to explain both the geochemical differences and the U-Pb age paradoxon. We believe that the granitic magma chamber must have faced strong modification of the initial composition by assimilation of considerable amounts of felsic country rock that included also detrital zircon and that modified the geochemical signature to an A-type signature for the Asterousia-type granite.

3.6.2 Tectonometamorphic evolution of the Uppermost Unit in the study area

Geological mapping of the metamorphic rocks west of Melambes yielded two units differing in grade of metamorphic overprint. The upper unit consists of amphibolite facies metasedimentary rocks, slices of serpentinite and igneous intrusions and corresponds to the ACC. Foliated low-grade metamorphic rocks in the valley of the ephemeral Akoumianos River were previously mapped erroneously as ‘Pindos volcanite’ by Krahl et al. (1982). However, rocks of the Pindos Unit should be free from metamorphism and ductile foliation. For this reason, the low-grade rocks are referred to as Akoumianos Greenschist.

3.6.2.1 Akoumianos Greenschist

The mineral assemblage of greenschist (epidote-amphibole schist) from the Akoumianos Greenschist (albite/oligoclase + actinolite + chlorite + magnesio-hornblende +epidote ± titanite) indicates upper greenschist facies conditions and the low aluminium content in hornblende suggests a relatively low pressure. The hornblende-plagioclase geothermobarometer of Plyusnina (1982; fig. 5) yielded metamorphic conditions of P = 250–400 MPa and T = 500 +15/–30 °C, while geothermometry using the edenite-richterite geothermometer for hornblende-plagioclase assemblages lacking quartz of Holland and Blundy (1994) yielded a temperature of 400 to 560 °C for deformation. CPO patterns of

quartz c-axes of Akoumianos-type quartzite indicate non-coaxial deformation with rhomb <a> slip and prism <a> slip. This is consistent with deformation at ca. 500 °C (e.g. Lister and Dornsiepen 1982). Petrographic, EMP and EBSD data therefore suggest uppermost greenschist to epidote-amphibolite facies conditions during the deformation of the rocks of the Akoumianos Greenschist.

All Akoumianos-type rocks display a pervasive NW-dipping foliation with a pronounced NW–SE-trending mineral/stretching lineation. All shear sense indicators observed (e.g. asymmetrically shaped mineral clasts, asymmetric boudins) indicate a consistent top-to-the SE tectonic transport. This sense of shear has previously been reported as the dominant sense of shear from the Anafi tectonometamorphic sequence as well (Martha et al. 2016).

3.6.2.2 Asterousia Crystalline Complex

The rock assemblage of the Asterousia-type metasedimentary succession indicates that we deal with an amphibolite facies variegated series resulting from previous limestone, marl, pelite and sandstone (cf. Thorbecke 1987). This is a typical rock assemblage of sediments deposited on a continental platform. Mineral assemblages as well as deformation microfabrics are consistent with amphibolite facies conditions for deformation (P = 400–500 MPa and $T_{max} \approx 700$ °C), CPO patterns of quartz c-axes from Asterousia-type quartzite indicate non-coaxial deformation with dominant prism <a> slip and subordinate rhomb <a> slip. This corresponds to comparable or only slightly higher temperature conditions to those observed in Akoumianos-type quartzite (Stipp et al. 2002).

All Asterousia-type metamorphic rocks (with the exception of serpentinite, metadiorite and marble) display a pervasive NW- or SE-dipping foliation with a pronounced NW–SE-trending mineral/stretching lineation. Shear sense indicators indicate a consistent top-to-the SE tectonic transport. Folds showing a WSW-vergence were found both within the Asterousia-type section and within the underlying Pindos flysch, thus suggesting a joint evolution of the units during ENE–WSW shortening, the latter responsible for the folding. E(NE)–W(SW) shortening must therefore be younger than thrusting of the ACC on top of the Pindos Unit. The exact age, however, cannot be constrained based on our observations (cf. Klein et al. 2013).

3.6.3 Correlation of the tectonometamorphic evolution of the study area with that of adjacent domains

Comparable Uppermost Unit successions like those found in the study area west of Melambes are reported from at least four domains on Crete (Fig. 3.1) and from the southern Cyclades. In the western Asterousia Mountains of Crete, orthoamphibolite rests on top of Pindos flysch and is overlain by Asterousia-type metasedimentary rocks intruded by granitoids and including slices of serpentinite, which

are also found in the topmost position (Koepke and Seidel 1984; Thorbecke 1987). In eastern Crete, diorite and granite intruded into marble at upper structural levels. Orthoamphibolite is found in the Kritsa area only. However, it is unclear, whether the contact between diorite and orthoamphibolite is intrusive or tectonic (Wachendorf et al. 1980). The Uppermost Unit south of the Dikti Mountains in the area of Pefkos, Kalami and Sykologos consists of metasedimentary rocks, orthoamphibolite and serpentinite (Bonneau 1972a; Seidel et al. 1981). The Asterousia-type sequence of Anafi (southern Cyclades) shows three tectonometamorphic units found on top of Eocene flysch and at the base of Neogene sediments (Reinecke et al. 1982; Martha et al. 2016). They comprise a greenschist facies unit at the base (Anafi Greenschist) comparable to the Akoumianos Greenschist SW of Nea Krya Vrysi and overlain by Asterousia-type rocks consisting of the Anafi Amphibolite Group and metasedimentary rocks with slices of serpentinite and intrusions of granitoids and dykes (Chalepa Group).

The mineral assemblages observed in the metasedimentary rocks of the Melambes area are comparable with those of the Asterousia-type metasedimentary rocks in the western Asterousia Mountains (Seidel et al. 1981; Koepke and Seidel 1984) and on Anafi (Reinecke et al. 1982) and corroborate a correlation of these units. Orthoamphibolite of the ACC has a tholeiitic signature (Reinecke et al. 1982; Thorbecke 1987) but was not found in the Melambes area. Greenschist facies rocks at the base of amphibolite facies Asterousia-type rocks have previously been reported only from Anafi. The Anafi Greenschist is homogeneous and consists of epidote-amphibole schist with a mid-ocean ridge basalt (MORB)-type signature (Reinecke et al. 1982).

Comparison of the geochronological data reported from the ACC on Crete and on Anafi suggests a similar cooling history (Fig. 3.18). K-Ar hornblende and biotite ages indicate a common cooling of metagranitoids and country rocks below the closure temperatures of hornblende (530 ± 40 °C; Harrison 1981) and biotite (310 ± 30 °C; Harrison et al. 1985), respectively. Furthermore, K-Ar ages indicate that post-intrusive cooling of the Asterousia-type granitoids on Anafi and in the Melambes area, where intrusions occurred at deep structural levels, was slow, while in eastern Crete (cf. Tortorici et al. 2012), granitoids intruded at upper structural levels and cooled down fast (Kneuker et al. 2015; see also section 3.6.1.1).

In the vicinity of Melambes, in the area between Karines and Akoumia and at the Preveli Monastery, low-grade metamorphic rocks associated with serpentinite intruded by gabbroic dykes and described as the Preveli, Spili and Vatos units (e.g. Krahl et al. 1982), are found. Greenschist facies rocks have been reported from the Vatos and Spili units, while the Preveli Unit comprises blueschist facies rocks. Seidel et al. (1977) constrained metamorphic conditions at P > 700 MPa and T □ 500 °C for the Preveli Unit, while Tortorici et al. (2012) reported completely different metamorphic conditions at P = 1200–1400 MPa and T ≈ 350 °C. Tortorici et al. (2012) suggested that the low-grade metamorphic

rocks of the Uppermost Unit belong to the Pindos realm and faced blueschist to greenschist facies metamorphism during Palaeocene to Eocene subduction beneath the Pelagonian domain. They also suggested a correlation of the Preveli Unit with the Cycladic Blueschist Unit (CBU) pointing to similarities in the metamorphic grade and in the structural position in the Cretan and Cycladic nappe piles. The CBU underwent Early to Middle Eocene (ca. 53–40 Ma) blueschist to eclogite facies (P = 1200–2000 MPa, T = 450–500 °C) metamorphism (e.g. Altherr et al. 1979; Wijbrans and McDougall 1986).

A correlation of the Preveli Unit with the CBU is very divisive since K-Ar hornblende and phengite ages from metasedimentary rocks and metavolcanics of the Preveli Unit on Crete and on Gavdos of ca. 150 Ma are interpreted as cooling from blueschist facies metamorphism (Seidel et al. 1977). Still, the closure temperature of hornblende is 530 ± 40 °C (Harrison 1981) and it has been shown that the closure temperature of phengitic mica (usually estimated at ca. 380 °C) depends on the pressure and can be as high as 550 °C under blueschist facies conditions (Lister and Baldwin 1996; Harrison et al. 2009). It is therefore possible that the Preveli Unit underwent Early Palaeogene blueschist facies metamorphism without disturbance of the K-Ar systems of hornblende and phengite meaning that the Late Jurassic cooling ages reflect cooling after magmatic emplacement of the protolith.

A correlation of the low-grade metamorphic rocks of the Uppermost Unit with the CBU is further indicated by U-Pb dating (SHRIMP) of zircon from metagabbroic dykes inside metaserpentinite from Andros, Syros and Tinos (northern Cyclades) yielding ages at ca. 160 Ma and at ca. 80 Ma (Bröcker and Pidgeon 2007; Tomaschek et al. 2008; Bulle et al. 2010). These ages compare well with gabbroic intrusions inside serpentinite from the low-grade metamorphic units on Crete, K-Ar hornblende ages of which yielded cooling at ca. 120 to 160 Ma and at ca. 80 to 90 Ma (Delaloye et al. 1977; Seidel et al. 1981; Koepke et al. 2002). A correlation is further suggested by the existing structural data, a NW–SE-oriented stretching lineation being well reported from the CBU (e.g. Ridley 1982; Vandenberg and Lister 1996; Xypolias et al. 2012; Aravadinou et al. 2016) and having been correlated with Early to Middle Eocene SE-directed ductile thrusting during blueschist facies metamorphism (Aravadinou et al. 2016). However, fission track thermochronometry on zircon from Preveli rocks yields ages scattering between about 300–80 Ma and were interpreted as mixed ages (Brix et al. 2008). They are not consistent with Early Palaeogene blueschist facies overprint since the closure temperature of zircon fission tracks has been constrained at 230–310 °C (Tagami and Dumitru 1996). This puts into question a correlation of the Preveli Unit with the CBU and suggests a possible correlation with the Vardar-Izmir-Ankara Zone that faced high-pressure metamorphism at 83–80 Ma (e.g. Sherlock et al. 1999; Ring and Layer 2003). However, more data from the low-grade metamorphic rocks of the Uppermost Unit on Crete are needed to constrain the origin of the Preveli, Spili and Vatos units and a clear statement cannot be made herein.

Geochronological data obtained from the greenschist facies rocks of the Uppermost Unit on Crete are still lacking. K-Ar actinolite ages (Reinecke et al. 1982) from the Anafi Greenschist (58.9 ± 3.4 to 61.8 ± 3.0 Ma) indicate Palaeocene cooling below the closure temperature of actinolite (470 ± 25 °C; Dahl 1996), which is close to the peak of the estimated peak temperature for greenschist facies metamorphism. Krahl et al. (1982) and Tortorici et al. (2012) reported the mineral assemblage albite + chlorite + actinolite + epidote + titanite for greenschist facies metamorphic rocks of the Vatos Unit. However, Tortorici et al. (2012) also reported riebeckite/crossite in some samples and suggest HP-greenschist facies metamorphic deformation conditions for deformation of the Vatos Unit. The structural data reported by Tortorici et al. (2012) from the low-grade metamorphic units of the Uppermost Unit (e.g. orientation of stretching lineation in the Preveli Unit, slickensides on thrust planes) confirm top-to-the SE as the dominant shear sense for the Preveli, Spili and Vatos units as well. The mineral assemblages observed in the Akoumianos and Anafi greenschists and the EMP data presented herein, however, indicate HT-greenschist facies metamorphic overprint, not compatible with metamorphic conditions deduced from the mineral assemblages from the Preveli, Spili and Vatos units. Therefore, the Akoumianos and Anafi greenschists are not considered to belong to any of these subunits, but are regarded as a separate unit.

Apatite fission track ages obtained from the Uppermost and the Pindos units in the area of Melambes and in the western Asterousia Mountains indicate common cooling of the rocks below the apatite partial annealing zone (110 ± 10 °C) at ca. 30 Ma and at ca. 15 Ma (Thomson et al. 1998, 1999). This proves that the low- and high-grade metamorphic rocks of the Uppermost Unit and the non-metamorphic rocks of the Pindos Unit have faced a common tectonic evolution at upper structural levels since at least the Latest Eocene to Early Oligocene (Thomson et al. 1998, 1999). This is also consistent with components from the ACC being widespread inside Neogene sediments of Middle Miocene age from the Ierapetra Graben (Fortuin 1977). The thermal history of the ACC and of the low-grade metamorphic units since the Late Cretaceous is shown in a temperature–time path combining geochronological data from the Melambes area and from Anafi (Fig. 3.19). It is believed that the low-grade metamorphic rocks and the rocks of the ACC had a different thermal history until at least the Eocene.

3.6.4 Geodynamic model

Based on the new and published data, a new geodynamic model is presented for the evolution of the southern Aegean during the Late Cretaceous to Late Eocene (Fig. 3.20). In this model, we suppose that the Pindos realm was subducted underneath the southern margin of the Pelagonian-Lycian Block. The Pindos Ocean consisted of deep-water carbonates (Pindos Unit) that were followed to the south by shallow-water sediments (Tripolitsa Unit) and further to the south by the other units of the lower

nappe system of the Cretan nappe pile (cf. Klein et al. 2013; their fig. 12). Basalts with MORB-type signature (the protoliths of greenschist facies rocks; Reinecke et al. 1982) and ocean sediments may have formed the deeper parts of the Pindos Ocean that were subducted underneath the Pelagonian-Lycian microterrane. The southern margin of the Pelagonian-Lycian Block (upper plate) was characterized by continental platform sediments and basalt with tholeiitic signature, which are the protolith rocks of the ACC. Since no tectonic contact of the Preveli, Spili and Vatos units with the ACC or the Akoumianos Greenschist is known, it is unclear whether these units formed part of the Pindos Ocean or are derived from the Vardar-Izmir-Ankara Ocean (see above).

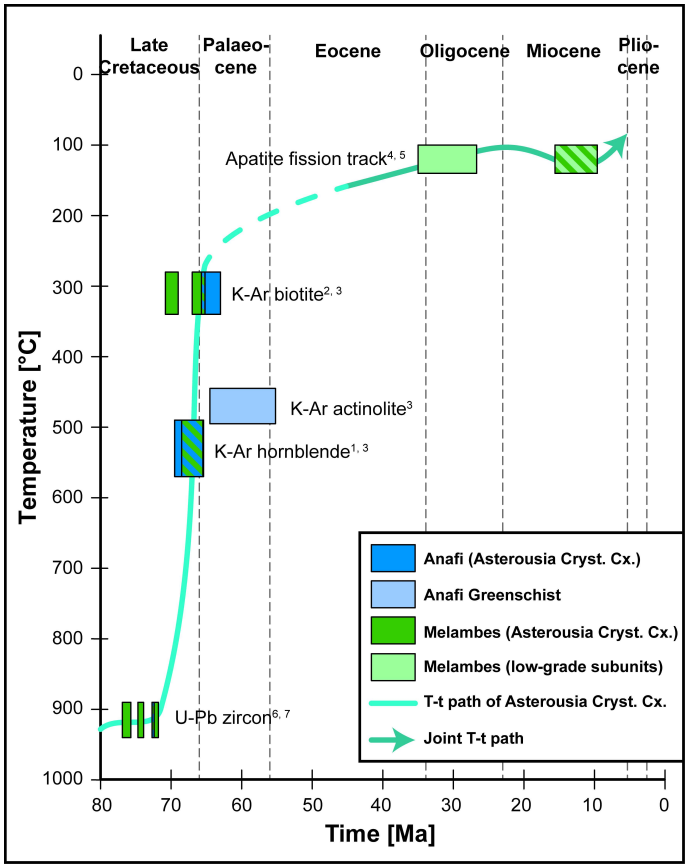

Fig. 3.19 Temperature–time path showing the thermal history of the Uppermost Unit as reconstructed from geochronological data from the Melambes area and Anafi. Data sources: [1]Seidel et al. (1976), [2]Seidel et al. (1981), [3]Reinecke et al. (1982), [4]Thomson et al. (1998), [5]Thomson et al. (1999), [6]Martha et al. (2016), [7]this study. Closure temperatures for the K-Ar systems of hornblende after Harrison (1981), of actinolite after Dahl (1996) and of biotite after Harrison et al. (1985), for the Pb-U-Th system of zircon after Lee et al. (1997), for the fission tracks of apatite as indicated in Thomson et al. (1998).

Subduction of the Pindos realm underneath Pelagonia-Lycia started probably during the mid-Late Cretaceous. The Pindos realm formed an accretionary wedge (cf. Tortorici et al. 2012) and serpentinized ocean floor was offscraped and obducted to the upper plate (Fig. 3.20a), which pre-dates amphibolite facies metamorphism of the ACC, as serpentinite was also affected by amphibolite facies metamorphism (Reinecke et al. 1982; Thorbecke 1987; Be'eri-Shlevin et al. 2009). Progressive subduction and collision led to thickening of the upper plate accompanied by pre-middle Campanian amphibolite facies shearing and stacking (Fig. 3.20b). Tholeiitic basalt was transformed into orthoamphibolite. Continental platform sediments were thrust on top of the orthoamphibolite, while thick layers of marble are usually found in the topmost position. In the study area, SE-vergent drag folds in calcsilicate rock and marble and asymmetric boudins of calcsilicate rock are considered to have originated during amphibolite facies top-to-the SE shearing as calcsilicate rocks usually preserves the oldest structures. Pre-intrusive amphibolite facies metamorphism is consistent with Asterousia-type granitoid intrusions showing different grade of deformation at several localities, where Asterousia-type rocks crop out. Granitoids in eastern Crete are unfoliated, while granite in the Melambes area is foliated and was transformed into orthogneiss and

diorite shows also evidence for HT-deformation (cf. Section 3.6.1.1). Granodiorite and quartz diorite on Anafi show evidence for HT-deformation as well (Martha et al. 2016). Still, orthoamphibolite and metasedimentary rocks show evidence of amphibolite facies deformation under similar conditions in all areas, where the ACC crops out (Seidel et al. 1976, 1981; Reinecke et al. 1982). We therefore assume a similar pre-intrusive metamorphic evolution of the ACC, but a different evolution during Campanian intrusions and post-intrusively.

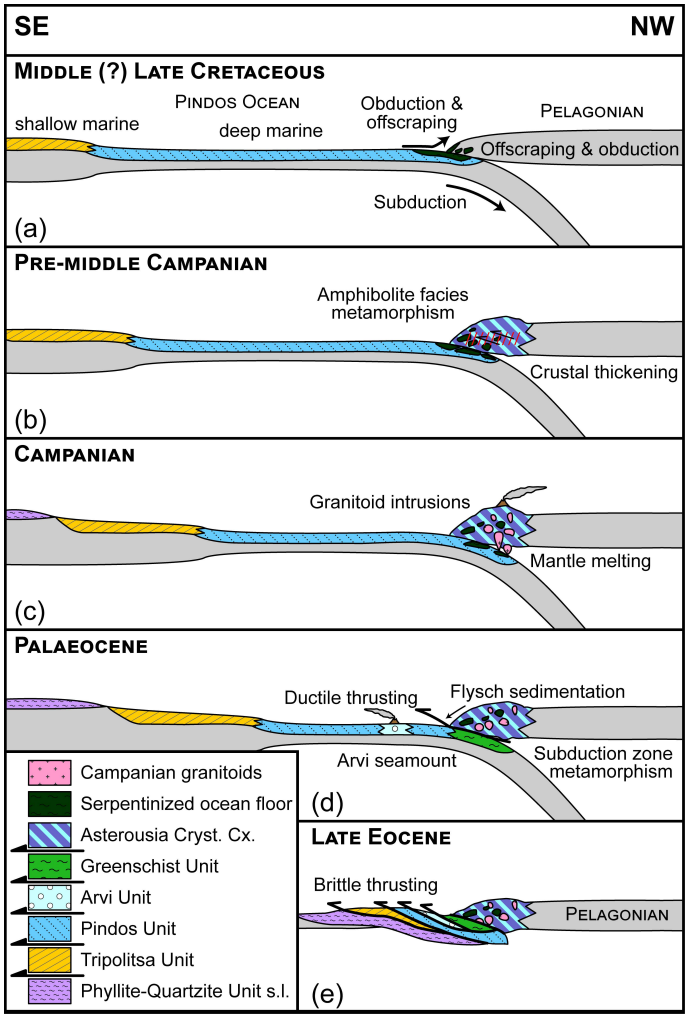

Fig. 3.20 Geodynamic model for the tectonometamorphic evolution of the upper nappe stack in the southern Aegean: (a) accretion and obduction of serpentinite to the Pelagonian-Lycian terrane during Middle (?) Late Cretaceous subduction of the Pindos realm; (b) amphibolite facies metamorphism during crustal thickening and top-to-the SE stacking of the Pelagonian-Lycian southern margin (pre-middle Campanian); (c) mantle melting and intrusion of granitic and dioritic rocks within a magmatic arc (Campanian); (d) subduction zone metamorphism of the low-grade metamorphic units of the Pindos realm and Palaeocene ductile top-to-the SE thrusting of Asterousia Crystalline Complex; (e) brittle top-to-the SE thrusting of Uppermost Unit on Arvi and Pindos units (Late Eocene).

Subduction of the Pindos realm underneath the Pelagonian-Lycian lithosphere caused mantle melting and rise of mantle-derived magma led to continuous intrusion of granitoids, which are major constituents of a Campanian magmatic arc setting along the southern margin of the Pelagonia-Lycian microterrane (Fig. 3.20c). The lack of a contact aureole and/or hornfels surrounding the intrusions in the study area and on Anafi is considered as further evidence that intrusions in these areas occurred at deep structural levels, where amphibolite facies rocks were still hot during Campanian magma emplacement. Campanian intrusion at upper structural levels of eastern Crete, however, led to contact metamorphism in the country rocks (Kneuker et al. 2015).

The (meta)granitoids and the amphibolite facies country rocks collectively cooled down below the closure temperatures of hornblende and biotite during the Maastrichtian. During initial cooling of the ACC, pervasive top-to-the SE mylonitic shearing affected both the country rocks and the (meta)granitoids. While granite was pervasively sheared, diorite and quartz-poor metagranitic dykes behaved rigidly because of lacking weak phases. On Anafi, however, both late Campanian granodiorite and

diorite remained unfoliated. The magnitude of finite strain affecting the ACC in the Melambes area should therefore have been significantly higher than on Anafi.

During the late Maastrichtian, a seamount was active in the Pindos Ocean that was described in literature along with surrounding sediments as the Arvi Unit (Robert and Bonneau 1982; Palamakumbura et al. 2013). Subduction and related metamorphism affected the northern margin of the Pindos realm during the Palaeocene to Middle Eocene (Fig. 3.20d). The Akoumianos and the Anafi greenschists faced HT-greenschist facies metamorphism during subduction. Evidence from Anafi (Martha et al. 2016) shows that ductile SE-directed thrusting of the ACC on top of the HT-greenschists was coeval with greenschist facies metamorphism and hence occurred during the Middle to Late Palaeocene (K-Ar actinolite ages from Reinecke et al. 1982). Furthermore, the upper Pindos flysch is Middle Palaeocene to Middle Eocene in age, showing that trench sediments were deposited during this time.

Continuous shortening and steady uplift and exhumation resulted in subsequent brittle thrusting of the ACC on top of the Arvi and Pindos units. The Arvi Unit had faced prehnite-pumpellyite facies metamorphism from sub-seafloor alteration (Robert and Bonneau 1982) during subduction of the Pindos realm, while the Pindos Unit remained free from metamorphism. Structural and kinematic data obtained from rocks of Anafi (Martha et al. 2016) suggest that thrusting of the Uppermost Unit on top of Eocene flysch occurred under brittle conditions and in a SE-direction. This event is constrained as Late Eocene in age (Fig. 3.20e). Apatite fission track ages of Thomson et al. (1998, 1999) confirm that the Pindos and Uppermost units collectively cooled down below 110 °C during the Latest Eocene to Early Oligocene (Fig. 3.19). Hence, the upper nappe system should have been situated at upper crustal levels by then.

3.7 Conclusions

The following conclusions can be drawn from this study:

(1) Intrusion of granitoids occurred inside a middle to late Campanian magmatic arc along the southern margin of the Pelagonian-Lycian Block. Our U-Pb age data suggests continuous intrusion of dioritic and granitic melts from 71.9 ± 0.6 to 76.9 ± 0.3 Ma. Pre-Campanian, inherited zircon is almost absent in Asterousia-type granitoids pointing to partial melting of young, igneous crust as source for the granitoids.

(2) The higher amount of weak phases in metagranite is the reason why granite was foliated, but metadiorite and monzogranitic dykes remained unfoliated during post-intrusive slow cooling and ductile shearing.

(3) Published K-Ar hornblende and biotite ages from the ACC of Crete and Anafi indicate joint cooling of (meta)granitoids and amphibolite facies country rocks in the HT range during the Maastrichtian. Amphibolite facies metamorphism of the country rocks predates middle to late Campanian arc magmatism.

(4) The dominant shear sense responsible for pre-middle Campanian mylonitic shearing under amphibolite facies conditions, post-intrusive shearing of granitoids and Palaeocene shearing of the ACC on top of the greenschist facies metamorphic rocks is top-to-the SE.

(5) Stacking of the tectonometamorphic units of the Uppermost Unit occurred during a period of continuous NW–SE shortening related to subduction and collision of the Pindos realm underneath the Pelagonian-Lycian active margin starting in the mid-Late (?) Cretaceous and lasting until the Late Eocene.

3.8 Acknowledgements

We thank Maria Bladt and Nils Prawitz for help with thin section production, Linda Marko and Janina Schastok for help with isotopic analyses and Heidi Höfer and Markus Schölmerich for help with EMP analysis. Caroline Mantey (Ruhr University Bochum), Michael Stipp (GEOMAR Kiel) and Bastian Wiesenbach (Ulm) are thanked for fruitful discussions and useful information. Manfred Brix (Ruhr University Bochum), Timur Ustaömer (Istanbul University) and Paraskevas Xypolias (University of Patras) are thanked for fair and helpful reviews on the manuscript and the associate editor Inna Safonova (Sobolev Institute of Geology and Mineralogy, Novosibirsk) is thanked for editing our manuscript. S.O.M. gratefully acknowledges financial support for fieldwork by ERASMUS (Leonardo-da-Vinci programme; grant agreement no. 2013-1-DE2-LEO02-16568).

3.9 References

Allmendinger, R.W., Cardozo, N. & Fisher, D.M. (2012): *Structural geology algorithms: vectors and tensors*. – Cambridge University Press, 289 p.; Cambridge.

Altherr, R., Kreuzer, H., Lenz, H., Wendt, I., Harre, W. & Dürr, S. (1994): Further evidence for a Late-Cretaceous low pressure/high-temperature terrane in the Cyclades, Greece. Petrology and geochronology of crystalline rocks from the islands of Donoussa and Ikaria. – *Chemie der Erde*, **54**: pp. 319–328.

Altherr, R., Schliestedt, M., Okrusch, M., Seidel, E., Kreuzer, H., Harre, W., Lenz, H., Wendt, I. & Wagner, G.A. (1979): Geochronology of high-pressure rocks on Sifnos (Cyclades, Greece). – *Contributions to Mineralogy and Petrology*, **70** (3): pp. 245–255. DOI: 10.1007/BF00375354.

Altherr, R., Seidel, E., Okrusch, M., Schliestedt, M., Reinecke, T., Kreuzer, H., Harre, W., Klein, H. & Dürr, S. (1980): Metamorphic rocks associated with ophiolites in Greece: petrology and geochronology. – In: Panayiotou, A. (ed.) *International Ophiolite Symposium, Nicosia - Cyprus, 1–8 April, 1979. Abstracts of papers submitted*. Τμήμα Γεωλογικής Επισκόπησης [Geological Survey Department], pp. 9–10; Λευκωσία [Nicosia].

Anders, B., Reischmann, T., Kostopoulos, D. & Poller, U. (2006): The oldest rocks of Greece: first evidence for a Precambrian terrane within the Pelagonian Zone. – *Geological Magazine*, **143** (1): pp. 41–58. DOI: 10.1017/S0016756805001111.

Aravadinou, E., Xypolias, P., Chatzaras, V., Iliopoulos, I. & Gerogiannis, N. (2016): Ductile nappe stacking and refolding in the Cycladic Blueschist Unit: insights from Sifnos Island (south Aegean Sea). – *International Journal of Earth Sciences*, **105** (7): pp. 2075–2096. DOI: 10.1007/s00531-015-1255-2.

Aubouin, J. & Dercourt, J. (1965): Sur la géologie de l'Égée: regard sur la Crète (Grèce). – *Bulletin de la Société Géologique de France, série 7*, **7**: pp. 787–821.

Be'eri-Shlevin, Y., Avigad, D. & Matthews, A. (2009): Granitoid intrusion and high temperature metamorphism in the Asteroussia Unit, Anafi Island (Greece): petrology and geochronology. – *Israel Journal of Earth Sciences*, **58** (1): pp. 13–27. DOI: 10.1560/IJES.58.1.13.

Bonneau, M. (1972a): La nappe métamorphique de l'Asteroussia, lambeau d'affinités pélagoniennes charrié jusque sur la zone de Tripolitza de la Crète moyenne (Grèce). – *Comptes Rendus de l'Académie des Sciences, série D*, **275**: pp. 2303–2306.

Bonneau, M. (1972b): Existence d'un lambeau de cristallin chevauchant sur la série du Pinde en Crète moyenne (Grèce). – *Comptes Rendus de l'Académie des Sciences, série D*, **274**: pp. 2133–2136.

Bonneau, M. (1973): Les différentes «séries ophiolitifères» de la Crète: une mise au point. – *Comptes Rendus de l'Académie des Sciences, série D*, **276**: pp. 1249–1252.

Bonneau, M. (1982): Évolution géodynamique de l'arc égéen depuis le Jurassique supérieur jusqu'au Miocène. – *Bulletin de la Société Géologique de France, série 7*, **24** (2): pp. 229–242.

Bonneau, M. (1984): Correlation of the Hellenide nappes in the south-east Aegean and their tectonic reconstruction. – *Geological Society, London, Special Publications*, **17**: pp. 517–527. DOI: 10.1144/GSL.SP.1984.017.01.38.

Bonneau, M. (1985): *Γεωλογικός χάρτης της Ελλάδος 1:50.000. Φύλλο Μέλαμπες [Geological map of Greece 1:50,000. Melambes sheet]*. – Geological map, Ινστιτούτο γεωλογικών και μεταλλεύτικων έρευνων [Institute of Geology and Mineral Exploration]; Αθήνα [Athens].

Bonneau, M., Angelier, J. & Epting, M. (1977): Réunion extraordinaire de la Société Géologique de France en Crète. – *Bulletin de la Société Géologique de France, série 7*, **19** (1): pp. 87–102. DOI: 10.2113/gssgfbull.S7-XIX.1.87.

Bonneau, M., Beauvais, L. & Middlemiss, F.A. (1974): L'unité de Miamou (Crète - Grèce) et sa macrofaune d'âge Jurassique supérieur (Brachiopodes. Madreporaires). – *Annales de la Société Géologique du Nord*, **94** (2): pp. 71–85.

Bonneau, M. & Fleury, J.-J. (1971): Précisions sur la série d'Ethia (Crète, Grèce) : existence d'un premier flysch mésocrétacé. – *Comptes Rendus de l'Académie des Sciences, série D*, **272**: pp. 1840–1842.

Bonneau, M., Geyssant, J., Kienast, J.-R., Lepvrier, C. & Maluski, H. (1980): Tectonique et métamorphisme haute pression d'âge éocène dans les Hellénides: exemple de l'île de Syros (Cyclades, Grèce). – *Comptes Rendus de l'Académie des Sciences, série D*, **291**: pp. 171–174.

Bonneau, M. & Lys, M. (1978): Sur la présence de Permien fossilifère dans l'unité de Vatos (Crète): sa nature interne et l'ampleur des charriages dans l'arc égéen. – *Comptes Rendus de l'Académie des Sciences, série D*, **287**: pp. 423–426.

Brix, M.R., Thomson, S.N. & Stöckhert, B. (2008): Shallow subduction erosion at a retreating convergent margin – The thermochronometric record of the "Uppermost Unit" on Crete, Greece. – In: Garver, J.I., Montario, M.J. (eds.) *Proceedings from the 11th International Conference on thermochronometry, Anchorage Alaska, Sept. 2008*. p. 42; Anchorage.

Bröcker, M. & Pidgeon, R.T. (2007): Protolith ages of meta-igneous and metatuffaceous rocks from the Cycladic Blueschist Unit, Greece: results of a reconnaissance U-Pb zircon study. – *The Journal of Geology*, **115** (1): pp. 83–98. DOI: 10.1086/509269.

Bulle, F., Bröcker, M., Gärtner, C. & Keasling, A. (2010): Geochemistry and geochronology of HP mélanges from Tinos and Andros, cycladic blueschist belt, Greece. – *Lithos*, **117** (1–4): pp. 61–81. DOI: 10.1016/j.lithos.2010.02.004.

Burkhard, M. (1993): Calcite twins, their geometry, appearance and significance as stress-strain markers and indicators of tectonic regime: a review. – *Journal of Structural Geology*, **15** (3–5): pp. 351–368. DOI: 10.1016/0191-8141(93)90132-T.

Cardozo, N. & Allmendinger, R.W. (2013): Spherical projections with OSXStereonet. – *Computers & Geosciences*, **51**: pp. 193–205. DOI: 10.1016/j.cageo.2012.07.021.

Creutzburg, N. & Seidel, E. (1975): Zum Stand der Geologie des Präneogens auf Kreta. – *Neues Jahrbuch für Geologie und Paläontologie, Abhandlungen*, **149** (3): pp. 363–383.

Dahl, P.S. (1996): The effects of composition on retentivity of argon and oxygen in hornblende and related amphiboles: a field-tested empirical model. – *Geochimica et Cosmochimica Acta*, **60** (19): pp. 3687–3700. DOI: 10.1016/0016-7037(96)00170-6.

Davis, E.N. (1967): Παρουσία γρανιτικών πετρωμάτων εντός του μεταμορφωμένον συστήματος της περιοχης των Αστερουσίων όρέων της Νοτίου Κρήτης [On the occurrence of granitic rocks within the metamorphic system of the Asteroussia area of the island of Crete]. – *Πρακτικά της Ακαδημίας Αθηνών [Praktika tis Akadimias Athinon]*, **42**: pp. 253–270.

Delaloye, M., Economou, C. & Skounakis, S. (1977): Ages radiométrique de quelques roches ophiolitiques de l'îIe de Crète. – In: Kallergis, G. (ed.) *Proceedings of the VI colloquium on the geology of the Aegean region. Athens 1977*. Ινστιτούτο γεωλογικών και μεταλλεύτικων έρευνων [Institute of Geology and Mineral Exploration], pp. 129–135; Αθήνα [Athens].

Dornsiepen, U.F. & Manutsoglu, E. (1994): Zur Gliederung der Phyllit-Decke Kreta und des Peloponnes. – *Zeitschrift der Deutschen Geologischen Gesellschaft*, **145**: pp. 286–304.

Doutsos, T., Pe-Piper, G., Boronkay, K. & Koukouvelas, I.K. (1993): Kinematics of the central Hellenides. – *Tectonics*, **12** (4): pp. 936–953. DOI: 10.1029/93TC00108.

Dürr, S., Seidel, E., Kreuzer, H. & Harre, W. (1978): Témoins d'un métamorphisme d'âge crétacé supérieur dans l'Égéide: datations radiométriques de minéraux provenant de l'île de Nikouriá (Cyclades, Grèce). – *Bulletin de la Société Géologique de France, série 7*, **20** (2): pp. 209–213.

Fassoulas, C. (1998): The structural evolution of central Crete: insight into the tectonic evolution of the south Aegean (Greece). – *Journal of Geodynamics*, **27** (1): pp. 23–43. DOI: 10.1016/S0264-3707(97)00026-4.

Fortuin, A.R. (1977): Stratigraphy and sedimntary history of the Neogene deposits in the Ierapetra region, eastern Crete. – *GUA Papers of Geology*, **8**: pp. 1–164.

Fynn, G.W. & Powell, W.J.A. (1979): *The cutting and polishing of electro-optic materials*. – Wiley, 215 p.; New York.

Gerdes, A. & Zeh, A. (2009): Zircon formation versus zircon alteration — New insights from combined U–Pb and Lu–Hf in-situ LA-ICP-MS analyses, and consequences for the interpretation of Archean zircon from the central zone of the Limpopo Belt. – *Chemical Geology*, **261** (3–4): pp. 230–243. DOI: 10.1016/j.chemgeo.2008.03.005.

Gessner, K., Ring, U. & Güngör, T. (2011): *Field guide to Samos and the Menderes Massif: along-strike variations in the Mediterranean Tethyan Orogen*. – Geological Society of America, 52 p.; Boulder.

Goscombe, B.D., Passchier, C.W. & Hand, M. (2004): Boudinage classification: end-member boudin types and modified boudin structures. – *Journal of Structural Geology*, **26** (4): pp. 739–763. DOI: 10.1016/j.jsg.2003.08.015.

Hall, R., Audley-Charles, M.G. & Carter, D.J. (1984): The significance of Crete for the evolution of the Eastern Mediterranean. – *Geological Society, London, Special Publications*, **17** (1): pp. 499–516. DOI: 10.1144/GSL.SP.1984.017.01.37.

Harrison, T.M. (1981): Diffusion of ^{40}Ar in hornblende. – *Contributions to Mineralogy and Petrology*, **78** (3): pp. 324–331. DOI: 10.1007/BF00398927.

Harrison, T.M., Célérier, J., Aikman, A.B., Hermann, J. & Heizler, M.T. (2009): Diffusion of ^{40Ar} in muscovite. – *Geochimica et Cosmochimica Acta*, **73** (4): pp. 1039–1051. DOI: 10.1016/j.gca.2008.09.038.

Harrison, T.M., Duncan, I. & McDougall, I. (1985): Diffusion of ^{40}Ar in biotite: temperature, pressure and compositional effects. – *Geochimica et Cosmochimica Acta*, **49** (11): pp. 2461–2468. DOI: 10.1016/0016-7037(85)90246-7.

Hinsken, T., Bröcker, M., Berndt, J. & Gärtner, C. (2016): Maximum sedimentation ages and provenance of metasedimentary rocks from Tinos Island, Cycladic blueschist belt, Greece. – *International Journal of Earth Sciences*, **105** (7): pp. 1923–1940. DOI: 10.1007/s00531-015-1258-z.

Holland, T. & Blundy, J. (1994): Non-ideal interactions in calcic amphiboles and their bearing on amphibole-plagioclase thermometry. – *Contributions to Mineralogy and Petrology*, **116** (4): pp. 433–447. DOI: 10.1007/BF00310910.

Hoskin, P.W.O. & Schaltegger, U. (2003): The composition of zircon and igneous and metamorphic petrogenesis. – *Reviews in Mineralogy and Geochemistry*, **53** (1): pp. 27–62. DOI: 10.2113/0530027.

Jackson, S.E., Pearson, N.J., Griffin, W.L. & Belousova, E.A. (2004): The application of laser ablation-inductively coupled plasma-mass spectrometry to in situ U-Pb zircon geochronology. – *Chemical Geology*, **211** (1–2): pp. 47–69. DOI: 10.1016/j.chemgeo.2004.06.017.

Klein, T., Craddock, J.P. & Zulauf, G. (2013): Constraints on the geodynamical evolution of Crete: insights from illite crystallinity, Raman spectroscopy and calcite twinning above and below the "Cretan detachment." – *International Journal of Earth Sciences*, **102** (1): pp. 139–182. DOI: 10.1007/s00531-012-0781-4.

Kneuker, T., Dörr, W., Petschick, R. & Zulauf, G. (2015): Upper crustal emplacement and deformation of granitoids inside the Uppermost Unit of the Cretan nappe stack: constraints from U-Pb zircon dating, microfabrics and paleostress analyses. – *International Journal of Earth Sciences*, **104** (2): pp. 351–367. DOI: 10.1007/s00531-014-1088-4.

Koepke, J. & Seidel, E. (1984): Oberkretazisches Kristallin an der Basis von Ophiolithen der Südägäis: Charakterisierung der Metamorphose-Fazies. – *Tschermaks Mineralogische und Petrographische Mitteilungen*, **33** (4): pp. 263–286. DOI: 10.1007/BF01082673.

Koepke, J., Seidel, E. & Kreuzer, H. (2002): Ophiolites on the southern Aegean islands Crete, Karpathos and Rhodes: composition, geochronology and position within the ophiolite belts of the Eastern Mediterranean. – *Lithos*, **65** (1–2): pp. 183–203. DOI: 10.1016/S0024-4937(02)00165-2.

Koutsovitis, P., Soukis, K.I. & Lozios, S. (2012): Implications for the Upper Cycladic Unit: petrological, mineralogical and structural study of intrusive rocks from the Late-Cretaceous volcanic-arc in Anafi Island, Cyclades, Greece. *EGU General Assembly Conference Abstracts*. p. 13303; Wien.

Krahl, J., Herbart, H. & Katzenberger, S. (1982): Subdivision of the allochthonous "ophiolites"-bearing formation upon the Pindos Group, southwestern part of central Crete, Greece. *International Symposium on the Hellenic Arc and Trench (H.E.A.T.). April 8–10. 1981, Athens. Proceedings. Volume 1*. Εθνικό Μετσόβιο Πολυτεχνείο [Ethnikó Metsóvio Polytechneío], pp. 324–341; Αθήνα [Athens].

Langosch, A. (1999): *Petrologie der plutonischen Gesteine im oberkretazischen Hochtemperaturkrisallin der Insel Kreta*. – Tectum, 201 p.; Marburg

Langosch, A., Seidel, E., Stosch, H.-G. & Okrusch, M. (2000): Intrusive rocks in the ophiolitic mélange of Crete – Witnesses to a Late Cretaceous thermal event of enigmatic geological position. – *Contributions to Mineralogy and Petrology*, **139** (3): pp. 339–355. DOI: 10.1007/s004100000136.

Le Maitre, R.W., Streckeisen, A., Zanettin, B., Le Bas, M.J., Bonin, B. & Bateman, P. (2002): *Igneous rocks: a classification and glossary of terms*. – Cambridge University Press, 252 p.; Cambridge.

Leake, B.E. (1978): Nomenclature of amphiboles. – *American Mineralogist*, **63** (11–12): pp. 1023–1052.

Lee, J.K.W., Williams, I.S. & Ellis, D.J. (1997): Pb, U and Th diffusion in natural zircon. – *Letters to Nature*, **390**: pp. 159–162. DOI: 10.1038/36554.

Lippolt, H.J. & Baranyi, I. (1976): Oberkretazische Biotit- und Gesteinsalter aus Kreta. – *Neues Jahrbuch für Geologie und Paläontologie, Monatshefte*, **7**: pp. 405–414.

Lister, G. & Baldwin, S.L. (1996): Modelling the effect of arbitrary P–T–t histories on Ar diffusion in minerals using the MacArgon program for the Apple Macintosh. – *Tectonophysics*, **253**: pp. 83–109.

Lister, G.S. & Dornsiepen, U.F. (1982): Fabric transitions in the Saxony granulite terrain. – *Journal of Structural Geology*, **4** (1): pp. 81–92. DOI: 10.1016/0191-8141(82)90009-8.

Ludwig, K.R. (1980): Calculation of uncertainties of U-Pb isotope data. – *Earth and Planetary Science Letters*, **46** (2): pp. 212–220. DOI: 10.1016/0012-821X(80)90007-2.

Ludwig, K.R. (2012): User's manual for Isoplot 3.75. A geochronological toolkit for Microsoft Excel. – *Berkeley Geochronology Center Special Publication*, **5**: pp. 1–75.

Ludwig, K.R. & Mundil, R. (2002): Extracting reliable U-Pb ages and errors from complex populations of zircons from Phanerozoic tuffs. – *Geochimica et Cosmochimica Acta*, **66**: pp. 463. DOI: 10.1016/S0016-7037(02)01011-6.

Martha, S.O., Dörr, W., Gerdes, A., Petschick, R., Schastok, J., Xypolias, P. & Zulauf, G. (2016): New structural and U–Pb zircon data from Anafi crystalline basement (Cyclades, Greece): constraints on the evolution of a Late Cretaceous magmatic arc in the Internal Hellenides. – *International Journal of Earth Sciences*, **105** (7): pp. 2031–2060. DOI: 10.1007/s00531-016-1346-8.

Meinhold, G. & Frei, D. (2008): Detrital zircon ages from the islands of Inousses and Psara, Aegean Sea, Greece: constraints on depositional age and provenance. – *Geological Magazine*, **145** (6): pp. 886–891. DOI: 10.1017/S0016756808005505.

Meulenkamp, J.E. (1969): Stratigraphy of Neogene deposits in the Rethymnon Province, Crete, with special reference to the phylogeny of uniserial *Uvigerina* from the Mediterranean. – *Utrecht Micropaleontological Bulletins*, **2**: pp. 1–168.

Middleton, A.P., Freestone, I.C. & Leese, M.N. (1985): Textural analysis of ceramic thin sections: Evaluation of grain sampling procedures. – *Archaeometry*, **27** (1): pp. 64–74. DOI: 10.1111/j.1475-4754.1985.tb00348.x.

Palamakumbura, R.N., Robertson, A.H.F. & Dixon, J.E. (2013): Geochemical, sedimentary and micropaleontological evidence for a Late Maastrichtian oceanic seamount within the Pindos ocean (Arvi Unit, S Crete, Greece). – *Tectonophysics*, **595**–**596**: pp. 250–262. DOI: 10.1016/j.tecto.2012.04.019.

Passchier, C.W. & Trouw, R.A.J. (2005): *Microtectonics*. – Springer, 366 p.; Berlin, Heidelberg.

Patzak, M., Okrusch, M. & Kreuzer, H. (1994): The Akrotiri unit on the island of Tinos, Cyclades, Greece: witness to a lost terrane of Late Cretaceous age. – *Neues Jahrbuch für Geologie und Paläontologie, Abhandlungen*, **194**: pp. 211–252.

van der Plas, L. & Tobi, A.C. (1965): A chart for judging the reliability of point counting results. – *American Journal of Science*, **263** (1): pp. 87–90. DOI: 10.2475/ajs.263.1.87.

Plyusnina, L.P. (1982): Geothermometry and geobarometry of plagioclase-hornblende bearing assemblages. – *Contributions to Mineralogy and Petrology*, **80** (2): pp. 140–146. DOI: 10.1007/BF00374891.

Reinecke, T., Altherr, R., Hartung, B., Hatzipanagiotou, K., Kreuzer, H., Harre, W., Klein, H., Keller, J., Geenen, E. & Böger, H. (1982): Remnants of a Late Cretaceous high temperature belt on the island of Anafi (Cyclades, Greece). – *Neues Jahrbuch für Mineralogie, Abhandlungen*, **145** (2): pp. 157–182.

Ridley, J. (1982): Arcuate lineation trends in a deep level, ductile thrust belt, Syros, Greece. – *Tectonophysics*, **88** (3–4): pp. 347–360. DOI: 10.1016/0040-1951(82)90246-3.

Ring, U. & Layer, P.W. (2003): High-pressure metamorphism in the Aegean, eastern Mediterranean: underplating and exhumation from the Late Cretaceous until the Miocene to Recent above the retreating Hellenic subduction zone. – *Tectonics*, **22** (3): pp. n/a-n/a. DOI: 10.1029/2001TC001350.

Robert, U. & Bonneau, M. (1982): Les basalts des nappes du Pinde et d'Arvi et leur signification dans l'évolution géodynamique de la Méditerrannée orientale. – *Annales Géologiques des Pays Helléniques*, **31**: pp. 373–408.

Robertson, A.H.F., Dixon, J.E., Brown, S., Collins, A., Morris, A.P., Pickett, E., Sharp, I. & Ustaömer, T. (1996): Alternative tectonic models for the Late Palaeozoic-Early Tertiary development of Tethys in the Eastern Mediterranean region. – *Geological Society, London, Special Publications*, **105** (1): pp. 239–263. DOI: 10.1144/GSL.SP.1996.105.01.22.

Schliestedt, M. & Seidel, E. (1976): Petrologische Untersuchung des Metamorphikums der Insel Gavdos, Griechenland. – *Fortschritte der Mineralogie*, **54** (Beiheft 1): pp. 79–81.

Schmidt, N.-H. & Olesen, N.O. (1989): Computer-aided determination of crystal-lattice orientation from electron-channeling patterns in the SEM. – *The Canadian Mineralogist*, **27** (1): pp. 15–22.

Seidel, E., Kreuzer, H. & Harre, W. (1982): A Late Oligocene/Early Miocene high pressure belt in the external Hellenides. – *Geologisches Jahrbuch, Reihe E*, **23**: pp. 165–206.

Seidel, E., Okrusch, M., Kreuzer, H., Raschka, H. & Harre, W. (1976): Eo-Alpine metamorphism in the Uppermost Unit of the Cretan nappe system – petrology and geochronology. Part 1. The Léndas area (Asteroúsia Mountains). – *Contributions to Mineralogy and Petrology*, **57** (3): pp. 259–275.

Seidel, E., Okrusch, M., Kreuzer, H., Raschka, H. & Harre, W. (1981): Eo-Alpine metamorphism in the Uppermost Unit of the Cretan nappe system – petrology and geochronology. Part 2. Synopsis of high-temperature metamorphics and associated ophiolites. – *Contributions to Mineralogy and Petrology*, **76** (3): pp. 351–361. DOI: 10.1007/BF00375462.

Seidel, E., Schliestedt, M., Kreuzer, H. & Harre, W. (1977): Metamorphic rocks of Late Jurassic age as components of the ophiolitic mélange on Gavdos and Crete (Greece). – *Geologisches Jahrbuch, Reihe B*, **28**: pp. 3–21.

Sherlock, S., Kelley, S., Inger, S., Harris, N. & Okay, A. (1999): ^{40}Ar-^{39}Ar and Rb-Sr geochronology of high-pressure metamorphism and exhumation history of the Tavsanli Zone, NW Turkey. – *Contributions to Mineralogy and Petrology*, **137** (1–2): pp. 46–58. DOI: 10.1007/PL00013777.

Stipp, M., Stünitz, H., Heilbronner, R. & Schmid, S.M. (2002): The eastern Tonale fault zone: a "natural laboratory" for crystal plastic deformation of quartz over a temperature range from 250 to 700°C. – *Journal of Structural Geology*, **24** (12): pp. 1861–1884. DOI: 10.1016/S0191-8141(02)00035-4.

Streckeisen, A. (1974): Classification and nomenclature of plutonic rocks recommendations of the IUGS subcommission on the systematics of igneous rocks. – *Geologische Rundschau*, **63** (2): pp. 773–786. DOI: 10.1007/BF01820841.

Tagami, T. & Dumitru, T.A. (1996): Provenance and thermal history of the Franciscan accretionary complex: constraints from zircon fission track thermochronology. – *Journal of Geophysical Research: Solid Earth*, **101** (B5): pp. 353–364. DOI: 10.1029/96JB00407.

Thomson, S.N., Stöckhert, B. & Brix, M.R. (1999): Miocene high-pressure metamorphic rocks of Crete, Greece: rapid exhumation by buoyant escape. – *Geological Society, London, Special Publications*, **154** (1): pp. 87–107. DOI: 10.1144/GSL.SP.1999.154.01.04.

Thomson, S.N., Stöckhert, B., Rauche, H. & Brix, M.R. (1998): Apatite fission-track thermochronology of the Uppermost Tectonic Unit of Crete, Greece: implications for the post-Eocene tectonic evolution of the Hellenic Subduction System. – In: van den Haute, P., de Corte, F. (eds.) *Advances in Fission-Track Geochronology*. – Solid Earth Sciences Library, **10**: pp. 187–205.

Thorbecke, G. (1987): *Die Zonengliederung der ägäischen Helleniden und westlichen Tauriden*. – Gesellschaft der Geologie- und Bergbaustudenten in Österreich, 161 p.; Wien.

Tomaschek, F., Keiter, M., Kennedy, A.K. & Ballhaus, C. (2008): Pre-Alpine basement within the northern Cycladic Blueschist Unit on Syros Island, Greece. – *Zeitschrift der Deutschen Gesellschaft für Geowissenschaften*, **159** (3): pp. 521–531. DOI: 10.1127/1860-1804/2008/0159-0521.

Tortorici, L., Catalano, S., Cirrincione, R. & Tortorici, G. (2012): The Cretan ophiolite-bearing mélange (Greece): a remnant of Alpine accretionary wedge. – *Tectonophysics*, **568**–**569**: pp. 320–334. DOI: 10.1016/j.tecto.2011.08.022.

Vandenberg, L.C. & Lister, G.S. (1996): Structural analysis of basement tectonites from the Aegean metamorphic core complex of Ios, Cyclades, Greece. – *Journal of Structural Geology*, **18** (12): pp. 1437–1454. DOI: 10.1016/S0191-8141(96)00068-5.

Vavra, G., Schmid, R. & Gebauer, D. (1999): Internal morphology, habit and U-Th-Pb microanalysis of amphibolite-to-granulite facies zircons: geochronology of the Ivrea Zone (Southern Alps). – *Contributions to Mineralogy and Petrology*, **134** (4): pp. 380–404. DOI: 10.1007/s004100050492.

Vernon, R.H. & Flood, R.H. (1988): Contrasting deformation of S- and I-type granitoids in the Lachlan Fold Belt, eastern Australia. – *Tectonophysics*, **147** (1–2): pp. 127–143. DOI: 10.1016/0040-1951(88)90152-7.

Wachendorf, H., Gralla, P., Koll, J. & Schulze, I. (1980): Geodynamik des mittelkretischen Deckenstapels (nördliches Dikti-Gebirge). – *Geotektonische Forschungen*, **59**: pp. 1–72.

Wiesenbach, B. (2014): *Kartierung und strukturgeologische Untersuchung des Asteroussia-Kristallins NW von Melambes (Westteil), Kreta*. – Master thesis, Goethe-Universität Frankfurt am Main, 105 p. (unpubl.); Frankfurt am Main.

Wijbrans, J.R. & McDougall, I. (1986): $^{40}Ar/^{39}Ar$ dating of white micas from an Alpine high-pressure metamorphic belt on Naxos (Greece): the resetting of the argon isotopic system. – *Contributions to Mineralogy and Petrology*, **93** (2): pp. 187–194. DOI: 10.1007/BF00371320.

Xypolias, P., Iliopoulos, I., Chatzaras, V. & Kokkalas, S. (2012): Subduction- and exhumation-related structures in the Cycladic Blueschists: insights from south Evia Island (Aegean region, Greece). – *Tectonics*, **31** (2): pp. n/a-n/a. DOI: 10.1029/2011TC002946.

Zlatkin, O., Avigad, D. & Gerdes, A. (2014): Peri-Amazonian provenance of the Proto-Pelagonian basement (Greece), from zircon U–Pb geochronology and Lu–Hf isotopic geochemistry. – *Lithos*, **184**–**187**: pp. 379–392. DOI: 10.1016/j.lithos.2013.11.010.

Zulauf, G., Klein, T., Kowalczyk, G., Krahl, J. & Romano, S.S. (2008): The Mirsini Syncline of eastern Crete, Greece: a key area for understanding pre-Alpine and Alpine orogeny in the eastern Mediterranean. – *Zeitschrift der Deutschen Gesellschaft für Geowissenschaften*, **159** (3): pp. 399–414. DOI: 10.1127/1860-1804/2008/0159-0399.

4 The Uppermost Unit south of the Dikti Mountains, eastern Crete: constraints on the tectonometamorphic evolution of the Internal Hellenides

Silviu O. Martha[1*], Gernold Zulauf[1], Wolfgang Dörr[1], Jannes J. Binck[1], Patrick M. Nowara[1], Paraskevas Xypolias[2]

[1]Institut für Geowissenschaften, Goethe-Universität Frankfurt, Altenhöferallee 1, 60438 Frankfurt am Main, Germany. E-mail: s.martha@em.uni-frankfurt.de, g.zulauf@em.uni-frankfurt.de, w.doerr@em.uni-frankfurt.de, jannes.binck@web.de, nowa90@gmx.de

[2]Department of Geology, University of Patras, 26500, Patras, Greece. E-mail: p.xypolias@upatras.gr

Keywords: Crete • Uppermost Unit • U-Pb dating • Electron microprobe • Cretan nappe pile • Hellenides • Eastern Mediterranean

Submitted to: *Geological Magazine*. Manuscript ID: GEO-17-1753.

4.1 Abstract

New structural, petrographic and geochronological data from the Uppermost Unit south of the Dikti Mountains (Crete) allow constraining the pre-Eocene tectonometamorphic evolution of the Internal Hellenides in the southern Aegean. New mapping of this area suggests that the Uppermost Unit can be subdivided into (from bottom to top): Arvi Unit, Theodorii Greenschist, and Asterousia Crystalline Complex (ACC)-type rocks. The ACC-type rocks bear evidence for at least three ductile deformation phases, the oldest of which (D_1) is preserved as internal foliation in garnet porphyroblasts. D_2 shear-sense indicators, related to the main pervasive foliation, reveal top-to-the SE kinematics under amphibolite facies conditions. After significant post-D_2 exhumation, chiastolite hornfels developed in the contact aureole of a shallowly intruded (< 10 km depth) pluton at 74 ± 2 Ma (LA-ICP-MS U-Pb age dating on metamorphic grown zircon). This age is in line with published intrusion ages of ACC-type intrusions on Crete and on Anafi. The S_2-foliation of the ACC-type rocks was reactivated during the late phase of contact metamorphism by D_3 top-to-the SE shearing. Latest Cretaceous cross-mica with low Si content post-dates this shearing event. During the Middle Palaeocene, the ACC was thrust on top of the Theodorii Greenschist. This thrusting event as well as subsequent brittle thrusting of the greenschists and the ACC-type rocks on top of the very low-grade metamorphic Arvi Unit was still accommodated by top-to-the SE kinematics. All these thrusting events are related to the Eo-Alpine convergent movements and coeval slab roll-back along the northern margin of the Neotethys.

4.2 Introduction

In contrast to the well-constrained Eocene to Recent geodynamic evolution of the External Hellenides (e.g. Klein et al. 2013), the pre-Eocene early Alpine evolution of the Internal Hellenides is still poorly understood. The Uppermost Unit of the Cretan nappe pile is a key in understanding the early Alpine evolution of the Hellenides since this unit escaped Oligocene to Miocene subduction as well as related deformation and metamorphism that affected most of the underlying nappes (Seidel et al. 1982). The Uppermost Unit is exposed in central and eastern Crete, on Gavdos and Chrysi as well as on several Cycladic islands (e.g. Bonneau 1972; Seidel et al. 1976; Dürr et al. 1978). It consists of several subunits differing in grade and timing of metamorphism.

Amphibolite facies rocks (P = 400–500 MPa and $T_{max} \approx 700$ °C; Seidel et al. 1976, 1981) that are intruded by Late Cretaceous granitoids (Kneuker et al. 2015; Martha et al. 2016, 2017) are usually referred to as the Asterousia Crystalline Complex (ACC; Bonneau 1972). The ACC occupies the top of the Cretan nappe pile and is usually correlated with the Pelagonian domain (e.g. Aubouin & Dercourt 1965; Bonneau 1972). Maastrichtian to Danian K-Ar hornblende and biotite cooling ages of metamorphic and intrusive rocks (Baranyi et al. 1975; Lippolt & Baranyi 1976; Seidel et al. 1976,

1981; Dürr et al. 1978; Reinecke et al. 1982; Koepke & Seidel 1984; Altherr et al. 1994; Langosch et al. 2000) indicate collective post-intrusive cooling. Thus, amphibolite facies metamorphism of the country rocks should pre-date middle to late Campanian intrusions (Martha et al. 2017). The ACC has been thrust on top of greenschist facies rocks that have been correlated with the northern margin of the Pindos realm (Martha et al. 2017). Other tectonometamorphic nappes ascribed to the Uppermost Unit include the prehnite-pumpellyite facies Arvi Unit that might represent a Maastrichtian seamount at the northern margin of the Pindos realm (Palamakumbura et al. 2013).

In the present study, we examined the Uppermost Unit south of the Dikti Mountains in the areas of Pefkos, Kalami and Sykologos (Viannos Municipality, eastern Crete). We present (1) a new geological map of the study area; (2) kinematic and microfabric data from the different subunits of the Uppermost Unit; (3) P-T constraints for greenschist and chiastolite hornfels; and (4) U-Pb zircon data, which reflect the age of contact metamorphism of a non-exposed pluton. The new results, combined with published radiometric ages, shed light on the Late Cretaceous to Eocene tectonometamorphic evolution of the Hellenides in the southern Aegean.

4.3 Geological setting

4.3.1 The Uppermost Unit of the Cretan nappe pile

In the study area (Fig. 4.1), the Tripolitsa, Pindos and Uppermost units of the Cretan nappe pile are exposed (Creutzburg & Papastamatiou 1969; Creutzburg et al. 1977; Vidakis 1993; Bonneau & Vidakis 2002). The Triassic to Oligocene shallow-water carbonates and flysch sediments of the Tripolitsa Unit are ascribed to the lower nappe system of the Cretan nappe pile that was affected by Late Oligocene to Early Miocene subduction-related metamorphism (Seidel et al. 1982; Feldhoff et al. 1991; Klein et al. 2013). The non-metamorphic Jurassic to Eocene deep-water sediments of the Pindos Unit and the low- to high-grade metamorphic rocks of the variegated Uppermost Unit belong to the upper Cretan nappe system. Fission-track data revealed that the upper Cretan nappe system should have been situated at brittle crustal levels since at least the Latest Eocene or Earliest Oligocene (Thomson et al. 1999), thus escaping Oligocene to Miocene tectonometamorphic events that have affected the lower nappe system.

The Uppermost Unit consists of several subunits, which correspond to different tectonometamorphic nappes. From bottom to top, it consists of:

(a) Very low-grade metamorphic rocks (Arvi, Miamou, Spili and Vatos units), the origin of which is unclear and controversially discussed in literature.

(b) Low grade metamorphic rocks (Kalypso, Preveli and Greenschist units) that have been correlated with the northern margin of the Pindos Ocean (Bonneau et al. 1977; Krahl et al. 1982; Robert &

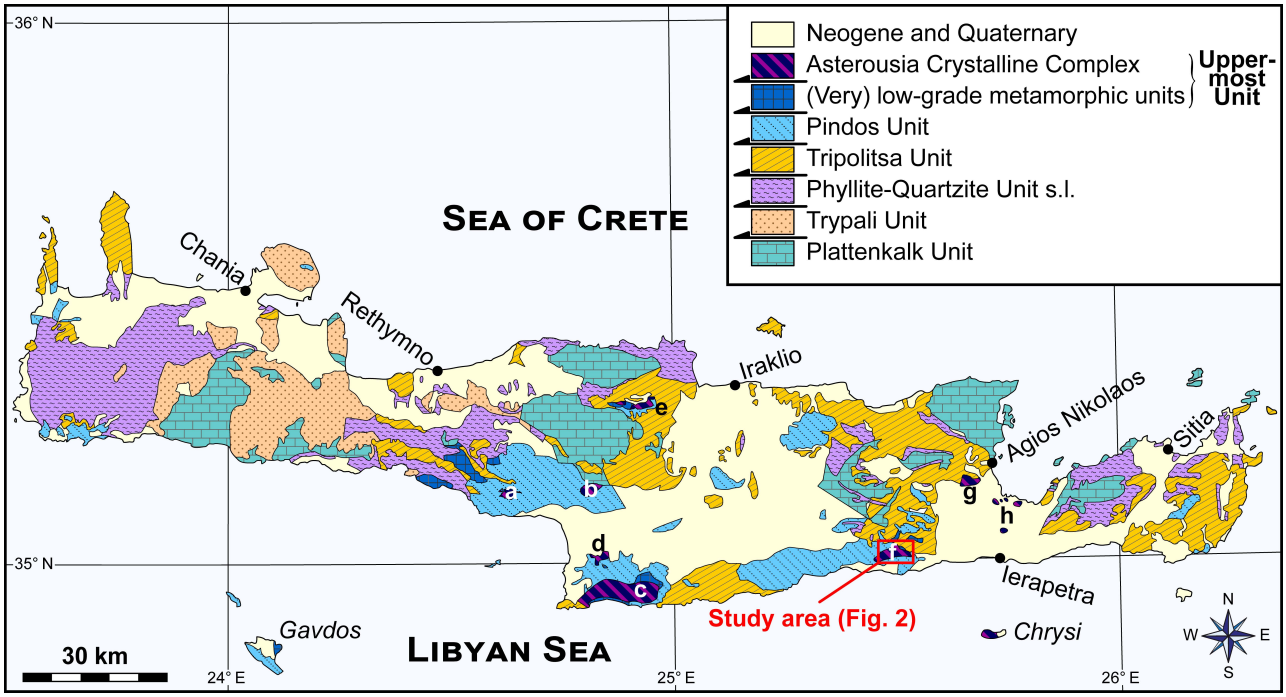

Fig. 4.1 Geological map of Crete (modified after Creutzburg & Seidel 1975). Exposures of the Asterousia Crystalline Complex on Crete: (a) west of Melambes; (b) between Kamares and Magarikari; (c) western Asterousia Mountains between Kali Limenes and Lendas; (d) between Petrokefali and Kouses; (e) north of Anogia and Gonies; (f) south of the Dikti Mountains (study area); (g) Kritsa; (h) between Kalo Chorio and Pachia Ammos and near Stavros (northern Ierapetra Graben). A detailed geological map of the study area is shown in Fig. 4.2.

Bonneau 1982; Bonneau 1984; Fassoulas 1998; Tortorici et al. 2012; Palamakumbura et al. 2013; Martha et al. 2017). The presence of an additional low-grade metamorphic *nappe des serpentines* within the Uppermost Unit is controversial (e.g. Bonneau 1972; Seidel et al. 1981; Krahl et al. 1982).

(c) High-grade metamorphic rocks and (meta)granitoids, i.e. the Asterousia Crystalline Complex (ACC; Bonneau 1972). Rocks of the ACC are exposed in central and eastern Crete as well as on the Cycladic islands of Anafi, Donousa, Gramvonisi, Ikaria, Makra, Nikouria, Syros and Tinos (Dürr et al. 1978; Altherr et al. 1980, 1994; Bonneau et al. 1980; Reinecke et al. 1982; Dürr 1985; Thorbecke 1987; Patzak et al. 1994).

Conditions of the metamorphic overprint of the ACC, i.e. orthoamphibolite and metasedimentary rocks (calcsilicate rock, paraamphibolite, paragneiss, quartzite and micaschist), have been constrained at P = 400–500 MPa and T_{max} = 700 °C (Seidel et al. 1981). Slices of serpentinite have been incorporated into the metasedimentary rocks prior to amphibolite facies metamorphism (Bonneau 1973; Reinecke et al. 1982; Thorbecke 1987; Be'eri-Shlevin et al. 2009), while granitoids intruded the metasedimentary succession of the ACC during the middle to late Campanian (Kneuker et al. 2015; Martha et al. 2016, 2017). Amphibolite facies metamorphism is associated with pre-intrusive SE-directed shearing and stacking at the southern margin of the Pelagonian-Lycian domain during collision and subduction of the Pindos realm (Tortorici et al. 2012; Martha et al. 2017). Ongoing subduction

caused mantle melting and was followed by continuous intrusion of granitoids in a magmatic arc setting along the southern margin of the Pelagonian-Lycian domain. K-Ar biotite and hornblende ages of Cretan Asterousia-type (meta)granitoids and metamorphic rocks range from 76–66 Ma (Seidel et al. 1976, 1981; Reinecke et al. 1982; Langosch et al. 2000) and indicate mutual cooling during the Maastrichtian. Pervasive top-to-the SE mylonitic shearing locally affected the ACC during the initial cooling phase (Martha et al. 2017). Pelagic carbonates have been deposited along the northern margin of the Pindos Ocean during the late Maastrichtian (Robert & Bonneau 1982). Geochemical and sedimentary evidence of pillow basalts in association with these carbonates suggest the existence of a seamount (the 'Arvi Seamount') in the Pindos realm (Palamakumbura et al. 2013). Subduction-related metamorphism affected the northern margin of the Pindos realm during the Palaeocene. K-Ar actinolite ages (Reinecke et al. 1982) reveal thrusting of the ACC on top of greenschist facies rocks of the northern Pindos margin during the Middle to Late Palaeocene. Continuous shortening and steady uplift resulted in brittle thrusting of both the ACC-type rocks and the greenschists on top of the non-metamorphic flysch of the Pindos Unit until the Late Eocene (Martha et al. 2017).

4.3.2 The Uppermost Unit south of the Dikti Mountains

The first geological map of the study area was published by Creutzburg & Papastamatiou (1969). These authors erroneously ascribed the metamorphic rocks of the Uppermost Unit to the Late Eocene Tripolitsa flysch (assigned by subsequent authors to the Pindos Unit). Serpentinite bodies in the area were regarded as components of the Ethia Series of the Pindos Unit. Further geological maps of the study area have been produced at a scale of 1:50,000 by Vidakis (1993) and Bonneau & Vidakis (2002). Concerning the Uppermost Unit, however, these maps are less detailed than the general geological map of Crete at a scale of 1:200,000 published by Creutzburg et al. (1977). Previous works in the study area (Creutzburg & Seidel 1975; Seidel et al. 1981; Koepke & Seidel 1984) have reported amphibolite facies calcsilicate rock, marble, andalusite-bearing metapelite, micaschist and orthoamphibolite. Orthoamphibolite has chemical affinities to olivine tholeiites (Seidel et al. 1981) and compares well with Asterousia-type orthoamphibolite from other exposures on Crete and on Anafi (Seidel et al. 1981; Reinecke et al. 1982). Furthermore, K-Ar hornblende ages from orthoamphibolite (66.3 ± 2.9 Ma and 68.6 ± 1.9 Ma) and K-Ar biotite ages from sillimanite-bearing micaschist (68.3 ± 0.9 Ma and 68.8 ± 0.9 Ma) confirm a correlation with the ACC (Seidel et al. 1976, 1981).

In the study area, the amphibolite facies rocks are associated with serpentinite cut by gabbroic dykes (Bonneau 1972; Koepke et al. 2002). Serpentinite from the Pefkos area consists of antigorite and relics of spinel lherzolite (Koepke et al. 2002). K-Ar hornblende cooling ages from metagabbro dykes cutting the lherzolites range from 91.9 ± 3.5 Ma to 97.1 ± 4.1 Ma (Cenomanian to Turonian) (Delaloye et al.

1977; Koepke et al. 2002). However, K-Ar hornblende ages from gabbroic dykes cutting serpentinite at other places of the Uppermost Unit on Crete yielded mostly Upper Jurassic cooling ages (Delaloye et al. 1977; Koepke et al. 2002).

The Arvi Unit of the study area and adjacent domains (areas of Kato Symi and Kalami) consists of reddish pelagic limestone, terrigenous turbidites, pillow basalt and dolerite. Mineral parageneses from the pillow basalts point to prehnite-pumpellyite facies overprint (Robert & Bonneau 1982). Based on findings of planktonic foraminifera in the Arvi limestone (Tataris 1964), the deposition age has been constrained as Maastrichtian whilst basaltic volcanism is probably of the same age (Robert & Bonneau 1982). Geochemical data (X-ray fluorescence analyses) from the pillow basalts revealed ocean island basalt (OIB) spectra (Palamakumbura et al. 2013). Terrigenous detritus within sandstone include fragments of quartzite and serpentinite and are possibly derived from the ACC (Palamakumbura et al. 2013). Thus, the Arvi Unit has been inferred as the remnant of a Maastrichtian seamount at the northern margin of the Pindos Ocean later accreted to the southern active margin of the Pelagonian domain (Palamakumbura et al. 2013).

4.4 Methods

4.4.1 Sampling and petrographic analyses

Geological mapping was conducted using topographic maps at a scale of 1:5,000 obtained from the Hellenic Military Geographical Service in Athens. Statistical analyses of structural data were carried out using the open source software Stereonet 9.2.0 applying the algorithms described in Allmendinger et al. (2012) and Cardozo & Allmendinger (2013).

Thin sections of oriented samples were analysed using a petrographic microscope focusing on mineral content and deformation microfabrics. Thin sections of oriented samples were cut parallel to the stretching lineation and normal to the foliation. Selected samples were additionally investigated using X-ray powder diffraction analysis (XRD). The samples were powdered using a disc mill and about 1 g per sample was measured using a PANalytical X'Pert Pro diffractometer. Data evaluation was performed using the software X'pert HighScore Plus.

4.4.2 X-ray microtomography

One sample of chiastolite hornfels (PKS23) was studied using a Phoenix nanotom s X-ray microtomograph (micro-CT) equipped with an XS 180 NF tube and a Hamamatsu detector at the Goethe-University in Frankfurt. The sample was fixed into a rotating specimen holder between the X-ray source (tungsten filament and beryllium target) and the detector. Scan parameters for CT imaging were: voltage = 170 kV; current = 30 µA; scan time = 326 minutes; raw images = 2400 projections;

original size = 2284 × 1516 × 2303; resolution = 19.0 µm. The resolution was chosen after thin section analysis and determination of the size of microstructures in the sample in order to obtain a reasonable balance between richness of detail and size of the generated dataset.

The 3D volumetric data were examined and visualized using the softwares ImageJ (https://imagej.net/), MeshLab v. 1.3.2 (http://meshlab.sourceforge.net), Amira 5.4.5 and Smoooth. A cube section containing two chiastolite grains, one of which with a well-developed pressure shadow, was cropped from the CT data using ImageJ and was used for further processing to obtain a 3D model. Subsequent to data processing, image segmentation was performed using Smoooth and applying the thresholding method. We distinguished between biotite, chiastolite and graphite, as other phases could not be distinguished in the dataset. 3D models for biotite, chiastolite and graphite were produced using the marching cubes method. Visualisation of the 3D models was performed with MeshLab.

4.4.3 Electron microprobe analysis

Two samples of greenschist (samples PKS11 and PKS12) and two samples of chiastolite hornfels (samples PKS23 and PKS24) were selected for quantitative mineral analysis using the electron microprobe (EMP) analyser JEOL JXA-8900 at Goethe-University Frankfurt. Sample preparation followed the same procedures as described in Martha et al. (2017). Twelve major elements were measured simultaneously using a wavelength dispersive spectrometer and reported as oxides (SiO_2, TiO_2, Al_2O_3, Cr_2O_3, FeO, MnO, MgO, CaO, NiO, Na_2O, K_2O, P_2O_5). Analysis parameters were 15 kV and 20 nA for greenschist samples and 15 kV but 12 nA for chiastolite hornfels samples. The spot size was 3 µm. Most amphibole grains were measured one-by-one and with a spot size of 1 µm and a reduced current of 12 nA due to their small grain size. Peak integration times were 20 s (Na), 30 s (K, Mn, Ca, P and Ni), 40 s (Al, Ti, Si, Mg and Cr) and 60 s (Fe), while the background was measured at integration times ranging from 15–40 s. Several standards ($CaSiO_3$, Al_2O_3, Mg_2SiO_4, Fe_2SiO_4, $KTiOPO_4$) were analysed at the beginning and at the end of the analytical session under the same conditions to verify the accuracy of our measurements. Calculation of the structural formulae was conducted using the worksheets of Andy Tindle and the Carleton College available online at http://www.open.ac.uk/earth-research/tindle/AGTHome.html and http://serc.carleton.edu/research_education/equilibria/mineralformulaerecalculation.html.

4.4.4 LA-ICP-MS analysis

U-Pb zircon ages of one sample of chiastolite hornfels were determined using a laser ablation inductively coupled plasma mass spectrometry (LA-ICP-MS) and under the same procedures as described in Martha et al. (2016). Cathodoluminescence images of zircon were produced prior to LA-

ICP-MS analyses, but after polishing, using a JEOL JSM 6490 scanning electron microscope equipped with a Gatan MiniCL detector at the Goethe-University Frankfurt. Laser-induced elemental fractionation and instrumental mass discrimination in LA-ICP-MS analyses were corrected by normalisation to standard zircon GJ-1 (Jackson et al. 2004), which was analysed during the analytical session under the same conditions as the samples. U-Pb data were calculated using the program PBDAT (Ludwig 1980), and isotope ratios were plotted using Isoplot (Ludwig 2012), with error ellipses reflecting 2σ uncertainties.

4.5 Results

A new geological map of the eastern part of the Uppermost Unit south of the Dikti Mountains is presented in Fig. 4.2. The metamorphic rocks of the Uppermost Unit have been thrust on top of Late Eocene Pindos flysch. Based on the grade of metamorphism, the rocks of the Uppermost Unit are subdivided into three tectonometamorphic subunits, i.e. the Arvi Unit, the Theodorii Greenschist and ACC-type rocks, which are separated by thrust faults. The contact between the Uppermost and Tripolitsa units towards the north is poorly exposed, but seems to be a steep normal fault (Robert & Bonneau 1982).

4.5.1 Petrography and microstructures

4.5.1.1 Arvi Unit

The lowest structural unit in the study area consists of meta-pillow basalt, green and red slates and metadolerite. These rocks were assigned to the prehnite-pumpellyite facies Arvi Unit (Robert & Bonneau 1982). Red, pelagic *Globotruncana* limestone reported from the Arvi Unit at Ano Symi, just 1 km north of Kalami (see Palamakumbura et al. 2013; their Fig. 6b), are lacking in the study area. The metabasalt pillows are strongly deformed, while the metadolerite is present as massive rock without significant strain. The cleavage of the slates dips towards the NW or the SE (Fig. 4.3a), while the mineral/stretching lineation, defined by the alignment of feldspar and quartz, is trending NW–SE (Fig. 4.3b). Kink bands, which are perpendicular to the cleavage and to the mineral/stretching lineation, are widespread (Fig. 4.4a).

Petrographic data of the Arvi rocks are reported by Robert & Bonneau (1982) and Palamakumbura et al. (2013). For this reason, we focussed on the microstructures, which are pronounced in slates. Slates consist of chlorite, white mica, K-feldspar, plagioclase, quartz and opaque phases. Calcite occurs in veins, fibrous calcite being oriented parallel to the main foliation and at high angles to the vein walls. Feldspar and quartz are largely intact and show no evidence for recrystallization or significant

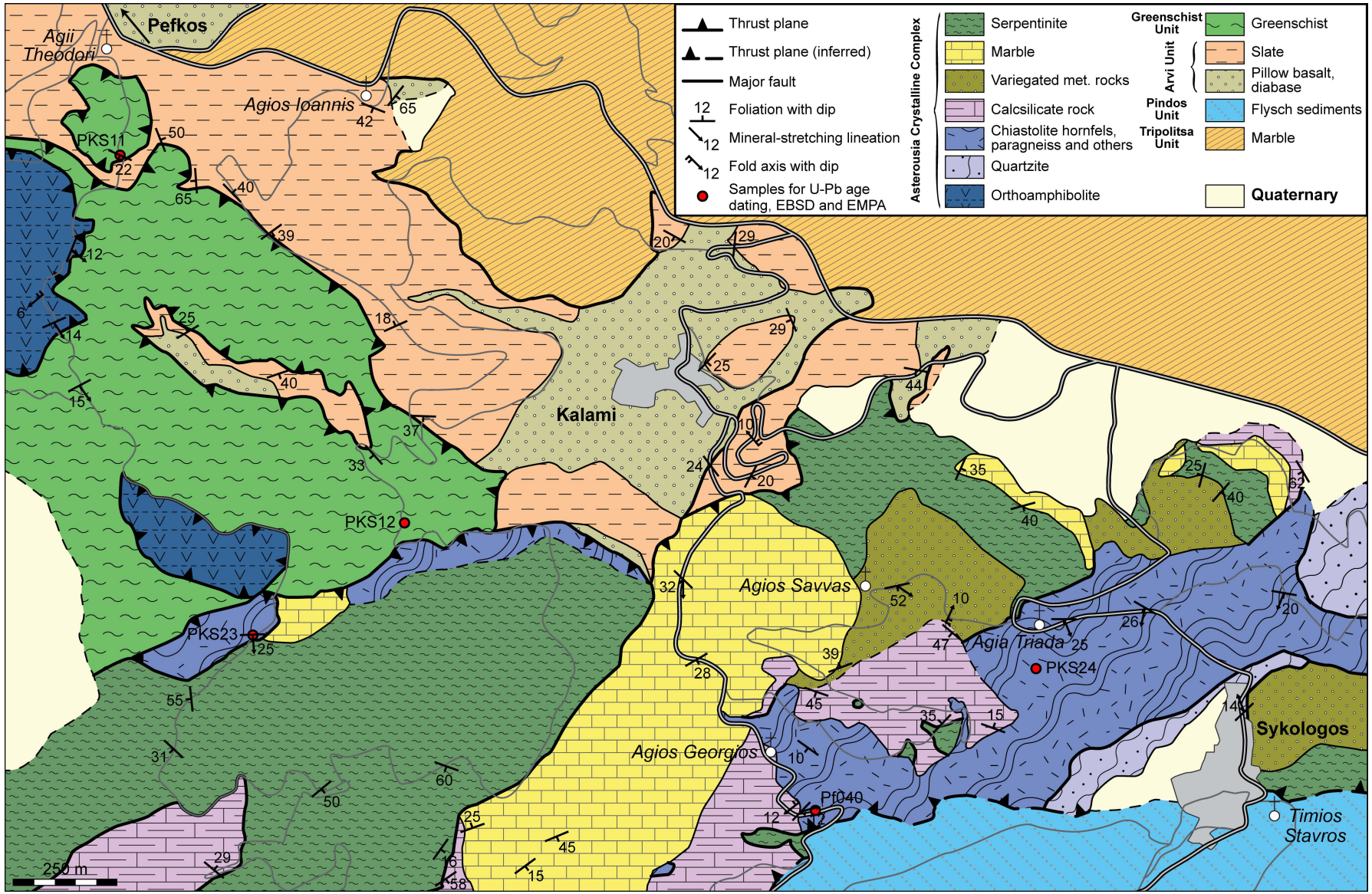

Fig. 4.2 Geological map of the Uppermost Unit exposed south of the Dikti Mountains in the area of Pefkos, Kalami and Sykologos (Viannos Municipality). Structural data and location of samples for geochronological, EMP and EBSD analyses are shown.

deformation. Asymmetric pressure shadows of phyllosilicates behind K-feldspar and plagioclase indicate a top-to-the SE sense of shear (Fig. 4.4b).

4.5.1.2 Theodorii Greenschist

South of Agii Theodorii, greenschist facies rocks are tectonically emplaced onto the Arvi Unit via a brittle thrust fault. Slickenside striations on the main and second-order thrust planes reveal NW–SE-oriented tectonic transport. The Theodorii Greenschist is very homogeneous in composition and consists of albite, amphibole (actinolite and hornblende), biotite, chlorite, epidote and quartz. Calcite, K-

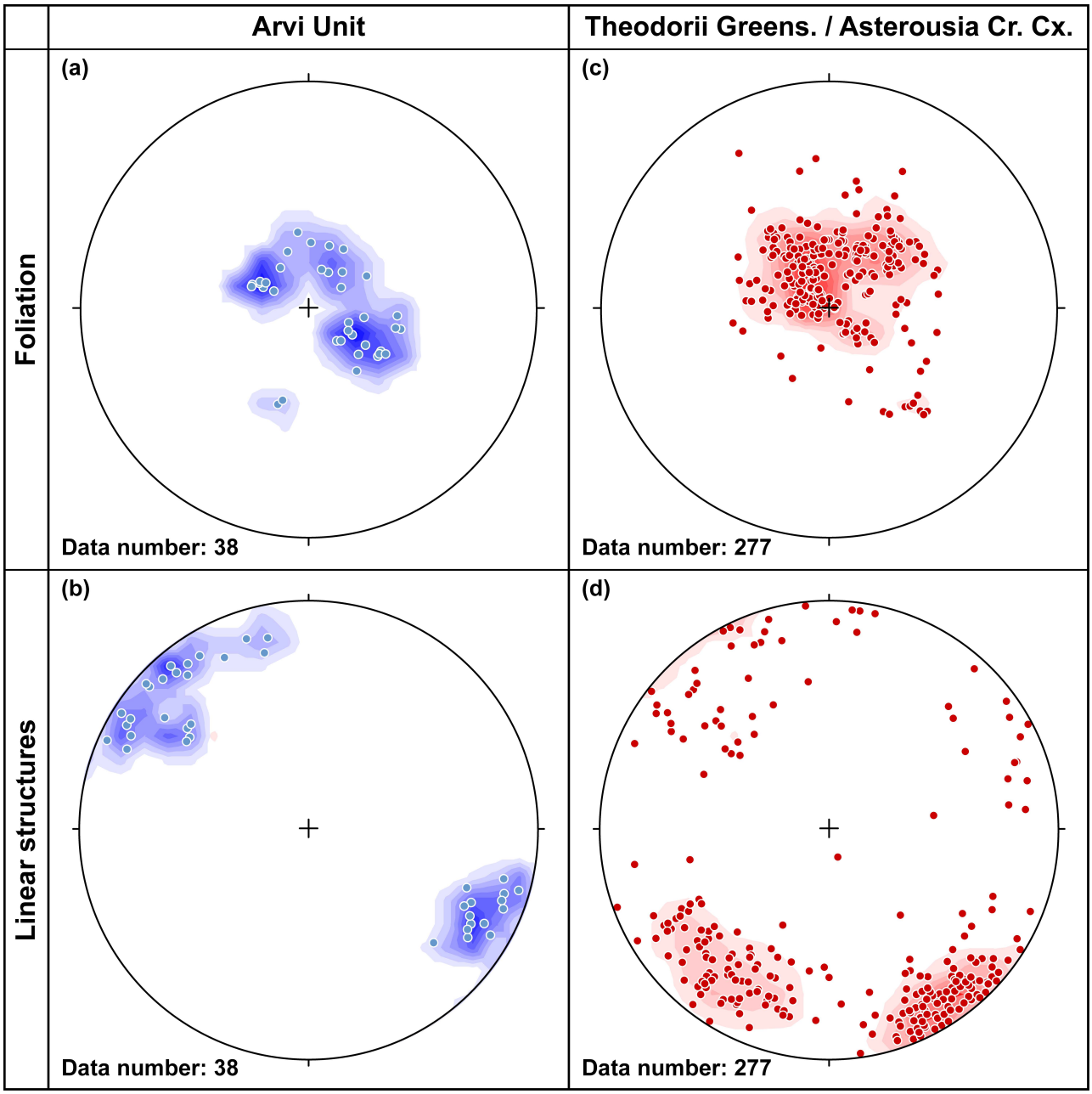

Fig. 4.3 Equal area, lower hemisphere stereoplots of structural data (dominant foliation and mineral/stretching lineation) from the Arvi Unit (a, b) and the Theodorii Greenschist and the Asterousia Crystalline Complex (c, d) in the area of Pefkos, Kalami and Sykologos. Statistical analyses using the 1 % area contouring method are indicated.

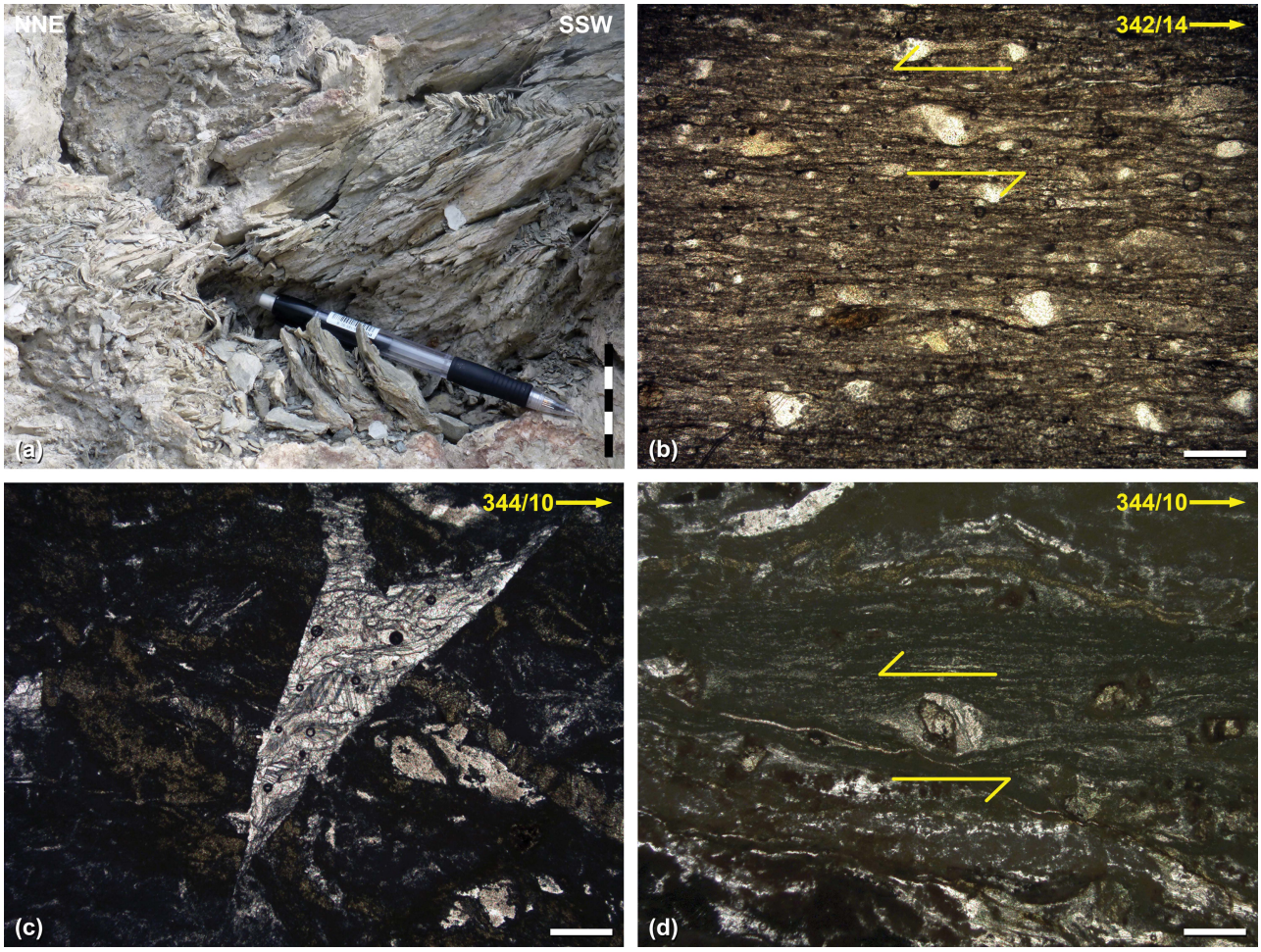

Fig. 4.4 Photographs (a) and microphotographs (b–d) from rocks of the Arvi Unit and the Theodorii Greenschist of the study area. (a) SSW-vergent kinking in greenish Arvi slate. Road cut 100 m S of the Kalami Cemetery (35° 01′ 39.64″ N; 25° 30′ 00.73″ E). Scale bar: 5 cm. (b) Asymmetric pressure shadows of phyllosilicates behind K-feldspar in Arvi slate indicate a top-to-the SE sense of shear. Plane-polarized light. Sample: Pf048. Road cut 1.5 km SW of Ano Viannos (35° 02′ 36.60″ N; 25° 24′ 08.17″ E) (Locality not included in Fig. 4.2). Scale bar: 150 µm. (c) Calcite-filled crack in greenschist. Plane-polarized light. Sample: PKS11. Road cut 225 m SSE of Agii Theodorii (35° 02′ 02″ N; 25° 29′ 01″ E). Scale bar: 300 µm. (d) Asymmetric pressure shadow of actinolite and chlorite behind K-feldspar and an unidentified phase with high relief in greenschist. The shear sense indicated is top-to-the SE. Plane-polarized light. Same sample as in (c). Scale bar: 300 µm.

feldspar and white mica may occur as accessories. The foliation and the mineral/stretching lineation, defined by the alignment of feldspar, are both dipping/plunging at low angles to the NW or to the SE (Fig. 4.3c, d).

A spaced foliation is defined by actinolite- and chlorite-rich domains (AC domains). Quartz and albite usually form lens-shaped domains (QF domains) aligned parallel to the AC domains and albite and epidote may occur as single grains within the AC domains. Quartz of the QF domains is very fine-grained (< 0.5 mm). Calcite always forms large clusters or is filling cracks (Fig. 4.4c). It often co-occurs with white mica, both being probably of secondary origin. Calcite twins are straight, rational and thin. They can be classified as type I or II according to the classification of Burkhard (1993). Shear sense indicators are sparse. One grain, presumably K-feldspar, which exhibits an asymmetric pressure shadow of actinolite and chlorite, suggests a top-to-the SE transport (Fig. 4.4d).

4.5.1.3 Asterousia-type rocks

The Theodorii Greenschist is overlain by amphibolite facies rocks, which have been correlated with the ACC (Bonneau 1972). In the study area, the ACC-type rocks include orthoamphibolite, metasedimentary rocks and serpentinite. Metasedimentary rocks are exposed in the southern and eastern part of the study area. They include calcsilicate rock, chiastolite hornfels, marble, micaschist, quartzite and minor occurrences of paragneiss and other rock types. Metasedimentary rocks are resting on top of the Arvi Unit south and east of Kalami. A contact between the metasedimentary succession and underlying units is not exposed. Intrusive rocks, which are common in other exposures of the ACC on Crete and the Cyclades, have not been found. Both the orthoamphibolite and the metasedimentary rocks display a foliation that usually dips either to the NW or to the SE (Fig. 4.3c), but local variation of the foliation with NE- and SW-dip was observed in several outcrops. A NW–SE-trending mineral/stretching lineation is pronounced in orthoamphibolite and micaschist, but it is weakly developed in other rock types (Fig. 4.3d). A top-to-the SE sense of shear is indicated by few asymmetric boudins of calcsilicate rock, serpentinite or quartzite, which are embedded in metapelitic rocks. Isoclinal to open SE- and SW-vergent folds with NE–SW- and NW–SE-trending axes, respectively, were also observed (Fig. 4.5). Symmetric calcsilicate boudins inside quartzite have been affected by subsequent folding (Fig. 4.6a).

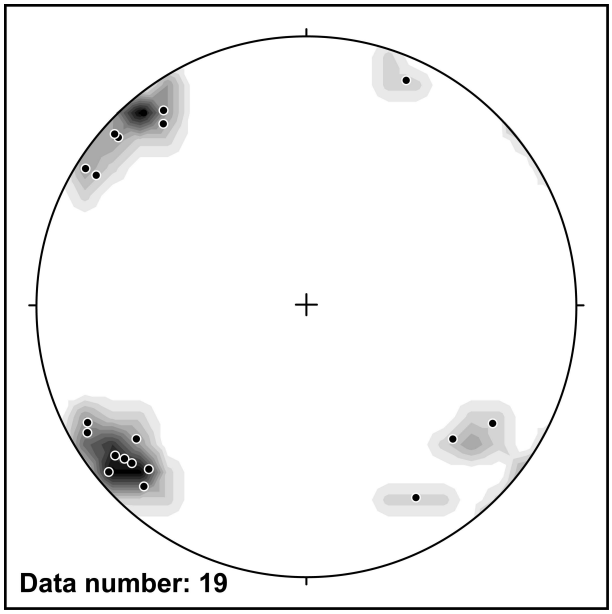

Fig. 4.5 Equal area, lower hemisphere stereoplot summarizing the orientation of fold axes from the Uppermost Unit of the study area.

Orthoamphibolite was found south of Pefkos and southwest of Kalami. Large orthoamphibolite exposures occur west of the mapped area between Agios Vasilios and Pefkos. Orthoamphibolite has been emplaced on top of the Theodorii Greenschist via a thrust that dips moderately NW-wards (Fig. 4.6b). Both orthoamphibolite and greenschist are strongly disintegrated and fractured near the contact and calcite veins are common. Slices of serpentinite inside the orthoamphibolite are frequent near the contact. Orthoamphibolite is massive and consists of hornblende and plagioclase as the main constituents, while chlorite, quartz and opaque phases occur as accessories. Both hornblende and plagioclase show shape-preferred orientation resulting in a NW–SE-trending mineral/stretching lineation. Plagioclase shows deformation twins according to the albite law, kinking and microfractures. In sections cut perpendicular to the mylonitic foliation and parallel to the stretching/mineral lineation, kinematic indicators such as plagioclase σ-clasts and asymmetric pressure shadows of quartz and hornblende behind plagioclase indicate top-to-the SE shearing (Fig. 4.6c, d).

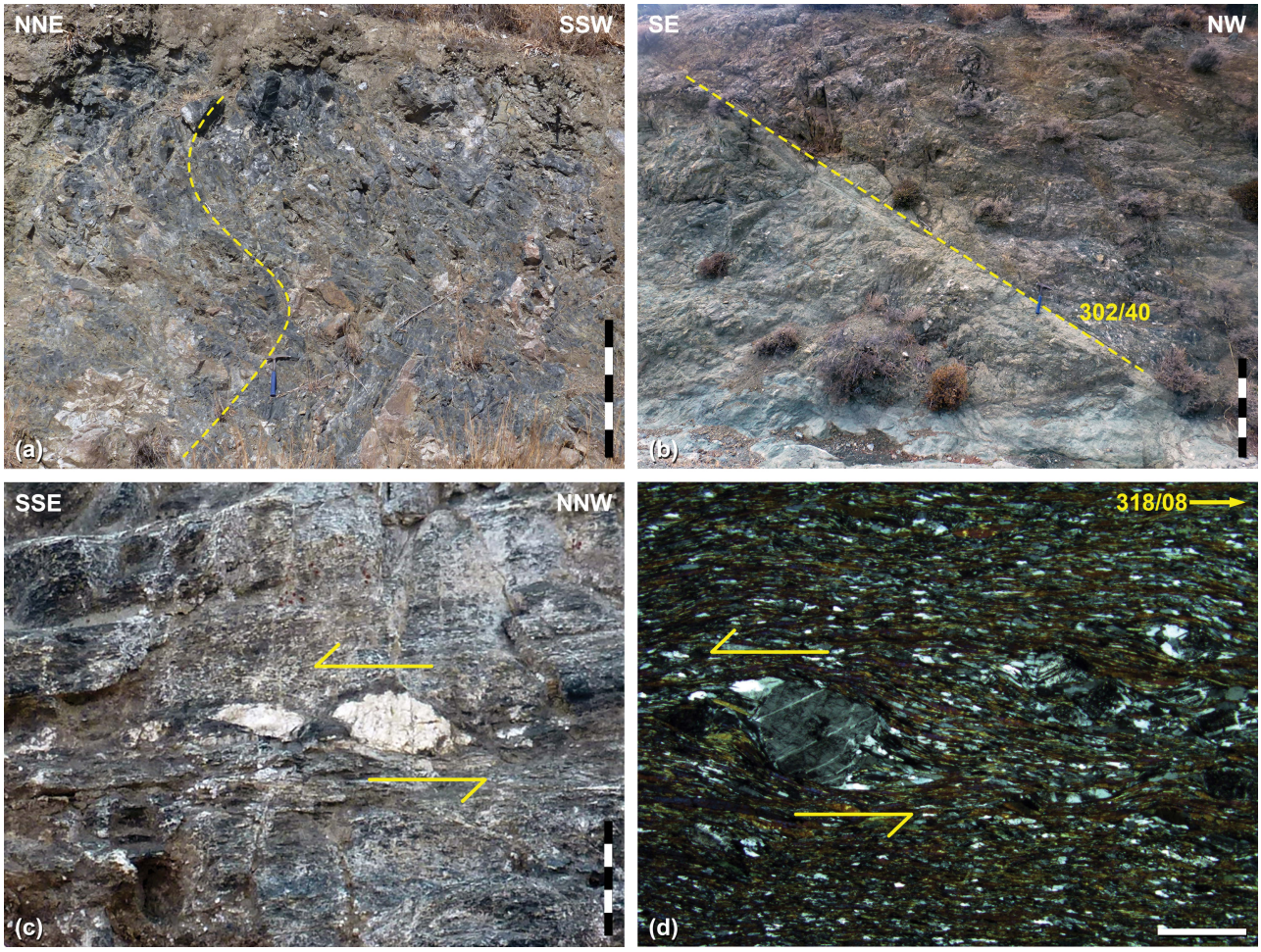

Fig. 4.6 Photographs (a–c) and microphotograph (d) from the Asterousia Crystalline Complex of the study area. (a) Lens of calcsilicate rock and quartzite inside marble (dark grey, at the margins). Calcsilicate rock forms symmetric boudins that have been affected by subsequent folding. Road cut 300 m NNW of Agios Georgios (35° 01′ 21.68″ N; 25° 29′ 55.38″ E). Scale bar: 1 m. (b) Thrust plane between orthoamphibolite (hanging wall) and Theodorii Greenschist (foot wall). Road cut 700 m S of Agii Theodorii (35° 01′ 46.76″ N; 25° 28′ 54.63″ E). Scale bar: 1 m. (c) Plagioclase σ-clasts in orthoamphibolite indicating a top-to-the SE sense of shear. Road cut 475 m S of Agii Theodorii (35° 01′ 54.47″ N; 25° 28′ 55.08″ E). Scale bar: 1 cm. (d) Orthoamphibolite showing asymmetric pressure shadows of quartz and hornblende behind plagioclase that indicate a top-to-the SE sense of shear. Cross-polarized light. Sample: Pf021y. Road cut 550 m SSW of Agii Theodorii (35° 01′ 52.08″ N; 25° 28′ 53.11″ E). Scale bar: 1 mm.

Calcsilicate rock is present in the area of Agios Georgios and in thin layers between chiastolite hornfels exposed north and west of Sykologos. It consists of diopside, plagioclase, K-feldspar, quartz, green amphibole (presumably hornblende and pargasite), calcite, opaque phases and phyllosilicates. Xenomorphic garnet may occur in layers within the matrix but was never found as porphyroblasts. Diopside is strongly fractured. Calcite occurs both in the matrix and in almost pure layers subparallel to the main foliation. A shape-preferred orientation is weakly developed and almost faint in diopside-rich samples. Quartz occasionally forms thin lens-shaped layers and exhibits undulatory extinction and lobate grain boundaries (Fig. 4.7a). A NW–SE-trending mineral/stretching lineation is defined by the alignment of amphibole, quartz and/or K-feldspar.

Serpentinite has been found both as slices incorporated into the metasedimentary rocks and on top of the metasedimentary succession separated from the latter by normal faults (Fig. 4.7b). From our observations, it is not evident whether serpentinite on top of the amphibolite facies rocks constitutes a

separate nappe (the *nappe des serpentines*) or not. Serpentinite was frequently intruded by mafic dykes (see also Koepke et al. 2002) and is cut by NW–SE- to N–S-striking normal faults. Microscopic and XRD analyses reveal lizardite as the main serpentine phase (> 75 %) as well as magnetite and chlorite as accessories (Fig. 4.7c). Talc is found along shear planes. Relics of possibly clinopyroxene and/or olivine are rare.

Marble is often found in close association with serpentinite and in thin layers between other rock types. It is granoblastic, fine-grained (< 500 µm), impure and consists to ca. 85 % of calcite. Quartz, plagioclase, K-feldspar, biotite and white mica occur as accessories. Calcite twins are tabular, thick and rarely slightly curved (Fig. 4.7d). They can be classified as type II using the classification of Burkhard (1993). Other constituents are very fine-grained and irregularly interspersed among calcite. Quartz may form NW–SE-oriented symmetric boudins with a diameter of up to 15 cm. In these cases, quartz is polycrystalline and shows evidence for dynamic recrystallization. Grain boundaries are straight and undulatory extinction is weakly pronounced. The quartz boudins are cut by veins, which are mineralized with coarse-grained calcite (grain size = 0.75–3.8 mm).

Micaschist occurs as minor intercalations among other rock types and is usually associated with chiastolite hornfels in the area of Agia Triada and Agios Georgios. The main constituents are biotite, quartz, K-feldspar and plagioclase, while epidote and chlorite were observed as accessories in some samples. The shape-preferred orientation of biotite defines a pronounced foliation that is separated by planar QF domains. K-feldspar and plagioclase may form rare sigmoidal inclusions. The appearance and deformation microstructures of quartz compare well with those described from quartz of quartzite (see below). Garnet was observed in micaschist intercalations within chiastolite hornfels from Agia Triada. It occurs as small, euhedral, octagonal to roundish porphyroblasts with internal fractures. Cordierite was found as small, subhedral porphyroblasts. White mica is present in form of cross-mica growing oblique to the main foliation.

Quartzite is found in the Sykologos area and is full of discrete brittle shear zones, which are dipping at low to medium angles to the NW or to the SE (Fig. 4.7e). Striations on the shear zones plunge to the SW or to the NE (Fig. 4.3d). Quartzite consists to > 75 % of quartz, while diopside, biotite, white mica, clay minerals and opaque phases are found as accessories. Quartz shows an equilibrium fabric of polygonal and small grains with few larger grains building clusters or thin layers. Grain boundaries are straight or slightly curved and contacts are triple junctions with interfacial angles of ca. 120° (Fig. 4.7f). Undulatory extinction is weakly pronounced. Other constituents are very fine-grained and frequently interspersed between quartz. Grain size of quartz is correlated with the amount of impurities, quartz grains being larger in almost pure layers. The shape-preferred orientation in quartzite is defined

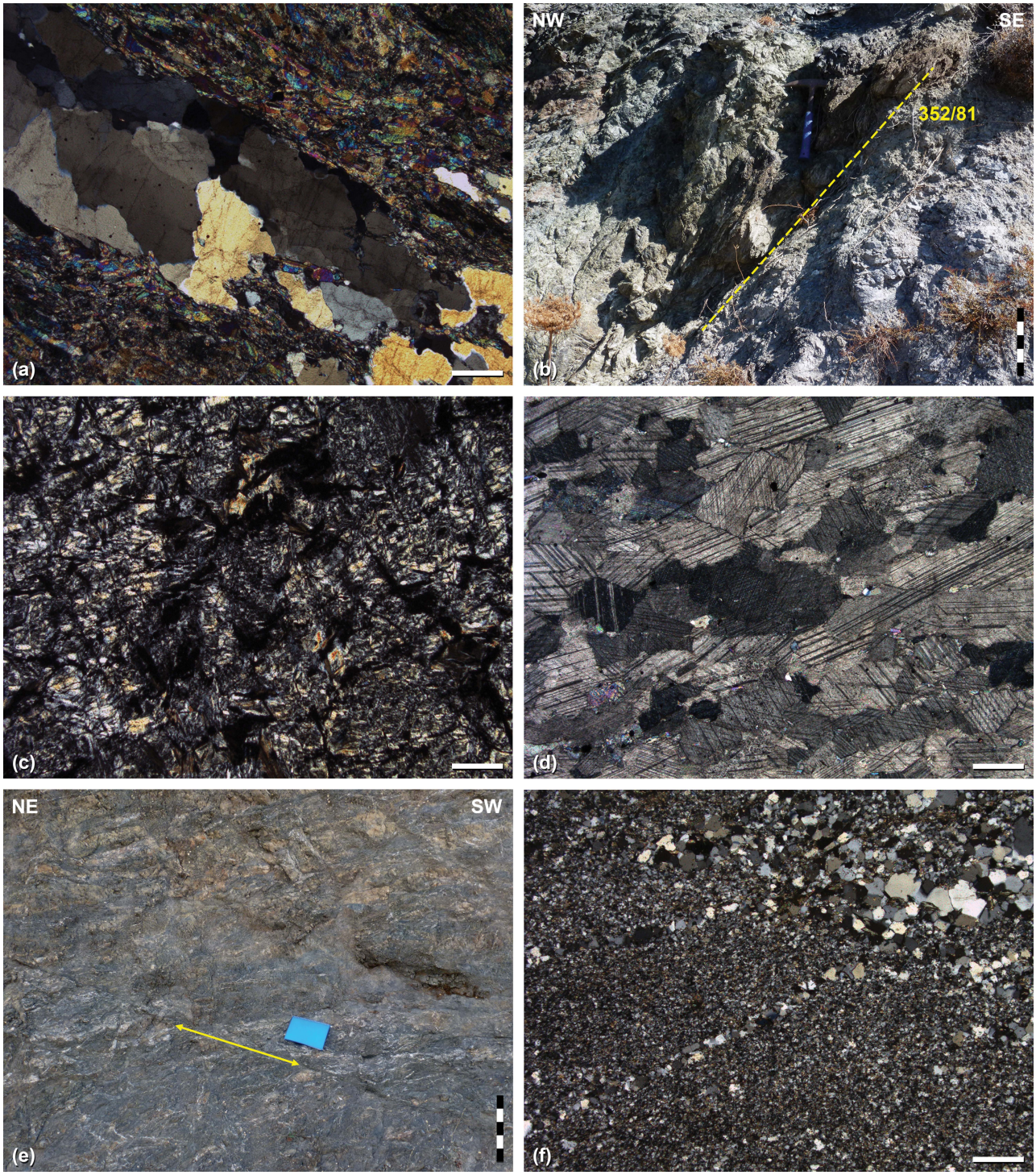

Fig. 4.7 Photographs (b, e) and microphotographs (a, c, d, f) from the Asterousia Crystalline Complex in the study area. (a) Quartz layer inside calcsilicate rock. Quartz shows evidence for high-temperature grain boundary migration recrystallization (lobate grain boundaries), subgrains, healed fractures (decorated with fluid inclusions) and undulatory extinction and. Cross-polarized light. Sample: PKS20. Road cut 600 m N of Sykologos (35° 01′ 34.90″ N; 25° 30′ 50.95″ E). Scale bar: 300 µm. (b) Normal fault between serpentinite (hanging wall) and Asterousia-type micaschist (foot wall). Road cut 40 m NW of Agia Triada (35° 01′ 25.38″ N; 25° 30′ 26.56″ E). Scale bar: 25 cm. (c) Serpentinite composed of lizardite, magnetite and chlorite. Cross-polarized light. Sample: PKS14. Road cut 250 m ESE of Agios Savvas (35° 01′ 26″ N; 25° 30′ 18″ E). Scale bar: 300 µm. (d) Marble showing tabular and thick type II twins according to the classification of Burkhard (1993). Quartz and white mica occur as accessories. Cross-polarized light. Sample: PKS07. Road cut 250 m SW of Agios Savvas (35° 01′ 22″ N; 25° 30′ 03″ E). Scale bar: 300 µm. (e) NE–SW-trending discrete shear band in quartzite. The shear band dips 266/24°. Road cut in the southeastern part of Sykologos (35° 01′ 08.90″ N; 25° 30′ 46.94″ E). Scale bar: 50 cm. (f) Quartzite showing an equilibrium fabric of polygonal and small grains. Larger grains occur in clusters (upper right) and thin layers. Grain boundaries are straight or slightly curved and contacts are triple junctions. Sample: PKS08. On the hill 250 m NE of Sykologos (35° 01′ 21″ N; 25° 30′ 53″ E). Scale bar: 300 µm.

by the alignment of biotite and clay minerals. A NW–SE-trending mineral/stretching lineation is vaguely defined.

Chiastolite hornfels is present in the area between the Agios Georgios chapel and Sykologos. It is largely massive and at some places weakly foliated (Fig. 4.8a). Andalusite is present in form of bright ledges (length: < 2.5 cm; width: < 1.2 cm). Besides andalusite (5–15 %), other main constituents are quartz (30–50 %), biotite (20–35 %), plagioclase (< 15 %) and K-feldspar (< 10 %), while white mica (< 5 %), clay minerals (< 2 %) and graphite (< 1 %) occur as accessories. Garnet and chlorite were observed in some samples only. A shape-preferred orientation of biotite results in the weak foliation, which is dipping to the SW or to the NE. A mineral/stretching lineation on the foliation planes is poorly developed. Biotite is sometimes kinked. Quartz, plagioclase and K-feldspar co-occur with biotite in the matrix. Quartz may be fine-grained and recrystallized but also forms aggregates of large recrystallized grains. Quartz from aggregates shows undulatory extinction and weakly developed chessboard patterns based on prism- and basal-parallel subgrains (Fig. 4.8b). Recrystallized grains are large and slightly polygonal with contacts tending to form triple junctions. Biotite inclusions and pinning of quartz grain boundaries by biotite are common. K-feldspar shows undulatory extinction, while Karlsbad twinning is rare. Garnet may occur as idiomorphic porphyroblasts or xenomorphic in layers. Garnet porphyroblasts are strongly disintegrated and were partly replaced by white mica, chlorite and clay minerals. Zoning is sometimes weakly recognizable. There are two types of garnet porphyroblasts. Intertectonic garnet porphyroblasts include aligned, elongate inclusions as internal foliation ($S_i = S_1$) that is perpendicular to the external foliation ($S_e = S_2$), which is the younger, dominant foliation of the rock (Fig. 4.8c). Syn-D_2 garnet porphyroblasts with inclusions of feldspar, quartz and white mica were observed in one sample and indicate dextral rotation during deformation (Fig. 4.8d). In one sample, garnet is xenomorphic and intergrown with biotite. Andalusite is present in form of euhedral porphyroblasts and may form cross-shaped twins (Fig. 4.8e). Andalusite was growing across the pre-existing foliation (S_2) and shows re-entrant zones with feather-edge structures. Inclusions of cryptocrystalline graphite take the shape of a cross in sections along the C-axis. Thus, andalusite is classified as chiastolite. The centres of chiastolite grains consist of graphite. Graphite may also surround chiastolite porphyroblasts. Pre- to early-kinematic growth of andalusite (with respect to the following D_3 deformation phase) is indicated by D_3 boudinage of chiastolite grains and by D_3 pressure shadows of biotite and quartz behind chiastolite. In cases where the pressure shadows are asymmetrical, a top-to-the SE sense of shear is indicated for D_3. Incipient sericitization of chiastolite was observed. White mica is present as cross-mica that grew post-kinematically across the main foliation (S_2 // S_3). It may replace garnet and forms pseudomorphs, presumably after cordierite (Fig. 4.8f). However, real cordierite was not observed. Chlorite is present as secondary phase replacing biotite.

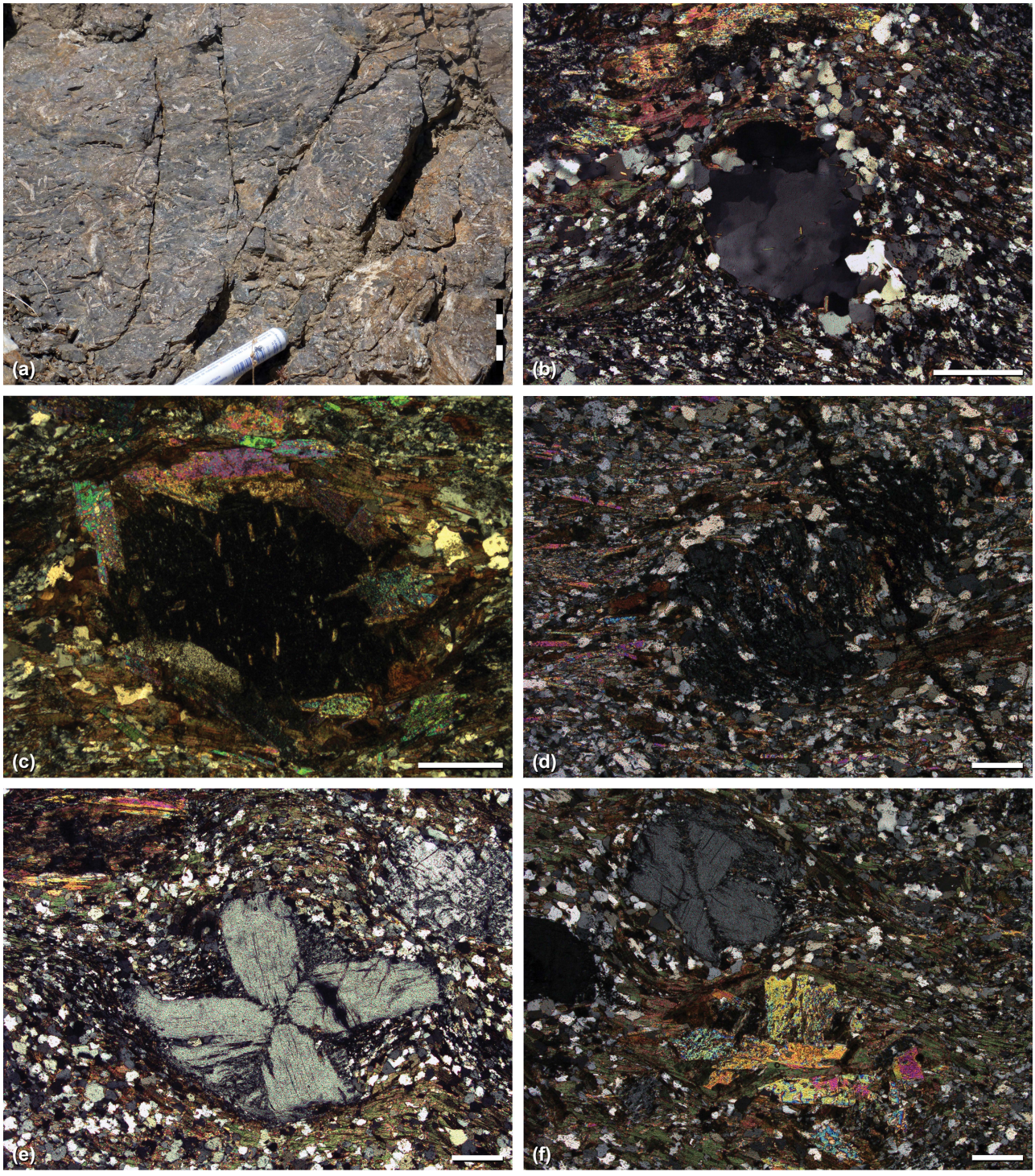

Fig. 4.8 Photograph (a) and microphotographs (b–f) of chiastolite hornfels from the Asterousia Crystalline Complex of the study area. (a) Massive, bluish-violet chiastolite hornfels showing columnar, white porphyroblasts of chiastolite. Road cut 200 m SE of Agios Georgios (35° 01′ 09.40″ N; 25° 30′ 07.26″ E). Scale bar: 5 cm. (b) Quartz porphyroclast showing poorly developed chessboard-type subgrains. Cross-polarized light. Sample: PKS24. Road cut 125 m S of Agia Triada (35° 01′ 21.26″ N; 25° 30′ 28.53″ E). Scale bar: 500 µm. (c) Intertectonic garnet porphyroblast replaced by white mica at the margins. The shape-preferred orientation of elongate tiny inclusions define an internal foliation ($S_i = S_1$) perpendicular to the external foliation ($S_e = S_2$). Sample: Pf040y. Same locality as in (a). Scale bar: 500 µm. (d) Syntectonic garnet porphyroblast with inclusions of feldspar, quartz and white mica. The asymmetry of the fabric indicates a dextral rotation (in the microphotograph). Cross-polarized light. Sample: Pf002z. Road cut 25 m E of Agia Triada (35° 01′ 25.04″ N; 25° 30′ 29.66″ E). Scale bar: 300 µm. (e) Chiastolite porphyroblast showing a pronounced internal dark cross made of cryptocrystalline graphite and a small lozenge-shaped graphite core. Graphite was also dissolved from the interior during growth and is found at the margins. Pressure shadows of biotite and quartz as well as marginal drag and fracturing of andalusite suggest inter- to syntectonic evolution with respect to D_3. Cross-polarized light. Same sample as in (b). Scale bar: 1 mm. (f) Relatively large crystals of white mica probably forming pseudomorphs after cordierite. Cross-polarized light. Same sample as in (b). Scale bar: 300 µm.

CT images of chiastolite hornfels show a compact rock with no pores or cracks. Quartz, white mica, plagioclase and K-feldspar cannot be distinguished because of similar densities resulting in similar X-ray absorption properties. However, chiastolite (ρ = 3.2 g/cm³) and graphite (ρ = 2.25 g/cm³) are well discriminated, while biotite (ρ = 2.8–3.2 g/cm³) could at least in part be distinguished from other phases. Chiastolite porphyroblasts are dark grey in CT images, thus contrasting well with other phases (Fig. 4.9a). Most porphyroblasts grew with their long axis oriented NW–SE or NE–SW. Few grains show symmetrical pressure shadows in sections perpendicular to the main foliation (Fig. 4.9b). Graphite surrounds many of the chiastolite porphyroblasts. The chiastolite cross cannot be examined as cryptocrystalline graphite is too fine-grained. In the 3D model (Fig. 4.9c), chiastolite is shown as hollow structures, while graphite was visualised in red and biotite was visualised using pseudocolours. Symmetric pressure shadows of biotite surrounding the chiastolite porphyroblasts could be modelled (Fig. 4.9d).

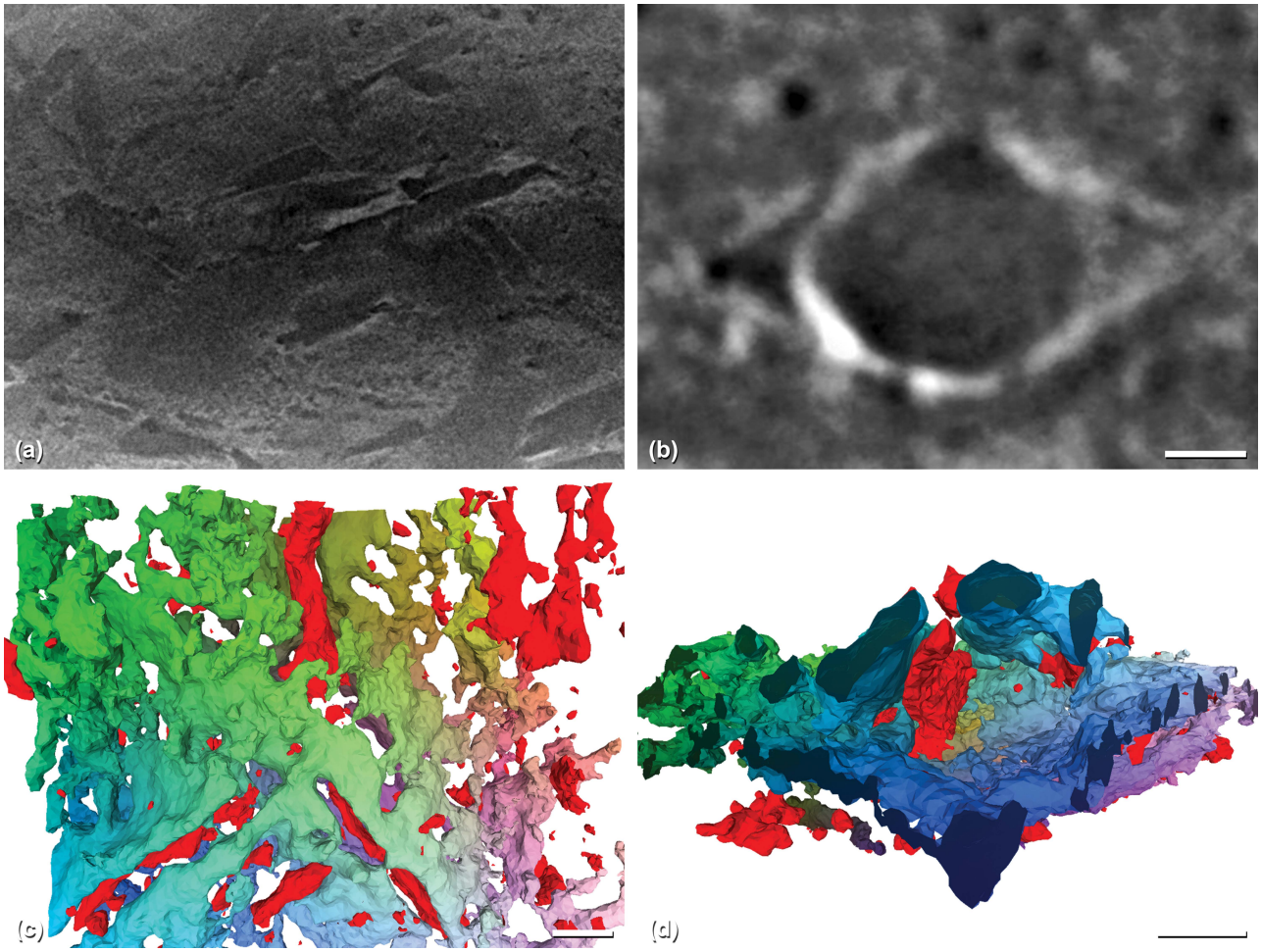

Fig. 4.9 Micro-CT images of chiastolite hornfels (sample PKS23). (a) Section parallel to the foliation showing chiastolite porphyroblasts without s shape-preferred orientation. (b) Section perpendicular to the foliation showing a chiastolite porphyroblast with symmetric pressure shadows. (c) 3D model of a section with two adjacent chiastolite porphyroblasts perpendicular to one another. Chiastolite is not visualised but can be inferred from the bending of biotite (pseudocolours). One porphyroblast starts at the upper left and proceeds to the upper right, while the other porphyroblast starts near the centre and can be followed to the upper left. Graphite (red) surrounds chiastolite. (d) 3D model of chiastolite (hollow structure) surrounded by graphite and matrix minerals (pseudocolours) that form a pressure shadow. Similar view as in (b). Scale bars: 1 mm.

4.5.2 Electron microprobe analysis

4.5.2.1 Theodorii Greenschist

Representative chemical analyses of two samples from the Theodorii Greenschist (samples PKS11 and PKS12) are listed in Tables 4.1 and 4.2. From the chemical analyses, albite (An 0.54–7.73 %), actinolite, biotite, chlorite, epidote, magnesio-hornblende and quartz have been identified. Actinolite occurs as very thin acicular needles with an average width < 5 µm, while hornblende may form typical six-sided diamonds with a length of up to 25 µm. The matrix consists of albite, epidote and few quartz grains. Chlorite has been found adjacent to amphibole. As the mineral assemblage of the Theodorii Greenschist consists of amphibole, plagioclase and quartz, the edenite-tremolite geothermometer of Holland and Blundy (1994) could be applied for different mineral pairs of albite and amphibole (Table 4.3). The Al content of hornblende is low (5.90–8.00 %) suggesting low pressure (150, 225 and 300 MPa) for greenschist facies metamorphism (Table 4.1). Calculated temperatures range from 364 °C, for the mineral pairs albite and actinolite at P = 300 MPa, to 520 °C, for albite and actinolite at P = 300 MPa.

4.5.2.2 Asterousia-type chiastolite hornfels

The Si values of phengitic white mica in the limiting assemblage with K-feldspar, phlogopite (biotite) and quartz are pressure dependent and can be used for geobarometry (Massonne & Schreyer 1987). White mica shows a pronounced cleavage and may occur within the rock matrix as well as forming large new crystals. Results of chemical analyses on two samples of chiastolite hornfels (samples PKS23 and PKS24) are presented in Tables 4.4 and 4.5. 43 analyses reflect restricted variability of the Si values, which are ranging from 3.046 to 3.097 p.f.u. (per formula unit) with a mean of 3.077 ± 0.002 p.f.u. (Fig. 4.10). No significant differences between Si values from cores to rims of white mica were observed.

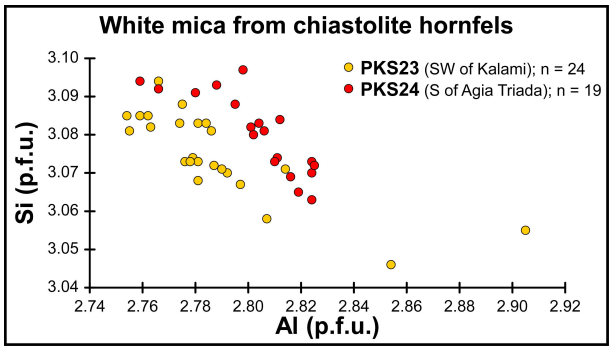

Fig. 4.10 Si–Al diagrams of phengitic white mica from chiastolite hornfels samples PKS23 SW of Kalami and PKS24 S of Agia Triada. The values are from Tables 4.4 and 4.5.

4.5.3 Geochronological analyses

One zircon grain from chiastolite hornfels, exposed 200 m SE of Agios Georgios (sample Pf040; 35° 01′ 09.40″ N; 25° 30′ 07.26″ E) is pristine, euhedral, subangular and shows growth zoning (Fig. 4.11). The uranium content ranges from 736–1300 ppm and the amount of common lead (Pbc) should have either no or (for analysis A307) minor influence on the concordance (Table 4.6). The most concordant analysis (A306) yielded a $^{206}Pb/^{238}U$ age of 74 ± 2 Ma, while two further analyses (A305 and

Table 4.1 Representative chemical analyses on greenschist PKS11 from 250 m SSE of the Agii Theodorii chapel and calculation of structural formulae. Chemical composition of oxides in weight percent. For epidote all iron is converted to Fe^{3+}; Fe^{2+}/Fe^{3+} estimations for amphiboles are made by assuming 13 total cations excluding Ca, Na and K (Leake 1978). [1]An content = anorthite content of plagioclase [Ca/(Na+K+Ca)]. [2]Mineral abbreviations: alb = albite; act = actinolite; epd = epidote. Asterisk (*) indicates one-by-one analyses with a spot size of 1 µm and a reduced current of 12 nA.

Analysis	p1	p2*	p6*	p7	p8	p10	p11	p12	p13	p16*	p19	p20	p21*	p22*	p23*	p24*	p25*
SiO_2	56.99	57.18	57.04	69.08	68.15	68.33	68.43	38.34	55.90	56.20	67.09	69.08	56.73	54.92	55.47	54.64	55.54
TiO_2	0.01	—	0.01	—	—	—	—	0.05	0.07	0.02	—	—	—	0.05	0.04	0.07	0.02
Al_2O_3	0.67	0.61	0.49	19.19	19.15	19.47	19.52	23.12	1.21	0.75	20.24	19.47	0.86	0.75	1.02	1.16	1.04
Cr_2O_3	—	0.05	—	0.01	—	0.01	0.02	—	0.02	0.07	—	—	0.03	0.07	0.03	0.18	0.05
FeO	6.85	6.97	7.53	0.12	0.12	0.06	0.05	12.45	9.42	9.13	0.09	0.05	8.92	9.25	7.73	9.07	8.33
MnO	0.27	0.28	0.25	0.01	—	—	0.01	0.07	0.28	0.24	—	—	0.28	0.23	0.24	0.27	0.24
MgO	20.05	19.80	19.58	0.01	0.01	—	—	0.03	18.25	18.38	0.01	0.01	18.79	18.81	19.24	18.81	18.92
CaO	12.80	12.88	13.02	0.18	0.12	0.31	0.40	23.73	12.34	12.40	1.26	0.33	12.47	12.25	12.72	12.01	12.27
NiO	0.02	0.05	0.04	—	0.03	0.01	0.01	—	0.03	0.03	—	0.02	0.06	0.07	0.07	0.10	0.06
Na_2O	0.20	0.28	0.30	12.00	12.02	11.84	11.94	—	0.47	0.40	11.26	11.80	0.34	0.44	0.42	0.33	0.56
K_2O	0.03	0.02	0.01	0.07	0.06	0.09	0.06	—	0.09	0.05	0.11	0.10	0.04	0.05	0.02	0.04	0.02
P_2O_5	—	0.01	—	—	—	—	—	—	—	0.04	—	0.01	—	0.02	—	0.02	0.03
Total	97.88	98.128	98.28	100.66	99.66	100.12	100.44	97.78	98.07	97.84	100.05	100.87	98.51	96.91	97.00	96.69	97.08
Oxygens	O = 23	O = 23	O = 23	O = 8	O = 8	O = 8	O = 8	O = 12.5	O = 23	O = 23	O = 8	O = 8	O = 23	O = 23	O = 23	O = 23	O = 23
Si	7.912	7.945	7.943	3.002	2.994	2.987	2.983	3.019	7.836	7.889	2.943	2.995	7.886	7.767	7.827	7.710	7.827
Ti	0.001	—	0.001	—	—	—	—	0.003	0.007	0.002	—	—	—	0.005	0.004	0.007	0.002
$^{[4]}$Al	0.088	0.055	0.057	0.983	0.992	1.003	1.003	—	0.164	0.111	1.046	0.995	0.114	0.125	0.169	0.192	0.173
$^{[6]}$Al	0.021	0.045	0.024	—	—	—	—	2.145	0.036	0.047	—	—	0.028	—	—	—	—
Fe^{3+}	0.199	0.092	0.062	0.004	0.004	0.002	0.002	0.820	0.261	0.211	0.003	0.002	0.269	0.482	0.201	0.624	0.303
Fe^{2+}	0.596	0.718	0.814					—	0.843	0.861			0.768	0.612	0.711	0.447	0.679
Mn	0.031	0.032	0.030	0.000	—	—	0.000	0.004	0.033	0.028	—	—	0.032	0.028	0.029	0.032	0.029
Mg	4.150	4.101	4.064	0.001	0.001	—	—	0.003	3.814	3.846	0.001	0.001	3.894	3.966	4.047	3.957	3.975
Ca	1.904	1.917	1.942	0.008	0.006	0.015	0.019	2.002	1.853	1.865	0.059	0.015	1.857	1.856	1.923	1.816	1.853
Na	0.053	0.074	0.082	1.011	1.024	1.003	1.009	—	0.127	0.109	0.958	0.992	0.092	0.120	0.114	0.091	0.152
K	0.005	0.003	0.002	0.004	0.003	0.005	0.003	—	0.016	0.008	0.006	0.005	0.008	0.010	0.004	0.007	0.004
∑ cations	16.962	16.995	17.027	5.014	5.024	5.016	5.021	7.996	16.996	16.982	5.016	5.006	16.957	16.985	17.041	16.914	17.008
An content[1]	—	—	—	0.801	0.542	1.437	1.816	—	—	—	5.794	1.523	—	—	—	—	—
Mineral phase[2]	act	act	act	alb	alb	alb	alb	epd	act	act	alb	alb	act	act	act	act	act

Table 4.2 Representative chemical analyses on greenschist PKS12 from 700 m SW of Kalami and calculation of structural formulae. Chemical composition of oxides in weight percent. For epidote all iron is converted to Fe^{3+}; Fe^{2+}/Fe^{3+} estimations for amphiboles are made by assuming 13 total cations excluding Ca, Na and K (Leake 1978). [1]An content = anorthite content of plagioclase [Ca/(Na+K+Ca)]. [2]Mineral abbreviations: alb = albite; act = actinolite; bio = biotite; chl = chlorite; epd = epidote; hbl = hornblende; qtz = quartz.

Analysis	p1	p2	p3	p4	p7	p8	p9	p10	p11	p15	p16	p18	p20	p21	p22	p23
SiO_2	99.58	68.35	68.64	68.23	38.19	56.55	55.77	41.36	33.32	66.23	48.26	56.06	67.10	39.32	50.54	40.04
TiO_2	—	—	—	—	—	0.07	0.07	0.62	0.10	0.56	0.01	0.02	0.07	0.14	0.01	0.03
Al_2O_3	0.42	19.45	18.93	18.99	22.05	1.12	1.19	14.41	17.44	18.51	5.90	1.39	18.43	21.43	8.00	11.61
Cr_2O_3	—	—	0.01	—	—	0.23	0.19	0.96	0,02	—	0.02	—	—	0.01	0.03	0.07
FeO	0.52	0.10	0.09	0.14	13.09	7.61	7.98	12.12	13.58	0.32	9.39	7.04	0.36	12.49	7.97	11.49
MnO	0.03	—	—	0.01	0.11	0.25	0.29	0.17	0.32	0.02	0.27	0.27	0.02	0.12	0.25	0.31
MgO	0.48	0.01	0.01	0.01	0.04	19.33	18.79	15.09	18.90	0.21	20.27	19.23	0.40	0.04	17.80	22.71
CaO	0.06	0.76	0.44	0.57	22.84	12.38	12.77	0.04	0.37	1.67	8.70	12.44	1.20	21.91	7.31	4.57
NiO	0.01	—	—	—	—	0.03	—	0.07	0.04	—	0.07	0.02	—	—	0.05	0.08
Na_2O	—	11.53	11.41	11.65	0.03	0.37	0.35	0.01	0.66	10.94	0.23	0.38	11.38	0.94	1.97	0.11
K_2O	—	0.08	0.50	0.08	—	0.06	0.12	9.64	0.03	0.12	0.03	0.05	0.06	0.01	0.03	0.02
P_2O_5	0.03	0.01	—	—	—	—	—	—	0.04	0.29	—	—	0.15	0.01	0.01	—
Total	101.13	100.29	100.04	99.69	96.35	98.01	97.52	94.50	84.82	98.88	93.15	96.90	99.18	96.41	93.97	91.04
Oxygens	O = 2	O = 8	O = 8	O = 8	O = 12.5	.O = 23	O = 23	O = 11	O = 28	O = 8	O = 23	O = 23	O = 8	O = 12.5	O = 23	O = 28
Si	0.990	2.984	3.005	2.997	3.052	7.860	7.854	3.072	6.621	2.958	6.988	7.879	2.979	3.132	7.183	7.390
Ti	—	—	—	—	—	0.008	0.008	0.035	0.015	0.019	0.001	0.002	0.002	0.008	0.001	0.015
$^{[4]}Al$	0.005	1.001	0.977	0.983	—	0.140	0.146	0.928	1.379	0.975	1.007	0.121	0.965	—	0.817	1.379
$^{[6]}Al$	—	—	—	—	2.077	0.044	0.052	0.333	2.776	—	—	0.110	—	2.012	0.523	2.776
Fe^{3+}	0.004	0.004	0.003	0.005	0.875	0.257	0.089	—	0.683	0.012	1.137	0.148	0.013	0.832	0.947	0.683
Fe^{2+}					—	0.628	0.851	0.753	1.574		—	0.680		—	—	1.574
Mn	—	—	—	0.001	0.007	0.030	0.035	0.011	0.054	0.001	0.034	0.032	0.001	0.008	0.030	0.048
Mg	0.007	0.001	0.001	0.001	0.005	4.005	3.945	1.671	5.598	0.014	4.376	4.029	0.027	0.005	3.772	6.248
Ca	0.001	0.035	0.021	0.027	1.956	1.844	1.927	0.003	0.079	0.080	1.350	1.873	0.057	1.870	1.113	0.904
Na	—	0.976	0.969	0.992	0.005	0.101	0.095	0.001	0.510	0.948	0.064	0.104	0.980	0.145	0.543	0.080
K	—	0.004	0.028	0.004	—	0.010	0.021	0.913	0.015	0.007	0.005	0.010	0.004	0.001	0.006	0.007
∑ cations	1.007	5.006	5.004	5.010	7.975	14.954	15.042	7.720	19.313	5.013	14.972	14.987	5.028	8.011		19.040
An content[1]	—	3.486	2.047	2.639	—	—	—	—	—	7.726	—	—	5.483	—	—	—
Mineral phase[2]	qtz	alb	alb	alb	epd	act	act	bio	chl	alb	hbl	act	alb	epd	hbl	chl

Table 4.3 Geothermometry calculations for several amphibole-plagioclase pairs from greenschist samples PKS11 and PKS12 using the representative chemical analyses (Tables S1 and S2 in the electronic supplementary material). *Mineral pairs of plagioclase + amphibole using the analysis numbers indicated in Tables S1 and S2 in the electronic supplementary material; **Temperature calculations using the edenite-tremolite geothermometer for hornblende-plagioclase assemblages with quartz (Holland & Blundy 1994).

Sample	**PKS11**									**PKS12**								
Pairs*	**p6/p8**	**p21/p8**	**p24/p8**	**p6/p19**	**p21/p19**	**p24/p19**	**p6/p20**	**p21/p20**	**p24/p20**	**p8/p3**	**p18/p3**	**p22/p3**	**p8/p15**	**p18/p15**	**p22/p15**	**p8/p20**	**p18/p20**	**p22/p20**
	Estimated pressure P = 150 MPa																	
T [°C]**	383.6	379.3	513.1	386.3	382.1	517.2	384.2	379.9	514.0	372.9	372.5	512.8	374.8	374.4	516.4	373.5	373.0	513.8
	Estimated pressure P = 225 MPa																	
T [°C]**	378.6	374.7	506.8	381.3	377.5	510.9	379.2	375.3	507.7	368.6	368.5	514.7	370.5	370.3	518.3	369.2	369.0	515.7
	Estimated pressure P = 300 MPa																	
T [°C]**	373.6	370.2	500.5	376.3	372.9	504.5	374.2	370.7	501.3	364.3	364.5	516.6	366.2	366.3	520.1	364.8	365.0	517.6

Table 4.4 Results of electron microprobe analysis on phengite of chiastolite hornfels sample PKS23 from 1.1 km SW of Kalami and calculation of structural formulae. Chemical composition of oxides in weight percent. Cations are indicated on the basis of 11 oxygens. All iron is treated as ferrous iron (Fe^{2+}).

Analysis	**p1**	**p2**	**p3**	**p4**	**p5**	**p6**	**p7**	**p8**	**p9**	**p19**	**p20**	**p25**	**p26**	**p27**	**p28**	**p29**	**p30**	**p31**	**p32**	**p33**	**p34**	**p35**	**p36**	**p37**
SiO_2	45.79	45.90	46.28	46.39	45.75	45.74	45.76	45.96	45.96	45.28	45.44	45.48	45.43	45.61	45.67	45.71	45.38	45.36	46.11	46.52	46.18	46.11	46.34	45.85
TiO_2	0.80	0.87	1.05	0.82	0.91	0.98	0.90	1.03	0.69	0.02	0.63	0.58	0.73	0.74	0.53	0.55	0.74	1.01	1.11	1.01	0.92	0.95	0.60	0.86
Al_2O_3	35.25	35.18	35.12	35.51	35.10	34.65	35.32	34.96	35.22	36.53	36.13	34.89	34.89	34.82	34.64	34.86	34.81	34.42	35.46	35.34	35.60	35.68	36.02	35.71
Cr_2O_3	0.06	0.06	0.10	0.04	0.07	0.05	0.04	0.06	0.04	0.02	0.03	—	0.02	0.01	—	0.02	0.05	0.03	0.06	0.03	—	0.06	0.02	0.02
FeO	1.12	1.10	1.02	1.06	1.08	1.15	1.05	1.02	1.08	0.48	0.85	1.00	1.10	0.89	0.97	1.06	1.06	0.99	1.05	1.08	1.06	1.01	1.00	1.09
MnO	0.04	0.03	0.02	0.02	0.01	0.01	0.03	0.02	—	—	0.03	0.02	—	0.03	0.02	0.01	0.01	—	0.03	0.01	0.03	—	0.02	0.02
MgO	0.49	0.54	0.56	0.55	0.51	0.59	0.48	0.59	0.49	0.26	0.40	0.53	0.48	0.47	0.55	0.51	0.51	0.53	0.49	0.57	0.50	0.51	0.47	0.51
CaO	0.01	0.01	0.02	—	0.02	0.01	—	—	—	0.01	0.01	0.01	0.02	0.04	0.03	0.02	0.01	0.02	—	0.01	—	0.01	0.01	0.01
NiO	0.02	0.01	—	—	—	—	0.01	0.02	0.01	0.01	0.01	0.01	—	—	—	0.04	—	—	—	—	0.04	—	0.01	—
Na_2O	0.51	0.51	0.46	0.52	0.57	0.53	0.46	0.51	0.48	0.64	0.49	0.51	0.52	0.53	0.52	0.55	0.54	0.50	0.55	0.55	0.54	0.50	0.53	0.53
K_2O	10.43	10.55	10.36	10.25	10.27	10.21	10.34	10.22	10.44	10.11	10.37	10.53	10.70	10.69	10.71	10.61	10.71	10.57	10.33	10.23	10.29	10.25	10.38	10.33
P_2O_5	0.01	—	—	0.01	—	0.02	0.03	—	—	—	0.02	—	—	0.01	0.02	0.02	—	—	—	0.01	—	—	—	0.01
Total	94.54	94.76	94.99	95.16	94.29	93.94	94.42	94.38	94.41	93.35	94.40	93.56	93.89	93.86	93.65	93.95	93.83	93.42	95.18	95.36	95.16	95.08	95.40	94.95
Si	3.072	3.073	3.085	3.083	3.074	3.085	3.070	3.082	3.083	3.055	3.046	3.081	3.073	3.083	3.094	3.088	3.073	3.081	3.068	3.085	3.071	3.067	3.071	3.058
Ti	0.040	0.044	0.053	0.041	0.046	0.050	0.045	0.052	0.035	0.001	0.032	0.029	0.037	0.038	0.027	0.028	0.038	0.051	0.055	0.050	0.046	0.047	0.030	0.043
Al	2.787	2.776	2.759	2.781	2.779	2.754	2.792	2.763	2.784	2.905	2.854	2.786	2.781	2.774	2.766	2.775	2.778	2.755	2.781	2.762	2.790	2.797	2.814	2.807
Fe^{2+}	0.063	0.062	0.057	0.059	0.061	0.065	0.059	0.057	0.061	0.027	0.048	0.056	0.062	0.050	0.055	0.060	0.060	0.056	0.058	0.060	0.059	0.056	0.055	0.061
Mn	0.002	0.002	0.002	0.001	0.001	0.001	0.002	0.001	—	—	0.002	0.001	—	0.002	0.001	0.001	0.001	—	0.001	0.001	0.002	—	0.001	0.001
Mg	0.049	0.054	0.055	0.054	0.051	0.059	0.048	0.059	0.049	0.026	0.039	0.054	0.048	0.048	0.056	0.051	0.052	0.054	0.049	0.056	0.049	0.050	0.046	0.051
Ca	0.001	0.001	0.001	—	0.001	0.001	—	—	—	0.001	0.001	0.001	0.001	0.003	0.002	0.001	0.001	0.001	—	0.000	—	0.001	0.001	0.001
Na	0.067	0.066	0.060	0.066	0.074	0.070	0.060	0.066	0.063	0.083	0.063	0.068	0.068	0.070	0.068	0.072	0.071	0.066	0.071	0.070	0.070	0.065	0.067	0.069
K	0.893	0.901	0.881	0.869	0.880	0.878	0.885	0.874	0.893	0.870	0.887	0.910	0.923	0.922	0.926	0.914	0.925	0.916	0.877	0.866	0.873	0.870	0.878	0.879
∑ cations	6.974	6.978	6.953	6.954	6.968	6.962	6.961	6.954	6.968	6.968	6.971	6.986	6.995	6.988	6.993	6.990	6.999	6.981	6.960	6.951	6.960	6.954	6.964	6.969

Table 4.5 Results of electron microprobe analysis on phengite of chiastolite hornfels sample PKS24 from 125 m S of Agia Triada and calculation of structural formulae. Chemical composition of oxides in weight percent. Cations are indicated on the basis of 11 oxygens. All iron is treated as ferrous iron (Fe^{2+}).

Analysis	p1	p2	p3	p4	p5	p6	p7	p8	p9	p10	p13	p14	p15	p16	p17	p18	p19	p20	p21
SiO_2	45.68	45.74	46.04	45.63	46.00	46.16	46.49	46.32	46.79	46.05	46.04	45.99	46.21	45.86	45.83	46.10	45.89	46.12	46.15
TiO_2	0.38	0.31	0.37	0.49	0.44	0.55	0.59	0.47	0.42	0.64	0.45	0.35	0.52	0.54	0.56	0.44	0.50	0.72	0.90
Al_2O_3	35.66	35.67	35.53	35.70	35.47	35.63	35.70	35.79	35.86	35.72	35.62	35.88	35.27	35.78	35.69	35.26	35.61	35.01	34.92
Cr_2O_3	0.03	0.01	0.01	0.04	0.04	0.03	0.05	—	0.02	0.05	0.03	0.02	0.04	0.06	0.03	—	0.03	0.05	0.07
FeO	1.05	1.07	1.00	1.04	1.11	1.06	1.07	1.12	0.97	1.08	1.05	1.07	1.13	1.07	1.09	0.96	1.12	1.25	1.00
MnO	—	—	0.03	0.02	0.02	—	0.01	0.02	—	—	—	—	0.02	0.02	—	0.01	0.02	0.05	0.03
MgO	0.40	0.46	0.47	0.41	0.43	0.40	0.38	0.43	0.42	0.36	0.36	0.38	0.48	0.44	0.41	0.44	0.42	0.44	0.44
CaO	0.03	0.01	0.02	—	—	0.01	—	—	0.01	—	—	—	0.01	0.01	—	0.01	0.01	—	0.02
NiO	0.02	—	—	—	—	0.02	0.01	0.02	0.03	0.02	0.01	—	0.03	0.01	—	0.03	—	0.02	—
Na_2O	0.57	0.54	0.56	0.57	0.56	0.55	0.60	0.54	0.56	0.54	0.58	0.56	0.51	0.54	0.55	0.56	0.53	0.53	0.53
K_2O	10.44	10.35	10.51	10.52	10.42	10.52	10.28	10.39	10.33	10.33	10.24	10.56	10.55	10.47	10.40	10.56	10.51	10.35	10.41
P_2O_5	0.01	—	0.02	—	0.02	0.02	—	—	0.03	—	0.02	0.01	0.01	—	—	0.02	0.04	—	—
Total	94.27	94.16	94.54	94.41	94.52	94.95	95.17	95.09	95.43	94.79	94.39	94.82	94.77	94.80	94.55	94.38	94.67	94.53	94.47
Si	3.070	3.073	3.083	3.063	3.082	3.080	3.088	3.081	3.097	3.074	3.084	3.072	3.091	3.065	3.069	3.093	3.073	3.092	3.094
Ti	0.019	0.016	0.019	0.025	0.022	0.028	0.030	0.023	0.021	0.032	0.023	0.018	0.026	0.027	0.028	0.022	0.025	0.036	0.045
Al	2.824	2.824	2.804	2.824	2.801	2.802	2.795	2.806	2.798	2.811	2.812	2.825	2.780	2.819	2.816	2.788	2.810	2.766	2.759
Fe^{2+}	0.059	0.060	0.056	0.058	0.062	0.059	0.059	0.062	0.054	0.060	0.059	0.060	0.063	0.060	0.061	0.054	0.063	0.070	0.056
Mn	—	—	0.002	0.001	0.001	—	0.001	0.001	—	—	—	—	0.001	0.001	—	0.001	0.001	0.003	0.001
Mg	0.040	0.046	0.046	0.041	0.043	0.040	0.038	0.043	0.041	0.036	0.036	0.038	0.048	0.043	0.041	0.044	0.042	0.044	0.044
Ca	0.002	0.001	0.001	—	—	0.001	—	—	0.001	—	—	—	0.001	0.001	—	0.001	0.001	—	0.001
Na	0.075	0.070	0.072	0.074	0.072	0.071	0.077	0.070	0.072	0.070	0.075	0.073	0.066	0.070	0.071	0.073	0.069	0.069	0.069
K	0.895	0.887	0.898	0.901	0.891	0.895	0.871	0.882	0.872	0.880	0.875	0.900	0.900	0.893	0.888	0.904	0.898	0.885	0.890
∑ cations	6.984	6.978	6.981	6.987	6.976	6.975	6.958	6.968	6.955	6.963	6.963	6.984	6.976	6.980	6.974	6.979	6.981	6.966	6.961

Table 4.6 Pb, U and Th LA-ICP-MS results for one zircon grain from chiastolite hornfels sample Pf040 from the Asterousia Crystalline Complex SE of Agios Georgios. Spot size = 30 µm, depth of crater ca. 15 µm. $^{206}Pb/^{238}U$ error is the quadratic additions of the within run precision (2 standard errors) and the external reproducibility (2 standard deviations) of the reference zircon. $^{207}Pb/^{206}Pb$ error propagation (^{207}Pb signal dependent) following Gerdes & Zeh (2009). $^{207}Pb/^{235}U$ error is the quadratic addition of the $^{207}Pb/^{206}Pb$ and $^{206}Pb/^{238}U$ uncertainty. Errors of the mean values are given at 2σ level.

	$^{207}Pb^a$ [cps]	U^b [ppm]	Pb^b [ppm]	Th/U^b	$^{206}Pbc^c$ [%]	$^{206}Pb/^{238}U^d$	± 2σ [%]	$^{207}Pb/^{235}U^d$	± 2σ [%]	$^{207}Pb/^{206}Pb^d$	± 2σ [%]	ρ^e	$^{206}Pb/^{238}U$	± 2σ [Ma]	$^{207}Pb/^{235}U$	± 2σ [Ma]	$^{207}Pb/^{206}Pb$	± 2σ [Ma]	Conc.^{f} [%]
Pf040 (single zircon grain)																			
A305	10664	1300	19	0.00	0.7	0.01158	3.1	0.07560	5.5	0.04737	4.6	0.57	74	2	74	4	68	109	109
A306	7032	975	14	0.00	0.8	0.01164	3.2	0.07631	6.7	0.04755	5.9	0.47	75	2	75	5	77	141	97
A307	10562	736	11	0.33	3.9	0.01280	3.4	0.08466	14.8	0.04796	14.5	0.23	82	3	83	12	97	342	84

A307) yielded less concordant $^{206}Pb/^{238}U$ ages of 75 ± 2 Ma and 82 ± 3 Ma. The older age has the lowest concordance and also the lowest uranium content and the highest amount of Pbc. The two analyses with the younger ages yielded a concordia age at 74 ± 2 Ma with a mean standard weighted deviation (MSWD) of 0.0082 and a probability of concordance of 0.93 (Fig. 4.11). These two analyses have Th/U ratios of zero, while analysis A307 has a Th/U ratio of 0.33. Analyses on seven more zircon grains from the same sample yielded much older, inherited ages, most of which are Guadelupian to Early Triassic and Early Devonian. The results of these analyses will be published elsewhere along with further detrital zircon age data from Asterousia-type metasediments.

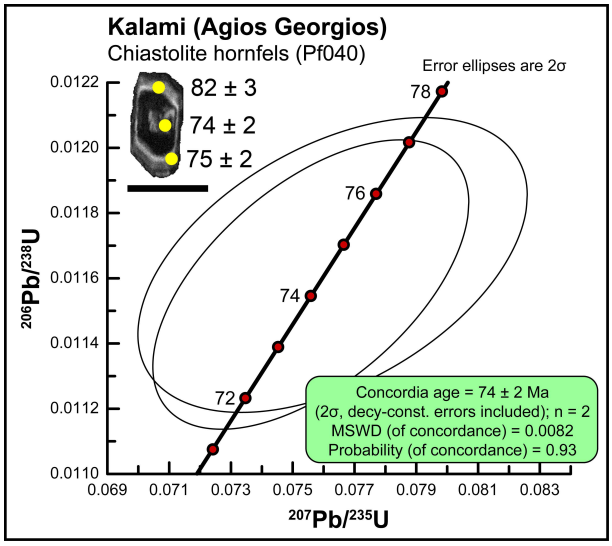

Fig. 4.11 U-Pb concordia diagram of two LA-ICP-MS analyses of one zircon grain from chiastolite hornfels (sample Pf040, SE of Agios Georgios). Numbering and error of the ellipses are given in Table 4.6. The cathodoluminescence image shows a euhedral, subangular and pristine zircon grain with growth zoning, and is free from inclusions. Scale bar: 100 µm.

4.6 Discussion

4.6.1 The Uppermost Unit south of the Dikti Mountains

Based on the new geological map and the data presented above, the Uppermost Unit south of the Dikti Mountains can be subdivided into three different tectonometamorphic subunits. These are from bottom to top: (1) the Arvi Unit consisting of prehnite-pumpellyite facies slates, meta-pillow basalts and metadolerite; (2) the Theodorii Greenschist; and (3) the ACC-type rocks consisting of orthoamphibolite, metasedimentary rocks and serpentinite. All these subunits have been thrust on top of non-metamorphic Late Eocene Pindos flysch. Prehnite-pumpellyite facies rocks of the study area have been ascribed to the Arvi Unit by Robert & Bonneau (1982). However, greenschist facies rocks resting tectonically on top of the Arvi Unit have not been described previously. The Theodorii Greenschist compares well with greenschist facies rocks exposed on Anafi (Reinecke et al. 1982) and in the area west of Melambes (Martha et al. 2017). In these areas, the greenschist is also resting below amphibolite facies ACC-type rocks.

Amphibolite facies rocks of the study area have been correlated with the ACC by Bonneau (1972). The ACC sequence south of the Dikti Mountains compares well with the sequences described from the western Asterousia Mountains (Koepke & Seidel 1984), the area west of Melambes (Martha et al. 2017) and from Anafi (Reinecke et al. 1982; Martha et al. 2016) (Fig. 4.12). A correlation is further confirmed by the composition of the metasedimentary succession and orthoamphibolite having a

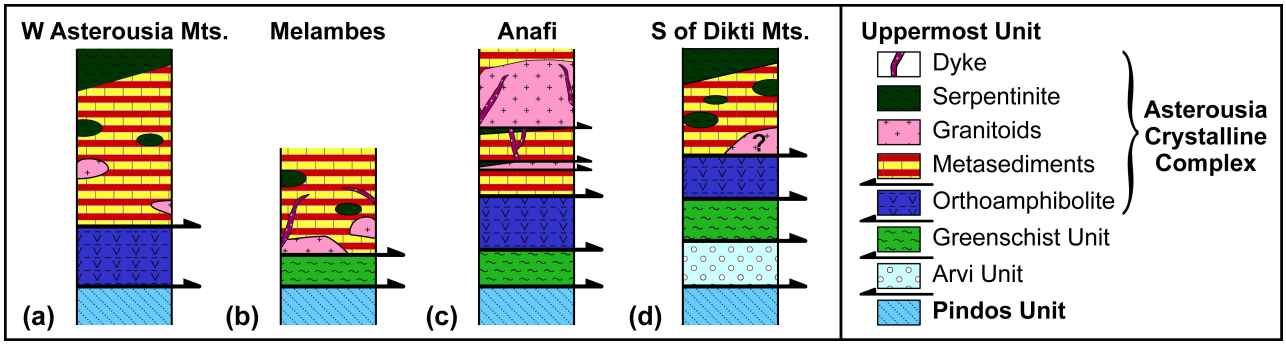

Fig. 4.12 Columns showing the tectonostratigaphic sequence of the Uppermost Unit in (a) the western Asterousia Mountains between Lendas and Miamou (after Koepke & Seidel 1984), (b) the area west of Melambes (after Martha et al. 2017), (c) Anafi (after Reinecke et al. 1982; Martha et al. 2016), and (d) the study area between Pefkos, Kalami and Sykologos. The columns are not to scale. Note that the Arvi Unit occurs in the western Asterousia Mountains (e.g. Thorbecke 1987) but has not been considered by Koepke & Seidel (1984).

tholeiitic geochemical signature similar to orthoamphibolite from the western Asterousia Mountains and Anafi (Seidel et al. 1976, 1981; Reinecke et al. 1982; Thorbecke 1987).

The Arvi Unit, the Theodorii Greenschist and the ACC-type rocks are separated by thrusts, with higher grade metamorphic rocks resting on top of lower grade metamorphic rocks. One additional thrust is present within the ACC between the orthoamphibolite and the metasedimentary rocks. The Arvi Unit and the Theodorii Greenschist are separated by a brittle thrust related with NW–SE-oriented transport while the thrust contact between the Theodorii Greenschist and the Asterousia-type rocks was active under semi-ductile conditions. On Anafi, however, the Anafi Greenschist is separated from the orthoamphibolite by a mylonitic shear zone (Martha et al. 2016). A considerable difference between the Asterousia-type rocks of the study area and those exposed at other places on Crete and in the Cyclades is the lack of granitoid intrusions inside the metasedimentary succession. These intrusions, however, should be close to the studied rocks because of the strong contact metamorphism recorded by chiastolite hornfels (see below).

4.6.2 Geochronological data

LA-ICP-MS data from one zircon grain of chiastolite hornfels yielded three $^{206}Pb/^{238}U$ ages between 74 ± 2 Ma and 82 ± 3 Ma. The concordia age calculated from the two most concordant analyses is 74 ± 2 Ma. Similar LA-ICP-MS and ID-TIMS zircon ages have previously been reported from Asterousia-type (meta)granitoids exposed in the northern Ierapetra Graben of eastern Crete (74.5 ± 0.25 Ma for quartzdiorite; Kneuker et al. 2015), west of Melambes in central Crete (71.9 ± 0.6 to 76.9 ± 0.3 Ma for metadiorite and orthogneiss; Martha et al. 2017) and on Anafi (74.0 ± 0.1 Ma for the main zircon population from granodiorite; Martha et al. 2016). Other similar U-Pb zircon ages (peak at 70–80 Ma) have been reported from detrital zircons of the Cycladic Blueschist Unit on Tinos (Hinsken et al. 2016), where Asterousia-type granitoids might have been a source for these zircons.

There are two possibilities to explain Campanian zircon inside chiastolite hornfels from the study area: (1) the zircon is of detrital origin derived from Asterousia-type (meta)granitoids and deposited together with the clastic components of the hornfels protolith; (2) the analysed zircon was growing due to contact metamorphism related to the intrusion of an adjacent Campanian pluton. The striking euhedral shape of the zircon rules out a detrital provenance. The cathodoluminescence images, in turn, imply a magmatic formation of the zircon while low Th/U ratios point to a metamorphic origin. Because chiastolite hornfels occurs only locally inside the Asterousia-type metasedimentary succession, we believe that it reflects a contact aureole around a non-exposed intrusive body. Based on the pressure constraints (see below), the intrusion should have occurred at a depth < 10 km. A comparable shallow level of intrusion was obtained for quartz diorite 25 km further northeast in the northern Ierapetra Graben (Pachia Ammos area; Kneuker et al. 2015). K-Ar biotite ages from sillimanite-bearing micaschist south of Pefkos (Seidel et al. 1981) are ca. 5–6 Ma years younger than our U-Pb zircon age. For this reason, the U-Pb age of 74 ± 2 Ma should reflect the time of the peak temperature during contact metamorphism and thus the time of pluton emplacement.

4.6.3 Deformation conditions and kinematics

The petrographic data and deformation microstructures presented above can be used to estimate the deformation temperature in the individual subunits of the Uppermost Unit. Mineral assemblages in the slates (chlorite + albite + quartz + white mica) and the volcanic rocks (albite + pumpellyite + chlorite + white mica ± epidote; Robert & Bonneau 1982) from the Arvi Units indicate deformation at very low temperatures compatible with the prehnite-pumpellyite facies (T = 250–350 °C; Liou et al. 1987). Kinking and asymmetric pressure shadows behind rigid feldspar indicating top-to-the SE shearing are consistent with these deformation conditions.

The mineral assemblage observed in the Theodorii Greenschist indicates greenschist facies conditions and compares well with mineral assemblages reported from the Anafi Greenschist (Reinecke et al. 1982; Martha et al. 2016) and the Akoumianos Greenschist (Martha et al. 2017). Asymmetric pressure shadows of actinolite and chlorite behind K-feldspar indicate a top-to-the SE sense of shear. Hornblende-plagioclase geothermometry using the edenite-tremolite geothermometer for hornblende-plagioclase assemblages with quartz of Holland and Blundy (1994) yielded temperature estimates of 360 to 520 °C. Lower deformation temperatures for greenschist facies deformation in the study area than for the Akoumianos Greenschist from the area west of Melambes (400–560 °C; Martha et al. 2017) is indicated by the very low anorthite content in plagioclase.

Except for serpentinite, all rock types from the Asterousia-type section show evidence for significant changes in both the degree of deformation and the finite strain. The oldest deformation event

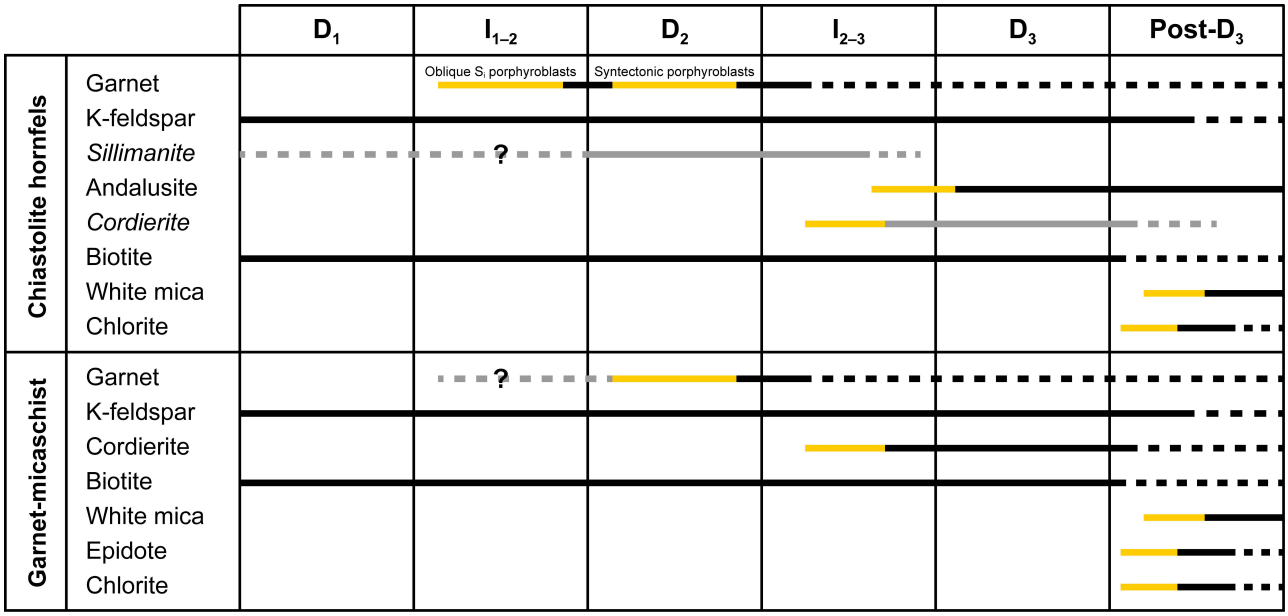

Fig. 4.13 Crystallization-deformation diagram for chiastolite hornfels and garnet-micaschist with respect to deformation (D) and intertectonic (I) stages. Stability of phases not observed but presumed is indicated in grey. Orange indicates growth of phases. Plagioclase and quartz are not indicated.

recognized is preserved in form of an internal foliation (S_i) in garnet porphyroblasts inside chiastolite hornfels. These garnet porphyroblasts must have grown intertectonically after development of $S_i = S_1$ (Fig. 4.13). Chessboard-type subgrains in quartz of calcsilicate rock and chiastolite hornfels indicate high-temperature deformation (T > ca. 650 °C; Passchier & Trouw 2005 and references therein). Furthermore, large and slightly polygonal quartz grains with contacts tending to form triple junctions suggest grain boundary area reduction, which is also a characteristic feature at T > 650 °C. Undulatory extinction in K-feldspar from chiastolite hornfels, kinking and deformation twinning in plagioclase from orthoamphibolite and fracturing of diopside inside calcsilicate rock should have developed at T > 650 °C. Moreover, shape-preferred orientation defined by the alignment of biotite in chiastolite hornfels should have developed during amphibolite facies shearing (D_2) in the muscovite-out field (Fig. 4.13). Garnet porphyroblasts imply rotation during syntectonic growth. Seidel et al. (1981) constrained metamorphic conditions for D_2 using thin sections of rocks south of the Dikti Mountains (area S and SW of Pefkos) and from other ACC exposures on Crete at P = 400–500 MPa and T_{max} = 700 °C (Fig. 4.14). A top-to-the SE sense of shear for D_2 in the study area is implied from plagioclase σ-clasts and asymmetric pressure shadows of plagioclase in orthoamphibolite.

The growth of large chiastolite grains in chiastolite hornfels post-dates the pre-existing S_2-foliation (Fig. 4.13). Growth of chiastolite should have occurred in the muscovite-out field at T = 600–680 °C and P_{max} = 200 MPa (Fig. 4.14) as white mica must have formed later (see below). Such very high temperatures at very low pressure are characteristic for contact metamorphism in the close vicinity to an intrusive body. The presence of a nearby pluton is consistent with the $^{206}Pb/^{238}U$ ages of one zircon grain from chiastolite hornfels. These granitoids have either been eroded or are present at slightly

deeper structural levels with respect to the recent exposures. Cordierite, which is typically found along with chiastolite in chiastolite hornfels, was not observed. However, cordierite was found in one sample of garnet-micaschist intercalated with chiastolite hornfels and should likewise have formed during contact metamorphism. Thus, we assume a static period following D_2 with no significant strain, but with intrusion of granitoids in its late stages that induced contact metamorphic growth of new phases. Andalusite might have formed at the expense of previously stable sillimanite (Fig. 4.13), which was not observed in chiastolite hornfels.

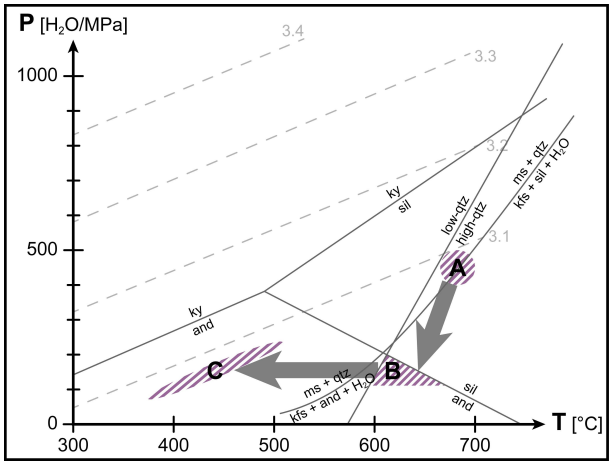

Fig. 4.14 Petrogenetic grid with isopleths of key metamorphic reactions in metapelites according to the KFMASH system of Spear & Cheney (1989) based on thermodynamic data of Berman, Brown & Greenwood (1985) and Berman (1988). The transition from low- to high-quartz marks the formation of chessboard subgrains in quartz (Kruhl 1996). Si isopleths for Si content p.f.u. in phengitic white mica (dashed lines) after Massonne & Schreyer (1987) and assuming the limiting assemblage K-feldspar – phlogopite (biotite) – quartz – phengite (white mica). Hashed lines indicate P–T estimations for A: HT–LP metamorphism of the ACC according to Seidel et al. (1981), corresponding to D_2, B: growth of chiastolite in chiastolite hornfels during contact metamorphism at the end of $I_{2–3}$ and C: growth of white mica deduced from Si content p.f.u. in phengite (Tables 4.4 and 4.5). Grey arrows indicate the inferred P–T path. Mineral abbreviations according to Kretz (1983).

Pressure shadows made of biotite and quartz behind chiastolite as well as boudinage of chiastolite grains. Marginal drag observed in some chiastolite grains indicate that subsequent deformation (D_3) affected chiastolite hornfels already before the end of chiastolite growth. Asymmetric pressure shadows behind chiastolite indicate a top-to-the SE sense of shear during D_3. Quartz in chiastolite hornfels did not recrystallize during D_3, probably because strain was not high enough. White mica in both chiastolite hornfels and micaschist is present as cross-mica, which shows no relation to any pre-existing fabric. Since white mica was not deformed, it should have grown post-kinematically with respect to the previously described deformation events ($D_{1–3}$). It must have formed in a static environment at the expense of biotite and garnet and probably cordierite during retrograde metamorphism following D_3. Chlorite and epidote should likewise have formed during retrograde metamorphism (Fig. 4.13). Taking into consideration that the Si values in phengitic white mica are very low (3.077 ± 0.002 p.f.u.) and that retrograde metamorphism should have taken place in the stability fields of chlorite and epidote, the growth of white mica should have taken place at T_{max} = 500 °C and P_{max} = 220 MPa (Fig. 4.14).

4.6.4 Timing of shearing and regional implications

The oldest deformation in the ACC-type rocks is preserved as $S_i = S_1$ in garnet porphyroblasts. The conditions during the related D_1 deformation stage are unknown. Subsequent D_2 top-to-the SE shearing must have taken place at deep structural levels and can be correlated with high temperature amphibolite facies shearing of the ACC from other areas (P = 400–500 MPa and T_{max} = 700 °C; Seidel et al. 1981).

It should be older than middle to late Campanian intrusion of granitoids inside the ACC (Martha et al. 2017).

Although (meta)granitoids are lacking in the study area, petrographic observations of chiastolite hornfels, garnet-micaschist and contact metamorphic zircon from chiastolite hornfels provide evidence for the development of a contact aureole around granitoid intrusions. This compares well with the situation in the Pachia Ammos area, where contact metamorphism related to Asterousia-type intrusions is revealed by increasing grain size of calcite in the surrounding rock (marble) with decreasing distance from a dioritic intrusion (Kneuker et al. 2015). The ACC in eastern Crete (study area and exposures in the northern Ierapetra Graben) should therefore have faced uplift and exhumation to upper crustal levels following peak metamorphic conditions (D_2). Furthermore, the rock sequence must have cooled down to that point that contact-metamorphic heating could trigger the growth of new phases under much lower pressure conditions compared to the metamorphic peak.

In the area west of Melambes in central Crete and in the Cyclades (Anafi), there is no evidence for contact metamorphism in the Asterousia-type sections. Granitoid intrusions inside the metasedimentary rocks occurred at deep crustal levels and while amphibolite facies rocks were still hot (Martha et al. 2016, 2017). Geochronological data suggest that the metasedimentary succession of the ACC on Crete and in the Cyclades was intruded by granitoids between 80 and 72 Ma (Be'eri-Shlevin et al. 2009; Kneuker et al. 2015; Martha et al. 2016, 2017) (Fig. 4.15). These U-Pb ages are in line with the concordia age calculated for zircon from chiastolite hornfels in the study area (74 ± 2 Ma). Thus, in the area south of the Dikti Mountains, the growth of chiastolite, which post-dates D_2 top-to-the SE shearing and pre-dates the main phase of D_3 top-to-the SE shearing, should be late Campanian in age. In the Pachia Ammos area, Kneuker et al. (2015) found no evidence for post-intrusive ductile top-to-the SE shearing of the granitoids, while in the Melambes area D_3-shearing is responsible for transforming the granitoids into orthogneiss and metadiorite (Martha et al. 2017). The ACC-type exposures south of the Dikti Mountains are therefore considered to occupy an intermediate position between the exposures in the area W of Melambes and in the northern Ierapetra Graben.

The observations on the different evolution of Asterousia-type exposures from central and eastern Crete during contact metamorphism are of particular interest as they suggest an E–W metamorphic field gradient for Crete that resulted from stronger uplift and exhumation of the ACC-type rocks of eastern Crete. Such an E–W metamorphic field gradient is also known for Late Oligocene to Early Miocene subduction-related metamorphism of the lower Cretan nappe system. P–T estimates for the Phyllite-Quartzite Unit s.l. from western Crete (P = 800–1700 MPa; T = 350–450 °C) indicate stronger metamorphic overprint than for exposures from eastern Crete (P = 400–800 MPa; T = 250–350 °C) (e.g. Seidel et al. 1982; Theye et al. 1992). The metamorphic field gradient for the Phyllite-Quartzite

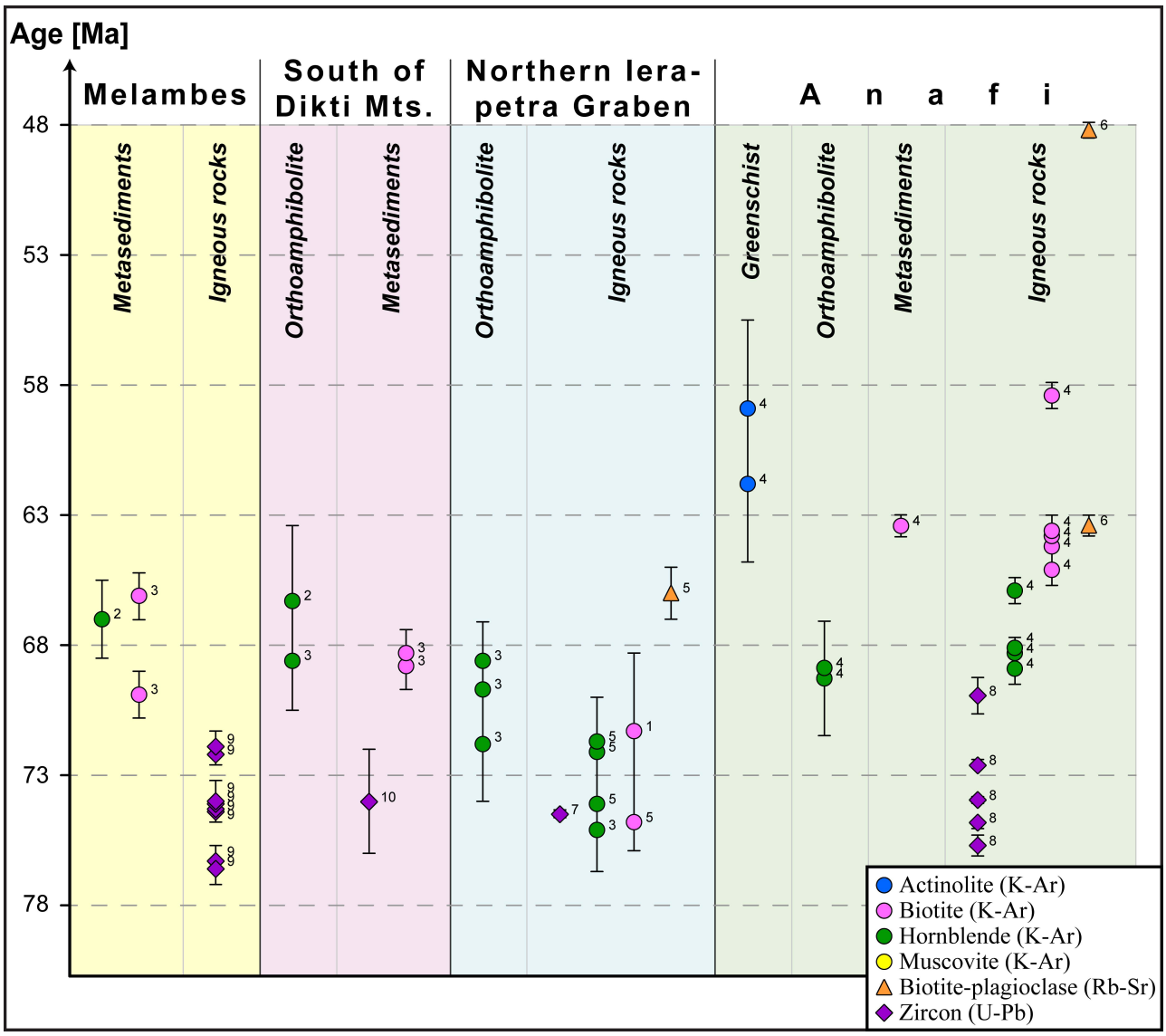

Fig. 4.15 Scatter chart summarizing radiometric age data from the Uppermost Unit of Crete and Anafi. Data sources: [1]Lippolt & Baranyi (1976), [2]Seidel et al. (1976), [3]Seidel et al. (1981), [4]Reinecke et al. (1982), [5]Langosch et al. (2000), [6]Be'eri-Shlevin et al. (2009), [7]Kneuker et al. (2015), [8]Martha et al. (2016), [9]Martha et al. (2017), [10]this study. Data from Lippolt & Baranyi (1976) and Seidel et al. (1976) were recalculated in Seidel et al. (1981). For convenience, no analyses with error margins > 3.0 Ma are included, except for one age obtained from the Anafi Greenschist (after Reinecke et al. (1982).

Unit s.l. shows the same direction as the one observed in the Uppermost Unit on Crete. The related westward crustal tilting of both nappe systems, however, occurred at strikingly different ages. Whereas the tilting of the lower Cretan nappe system occurred during the Miocene, the tilting of the Uppermost Unit occurred already during the Late Cretaceous, meaning that the metamorphic field gradient already existed when the Uppermost Unit was emplaced on top of the nappes resting underneath.

The ACC-type rocks south of the Dikti Mountains cooled down below the closure temperatures of hornblende (530 ± 40 °C; Harrison 1981) and biotite (310 ± 30 °C; Harrison et al. 1985) during the Maastrichtian. Orthoamphibolite from the Viannos Municipality yielded K-Ar hornblende ages of 66.3 ± 2.9 Ma to 68.6 ± 1.9 Ma (Seidel et al. 1976, 1981), while sillimanite-bearing micaschist yielded K-Ar biotite ages of 68.3 ± 0.9 Ma to 68.8 ± 0.9 Ma (Seidel et al. 1981). These ages compare well with

other K-Ar biotite and hornblende ages from the Melambes area, Anafi and the northern Ierapetra Graben (Fig. 4.15). Growth of white mica, chlorite and epidote in chiastolite hornfels and micaschist should have occurred during Maastrichtian cooling and retrograde metamorphism of the ACC.

Stacking of units commenced with top-to-the SE shearing of the ACC on top of the Theodorii Greenschist that formed the northern margin of the Pindos realm (see also the geodynamical model presented in Martha et al. 2017). K-Ar actinolite data from the comparable Anafi Greenschist yielded cooling ages of 58.9 ± 3.4 Ma to 61.8 ± 3.0 Ma. The closure temperature of actinolite (470 ± 25 °C; Dahl 1996) is close to the peak temperature of greenschist facies metamorphism. This is why greenschist facies shearing should be Middle to Late Palaeocene in age. Subsequent exhumation and ongoing top-to-the SE movement led to prehnite-pumpellyite facies thrusting of the Theodorii Greenschist and the ACC-type rocks on top of the Arvi Unit. The age of prehnite-pumpellyite facies metamorphism of the Arvi Unit has not been dated but must be post-Maastrichtian due to the protolith ages (Tataris 1964). Microstructures from the Arvi slates indicate a top-to-the SE sense of shear for this event.

The age of thrusting of the Uppermost Unit on top of the Pindos Unit should be Latest Eocene or younger considering the age of the Pindos flysch. The Pindos flysch compares well with the flysch sequences from the area west of Melambes and on Anafi, where brittle top-to-the SE kinematics during the Late Eocene have been constrained for thrusting of the Uppermost Unit on top of the Pindos Unit (Martha et al. 2016). NE–SW-trending striation in brittle shear zones in quartzite and SW-vergent folds observed in the Uppermost Unit are correlated with W(SW)-vergent folds found in the Pindos flysch south of Sykologos and indicate a mutual evolution of the Uppermost and Pindos units. The shear zone striation can be correlated with NNE–SSW to NE–SW-directed shortening related to strike-slip movements reported from brittle faulting of diorite and quartzdiorite from the ACC in the Pachia Ammos area (northern Ierapetra Graben) by Kneuker et al. (2015). Furthermore, Tortorici et al. (2012) reported semi-brittle to brittle top-to-the SSW structures from the Uppermost Unit west of Melambes and in the Ardaktos Graben. NE–SW shortening affecting the Uppermost and Pindos units took place at upper crustal levels and might result from crustal shortening following SW-directed movement of the Anatolian microplate starting in the late Tortonian (ten Veen & Postma 1999).

4.7 Conclusions

Based on our new geological map and the data presented above, the following conclusions are drawn:

(1) The Uppermost Unit south of the Dikti Mountains consists of the Arvi Unit at the base, the Theodorii Greenschist in the central part and ACC-type rocks on top.

(2) The ACC-type metasediments are affected by contact metamorphism, which is related to a non-exposed pluton. The age of the intrusion and contact metamorphism (74 ± 2 Ma) is compatible with published intrusion ages from other areas.

(3) The ACC-type rocks underwent at least three ductile deformation phases: D_1 with unknown kinematics and conditions, only preserved as internal foliation ($S_i = S_1$) in garnet porphyroblasts; D_2 = pre-middle Campanian amphibolite facies top-to-the SE shearing, which led to the dominant foliation; D_3 = top-to-the SE shearing, which started during the late phase of Campanian intrusions and related contact metamorphism.

(4) SE-directed thrusting emplaced the ACC-type rocks on top of the Theodorii Greenschist under greenschist facies conditions. Thrusting of the ACC-type rocks and the Theodorii Greenschist on top of the Arvi Unit occurred under prehnite-pumellyite facies conditions and is also associated with top-to-the SE kinematics. This compares well with the shear sense inferred from exposures of comparable rocks in the area west of Melambes and on Anafi.

(5) Tilting of the Cretan nappe pile responsible for the E–W directed metamorphic field gradient (with respect to the intrusion level of late Cretaceous granitoids) should have been established during the mid-Late Cretaceous.

4.8 Acknowledgements

We are grateful to Maria Bladt and Nils Prawitz for help with thin section production, Rainer Petschick for help with XRD analysis, Bärbel Schmincke for help with micro-CT analysis, Heidi Höfer and Markus Schölmerich for help with EMP analysis and Linda Marko for help with isotopic analyses (all Goethe-University Frankfurt). Mark Peinl (Limeshain) is thanked for invaluable help with evaluation of the micro-CT data and Jolien Linckens is thanked for fruitful discussions. The first author gratefully acknowledges financial support for fieldwork by ERASMUS (Leonardo-da-Vinci programme; grant agreement no. 2013-1-DE2-LEO02-16568) and J.J.B. and P.M.N. acknowledge the financial support for geological mapping by the *Vereinigung von Freunden und Förderern der Goethe-Universität Frankfurt*.

4.9 References

Allmendinger, R.W., Cardozo, N. & Fisher, D.M. (2012): *Structural geology algorithms: vectors and tensors*. – Cambridge University Press, 289 p.; Cambridge.

Altherr, R., Kreuzer, H., Lenz, H., Wendt, I., Harre, W. & Dürr, S. (1994): Further evidence for a Late-Cretaceous low pressure/high-temperature terrane in the Cyclades, Greece. Petrology and geochronology of crystalline rocks from the islands of Donoussa and Ikaria. – *Chemie der Erde*, **54**: pp. 319–328.

Altherr, R., Seidel, E., Okrusch, M., Schliestedt, M., Reinecke, T., Kreuzer, H., Harre, W., Klein, H. & Dürr, S. (1980): Metamorphic rocks associated with ophiolites in Greece: petrology and geochronology. – In: Panayiotou, A. (ed.) *International Ophiolite Symposium, Nicosia - Cyprus, 1–8 April, 1979. Abstracts of papers submitted*. Τμήμα Γεωλογικής Επισκόπησης [Geological Survey Department], pp. 9–10; Λευκωσία [Nicosia].

Aubouin, J. & Dercourt, J. (1965): Sur la géologie de l'Égée: regard sur la Crète (Grèce). – *Bulletin de la Société Géologique de France, série 7*, **7**: pp. 787–821.

Baranyi, I., Lippolt, H.J. & Todt, W. (1975): Kalium-Argon-Datierungen an zwei Magmatiten von Kalo Chorio, Nord-Ost-Kreta. – *Neues Jahrbuch für Geologie und Paläontologie, Monatshefte*, **5**: pp. 257–262.

Be'eri-Shlevin, Y., Avigad, D. & Matthews, A. (2009): Granitoid intrusion and high temperature metamorphism in the Asteroussia Unit, Anafi Island (Greece): petrology and geochronology. – *Israel Journal of Earth Sciences*, **58** (1): pp. 13–27. DOI: 10.1560/IJES.58.1.13.

Berman, R.G. (1988): Internally-Consistent Thermodynamic Data for Minerals in the System Na_2O–K_2O–CaO–MgO–FeO–Fe_2O_3–Al_2O_3–SiO_2–TiO2–H_2O–CO_2. – *Journal of Petrology*, **29** (2): pp. 445–522. DOI: 10.1093/petrology/29.2.445.

Berman, R.G., Brown, T.H. & Greenwood, H.J. (1985): An internally consistent thermodynamic data for rock-forming minerals in the system SiO_2–TiO_2–Al_2O_3–Fe_2O_3–CaO–MgO–FeO-K_2O–Na_2O–H_2O–CO_2. – *Atomic Energy of Canada Technical report*, **377**: pp. 1–62.

Bonneau, M. (1972): La nappe métamorphique de l'Asteroussia, lambeau d'affinités pélagoniennes charrié jusque sur la zone de Tripolitza de la Crète moyenne (Grèce). – *Comptes Rendus de l'Académie des Sciences, série D*, **275**: pp. 2303–2306.

Bonneau, M. (1973): Les différentes «séries ophiolitifères» de la Crète: une mise au point. – *Comptes Rendus de l'Académie des Sciences, série D*, **276**: pp. 1249–1252.

Bonneau, M. (1984): Correlation of the Hellenide nappes in the south-east Aegean and their tectonic reconstruction. – *Geological Society, London, Special Publications*, **17**: pp. 517–527. DOI: 10.1144/GSL.SP.1984.017.01.38.

Bonneau, M., Angelier, J. & Epting, M. (1977): Réunion extraordinaire de la Société Géologique de France en Crète. – *Bulletin de la Société Géologique de France, série 7*, **19** (1): pp. 87–102. DOI: 10.2113/gssgfbull.S7-XIX.1.87.

Bonneau, M., Blake Jr., M.C., Geyssant, J., Kienast, J.-R., Lepvrier, C., Maluski, H. & Papanikolaou, D.J. (1980): Sur la signification des séries métamorphiques (schistes bleus) des Cyclades (Hellénides, Grèce). L'exemple de l'île de Syros. – *Comptes Rendus de l'Académie des Sciences, série D*, **29**: pp. 1463–1467.

Bonneau, M. & Vidakis, M. (2002): *Γεωλογικός χάρτης της Ελλάδος 1:50.000. Φύλλο Άνω Βιάννος [Geological map of Greece 1:50,000. Ano Viannos sheet]*. – Geological map, Ινστιτούτο γεωλογικών και μεταλλεύτικων έρευνων [Institute of Geology and Mineral Exploration]; Αθήνα [Athens].

Burkhard, M. (1993): Calcite twins, their geometry, appearance and significance as stress-strain markers and indicators of tectonic regime: a review. – *Journal of Structural Geology*, **15** (3–5): pp. 351–368. DOI: 10.1016/0191-8141(93)90132-T.

Cardozo, N. & Allmendinger, R.W. (2013): Spherical projections with OSXStereonet. – *Computers & Geosciences*, **51**: pp. 193–205. DOI: 10.1016/j.cageo.2012.07.021.

Creutzburg, N., Drooger, C.W., Meulenkamp, J.E., Papastamiatou, I., Seidel, E. & Tataris, A. (1977): *Γενικός γεωλογικός χάρτης Ελλάδος. Νήσος Κρήτη. Κλίμαξ 1 : 200.000 [General geological map of Greece. Crete Island. Scale 1 : 200,000]*. – Geological map, Ινστιτούτο γεωλογικών και μεταλλεύτικων έρευνων [Institute of Geology and Mineral Exploration]; Αθήνα [Athens].

Creutzburg, N. & Papastamatiou, J. (1969): *Die Ethia-Serie des südlichen Mittelkreta und ihre Ophiolithvorkommen*. – Springer, 63 p.; Berlin, Heidelberg.

Creutzburg, N. & Seidel, E. (1975): Zum Stand der Geologie des Präneogens auf Kreta. – *Neues Jahrbuch für Geologie und Paläontologie, Abhandlungen*, **149** (3): pp. 363–383.

Dahl, P.S. (1996): The effects of composition on retentivity of argon and oxygen in hornblende and related amphiboles: a field-tested empirical model. – *Geochimica et Cosmochimica Acta*, **60** (19): pp. 3687–3700. DOI: 10.1016/0016-7037(96)00170-6.

Delaloye, M., Economou, C. & Skounakis, S. (1977): Ages radiométrique de quelques roches ophiolitiques de l'îIe de Crète. – In: Kallergis, G. (ed.) *Proceedings of the VI colloquium on the geology of the Aegean region. Athens 1977*. Ινστιτούτο γεωλογικών και μεταλλεύτικων έρευνων [Institute of Geology and Mineral Exploration], pp. 129–135; Αθήνα [Athens].

Dürr, S. (1985): *Γεωλογικός χάρτης της Ελλάδος 1:50.000. Φύλλο Αμοργός–Δονούσα [Geological map of Greece 1:50,000. Amorgos–Donoussa sheet]*. – Geological map, Ινστιτούτο γεωλογικών και μεταλλεύτικων έρευνων [Institute of Geology and Mineral Exploration]; Αθήνα [Athens].

Dürr, S., Seidel, E., Kreuzer, H. & Harre, W. (1978): Témoins d'un métamorphisme d'âge crétacé supérieur dans l'Égéide: datations radiométriques de minéraux provenant de l'île de Nikouriá (Cyclades, Grèce). – *Bulletin de la Société Géologique de France, série 7*, **20** (2): pp. 209–213.

Fassoulas, C. (1998): The structural evolution of central Crete: insight into the tectonic evolution of the south Aegean (Greece). – *Journal of Geodynamics*, **27** (1): pp. 23–43. DOI: 10.1016/S0264-3707(97)00026-4.

Feldhoff, R.A., Lücke, A. & Richter, D. (1991): Über die Diagenese-/Metamorphosebedingungen der Pindos-und Tripolitza-Serie auf der Insel Kreta (Griechenland). – *Zentralblatt für Geologie und Paläontologie, Teil I*, **1991**: pp. 1611–1622.

Gerdes, A. & Zeh, A. (2009): Zircon formation versus zircon alteration — New insights from combined U–Pb and Lu–Hf in-situ LA-ICP-MS analyses, and consequences for the interpretation of Archean zircon from the central zone of the Limpopo Belt. – *Chemical Geology*, **261** (3–4): pp. 230–243. DOI: 10.1016/j.chemgeo.2008.03.005.

Harrison, T.M. (1981): Diffusion of ^{40}Ar in hornblende. – *Contributions to Mineralogy and Petrology*, **78** (3): pp. 324–331. DOI: 10.1007/BF00398927.

Harrison, T.M., Duncan, I. & McDougall, I. (1985): Diffusion of ^{40}Ar in biotite: temperature, pressure and compositional effects. – *Geochimica et Cosmochimica Acta*, **49** (11): pp. 2461–2468. DOI: 10.1016/0016-7037(85)90246-7.

Hinsken, T., Bröcker, M., Berndt, J. & Gärtner, C. (2016): Maximum sedimentation ages and provenance of metasedimentary rocks from Tinos Island, Cycladic blueschist belt, Greece. – *International Journal of Earth Sciences*, **105** (7): pp. 1923–1940. DOI: 10.1007/s00531-015-1258-z.

Holland, T. & Blundy, J. (1994): Non-ideal interactions in calcic amphiboles and their bearing on amphibole-plagioclase thermometry. – *Contributions to Mineralogy and Petrology*, **116** (4): pp. 433–447. DOI: 10.1007/BF00310910.

Jackson, S.E., Pearson, N.J., Griffin, W.L. & Belousova, E.A. (2004): The application of laser ablation-inductively coupled plasma-mass spectrometry to in situ U-Pb zircon geochronology. – *Chemical Geology*, **211** (1–2): pp. 47–69. DOI: 10.1016/j.chemgeo.2004.06.017.

Klein, T., Craddock, J.P. & Zulauf, G. (2013): Constraints on the geodynamical evolution of Crete: insights from illite crystallinity, Raman spectroscopy and calcite twinning above and below the "Cretan detachment." – *International Journal of Earth Sciences*, **102** (1): pp. 139–182. DOI: 10.1007/s00531-012-0781-4.

Kneuker, T., Dörr, W., Petschick, R. & Zulauf, G. (2015): Upper crustal emplacement and deformation of granitoids inside the Uppermost Unit of the Cretan nappe stack: constraints from U-Pb zircon dating, microfabrics and paleostress analyses. – *International Journal of Earth Sciences*, **104** (2): pp. 351–367. DOI: 10.1007/s00531-014-1088-4.

Koepke, J. & Seidel, E. (1984): Oberkretazisches Kristallin an der Basis von Ophiolithen der Südägäis: Charakterisierung der Metamorphose-Fazies. – *Tschermaks Mineralogische und Petrographische Mitteilungen*, **33** (4): pp. 263–286. DOI: 10.1007/BF01082673.

Koepke, J., Seidel, E. & Kreuzer, H. (2002): Ophiolites on the southern Aegean islands Crete, Karpathos and Rhodes: composition, geochronology and position within the ophiolite belts of the Eastern Mediterranean. – *Lithos*, **65** (1–2): pp. 183–203. DOI: 10.1016/S0024-4937(02)00165-2.

Krahl, J., Herbart, H. & Katzenberger, S. (1982): Subdivision of the allochthonous “ophiolites”-bearing formation upon the Pindos Group, southwestern part of central Crete, Greece. *International Symposium on the Hellenic Arc and Trench (H.E.A.T.). April 8–10. 1981, Athens. Proceedings. Volume 1*. Εθνικό Μετσόβιο Πολυτεχνείο [Ethnikó Metsóvio Polytechneío], pp. 324–341; Αθήνα [Athens].

Kretz, R. (1983): Symbols for rock-forming minerals. – *American Mineralogist*, **68** (1–2): pp. 277–279.

Kruhl, J.H. (1996): Prism- and basal-plane parallel subgrain boundaries in quartz: a microstructural geothermobarometer. – *Journal of Metamorphic Geology*, **14** (5): pp. 581–589. DOI: 10.1046/j.1525-1314.1996.00413.x.

Langosch, A., Seidel, E., Stosch, H.-G. & Okrusch, M. (2000): Intrusive rocks in the ophiolitic mélange of Crete – Witnesses to a Late Cretaceous thermal event of enigmatic geological position. – *Contributions to Mineralogy and Petrology*, **139** (3): pp. 339–355. DOI: 10.1007/s004100000136.

Leake, B.E. (1978): Nomenclature of amphiboles. – *American Mineralogist*, **63** (11–12): pp. 1023–1052.

Liou, J.G., Maruyama, S. & Cho, M. (1987): Very low-grade metamorphism of volcanic and volcaniclastic rocks—mineral assemblages and mineral facies. – In: Frey, M. (ed.) *Low temperature metamorphism*. Blackie and Son, pp. 59–113; Glasgow.

Lippolt, H.J. & Baranyi, I. (1976): Oberkretazische Biotit- und Gesteinsalter aus Kreta. – *Neues Jahrbuch für Geologie und Paläontologie, Monatshefte*, **7**: pp. 405–414.

Ludwig, K.R. (1980): Calculation of uncertainties of U-Pb isotope data. – *Earth and Planetary Science Letters*, **46** (2): pp. 212–220. DOI: 10.1016/0012-821X(80)90007-2.

Ludwig, K.R. (2012): User’s manual for Isoplot 3.75. A geochronological toolkit for Microsoft Excel. – *Berkeley Geochronology Center Special Publication*, **5**: pp. 1–75.

Martha, S.O., Dörr, W., Gerdes, A., Krahl, J., Linckens, J. & Zulauf, G. (2017): The tectonometamorphic and magmatic evolution of the Uppermost Unit in central Crete (Melambes area): constraints on a Late Cretaceous magmatic arc in the Internal Hellenides (Greece). – *Gondwana Research*. DOI: 10.1016/j.gr.2017.04.004.

Martha, S.O., Dörr, W., Gerdes, A., Petschick, R., Schastok, J., Xypolias, P. & Zulauf, G. (2016): New structural and U–Pb zircon data from Anafi crystalline basement (Cyclades, Greece): constraints on the evolution of a Late Cretaceous magmatic arc in the Internal Hellenides. – *International Journal of Earth Sciences*, **105** (7): pp. 2031–2060. DOI: 10.1007/s00531-016-1346-8.

Massonne, H.-J. & Schreyer, W. (1987): Phengite geobarometry based on the limiting assemblage with K-feldspar, phlogopite, and quartz. – *Contributions to Mineralogy and Petrology*, **96** (2): pp. 212–224. DOI: 10.1007/BF00375235.

Palamakumbura, R.N., Robertson, A.H.F. & Dixon, J.E. (2013): Geochemical, sedimentary and micropaleontological evidence for a Late Maastrichtian oceanic seamount within the Pindos ocean (Arvi Unit, S Crete, Greece). – *Tectonophysics*, **595**–**596**: pp. 250–262. DOI: 10.1016/j.tecto.2012.04.019.

Passchier, C.W. & Trouw, R.A.J. (2005): *Microtectonics*. – Springer, 366 p.; Berlin, Heidelberg.

Patzak, M., Okrusch, M. & Kreuzer, H. (1994): The Akrotiri unit on the island of Tinos, Cyclades, Greece: witness to a lost terrane of Late Cretaceous age. – *Neues Jahrbuch für Geologie und Paläontologie, Abhandlungen*, **194**: pp. 211–252.

Reinecke, T., Altherr, R., Hartung, B., Hatzipanagiotou, K., Kreuzer, H., Harre, W., Klein, H., Keller, J., Geenen, E. & Böger, H. (1982): Remnants of a Late Cretaceous high temperature belt on the island of Anafi (Cyclades, Greece). – *Neues Jahrbuch für Mineralogie, Abhandlungen*, **145** (2): pp. 157–182.

Robert, U. & Bonneau, M. (1982): Les basalts des nappes du Pinde et d’Arvi et leur signification dans l’évolution géodynamique de la Méditerrannée orientale. – *Annales Géologiques des Pays Helléniques*, **31**: pp. 373–408.

Seidel, E., Kreuzer, H. & Harre, W. (1982): A Late Oligocene/Early Miocene high pressure belt in the external Hellenides. – *Geologisches Jahrbuch, Reihe E*, **23**: pp. 165–206.

Seidel, E., Okrusch, M., Kreuzer, H., Raschka, H. & Harre, W. (1976): Eo-Alpine metamorphism in the Uppermost Unit of the Cretan nappe system – petrology and geochronology. Part 1. The Léndas area (Asteroúsia Mountains). – *Contributions to Mineralogy and Petrology*, **57** (3): pp. 259–275.

Seidel, E., Okrusch, M., Kreuzer, H., Raschka, H. & Harre, W. (1981): Eo-Alpine metamorphism in the Uppermost Unit of the Cretan nappe system – petrology and geochronology. Part 2. Synopsis of high-temperature metamorphics and associated ophiolites. – *Contributions to Mineralogy and Petrology*, **76** (3): pp. 351–361. DOI: 10.1007/BF00375462.

Spear, F.S. & Cheney, J.T. (1989): A petrogenetic grid for pelitic schists in the system SiO_2-Al_2O_3-FeO-MgO-K_2O-H_2O. – *Contributions to Mineralogy and Petrology*, **101** (2): pp. 149–164. DOI: 10.1007/BF00375302.

Tataris, A. (1964): Έπι τής παρουσίας τής ζώνης 'Ωλονού - Πίνδου είς τήν περιοχήν Σύμης - Βιάννου (άνατ. Κρήτης) και τής ήλικίας τών σπιλιτών της [The Olonos-Pindos-Zone in the Symi-Viannos area (eastern Crete) and the age of spilites of this zone]. – *Πρακτικά της Ακαδημίας Αθηνών [Praktika tis Akadimias Athinon]*, **39**: pp. 298–314.

Theye, T., Seidel, E. & Vidal, O. (1992): Carpholite, sudoite, and chloritoid in low-grade high-pressure metapelites from Crete and the Peloponnese, Greece. – *European Journal of Mineralogy*, **4** (3): pp. 487–508. DOI: 10.1127/ejm/4/3/0487.

Thomson, S.N., Stöckhert, B. & Brix, M.R. (1999): Miocene high-pressure metamorphic rocks of Crete, Greece: rapid exhumation by buoyant escape. – *Geological Society, London, Special Publications*, **154** (1): pp. 87–107. DOI: 10.1144/GSL.SP.1999.154.01.04.

Thorbecke, G. (1987): *Die Zonengliederung der ägäischen Helleniden und westlichen Tauriden*. – Gesellschaft der Geologie- und Bergbaustudenten in Österreich, 161 p.; Wien.

Tortorici, L., Catalano, S., Cirrincione, R. & Tortorici, G. (2012): The Cretan ophiolite-bearing mélange (Greece): a remnant of Alpine accretionary wedge. – *Tectonophysics*, **568**–**569**: pp. 320–334. DOI: 10.1016/j.tecto.2011.08.022.

ten Veen, J.H. & Postma, G. (1999): Roll-back controlled vertical movements of outer-arc basins of the Hellenic subduction zone (Crete, Greece). – *Basin Research*, **11** (3): pp. 243–266. DOI: 10.1046/j.1365-2117.1999.00098.x.

Vidakis, M. (1993): *Γεωλογικός χάρτης της Ελλάδος 1:50.000. Φύλλο Ιεράπετρα [Geological map of Greece 1:50,000. Ierapetra sheet]*. – Geological map, Ινστιτούτο γεωλογικών και μεταλλεύτικων έρευνων [Institute of Geology and Mineral Exploration]; Αθήνα [Athens].

5 Summary and outlook

The present PhD thesis comprises structural geology, petrographic and geochronological investigations on crystalline rocks of the Uppermost Unit in the southern Aegean realm. Studies were carried out in three areas: (1) on the island of Anafi, (2) in the area west of Melambes in central Crete and (3) between the villages of Pefkos, Kalami and Sykologos in the municipality of Viannos in eastern Crete.

The Uppermost Unit forms together with the underlying, non-metamorphic Pindos Unit the upper nappe system of the Cretan nappe pile that, unlike the units of the lower nappe system, was not affected by Late Oligocene to Early Miocene subduction-related metamorphism. The upper nappe system must therefore have been at upper levels of the lithosphere in the Late Oligocene. This is of particular importance when reconstructing the tectonometamorphic evolution of the Uppermost Unit. The Uppermost Unit is very heterogeneous in composition and is subdivided into several subunits, which differ mainly in their lithological composition and the degree of metamorphic overprint. Usually, it is subdivided into several low-grade metamorphic subunits and one high-grade metamorphic subunit. Within the scope of this PhD thesis, three of these subunits were examined; (1) the anchimetamorphic Arvi Unit, (2) the newly described Greenschist Unit and (3) the Asterousia Crystalline Complex (ACC).

The analyses conducted during this PhD thesis include: (1) structural geology investigations in the field, (2) microstructural and petrographic analyses on thin sections, (3) radiometric dating of zircons using isotope dilution thermal ionisation mass spectrometry (ID-TIMS) and laser ablation inductively coupled plasma mass spectrometry (LA-ICP-MS), (4) electron microprobe (EMP) analysis, (5) quartz texture analysis using electron-backscattered diffraction (EBSD), (6) semiquantitative analysis of mineral phases using X-ray powder diffraction (XRD), (7) analysis of the modal composition of intrusive rocks applying point counting on thin sections and (8) X-ray microtomography (micro-CT) on chiastolite hornfels.

On the island of Anafi, crystalline rocks of the Uppermost Unit are found on top of Eocene flysch sediments. The crystalline rocks comprise greenschist facies and amphibolite facies metamorphic rocks, as well as granitoid intrusions in marble and dykes cutting through metasedimentary rocks and granitoids in northeastern Anafi. Based on field observation, the crystalline rocks were subdivided into three tectonometamorphic units: (1) Anafi Greenschist (epidote-amphibole schist), (2) Anafi Amphibolite Group (orthoamphibolite with a thin layer of metasediments at the base) and (3) Chalepa Group (amphibolite facies metasediments with slices of serpentinite and intrusion of granitoid bodies in marble). The crystalline rocks of Anafi are overlain by Neogene sediments (Theologou Beds). Granitoids

are classified as granodiorite, hornblende diorite and quartzdiorite, whereas dykes are of anorthositic and monzogranitic composition.

The crystalline rocks of Anafi were thrust on top of Eocene flysch under brittle conditions with slickenside striation on the thrust plane indicating NW–SE-kinematics. The contact area of the Anafi Greenschist and the Anafi Amphibolite Group is characterized by a mylonitic zone. The Chalepa Group was thrust on top of the Anafi Amphibolite Group and the Anafi Greenschist under brittle conditions. Slickenside striation on the thrust plane indicate N–S-kinematics. The foliation in the metasedimentary rocks, the orthoamphibolite and the greenschist facies rocks dips mainly to the NE or to the SW. A mineral/stretching lineation made of quartz, plagioclase or amphibole grains was observed on the foliation planes in most rock types and usually plunges to the NW or to the SE. Shear sense indicators include σ-clasts of quartz and asymmetric pressure shadows of chlorite behind euhedral pyrite crystals in the Anafi Greenschist as well as σ-clasts of vein quartz with asymmetric pressure shadows of fine-grained quartz in quartzite and plagioclase fish in orthoamphibolite of the Anafi Amphibolite Group. They all indicate consistent top-to-the SE kinematics.

$^{238}U/^{206}Pb$ dating on zircon from granodioritic intrusions yielded several zircon populations with similar age spectra and pointing to continuous intrusion of granitoids between 72.5 and 79 Ma in a magmatic arc setting of a subduction zone. The median age of the youngest zircon population, which indicates the minimum age, is 72.6 +0.1/–0.2 Ma. $^{238}U/^{206}Pb$ dating on zircon from monzogranitic dykes, which intruded in granodiorite in northeastern Anafi, yielded a median age of 69.9 ± 0.7 Ma. Granodioritic, quartzdioritic, and dioritic intrusions lack foliation, but microstructures in granodiorite, e.g. undulatory extinction and subgrain formation in quartz, lobate grain boundaries between feldspar and quartz as well as stress-induced myrmekite growth, indicate postintrusive deformation at temperatures above 600 °C. Quartzdiorite shows lobate grain boundaries, which is compatible with high-temperature deformation.

Published K-Ar biotite and hornblende ages of the granitoids and metasedimentary rocks of the Chalepa Group, as well as from orthoamphibolite of the Anafi Amphibolite Group, prove mutual cooling in the Maastrichtian and Danian. The granitoids must have intruded into a deep, ductile stockwork of the ACC and were deformed late- to post-intrusively. Subsequent cooling of the amphibolite facies rocks and granitoids was slow. Monzogranite and anorthosite intruded in dykes during the cooling phase. Published K-Ar actinolite ages of the Anafi Greenschist provide Middle to Late Palaeocene ages. The closure temperature of actinolite (470 °C) is close to the maximum of greenschist facies metamorphism, so it should be only slightly older than K-Ar ages. Ductile thrusting of the Anafi Amphibolite Group on top of the Anafi Greenschist thus should have taken place in the Palaeocene. Ongoing shortening and exhumation of the crystalline rocks resulted in brittle thrusting of the Uppermost

Unit on flysch sediments, based on the age of the flysch probably in the Late Eocene. Top-to-the S brittle thrusting of the Chalepa Group on top of the other units took place in the (Early) Oligocene during clockwise rotation of the Aegean block and change of kinematics from NW–SE (pre-Oligocene) to NE–SW (Oligocene to ?Early Miocene).

Comparable to Anafi, crystalline rocks of the Uppermost Unit are thrust onto Eocene flysch sediments, which are ascribed to the Pindos Unit, in the area west of the central Cretan village of Melambes. Neogene sediments are resting here on the crystalline rocks as well. Field observations allow a subdivision into two tectonometamorphic units; (1) Akoumianos Greenschist (epidote-amphibole schist, quartzite and micaschist) and (2) Asterousia-type rocks (amphibolite facies metasediments with slices of serpentinite and intrusions of granitoids). Orthoamphibolite is lacking west of Melambes. Intrusions, which are classified as dioritic and monzo- to syenogranitic based on point counting analysis on thin sections, occurred into the metasediments. Intrusions of granitic composition show a pronounced foliation and have been transformed to orthogneiss, while the original magmatic texture is still recognizable in dioritic intrusions. The foliation in greenschist facies rocks dips to the NW and in amphibolite facies rocks and orthogneiss, it dips mainly to the SW or to the NE. The mineral/stretching lineation on the foliation planes is NW–SE-oriented both in the Akoumianos Greenschist and in the Asterousia-type rocks. Asymmetric boudins and σ-clasts along with other shear sense indicators indicate a top-to-the SE sense of shear for both units.

$^{238}U/^{206}Pb$ zircon age dating on metadiorite, orthogneiss and monzogranite from a dyke yielded several concordia ages ranging from 71.9 ± 0.6 to 76.9 ± 0.3 Ma and emphasize that dioritic and granitic magmas intruded the Asterousia-type metasedimentary rocks over a long period. Only three of the dated zircon grains, all extracted from orthogneiss, yielded inherited, Proterozoic ages. This is considered evidence that relatively young magmatic crust has served as the protolith for the Asterousia-type granitoids. Dioritic and granitic magmas could have formed in different magma chambers, with the granitic magma chamber having undergone considerable modification of the original composition due to stronger incorporation of the felsic country rocks.

Hornblende-plagioclase geothermometry using results from EMP analysis yields metamorphic temperatures between 400–560 °C (edenite-richterite geothermometer) for the Akoumianos Greenschist. An estimation of pressure and temperature conditions based on the anorthite content in plagioclase and the aluminium content in hornblende yields P = 250–400 MPa and T = 500 +15/–30 °C. The c-axis crystallographic-preferred orientation (CPO) of quartz in Akoumianos-type and Asterousia-type quartzite indicate non-coaxial deformation with rhomb <a> slip and prism <a> slip at temperatures of ca. 500 °C.

Based on the results, a five-stage geodynamic model is proposed to explain the tectonometamorphic and magmatic evolution in the southern Aegean during the mid-Late Cretaceous to Eocene. (1) Collision and subduction of the Pindos lithosphere underneath the southern margin of the Pelagonian-Lycian terrane resulted in obduction and offscraping of serpentinized Pindos ocean floor and stacking of the ACC during top-to-the SE amphibolite facies shearing (mid-Late Cretaceous). (2) In the middle to late Campanian, granitic and dioritic melts intruded into a magmatic arc along the southern active continental margin of the Pelagonian-Lycian terrane. (3) Subsequently, collision and stacking of the magmatic arc occurred during mylonitic top-to-the SE shearing in the Maastrichtian. (4) Greenschist facies shearing of the Asterousia-type rocks on top of the Akoumianos Greenschist took place during the Palaeocene. (5) Finally, the Uppermost Unit was thrust on top of the Pindos Unit in the Late Eocene. Top-to-the SE is constrained as the dominant shear sense from the mid-Late Cretaceous to the Late Eocene.

In the eastern Cretan municipality Viannos, the Uppermost Unit is exposed in a graben structure south of the Dikti Mountains. Once again, the Uppermost Unit is thrust on top of Eocene flysch of the Pindos Unit. Neogene sediments are missing, however, and the Uppermost Unit is separated towards the Dikti Mountains from the Tripolitsa Unit via a steep normal fault. Besides greenschist facies rocks (Theodorii Greenschist) and amphibolite facies rocks (orthoamphibolite overlain by a succession of metasedimentary rocks), prehnite-pumpellyite facies diabase, pillow lava basalts and green and red slates were found. The greenschist and amphibolite facies rocks are separated from the Arvi Unit via a brittle thrust with NW–SE-oriented slickenside striation on the thrust plane. Hornblende-plagioclase geothermometry on greenschist yielded metamorphic temperatures of 360–520 °C (edenite tremolite geothermometer). In all three tectonometamorphic units, rocks with a pervasive foliation occur with the foliation planes usually dipping to the NW or to the SE. A mineral/stretching lineation on the foliation planes indicates NW–SE-oriented stretching. Asymmetric boudins, σ-clasts and other shear sense indicators suggest top-to-the SE shearing. Quartzite is full of shear zones with a NE–SW striation.

Microstructures of amphibolite facies rocks from the study area suggest three deformation stages. D_1 is preserved as internal foliation ($S_i = S_1$) in intertectonic garnet porphyroblasts from chiastolite hornfels. The main pervasive foliation (S_2) is associated with pre-middle Campanian top-to-the SE amphibolite facies (P = 400–500 MPa; T_{max} = 700 °C) shearing (D_2). Chiastolite and cordierite formed during middle to late Campanian contact metamorphism (T = 600–680 °C; P_{max} = 200 MPa) in the vicinity of a non-exposed pluton. One zircon grain from chiastolite hornfels yielded a concordant age of 74 ± 2 Ma, which compares well with the U-Pb zircon ages from intrusive rocks on Anafi and west

of Melambes. Th/U ratios and the euhedral shape of the grain are compatible with metamorphic grown zircon. Chiastolite bears evidence that top-to-the SE shearing (D_3) re-affected the amphibolite facies rocks before the end of crystal growth. Cross-mica, epidote and chlorite formed during post-D_3 retrograde metamorphism (T_{max} = 500 °C; P_{max} = 220 MPa) in the Maastrichtian.

The results show that the Uppermost Unit south of the Dikti Mountains has faced a similar pre-intrusive evolution as exposures on Anafi and west of Melambes. However, the Uppermost Unit should then have faced stronger uplift and exhumation in the study area, so hot middle to late Campanian intrusions triggered growth of new phases during contact metamorphism. During the late phase of chiastolite growth, top-to-the SE shearing re-commenced. The Uppermost Unit south of the Dikti Mountains thus takes an intermediate position on Crete between exposures in the area west of Melambes affected by ductile post-intrusive top-to-the SE shearing and exposures in the northern Ierapetra Graben not affected by post-intrusive shearing. The amphibolite facies rocks have been thrust on top of the Theodorii Greenschist probably during the Palaeocene. Both the amphibolite and greenschist facies rocks have then been thrust on top of the Arvi and Pindos units during the Eocene. NE–SW-oriented striations on shear zones must have developed during post-Eocene shortening and can be correlated to similar lineations reported from granitoids in the vicinity of Pachia Ammos.

The present PhD thesis has shown that the Uppermost Unit is key in understanding the early Alpine tectonometamorphic and magmatic evolution of the Hellenides in the southern Aegean realm. Further studies should first consider other areas in which rocks of the Uppermost Unit are exposed to allow comparison with the study areas of this PhD thesis. A key will be the exposures at the type locality of the Asterousia Crystalline Complex between Kali Limenes and Lendas. Of particular importance, however, are also the exposures of the low-grade metamorphic subunits of the Uppermost Unit in central Crete and on Gavdos. The origin of the low-grade metamorphic subunits as well as their exact position in the Cretan nappe pile have not been clearly illuminated. The serpentinite deposits within the Uppermost Unit also require more detailed studies and it remains questionable whether a topmost *nappe des serpentines* exists or not. Comprehensive structural geology investigations in all areas where the Uppermost Unit crops out would provide further information to illuminate key questions in the evolution of the Uppermost Unit and thus in the early Alpine evolution of the southern Aegean realm.

In all three study areas, greenschist facies rocks were found at the base of the Asterousia-type rocks that have previously been reported only from Anafi. This raises the question, whether comparable rocks have also been overlooked in other areas, where Asterousia-type rocks crop out. It is therefore considered necessary to comprehensively re-map the exposures of the Uppermost Unit. Further studies to encrypt the origin of the subunits of the Uppermost Unit are also regarded as necessary. Right now,

the affinity of the Asterousia Crystalline Complex to the Pelagonian-Lycian terrane is proven mainly by its structural position. Comparison of age spectra of detritital zircon from metasedimentary rocks of the Asterousia Crystalline Complex with those of adjacent terranes can provide further information as to whether it can be correlated with the Pelagonian Zone. A last suggestion for further studies concerns the Late Cretaceous magmatic arc along the southern margin of the Pelagonian-Lycian terrane suggested in this PhD thesis. The link with other magmatic arcs of similar age in southeastern Europe and Anatolia (Apuseni–Banat–Timok–Srednogorie Belt and Central Anatolian Crystalline Complex) remains unclear and requires further studies. For example, structural geology, geochemical, petrographic and geochronological investigations would provide further information on the association of these magmatic arcs.

6 Zusammenfassung und Ausblick

Die vorliegende Doktorarbeit umfasst strukturgeologische, petrographische und geochronologische Untersuchungen an Kristallingesteinen der obersten Deckeneinheit in der südlichen Ägäis. Die Untersuchungen erfolgten in drei Gebieten: (1) auf der Kykladeninsel Anafi, (2) in der Gegend westlich Melambes in Zentralkreta und (3) zwischen den Dörfern Pefkos, Kalami und Sykologos in der Gemeinde Viannos in Ostkreta.

Die oberste Deckeneinheit bildet zusammen mit der unterlagernden, unmetamorphen Pindos-Einheit das obere Deckensystem des kretischen Deckenstapels, das, anders als die Einheiten des unteren Deckensystems, nicht von spätoligozäner bis frühmiozäner subduktionsbezogener Metamorphose erfasst wurde. Das obere Deckensystem muss folglich im späten Oligozän bereits in den oberen Bereichen der Lithosphäre positioniert gewesen sein. Dieser Umstand ist bei der Rekonstruktion der tektonometamorphen Entwicklung der obersten Deckeneinheit von besonderer Bedeutung. Die oberste Deckeneinheit ist sehr heterogen zusammengesetzt und wird in mehrere Untereinheiten unterteilt, die sich in ihrer lithologischen Zusammensetzung und in ihrem Metamorphosegrad stark unterscheiden. Generell wird eine Unterteilung in mehrere niedriggradig metamorphe und einer hochgradig metamorphen Einheit vorgenommen. Im Rahmen dieser Doktorarbeit wurden drei dieser Untereinheiten untersucht; (1) die anchimetamorphe Arvi-Einheit, (2) die neu beschriebene Grünschiefer-Einheit und (3) das Asterousia-Kristallin.

Die Analysen im Rahmen dieser Doktorarbeit beinhalten eine Vielzahl von Methoden: (1) strukturgeologische Untersuchungen im Gelände, (2) mikrostrukturelle und petrographische Analysen an Dünnschliffen, (3) radiometrische Datierungen an Zirkonen mittels Isotopenverdünnungs-Thermische Ionisationsmassenspektrometrie (ID-TIMS) und Laserablations-Massenspektrometrie mit induktiv gekoppeltem Plasma (LA-ICP-MS), (4) Elektronenstrahlmikroanalyse (EMPA), (5) Quarz-Texturanalysen mittels Elektronenrückstreubeugung (EBSD), (6) semiquantitative Phasenanalyse mittels Röntgen-Pulverdiffraktometrie (XRD), (7) Modalbestandsbestimmung intrusiver Gesteine mittels Punktzählung an Dünnschliffen sowie (8) Mikrocomputertomografie (micro-CT) an Chiastolith-Hornfels.

Auf der Insel Anafi lagern Kristallingesteine der obersten Deckeneinheit auf eozänen Flyschsedimenten auf. Das Kristallin umfasst grünschiefer- und amphibolitfazielle Metamorphite, sowie granitoide Intrusionen in Marmor und Dykes, die im Nordosten der Insel Metasedimente und Granitoide durchsetzen. Aufgrund der Geländebeobachtungen wurde eine Einteilung des Kristallines in drei tektonometamorphe Einheiten vorgenommen: (1) Anafi-Grünschiefer (grünschieferfazielle Epidot-Am-

phibol-Schiefer); (2) Anafi Amphibolit-Gruppe (Orthoamphibolit mit geringmächtigen Einschaltungen von Metasedimenten an der Basis); und (3) Chalepa Gruppe (mehrere Schuppen amphibolitfazieller Metasedimente mit Einschaltungen von Serpentinit und mit Intrusion von Granitoidkörpern in Marmor). Das Anafi-Kristallin wird überlagert von neogenen Sedimenten (Theologou-Schichten). Granitoide wurden als Granodiorit, Hornblendediorit und Quarzdiorit klassifiziert, wohingegen Dykes anorthositischer und monzogranitischer Zusammensetzung sind.

Das Anafi-Kristallin wurde spröde auf eozänem Flysch überschoben, wobei Harnischlineare auf Verwerfungsflächen eine NW–SO-Kinematik belegen. Der Kontaktbereich der Anafi-Grünschiefer und der Anafi Amphibolit-Gruppe ist eine mylonitische Zone. Die Chalepa-Gruppe wurde spröde auf die Anafi Amphibolit-Gruppe und auf die Anafi-Grünschiefer überschoben. Harnischlineare auf der Verwerfungsfläche belegen eine N–S-Kinematik. Die Schieferung in den Metasedimenten, den Orthoamphiboliten und den Grünschiefern fällt vorzugsweise nach NO oder SW ein. Auf den Schieferflächen ist in den meisten Gesteinen eine Lineation von gestrecktem Quarz, Plagioklas bzw. Amphibol erkennbar, die zumeist nach NW oder SO einfällt. Schersinnindikatoren umfassen σ-Klasten von Quarz und asymmetrische Druckschatten von Chlorit hinter idiomorphen Pyritkristallen in den Anafi-Grünschiefern sowie σ-Klasten von Gangquarz mit asymmetrischen Druckschatten von feinkörnigem Quarz in Quarzit und Plagioklasfische in Orthoamphiboliten der Anafi Amphibolit-Gruppe. Sie zeigen alle durchgängig eine Topp-SO-Kinematik an.

$^{238}U/^{206}Pb$-Datierungen an Zirkonen aus granodioritischen Intrusiva ergaben mehrere Zirkonpopulationen, die ähnliche Altersspektren aufweisen und eine kontinuierliche Intrusion von Granitoiden zwischen 72,5 und 79 Ma in einem magmatischen Bogen einer Subduktionszone belegen. Das Medianalter der jüngsten Zirkonpopulation, die das minimale Platznahmealter anzeigt, beträgt 72,6 +0.1/−0.2 Ma. $^{238}U/^{206}Pb$-Datierungen an Zirkonen aus monzogranitischen Dykes, die in Granodiorite in Nordost-Anafi intrudierten, ergaben ein Medianalter von 69,9 ± 0,7 Ma. Granodioritische, quarzdioritische und dioritische Intrusiva sind nicht geschiefert, jedoch zeigen Mikrogefüge in Granodiorit, wie undulöse Auslöschung und Subkornbildung in Quarz, lobate Korngrenzen zwischen Feldspat und Quarz sowie spannungsinduzierte Bildung von Myrmekit, postintrusive Deformation bei Temperaturen von über 600 °C an. Quarzdiorit zeigt lobate Korngrenzen, die ebenfalls auf Hochtemperatur-Deformation hinweisen.

Publizierte K-Ar Biotit- und Hornblende-Alter der Granitoide und Metasedimente der Chalepa-Gruppe, sowie der Orthoamphibolite der Anafi Amphibolit-Gruppe belegen eine gemeinsame Abkühlung im Maastrichtium bzw. Danium. Die Granitoide müssen hierbei in einem tiefen, duktilen Stockwerk des Asterousia-Kristallines intrudiert sein, sodass sie spät- bis postintrusiv deformiert wurden. Die anschließende Abkühlung der amphibolitfaziellen Gesteine und Granitoide erfolgte langsam.

Monzogranit und Anorthosit intrudierten während der Abkühlungsphase in Gängen. Publizierte K-Ar-Datierungen an Aktinolith der Anafi-Grünschiefer ergeben mittel- bis spätpaläozäne Alter. Die Schließungstemperatur von Aktinolith (470 °C) ist nahe des Maximums der Grünschiefer-Metamorphose, sodass diese nur unwesentlich älter als die K-Ar-Alter sein sollte. Duktile Überschiebung der Anafi Amphibolit-Gruppe auf die Anafi-Grünschiefer dürfte somit im Paläozän erfolgt sein. Anhaltende Verkürzung und Heraushebung des Kristallines führte zu spröder Überschiebung der obersten Deckeneinheit auf Flyschsedimente, aufgrund des Alters des Flyschs vermutlich im Späteozän. Die spröde Überschiebung der Chalepa-Gruppe auf die anderen Einheiten erfolgte Topp-S wohl im (unteren) Oligozän während der Rotation der ägäischen Scholle im Uhrzeigersinn und Änderung der Kinematik von NW–SO (prä-Oligozän) auf NO–SW (Oligozän bis ?Frühmiozän).

Ähnlich wie auf Anafi sind in der Gegend westlich des mittelkretischen Dorfes Melambes Kristallingesteine der obersten Deckeneinheit auf eozänen Flyschsedimenten, die der Pindos-Einheit zugerechnet werden, aufgeschoben. Überlagert wird auch hier das Kristallin von neogenen Sedimenten. Geländebeobachtungen lassen eine Einteilung in zwei tektonometamorphe Einheiten zu; (1) Akoumianos-Grünschiefer (Epidot-Amphibol-Schiefer, Quarzite und Glimmerschiefer) und; (2) Asterousia-Kristallin (amphibolitfazielle Metasedimente mit Einschaltungen von Serpentinit und Intrusion von Granitoiden). In der Gegend westlich von Melambes fehlen Orthoamphibolite. Intrusionen, die mittels Punktzählung an Dünnschliffen als dioritischer und monzo- bis syenogranitischer Zusammensetzung bestimmt wurden, erfolgten in die Metasedimente. Intrusionen granitischer Zusammensetzung zeigen eine deutliche Schieferung und wurden zu Orthogneis umgewandelt, wohingegen das ursprüngliche magmatische Gefüge in dioritischen Intrusiva noch erkennbar ist. Die Schieferung fällt in den Grünschiefern flach nach NW und in den amphibolitfaziellen Gesteinen und Orthogneisen vorzugsweise nach SW oder NO ein. Die Streckungslineation auf den Schieferflächen verläuft sowohl im Akoumianos-Grünschiefer als auch im Asterousia-Kristallin NW–SO. Asymmetrische Boudins, σ-Klasten und andere Schersinnindikatoren belegen für beide Einheiten eine Topp-SO-Scherung.

$^{238}U/^{206}Pb$-Datierungen an Zirkonen aus Metadiorit, Orthogneis und einem Monzogranit aus einem Gang ergaben mehrere Concordia-Alter zwischen 71,9 ± 0,6 und 76,9 ± 0,3 Ma und belegen, dass dioritische und granitische Magmen über einen längeren Zeitraum in die Metasedimente des Asterousia-Kristallines intrudierten. Nur drei der datierten Zirkone lieferten ererbte, proterozoische Alter, wobei alle drei Zirkone aus Orthogneis extrahiert wurden. Dies gilt als Beleg dafür, dass relativ junge, magmatische Kruste als Protolith für die Asterousia-Granitoide gedient haben muss. Dioritische und

granitische Magmen könnten sich hierbei in unterschiedlichen Magmenkammern gebildet haben, wobei die granitische Magmenkammer starke Modifizierung der ursprünglichen Zusammensetzung infolge stärkerer Assimilierung des felsischen Nebengesteins erfahren hat.

Eine Abschätzung der Druck- und Temperaturbedingungen anhand des Anorthit-Gehalts in Plagioklas und des Aluminium-Gehalts in Hornblende ergibt P = 250–400 MPa und T = 500 +15/–30 °C. Die kristallographisch bevorzugte Orientierung der c-Achsen von Quarz in Akoumianos- und Asterousia-Quarziten (EBSD-Untersuchungen) zeigt non-koaxiale Deformation mit Rhomben <a>- und Prismen <a>-Gleiten bei Temperaturen von etwa 500 °C.

Basierend auf den Ergebnissen wird ein fünfstufiges geodynamisches Modell vorgestellt, das die tektonometamorphe und magmatische Entwicklung in der südlichen Ägäis während der mittleren Oberkreide bis ins Eozän erklären soll. (1) Kollision und Subduktion der Pindos-Lithosphäre unterhalb des südlichen Bereichs des pelagisch-lyzischen Mikrokontinentes führte zu Obduktion und frontaler Abscherung von serpentinisiertem Pindos-Ozeanboden und Stapelung des Asterousia-Kristallines während Topp-SO-gerichteter amphibolitfazieller Überschiebung (mittlere Oberkreide). (2) Im mittleren bis späten Campanium intrudierten granitische und dioritische Schmelze in einen magmatischen Bogen entlang des südlichen aktiven Kontinentalrands des pelagonisch-lyzischen Mikrokontinentes. (3) Anschließend kam es zur Kollision und Stapelung des magmatischen Bogens während mylonitischer topp-SO-Scherung im Maastrichtium. (4) Grünschieferfazielle Scherung des Asterousia-Kristallines auf die Grünschiefer-Einheit erfolgte im Paläozän. (5) Schließlich erfolgte eine Überschiebung der obersten Deckeneinheit auf die Pindos-Einheit im späten Eozän. Topp-SO war der dominante Schersinn von der mittleren Oberkreide bis ins späte Eozän.

In der ostkretischen Gemeinde Viannos ist die oberste Deckeneinheit am Fuße des Dikti-Gebirges in einer Grabenstruktur aufgeschlossen. Auch hier ist die oberste Deckeneinheit auf eozänem Flysch der Pindos-Einheit aufgeschoben. Neogene Sedimente fehlen jedoch und zum Dikti-Gebirge hin ist die oberste Deckeneinheit durch eine steilstehende Abschiebung von der Tripolitsa-Einheit getrennt. Außer grünschieferfaziellen (Theodorii-Grünschiefer) und amphibolitfaziellen (Orthoamphibolit überlagert von einer Abfolge aus Metasedimenten) Gesteinen wurden auch prehnit-pumpellyit-fazielle Diabase, Kissenlava-Basalte sowie grüne und rote Tonschiefer (Arvi-Einheit) vorgefunden. Die grünschiefer- und amphibolitfaziellen Gesteine sind auf die Arvi-Einheit spröd überschoben, wobei Harnischlineare auf der Verwerfungsfläche eine NW–SO-Orientierung aufweisen. Hornblende-Plagioklas-Geothermometrie an Grünschiefern ergibt Metamorphosetemperaturen von 360–520 °C (Edenit-Tremolit-Geothermometer). In allen drei tektonometamorphen Einheiten kommen Gesteine mit einer ausgeprägten Schieferung vor, die in der Regel nach NW oder SO einfällt. Minerallineare auf den

Schieferflächen zeigen eine NW–SO-Streckung an. Asymmetrische Boudins, σ-Klasten und andere Schersinnindikatoren belegen eine Topp-SO-Scherung. Quarzite werden von Scherbändern durchzogen, die eine NO–SW-Lineation aufweisen.

D_1 ist als Internfoliation ($S_i = S_1$) in zwischentektonisch gewachsenen Granat-Porphyroblasten in Chiastolith-Garbenschiefer nachgewiesen. Die durchdringende Schieferung (S_2) wurde während prä-mittelcampaner, amphibolitfazieller (P = 400–500 MPa; T_{max} = 700 °C) Topp-SO-Scherung (D_2) angelegt. Chiastolith und Cordierit wuchsen während mittel- bis spätcampaner Kontaktmetamorphose (T = 600–680 °C; P_{max} = 200 MPa) in der Nachbarschaft zu einem nicht aufgeschlossenem Pluton. Ein Zirkon aus Chiastolith-Garbenschiefer ergab ein konkordantes Alter von 74 ± 2 Ma, das gut mit U-Pb-Altern von Zirkonen aus Intrusivgesteinen auf Anafi und westlich Melambes korreliert. Th/U-Verhältnisse und die idiomorphe Gestalt des Zirkons stützen die Annahme, dass der Zirkon metamorph gewachsen ist. Chiastolith zeigt Anzeichen, dass Topp-SO-Scherung (D_3) die amphibolitfaziellen Gesteine vor Ende des Kristallwachstuns erfasste. Kreuz-Muskovit, Epidot und Chlorit bildeten sich während post-D_3 retrograder Metamorphose (T_{max} = 500 °C; P_{max} = 220 MPa) im Maastrichtium.

Die Ergebnisse zeigen, dass die oberste Deckeneinheit südliche des Dikti-Gebirges eine ähnliche prä-intrusive Entwicklung durchlaufen hat wie auf Anafi und westlich Melambes, jedoch sollte die Einheit anschließend stärker herausgehoben und exhumiert worden sein, sodass heiße mittel- bis spätcampane Intrusionen die Bildung neuer Phase während Kontaktmetamorphose bei sehr niedrigen Drücken begünstigten. In der Spätphase des Chiastolith-Wachstums setzte erneut Topp-SO-Scherung ein. Die oberste Deckeneinheit südlich des Dikti-Gebirges nimmt auf Kreta somit eine vermittelnde Stellung ein zwischen Vorkommen westlich Melambes, die von einer mylonitischen, postintrusiven Topp-SO-Scherung erfasst wurden und Vorkommen im nördlichen Ierapetra-Graben, wo keine postintrusive Scherung stattfand. Die amphibolitfaziellen Gesteine wurden wohl im Paläozän auf die Theodorii-Grünschiefer überschoben. Im Eozän erfolgte schließlich die Überschiebung der amphibolit- und grünschieferfaziellen Gesteine auf die Arvi- und Pindos-Einheit. NE–SW gerichtete Lineation auf Scherbändern in Quarzit müssen nach dem Eozän während Verkürzung entstanden sein und können mit ähnlichen Linearen, die von Granitoiden in der Nähe von Pachia Ammos bekannt geworden sind, korreliert werden.

Die vorliegende Doktorarbeit hat gezeigt, dass die oberste Deckeneinheit ein wichtiger Schlüssel zum Verständnis der frühalpidischen tektonometamorphen und magmatischen Entwicklung der Helleniden in der südlichen Ägäis ist. Weitere Untersuchungen sollten sich zuerst auf andere Gebiete erstrecken, in denen Gesteine der obersten Deckeneinheit aufgeschlossen sind, um einen Vergleich

mit den in dieser Doktorarbeit untersuchten Gebieten zu ermöglichen. Eine Schlüsselrolle dürfte hierbei das Vorkommen an der Typlokalität der Asterousia-Einheit zwischen Kali Limenes und Lendas spielen. Von besonderer Bedeutung dürften aber auch die Vorkommen der niedriggradig metamorphen Untereinheiten der obersten Deckeneinheit in Zentralkreta und auf Gavdos sein. Der Ursprung der niedriggradig metamorphen Untereinheiten als auch ihre genaue Stellung im kretischen Deckenstapel ist bisher nicht eindeutig geklärt. Auch die Serpentinitvorkommen in der obersten Deckeneinheit bedürfen genauerer Studien und es bleibt fraglich, ob es eine oberste *nappe des serpentines* gibt. Umfassende strukturgeologische Untersuchungen in allen Gebieten der obersten Deckeneinheit können weitere Hinweise zur Klärung fundamentaler Fragen in der Entwicklung der obersten Deckeneinheit und somit auch der frühalpidischen Entwicklung in der südlichen Ägäis liefern.

In allen drei Untersuchungsgebieten konnten an der Basis des Asterousia-Kristallins grünschieferfazielle Gesteine gefunden werden, die vorher nur von Anafi beschrieben wurden. Dies wirft die Frage auf, ob vergleichbare Gesteine auch in anderen Gebieten, in denen das Asterousia-Kristallin aufgeschlossen ist, übersehen wurden. Es ist deshalb notwendig, dass die Gebiete der obersten Deckeneinheit umfassend neu kartiert werden. Weitergehende Untersuchungen, um den Ursprung der Teileinheiten der obersten Deckeneinheit zweifelsfrei zu klären, erscheinen ebenfalls sinnvoll. Zurzeit ist die Zugehörigkeit des Asterousia-Kristallines zum pelagonisch-lyzischen Mikrokontinent hauptsächlich durch seine strukturelle Stellung belegt. Ein Vergleich der Altersspektren detritischer Zirkone aus Metasedimenten des Asterousia-Kristallines mit Altersspektren benachbarter Mikrokontinente können Hinweise liefern, ob es tatsächlich mit dem Pelagonikum korreliert werden kann. Eine abschließende Anregung zur weiteren Forschung betrifft den in dieser Doktorarbeit vorgeschlagenen oberkretazischen magmatischen Bogen am Südrand des pelagonisch-lyzischen Mikrokontinentes. Der Zusammenhang mit anderen magmatische Bögen ähnlichen Alters in Südosteuropa und Anatolien (Apuseni-Banat-Timok-Srednogorie-Bogen und Zentralanatolischer Kristallinkomplex) bleibt unklar und bedarf weiterer Untersuchungen. Zum Beispiel strukturgeologische, geochemische, petrographische und geochronologische Untersuchungen würden weitere Informationen zur Zugehörigkeit der magmatischen Bögen liefern.

Appendix A. Conference abstracts

A1 Structural evolution and kinematics of Pelagonian-type crystalline rocks of central Crete and Anafi island

Bastian Wiesenbach[1], Silviu O. Martha[1], Wolfgang Dörr[1], Rainer Petschick[1], Paris Xypolias[2], Gernold Zulauf[1]

[1] Goethe-Universität Frankfurt, Institut für Geowissenschaften, Altenhöferallee 1, 60438 Frankfurt am Main, Germany.
[2] Department of Geology, University of Patras, 26500, Patras, Greece.

Most of the Alpine nappes exposed on Crete belong to the External Hellenides. The so-called Uppermost Unit (UU), however, is ascribed to the Pelagonian domain towards the north and thus should belong to the Internal Hellenides. The UU consists of ophiolite-bearing nappes with associated continental basement rocks, which are referred to as Asteroussia crystalline complex (ACC). Rocks of the ACC are exposed in central and eastern Crete and presumably on the Cycladic islands of Anafi, Donoussa, Ikaria, and Nikouria. All these rocks were intruded by Cretaceous granitoids and underwent Upper Cretaceous HT-LP metamorphism (e.g. Seidel et al. 1976; Reinecke et al. 1982).

Because of the different geodynamic settings suggested so far for the origin of the UU, we studied and compared the structural records of the crystalline rocks on Anafi and in the Melambes area of central Crete.

The tectonometamorphic sequence of the high-grade rocks on Anafi consists of amphibolite, calcsilicate rock, and gneiss. This sequence is overlain by Upper Cretaceous granitoids, which intruded into marble. The amphibolite facies rocks have been thrust on top of isoclinally folded greenschists with MORB-like composition affected by mid-Palaeocene LP-LT metamorphism. Field observations indicate the contact between the greenschists and the overlying amphibolite facies rocks to be mylonitic. Shear sense indicators, such as σ-type clasts, show ductile top-to-the-SE tectonic transport within both the greenschist and the amphibolite facies rocks. The contact between the greenschists and amphibolite facies rocks with the overlying granitoids is cataclastic.

The ACC near Melambes in central Crete consists of greenschist and quartzite at the base overthrusted by schists, granitoids, calcsilicate rocks, gneisses, amphibolites, and marbles. SE-vergent folds, asymetrically shaped duplexes, and other shear sense indicators suggest a prominent top-to-the-

SE ductile transport inside the ACC. Less important are W-vergent folds, C-type shear bands and asymmetrically shaped prophyroclasts, which show a top-to-the-W tectonic transport.

Our preliminary data suggest that the amphibolite facies rocks of both Anafi and central Crete were affected by top-to-the-SE shearing under amphibolite facies conditions. Apart from Cretaceous granitoids and Cretacous K-Ar cooling ages, the similar kinematics under similar metamorphic conditions is further evidence that both crystalline complexes share a common tectonometamorphic history. Based on the K-Ar and fission-track ages, the amphibolite-facies top-to-the-SE movements must be Cretaceous in age. Top-to-the W movements, on the other hand, were probably related to the stacking of the ACC on top of the greenschist facies rocks underneath. As W-vergent folds are also present in the Pindos sediments (e.g. at Agios Pavlos), thrusting of the greenschist facies rocks on top of the Pindos sediments should have occurred in a similar kinematic framework, but under brittle conditions.

References

Reinecke, T., Altherr, R., Hartung, B., Hatzipangiotou, K., Kreuzer, H., Harre, W., Klein, H., Keller, J., Geenen, E. & Boeger, H. (1982): Remnants of a Late-Cretaceous high-temperature belt on the island of Anafi (Cyclades, Greece). – *Neues Jahrbuch für Mineralogie, Abhandlungen*, **145**: 157–182.

Seidel, E., Okrusch, M., Kreuzer, H., Raschka, H. & Harre, W. (1976): Eo-Alpine metamorphism in the uppermost unit of the Cretan nappe system - petrology and geochronology. Part 1: The Lendas area (Asterousia mountains). – *Contributions to Mineralogy and Petrology*, **57**, 259–275.

A2 The Asterousia Crystalline Complex in the Aegean region: insights from structural analyses and U-Pb zircon dating on Anafi Island (Cyclades, Greece)

Silviu O. Martha[1], Gernold Zulauf[1], Wolfgang Dörr[1], Paraskevas Xypolias[2], Rainer Petschick[1], Janina Schastok[1]

[1]Institut für Geowissenschaften, Goethe-Universität Frankfurt, Altenhöferallee 1, 60438 Frankfurt am Main, Germany.
[2]Department of Geology, University of Patras, 26500, Patras, Greece.

The Asterousia Crystalline Complex (ACC) belongs to the Uppermost Unit and consists of HT–LP metamorphic rocks and associated granitoids, both of which are Upper Cretaceous in age and attributed to the Pelagonian domain of the Internal Hellenides. The ACC is exposed on Crete and the Cyclades. We present geochronological, petrological and structural data obtained from crystalline rocks of Anafi Island attributed to the ACC. These rocks rest on top of Eocene flysch and comprise from bottom to top: a) LT–LP-metamorphosed rocks (Greenschist Unit); b) HT–LP metamorphosed rocks (Axina Group); c) tectonic mélange of HT–LP metamorphosed metasedimentary rocks, serpentinite, and marble intruded by granitoids (Chalepa Complex).

Concordant U-Pb (TIMS) ages of zircons separated from granodiorite reflect multiple emplacement of magma into the marble (73.95 ± 0.13 Ma in NE Anafi; 72.62 +0.03/–0.23 Ma in S Anafi). Thin section analyses of granodiorite and hornblende diorite reveal the granitoids of Anafi to have faced HT–LP metamorphism along with the rocks of the Axina Group and the Chalepa Complex. Metagranodiorite of NE Anafi is cut by synmetamorphic monzogranitic dykes, zircons of which yield a concordant age at 63.01 +0.08/–0.03 Ma.

The Axina Group and the Chalepa Complex are considered as subunits of the ACC formed in the back-arc domain of the Cretaceous Hellenic subduction zone. The Greenschist Unit is considered as a separate unit of the lower plate, which underwent Middle Palaeocene greenschist-facies metamorphism inside the same subduction zone. Thrusting of the different units occurred during continuous shortening with top-to-the SE tectonic transport and uplift of the high grade rocks from lower to higher structural levels, starting with ductile shearing of the Axina Group on top of the Greenschist Unit, followed by semibrittle shearing of the Chalepa Complex on both units and ceasing with thrusting of the crystalline rocks onto the Eocene flysch under brittle conditions.

A3 Structural and U-Pb zircon data from the Asterousia Crystalline Complex of central Crete: Insights on the evolution of the Eastern Mediterranean

Silviu O. Martha[1], Wolfgang Dörr[1], Jolien Linckens[1], Bastian Wiesenbach[1], Gernold Zulauf[1]

[1] Institut für Geowissenschaften, Goethe-Universität Frankfurt, Altenhöferallee 1, 60438 Frankfurt am Main, Germany.

Crete consists of a nappe pile composed of several metamorphic and non-metamorphic units, most of which are assigned to the External Hellenides. The Uppermost Unit, however, is usually ascribed to the Pelagonian domain of the Internal Hellenides. It comprises several low-grade metamorphic subunits and one subunit (Asterousia Crystalline Complex) consisting of amphibolite-facies metamorphic rocks intruded by granitoids.

Studies of Asterousia-type rocks in central Crete (Melambes area) show calsilicate rock, marble, micaschist, paragneiss, and quartzite to have been thrust on top of low-grade metamorphic rocks (quartzite and riebeckite epidote schist). Foliation planes display a NW–SE-trending mineral/stretching lineation in all rock types. Macroscopic and microscopic shear sense indicators such as asymmetrically shaped mineral clasts, C-type shear bands, shearband boudinage and vergence of folds (Fig. A3.1) indicate a top-to-the SE tectonic transport. LPO patterns of quartz obtained using EBSD on quartzite indicate simple shear with basal <a> slip, rhomb <a> slip and prism <a> slip for low-grade metamorphic quartzite and rhomb <a> slip and prism <a> slip for high-grade metamorphic quartzite.

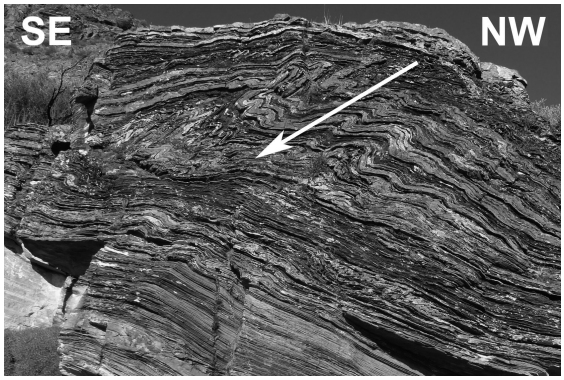

Fig. A3.6 SE vergent drag folds in calcsilicate rock and marble indicate top-to-the SE sense of shear.

Apart from metasedimentary rocks, the Asterousia-type sequence includes (meta-)igneous rocks with both granitic and dioritic affinity. Whereas the granite shows pervasive mylonitic foliation, the diorite is free from foliation. Concordia ages of zircon (ID-TIMS) reveal an emplacement age of the dioritic magma at 72.19 ± 0.44 Ma and an inherited event at 74.32 ± 0.40 Ma. U-Pb ages of diorite from the Melambes area corroborate U-Pb ages from unmetamorphosed granitoids of eastern Crete and Anafi (Kneuker et al. 2015, Martha et al. in rev.). The orthogneiss yields a concordia age (LA-ICP-MS) at 76.3 ± 0.6 Ma.

Published K-Ar hornblende and biotite ages obtained from metasediments range from 66.1 ± 0.9 Ma to 69.9 ± 1.1 Ma (Seidel et al. 1981). Combined with the new U-Pb zircon ages, the K-Ar ages indicate slow cooling of the Asterousia-type rocks, probably inside the back-arc domain of a subduction zone. The lack of foliation in diorite could be due to the low amount of quartz. LPO patterns indicate amphibolite-facies conditions for Uppermost Cretaceous shearing of the Asterousia-type rocks, but greenschist-facies conditions for quartzite and riebeckite epidote schist. A correlation with comparable rocks that experienced Palaeocene greenschist-facies

metamorphism found at the base of the Asterousia-type sequence on Anafi is likely. Ductile SE-directed thrusting of Asterousia-type rocks on low-grade metamorphic rocks should therefore be Palaeocene in age.

References

Kneuker, T., Dörr, W., Petschick, R., Zulauf, G. (2015): Upper crustal emplacement and deformation of granitoids inside the Uppermost Unit of the Cretan nappe stack: constraints from U-Pb zircon dating, microfabrics and paleostress analyses. *Int. J. Earth Sci.*, **104**: 351–367.

Martha, S.-O., Dörr, W., Petschick, R., Schastok, J., Xypolias, P., Zulauf, G. (in review): New structural and U-Pb zircon data from crystalline rocks of Anafi Island (Cyclades, Greece): Implications for the tectonic evolution of the Internal Hellenides. Submitted to: *Int. J. Earth Sci*.

Seidel, E., Okrusch, M., Kreuzer, H., Raschka, H., Harre, W. (1981): Eo-Alpine metamorphism in the uppermost unit of the Cretan nappe system – petrology and geochronology. Part 2. *Contrib. Mineral. Petrol.* **76**: 351–361.

A4 A Late Cretaceous magmatic arc in the southern Aegean (Crete and Cyclades): Constraints on the tectonometamorphic and magmatic evolution of the Internal Hellenides

Silviu O. Martha[1], Jannes J. Binck[1], Wolfgang Dörr[1], Axel Gerdes[1], Jolien Linckens[1], Patrick M. Nowara[1], Paraskevas Xypolias[2], Gernold Zulauf[1]

[1]Institut für Geowissenschaften, Goethe-Universität Frankfurt, Altenhöferallee 1, 60438 Frankfurt am Main, Germany.
[2]Department of Geology, University of Patras, 26500 Patras, Greece.

Records of Alpine orogenic imprints in the Internal Hellenides can be studied in the Uppermost Unit of Crete and on several Cycladic islands. The rocks exposed in these areas are attributed to the Pelagonian domain of central Greece.

We present new structural, petrographic and geochronological data obtained from greenschist and amphibolite-facies (Asterousia-type) rocks exposed on Crete (Melambes area and southern Dikti Mountains), Anafi and Donousa. On Anafi and Crete, greenschist-facies rocks were found at the base of the Asterousia-type sequence. New structural data combined with published K-Ar ages indicate Late Cretaceous and Palaeocene top-to-the SE shearing of amphibolite- and greenschist-facies rocks, respectively. In some exposures of the Asterousia-type rocks a secondary ill-defined NE–SW-trending mineral/stretching lineation can be observed.

U-Pb (LA-ICP-MS and ID-TIMS) dating of zircon from Asterousia-type (meta)granite yielded 76.3 ± 0.6 Ma (Melambes), while zircon from diorite intrusions near Melambes and granodiorite intrusions on Anafi yields ages at 72.2 to 74.8 Ma. The latter ages are consistent with an emplacement age of 74.5 ± 0.25 Ma for diorite from Pachia Ammos (eastern Crete, Kneuker et al. 2015). Granite underwent viscous deformation under amphibolite-facies conditions resulting in orthogneiss, while diorite and granodiorite are free from foliation. This indicates synmetamorphic intrusion of granitic magma, but late-metamorphic intrusion of dioritic magma. Mineral assemblages of diorite and granodiorite (plagioclase, quartz, apatite, titanite) are typical for I-type granitoids. Koutsovitis et al. (2012) interpreted the Anafi granodiorite as volcanic-arc granitoids based on REE patterns.

The new data combined with published results suggest the following orogenic processes in a magmatic arc setting: (1) obduction and accretion of mantle slices (serpentinite) to the Asterousia-type rocks; (2) Campanian intrusion of granitoids within a magmatic arc that underwent high-temperature/low-pressure metamorphism; (3) Maastrichtian intrusion of dykes; (4) Palaeocene ductile top-to-

the SE shearing of amphibolite-facies on top of greenschist-facies rocks; (5) post-Eocene brittle thrusting of the crystalline rocks on top of the Pindos Unit; (6) clockwise rotation of the Aegean block and change in the stress field to NE–SW compression during the Oligocene to early Miocene.

References

Kneuker et al. 2015, *Int. J. Earth Sci.*, **104**, 351–367.

Koutsovitis et al. 2012, *EGU General Assembly Conference Abstracts*, 13303.

Appendix B. Field data

The following tables summarize the data taken during fieldwork on Anafi (19–24 October 2013, 13–14 October 2014 and 26–30 October 2014), in the area west of Melambes (30 September and 20–28 November 2014) and in the area of Pefkos, Kalami and Sykologos (3–10 October 2014). Rock types, coordinates and height in metres above sea level are indicated. For the structural data, a colour code is used for the planar and linear elements measured.

Planar elements	**Linear elements**
Bedding	
Foliation	Mineral/stretching lineation
Fold plane	Fold axis
Fault plane	Slickenside striation
Shear zone	Striation on shear zone

B1 Field data from Anafi

Table B1.1 Summary of data collected during fieldwork on Anafi from the Eocene flysch, Anafi Greenschist, Anafi Amphibolite Group and Chalepa Group.

Outcrop	Rock type(s)	Planes		Lines		Coordinates	Height [m]
		Strike	Dip	Trend	Plunge		
Af001	Paragneiss	088	62			36° 21′ 42.76″ N; 25° 49′ 26.47″ E	141
Af002*	Calcsilicate rock	020	36	336	35	36° 21′ 39.75″ N; 25° 49′ 24.92″ E	112
Af003*	Quartz mica schist	070	36	330	06	36° 21′ 38.99″ N; 25° 49′ 26.05″ E	105
Af004*	Calcsilicate rock	026	42	328	40	36° 21′ 27.14″ N; 25° 49′ 32.97″ E	35
Af005*	Calcsilicate rock	325	73	255	18	36° 21′ 26.02″ N; 25° 49′ 31.22″ E	33
Af006*	Quartzite	040	46	318	28	36° 21′ 17.52″ N; 25° 48′ 55.28″ E	35
Af007	Flysch	012	55	032	38	36° 21′ 17.30″ N; 25° 48′ 56.65″ E	35
		348	70	002	40		
		320	65	014	38		
		316	70	020	30		
		328	70	008	40		
		328	70	014	30		
Af008*	Micaschist	042	40	112	22	36° 21′ 17.99″ N; 25° 48′ 53.71″ E	37
Af009*	Quartzite	028	58	302	20	36° 21′ 17.70″ N; 25° 48′ 50.79″ E	31
		025	56	298	15		
Af010*	Orthoamphibolite	022	72	308	38	36° 21′ 24.11″ N; 25° 48′ 35.92″ E	53
	Quartzite	024	62	325	34		
Af011*	Orthoamphibolite	025	45	308	22	36° 21′ 26.94″ N; 25° 48′ 26.41″ E	67
		018	50	034	50		
Af012*	Orthoamphibolite, quartzite	070	58	132	25	36° 21′ 26.75″ N; 25° 48′ 26.70″ E	65
Af013	Greenschist	052	82	132	12	36° 21′ 28.39″ N; 25° 48′ 12.87″ E	135
		046	62	134	05		
	Flysch	212	78				
		224	50	284	24		
		210	30	270	05		
	Flysch, greenschist	205	50				
Af014	Flysch	105	25	232	40	36° 21′ 16.11″ N; 25° 48′ 04.43″ E	106
Af015	Diorite					36° 21′ 13.82″ N; 25° 46′ 33.11″ E	170
Af016*	Granodiorite					36° 20′ 39.05″ N; 25° 46′ 41.88″ E	2
Af017*	Marble					36° 21′ 11.71″ N; 25° 45′ 15.11″ E	128
Af018*	Marble					36° 21′ 13.40″ N; 25° 45′ 15.52″ E	146
Af019*	Marble					36° 21′ 14.51″ N; 25° 45′ 15.75″ E	154
Af020*	Marble					36° 21′ 14.91″ N; 25° 45′ 16.86″ E	160
Af021*	Marble					36° 23′ 07.16″ N; 25° 46′ 27.85″ E	242
Af021*	Granodiorite					36° 23′ 07.42″ N; 25° 46′ 22.31″ E	269
Af022*	Granodiorite					36° 22′ 47.15″ N; 25° 47′ 01.46″ E	133
Af023*	Monzogranite					36° 23′ 09.38″ N; 25° 47′ 18.82″ E	105

Af024*	Gabbro					36° 23′ 09.88″ N; 25° 47′ 20.19″ E	107
Af025	Orthoamphibolite	200	90	295	22	36° 22′ 28.46″ N; 25° 46′ 56.89″ E	234
Af026*	Orthoamphibolite	220	64	132	05	36° 22′ 18.00″ N; 25° 47′ 09.50″ E	301
Af027	Orthoamphibolite	042	88	136	35	36° 22′ 15.69″ N; 25° 47′ 07.32″ E	316
		048	85	130	05		
Af028	Greenschist	355	45	314	42	36° 21′ 59.71″ N; 25° 46′ 48.41″ E	204
Af029*	Greenschist, amphibolite, quartzite	352	64	302	46	36° 22′ 01.66″ N; 25° 46′ 49.81″ E	209
		324	48	297	38		
Af030*	Quarzite, calcsilicate rock					36° 22′ 14.16″ N; 25° 47′ 49.03″ E	271
Af031*	Micaschist	036	76	294	65	36° 21′ 45.14″ N; 25° 48′ 07.33″ E	222
	Quartzite	032	78	316	65		
	Orthoamphibolite	032	78	298	36		
				288	25		
				308	36		
				300	27		
Af032*	Flysch, marble	082	67			36° 21′ 20.47″ N; 25° 48′ 12.47″ E	146
Af033	Greenschist, diorite	045	57	003	45	36° 21′ 12.27″ N; 25° 46′ 14.42″ E	212
Af034	Diorite, serpentinite	082	35	070	27	36° 21′ 14.25″ N; 25° 46′ 33.47″ E	170
		082	35	067	37		
Af035	Calcsilicate rock	044	48	320	05	36° 21′ 27.72″ N; 25° 49′ 33.60″ E	51
Af036	Diorite					36° 21′ 34.32″ N; 25° 49′ 29.17″ E	66
Af037	Diorite, marble	220	32			36° 21′ 35.67″ N; 25° 49′ 25.49″ E	76
Af038*	Micaschist	054	48	340	27	36° 21′ 38.25″ N; 25° 49′ 24.27″ E	98
Af039*	Orthogneiss					36° 21′ 37.65″ N; 25° 49′ 26.30″ E	94
Af040*	Marble, calcsilicate rock, micaschist	128	08	118	15	36° 21′ 20.38″ N; 25° 49′ 45.33″ E	43
Af041	Micaschist, calcsilicate rock	172	24	230	6	36° 21′ 23.64″ N; 25° 49′ 47.61″ E	45
Af042	Micaschist, calcsilicate rock	228	35	234	25	36° 21′ 24.72″ N; 25° 49′ 48.90″ E	51
Af043	Serpentinite, calcsilicate rock	032	35	008	30	36° 21′ 33.37″ N; 25° 49′ 41.44″ E	51
Af044	Micaschist	080	30	347	05	36° 21′ 32.82″ N; 25° 49′ 37.74″ E	63
Af045	Orthoamphibolite, marble	092	35			36° 21′ 20.85″ N; 25° 49′ 21.91″ E	41
Af046	Orthoamphibolite	156	88	108	55	36° 21′ 22.15″ N; 25° 49′ 17.36″ E	45
Af047	Orthoamphibolite	188	76	278	46	36° 21′ 23.74″ N; 25° 49′ 16.14″ E	39
Af048	Orthoamphibolite	016	72	328	68	36° 21′ 18.85″ N; 25° 49′ 11.73″ E	46
Af049*	Flysch	310	35			36° 20′ 45.96″ N; 25° 46′ 13.90″ E	30
				235	45		
Af050	Orthoamphibolite	218	32	146	30	36° 21′ 17.17″ N; 25° 49′ 00.79″ E	50
Af051*	Micaschist	052	55	132	25	36° 21′ 18.03″ N; 25° 48′ 53.99″ E	42
Af052	Micaschist	072	45	318	25	36° 21′ 18.51″ N; 25° 48′ 48.61″ E	40
Af053	Micaschist	088	40	146	40	36° 21′ 19.53″ N; 25° 48′ 45.78″ E	44
Af054	Micaschist	066	35	342	10	36° 21′ 19.63″ N; 25° 48′ 44.51″ E	45
Af055*		202	30	146	25	36° 21′ 20.25″ N; 25° 48′ 42.52″ E	42
		202	30	230	05		
				20	35		
Af056	Orthoamphibolite, micaschist, quartzite	024	50	306	12	36° 21′ 26.68″ N; 25° 48′ 29.44″ E	63
Af057	Orthoamphibolite	004	56	308	30	36° 21′ 29.83″ N; 25° 48′ 25.34″ E	81
Af058	Orthoamphibolite	356	60	236	65	36° 21′ 34.30″ N; 25° 48′ 24.68″ E	93
Af059	Orthoamphibolite	080	60	148	25	36° 21′ 35.79″ N; 25° 48′ 24.21″ E	105
Af060	Orthoamphibolite	004	80	292	60	36° 21′ 42.48″ N; 25° 48′ 25.18″ E	157
Af061	Orthoamphibolite	198	84	294	40	36° 21′ 31.20″ N; 25° 48′ 22.51″ E	95
Af062	Micaschist	106	40	152	26	36° 21′ 30.59″ N; 25° 48′ 18.00″ E	104
Af063	Micaschist	048	68	322	12	36° 21′ 33.92″ N; 25° 48′ 11.60″ E	120
Af064*	Flysch	026	80			36° 21′ 05.38″ N; 25° 48′ 07.39″ E	54
Af065	Flysch					36° 21′ 17.25″ N; 25° 48′ 05.00″ E	121
Af066	Flysch	330	25			36° 21′ 09.14″ N; 25° 47′ 34.14″ E	48
Af067	Flysch					36° 21′ 09.23″ N; 25° 47′ 32.83″ E	69
Af068	Greenschist	350	20	236	25	36° 20′ 58.79″ N; 25° 46′ 45.44″ E	143
Af069*	Greenschist	056	15	326	05	36° 21′ 02.87″ N; 25° 46′ 48.34″ E	152
		164	35	78	30		
		160	25	68	20		
Af070	Greenschist	112	24	152	15	36° 21′ 06.27″ N; 25° 46′ 41.87″ E	150
Af071	Greenschist	258	35	298	18	36° 21′ 06.22″ N; 25° 45′ 54.87″ E	195
Af072	Greenschist	048	14	332	15	36° 21′ 03.08″ N; 25° 45′ 53.64″ E	194
Af073	Greenschist	080	56	326	36	36° 21′ 00.81″ N; 25° 45′ 52.06″ E	193
Af074	Greenschist	058	58	334	24	36° 20′ 56.80″ N; 25° 45′ 53.89″ E	188
Af075	Flysch, greenschist					36° 20′ 55.72″ N; 25° 45′ 55.45″ E	185
Af076	Flysch, greenschist	034	60	302	36	36° 20′ 55.73″ N; 25° 45′ 58.43″ E	182
Af077	Greenschist	038	38	318	26	36° 20′ 56.42″ N; 25° 46′ 01.89″ E	182
Af078	Greenschist	036	54	326	25	36° 21′ 01.33″ N; 25° 46′ 05.90″ E	180
Af079	Greenschist	014	40	312	30	36° 21′ 02.03″ N; 25° 46′ 09.49″ E	182
Af080	Greenschist	010	20	310	14	36° 21′ 03.18″ N; 25° 46′ 25.05″ E	173
Af081	Greenschist	228	48	328	14	36° 21′ 06.90″ N; 25° 45′ 54.53″ E	183
Af082	Greenschist	000	20	336	24	36° 21′ 08.17″ N; 25° 46′ 00.30″ E	175
Af083	Greenschist	268	30	336	16	36° 21′ 08.54″ N; 25° 45′ 57.58″ E	165
Af084	Greenschist	234	62	310	24	36° 21′ 08.43″ N; 25° 45′ 53.47″ E	153
Af085	Greenschist	256	46	316	35	36° 21′ 12.12″ N; 25° 45′ 49.07″ E	140

Af086	Greenschist	058	80	138	56	36° 21′ 11.43″ N; 25° 45′ 45.97″ E	125
		236	54	188	38		
		238	48	192	30		
		202	66	12	10		
Af087	Flysch, greenschist	062	70	328	22	36° 21′ 10.29″ N; 25° 45′ 45.48″ E	122
		76	70	44	50		
		64	76				
Af088	Flysch, greenschist	48	64	316	36	36° 21′ 11.84″ N; 25° 45′ 44.07″ E	97
		30	74				
Af089	Greenschist	246	68	310	48	36° 21′ 15.71″ N; 25° 45′ 42.77″ E	79
		264	60	324	34		
Af090	Greenschist	020	38	322	18	36° 21′ 17.33″ N; 25° 45′ 37.05″ E	84
Af091	Flysch	058	26			36° 21′ 13.52″ N; 25° 45′ 34.62″ E	85
Af092*	Greenschist	044	32	144	14	36° 21′ 09.03″ N; 25° 45′ 17.05″ E	130
Af093	Greenschist, granitoid					36° 21′ 09.71″ N; 25° 45′ 15.62″ E	132
Af094*	Diorite, serpentinite	062	45			36° 21′ 11.77″ N; 25° 46′ 26.18″ E	229
Af095	Orthoamphibolite, marble					36° 22′ 23.53″ N; 25° 47′ 12.14″ E	317
Af096	Orthoamphibolite	328	64			36° 22′ 20.71″ N; 25° 47′ 10.26″ E	323
		300	50				
		308	65				
Af097*	Marble					36° 23′ 00.07″ N; 25° 47′ 12.46″ E	129
Af098*	Marble					36° 23′ 00.42″ N; 25° 47′ 11.59″ E	140
Af099*	Marble					36° 23′ 00.58″ N; 25° 47′ 10.39″ E	151
Af100	Orthoamphibolite	212	75	314	12	36° 22′ 34.46″ N; 25° 46′ 54.12″ E	217
Af101	Orthoamphibolite	212	82	308	20	36° 22′ 21.81″ N; 25° 46′ 58.18″ E	267
Af102	Orthoamphibolite	210	85	122	26	36° 22′ 17.50″ N; 25° 47′ 05.28″ E	295
		074	34				
Af103	Orthoamphibolite	238	88	138	35	36° 22′ 12.53″ N; 25° 47′ 04.35″ E	324
Af104	Orthoamphibolite	024	84	304	62	36° 22′ 07.94″ N; 25° 47′ 02.83″ E	304
Af105	Orthoamphibolite	014	80	284	30	36° 22′ 00.80″ N; 25° 47′ 02.45″ E	275
Af106	Orthoamphibolite	010	86	286	35	36° 22′ 02.32″ N; 25° 47′ 01.71″ E	266
Af107	Orthoamphibolite	012	78	290	35	36° 22′ 06.25″ N; 25° 46′ 53.97″ E	239
Af108	Orthoamphibolite	022	66	290	62	36° 22′ 07.29″ N; 25° 46′ 50.14″ E	235
Af109	Greenschist	160	36	312	24	36° 21′ 56.52″ N; 25° 46′ 44.66″ E	197
Af110	Greenschist	030	45	310	26	36° 21′ 52.01″ N; 25° 46′ 42.33″ E	184
Af111	Greenschist	048	50	328	15	36° 21′ 46.25″ N; 25° 46′ 38.31″ E	170
Af112	Greenschist	020	40	328	30	36° 21′ 39.19″ N; 25° 46′ 39.41″ E	170
Af113	Greenschist	058	36	340	05	36° 21′ 34.95″ N; 25° 46′ 37.33″ E	176
Af114	Greenschist	022	75	336	40	36° 21′ 35.28″ N; 25° 46′ 30.26″ E	174
Af115	Greenschist	014	24	322	30	36° 21′ 28.93″ N; 25° 46′ 33.14″ E	190
Af116	Flysch, greenschist	020	30	340	15	36° 20′ 59.76″ N; 25° 46′ 26.71″ E	172
		334	55				
Af117	Flysch	018	40			36° 20′ 58.73″ N; 25° 46′ 27.98″ E	162
Af118	Flysch	140	85	228	15	36° 20′ 56.56″ N; 25° 46′ 30.42″ E	153
		132	88	220	12		
Af119	Greenschist, diorite	018	56	318	45	36° 21′ 02.36″ N; 25° 46′ 30.21″ E	165
Af120	Diorite, serpentinite	168	50			36° 21′ 21.91″ N; 25° 46′ 34.73″ E	212
Af121	Greenschist, diorite	026	22	308	15	36° 21′ 27.84″ N; 25° 46′ 32.91″ E	185
Af122	Orthoamphibolite	028	82	306	36	36° 22′ 06.36″ N; 25° 47′ 05.23″ E	273
Af123	Orthoamphibolite	030	88	302	26	36° 22′ 08.95″ N; 25° 47′ 08.14″ E	271
	Quartzite	038	78	336	30		
		208	12				
Af124	Orthoamphibolite	028	90	128	08	36° 22′ 09.29″ N; 25° 47′ 15.09″ E	272
Af125	Orthoamphibolite	042	68	114	32	36° 22′ 07.59″ N; 25° 47′ 20.34″ E	269
Af126	Orthoamphibolite	014	78	098	14	36° 22′ 01.24″ N; 25° 47′ 31.78″ E	265
Af127	Orthoamphibolite	038	62	124	30	36° 21′ 58.97″ N; 25° 47′ 35.09″ E	270
Af128	Orthoamphibolite					36° 21′ 58.20″ N; 25° 47′ 39.03″ E	272
Af129	Orthoamphibolite	358	42	278	06	36° 22′ 03.88″ N; 25° 47′ 48.12″ E	258
Af130	Orthoamphibolite	312	72	36	22	36° 22′ 01.06″ N; 25° 47′ 59.72″ E	235
		304	82	28	30		
Af131	Orthoamphibolite	204	36	138	24	36° 22′ 03.32″ N; 25° 48′ 09.13″ E	236
Af132	Orthoamphibolite	200	76	118	38	36° 21′ 56.30″ N; 25° 48′ 06.83″ E	231
Af133	Orthoamphibolite	192	72	286	44	36° 21′ 51.56″ N; 25° 48′ 06.55″ E	235
Af134	Orthoamphibolite	008	76	280	40	36° 21′ 47.90″ N; 25° 48′ 07.25″ E	240
Af135	Orthoamphibolite	000	55	300	45	36° 21′ 43.71″ N; 25° 48′ 08.60″ E	201
Af136	Orthoamphibolite	312	48	188	60	36° 21′ 42.65″ N; 25° 48′ 09.30″ E	188
Af137	Orthoamphibolite	012	66	294	20	36° 21′ 39.55″ N; 25° 48′ 08.16″ E	166
Af138	Greenschist	210	85	294	12	36° 21′ 37.27″ N; 25° 48′ 07.40″ E	150
Af139	Greenschist	030	70	308	25	36° 21′ 32.78″ N; 25° 48′ 10.15″ E	127
Af140	Greenschist	220	85	318	20	36° 21′ 30.47″ N; 25° 48′ 11.78″ E	127
Af141	Flysch	222	72			36° 21′ 09.13″ N; 25° 48′ 07.39″ E	67
Af142	Flysch	212	64			36° 21′ 11.99″ N; 25° 47′ 59.74″ E	91
Af143	Diorite, flysch	218	20			36° 21′ 03.54″ N; 25° 47′ 26.07″ E	73
Af144	Flysch	210	24			36° 20′ 55.05″ N; 25° 46′ 32.42″ E	152
Af145	Flysch	348	64	50	26	36° 20′ 50.00″ N; 25° 46′ 25.50″ E	126

		310	44	46	30		
Af146	Flysch	340	80	56	16	36° 20′ 50.45″ N; 25° 46′ 20.52″ E	91
Af147	Greenschist	024	68	312	30	36° 21′ 43.06″ N; 25° 47′ 58.70″ E	239
Af148	Greenschist	038	55	324	35	36° 21′ 42.66″ N; 25° 47′ 55.87″ E	257
Af149	Limestone, greenschist	208	50	142	25	36° 21′ 38.32″ N; 25° 47′ 58.52″ E	235
Af150*	Limestone, flysch	060	60			36° 21′ 34.92″ N; 25° 47′ 55.13″ E	324
Af151	Greenschist	012	32	350	26	36° 22′ 52.65″ N; 25° 45′ 17.88″ E	118
		020	16	022	20		
		020	32	014	30		
Af152	Greenschist	096	34	008	16	36° 22′ 56.20″ N; 25° 45′ 20.19″ E	112
Af153*	Greenschist	110	45	192	15	36° 23′ 02.30″ N; 25° 45′ 11.05″ E	110
		108	35	182	10		
		118	36	190	16		
		110	64	188	28		
		128	45	194	10		
		122	42	204	24		
		104	40	186	12		
		130	48	198	18		
		108	35	190	15		
		110	36	196	16		
Af154	Greenschist	064	85	328	15	36° 21′ 10.70″ N; 25° 45′ 45.52″ E	131
		062	48	324	20		
		028	65	310	12		
		060	50	316	16		
		068	60	320	14		
		064	48	324	18		
		060	76	324	16		
		062	78	318	20		
		064	70	316	18		
		064	60	320	16		
Af155*	Marble					36° 20′ 55.35″ N; 25° 50′ 44.51″ E	460
Af156*	Marble					36° 21′ 17.18″ N; 25° 50′ 28.65″ E	189
Af157	Orthoamphibolite	196	32	290	25	36° 21′ 23.65″ N; 25° 49′ 13.80″ E	41
				314	15		
				298	20		
		248	56	294	34		
Af158*	Orthoamphibolite	060	60	132	18	36° 21′ 17.62″ N; 25° 48′ 55.21″ E	49
		024	56	320	15		
Af159*	Diorite					36° 21′ 11.60″ N; 25° 46′ 25.66″ E	226
Af160	Serpentinite	052	28	144	02	36° 21′ 35.05″ N; 25° 49′ 43.18″ E	85
		010	25	132	16		
		042	30	152	06		
		040	25	156	08		
		042	35	154	10		
		002	42	130	18		
		038	52	142	12		
		042	36	134	10		
		034	24	152	08		
		038	25	148	12		
Af161*	Plagiogranite, serpentinite	052	55			36° 21′ 40.24″ N; 25° 49′ 33.97″ E	115
Af162	Serpentinite	332	64	050	30	36° 21′ 44.38″ N; 25° 49′ 04.43″ E	232
		020	34	028	26		
		346	44	056	20		
		336	36	024	16		
		338	58	052	15		
		342	48	048	24		
		330	58	058	12		
		338	40	044	15		
		350	55	040	18		
		350	52	056	20		
Af163	Calcsilicate rock	308	58	218	26	36° 21′ 43.83″ N; 25° 48′ 47.12″ E	284
		312	46	238	28		
		296	52	216	36		
		282	45	238	36		
		300	50	224	25		
		304	56	230	30		
Af164	Plagiogranite, calcsilicate rock					36° 21′ 43.07″ N; 25° 48′ 46.13″ E	285
Af165	Diorite, serpentinite	058	48			36° 21′ 47.39″ N; 25° 48′ 34.91″ E	278
Af166*	Orthoamphibolite	024	58	304	32	36° 21′ 49.76″ N; 25° 48′ 08.34″ E	227
		026	64	308	28		
		012	68	300	40		
		020	70	302	28		
		028	70	300	32		
		018	68	312	38		
		022	65	302	30		

		018	64	308	26		
		024	70	306	30		
		020	72	300	36		
Af167	Greenschist	194	20	154	16	36° 21′ 05.95″ N; 25° 46′ 41.78″ E	170
		198	26	158	22		
		150	30	160	20		
		214	38	158	18		
		200	42	162	24		
		068	32	128	24		
		070	16	148	10		
		198	24	154	12		
		196	38	150	16		
		194	30	146	14		
Af168	Greenschist	108	58			36° 20′ 52.23″ N; 25° 46′ 48.50″ E	124
		222	20	160	12		
		202	26	152	18		
		194	20	150	18		
		204	24	158	10		
		218	16	162	08		
		190	26	154	14		
		220	30	152	16		
		206	26	160	10		
		210	24	150	12		
		204	28	152	18		
Af169	Granite					36° 21′ 04.87″ N; 25° 47′ 07.75″ E	44
Af170	Greenschist	182	42	170	20	36° 21′ 30.72″ N; 25° 48′ 11.63″ E	116
		208	14	134	14		
		194	28	152	16		
		200	36	148	18		
		184	48	168	20		
		204	26	148	12		
		196	28	152	16		
		194	30	160	18		
		182	46	158	16		
		190	36	150	20		
Af171	Chalepa	012	64	248	25	36° 21′ 25.92″ N; 25° 49′ 31.17″ E	38
		010	66	250	34		
		012	72	252	32		
		340	68	254	40		
		350	62	248	40		
Af172	Orthoamphibolite	012	64	302	36	36° 21′ 20.84″ N; 25° 49′ 19.79″ E	37
		010	66	332	50		
		012	72	318	68		
		340	68	062	48		
		350	62	058	42		
Af173*	Diorite, marble	248	45			36° 21′ 20.68″ N; 25° 49′ 23.98″ E	43
		254	74				
Af174*	Orthoamphibolite	168	88	246	64	36° 21′ 20.52″ N; 25° 49′ 23.96″ E	15
		176	84	238	80		
		188	80	248	60		
		170	84	240	65		
		164	86	236	58		
		180	80	240	60		
		174	84	236	64		
		164	88	254	80		
		346	84	072	68		
		340	86	068	64		
Af175	Calcsilicate rock	044	50	338	40	36° 21′ 17.47″ N; 25° 48′ 55.04″ E	50
		040	54	334	36		
		048	60	336	38		
		050	54	340	36		
		048	52	346	44		
		048	48	330	36		
		036	56	340	30		
Af176	Granodiorite					36° 23′ 05.99″ N; 25° 47′ 50.81″ E	1
Af177	Orthoamphibolite	192	82	112	16	36° 22′ 35.11″ N; 25° 46′ 54.99″ E	202
		192	88	118	22		
		354	80	290	24		
		358	88	296	36		
		350	84	300	30		
		190	84	110	20		
		196	80	114	18		
		350	80	294	28		
		358	86	298	34		
		352	82	294	32		

Af178	Orthoamphibolite	212	82	296	16	36° 22′ 28.90″ N; 25° 46′ 55.79″ E	226
		202	80	290	20		
		208	86	294	28		
		212	78	302	32		
		212	82	300	24		
		212	82	300	26		
		204	88	294	12		
		214	74	306	18		
		204	82	300	20		
		208	78	302	22		
Af179*	Orthoamphibolite	208	88	120	22	36° 22′ 19.89″ N; 25° 47′ 02.34″ E	275
		196	62	118	18		
		200	74	120	20		
Af180	Orthoamphibolite	022	75	312	35	36° 22′ 20.40″ N; 25° 48′ 10.75″ E	198
		024	80	298	32		
		016	85	280	32		
		022	78	304	45		
		020	78	306	40		
		024	72	298	48		
		012	78	300	36		
		020	84	294	30		
		024	88	310	40		
		018	84	300	38		
Af181*	Orthoamphibolite	144	52	204	30	36° 22′ 28.18″ N; 25° 48′ 22.98″ E	115
		132	58	212	34		
		136	55	196	30		
		140	56	200	32		
		130	62	208	30		
		130	52	198	26		
		126	70	192	25		
		130	60	202	28		
		134	68	194	32		
		150	64	204	30		
Af182*	Orthoamphibolite	010	60	290	34	36° 22′ 28.66″ N; 25° 48′ 41.62″ E	72
		020	80	282	40		
		008	68	296	45		
		018	64	306	38		
		012	65	288	16		
		018	68	294	28		
		020	72	286	40		
		014	74	294	24		
		014	68	300	36		
		010	62	294	38		
Af183*	Orthoamphibolite	014	80	292	48	36° 22′ 31.93″ N; 25° 48′ 48.46″ E	53
		012	72	284	28		
		006	88	284	20		
		008	74	282	30		
		020	82	294	30		
Af184*	Granite, metasediments					36° 22′ 37.26″ N; 25° 45′ 38.06″ E	307
Af185*	Granite, metasediments					36° 21′ 58.03″ N; 25° 45′ 06.08″ E	303
Af186	Granite					36° 22′ 08.19″ N; 25° 45′ 45.35″ E	352
Af187	Greenschist	058	30	324	25	36° 21′ 10.91″ N; 25° 46′ 09.60″ E	218
		040	52	320	22		
		038	50	336	20		
		050	50	346	35		
		054	54	324	30		
		056	52	318	24		
		046	46	328	18		
		048	52	330	20		
		040	54	334	24		
		050	56	324	20		

* One or more samples have been taken from these outcrops to the Goethe-Universität Frankfurt for further investigations thin section investigations.

B2 Field data from the area west of Melambes

Table B2.1 Summary of data collected during fieldwork in the area west of Melambes from the Eocene flysch, Anafi Greenschist, Anafi Amphibolite Group and Chalepa Group.

Outcrop	Rock type(s)	Planes		Lines		Coordinates	Height [m]
		Strike	Dip	Trend	Plunge		
Mb001	Metapelite, quarzite	002	12	334	15	35° 08′ 26.10″ N; 24° 37′ 56.88″ E	375
Mb002	Metapelite, calcsilicate rock, quarzite	002	20	342	25	35° 08′ 29.04″ N; 24° 37′ 51.78″ E	383
		004	18	338	30		
Mb003	Metapelite	040	12	170	35	35° 08′ 24.18″ N; 24° 37′ 48.54″ E	407
		220	12	332	07		
Mb004	Serpentinite	354	16	332	25	35° 08′ 27.42″ N; 24° 37′ 34.32″ E	401
Mb005	Serpentinite					35° 08′ 14.70″ N; 24° 36′ 58.86″ E	400
Mb006	Orthogneiss, calcsilicate rock	084	05	324	02	35° 08′ 09.12″ N; 24° 36′ 52.26″ E	370
Mb007	Calcsilicate rock, marble, quarzite	138	35	148	30	35° 08′ 07.00″ N; 24° 36′ 55.23″ E	381
		132	35	140	30		
Mb008	Orthogneiss	260	10	312	05	35° 08′ 04.98″ N; 24° 36′ 56.16″ E	376
Mb009	Paraamphibolite	340	40	320	35	—	—
Mb010	Micaschist	290	25			35° 08′ 32.31″ N; 24° 36′ 58.04″ E	318
Mb011	Micaschist	110	30	150	20	35° 08′ 34.38″ N; 24° 37′ 27.07″ E	293
Mb012	Quarzite	110	30	150	20	35° 08′ 31.65″ N; 24° 37′ 20.85″ E	297
Mb013	Micaschist					35° 08′ 33.66″ N; 24° 37′ 14.99″ E	305
Mb014	Micaschist	060	20	140	05	35° 08′ 33.78″ N; 24° 37′ 07.05″ E	309
Mb015	Greenschist	020	25	320	15	35° 08′ 35.84″ N; 24° 36′ 54.58″ E	312
Mb016	Micaschist					35° 08′ 41.31″ N; 24° 37′ 09.95″ E	364
Mb017	Greenschist	350	20	320	10	35° 08′ 37.45″ N; 24° 36′ 54.22″ E	300
Mb018	Greenschist	340	25	140	25	35° 08′ 33.58″ N; 24° 36′ 52.72″ E	300
Mb019	Greenschist	360	20	320	10	35° 08′ 31.34″ N; 24° 36′ 49.17″ E	267
Mb020	Greenschist					35° 08′ 29.52″ N; 24° 36′ 50.95″ E	248
Mb021	Greenschist	350	10	310	05	35° 08′ 26.65″ N; 24° 36′ 53.59″ E	227
Mb022	Orthogneiss, greenschist	130	20	130	20	35° 08′ 26.46″ N; 24° 36′ 51.84″ E	237
Mb023	Orthogneiss	020	15	350	10	35° 08′ 36.32″ N; 24° 37′ 20.25″ E	357
Mb024	Diorite					35° 08′ 42.62″ N; 24° 37′ 13.26″ E	372
Mb025	Metapelite, marble, calcsilicate rock	010	45	310	30	35° 08′ 07.77″ N; 24° 37′ 05.76″ E	442
Mb026	Metapelite	010	30	320	20	35° 08′ 07.53″ N; 24° 37′ 05.25″ E	435
Mb027	Calcsilicate rock, metapelite					35° 08′ 01.60″ N; 24° 37′ 07.86″ E	377
Mb028	Orthogneiss, calcsilicate rock	100	15	140	05	35° 08′ 03.87″ N; 24° 37′ 00.69″ E	378
Mb029	Orthogneiss, calcsilicate rock	300	30	300	30	35° 08′ 05.27″ N; 24° 36′ 56.28″ E	383
Mb030	Metapelite	220	25	160	15	35° 08′ 09.23″ N; 24° 36′ 52.15″ E	381
Mb031	Calcsilicate rock	020	15	320	05	35° 08′ 13.83″ N; 24° 36′ 57.85″ E	376
Mb032	Metapelite	320	15	320	15	35° 08′ 20.74″ N; 24° 37′ 04.90″ E	360
Mb033	Paraamphibolite, marble	190	30	140	20	35° 07′ 45.44″ N; 24° 37′ 23.59″ E	429
Mb034	Pindos					35° 07′ 14.42″ N; 24° 36′ 49.49″ E	505
Mb035	Pindos					35° 07′ 41.25″ N; 24° 37′ 20.51″ E	431
Mb036	Paraamphibolite	120	30	140	20	35° 07′ 49.29″ N; 24° 37′ 30.82″ E	400
Mb037	Metapelit, paraamphibolite	190	30	150	20	35° 07′ 57.92″ N; 24° 37′ 31.38″ E	416
Mb038	Paraamphibolite	10	30	320	20	35° 07′ 59.56″ N; 24° 37′ 24.48″ E	426
Mb039	Micaschist	300	20	340	10	35° 08′ 22.44″ N; 24° 37′ 57.05″ E	421
Mb040	Metapelite	20	30	320	05	35° 07′ 44.98″ N; 24° 38′ 42.12″ E	511
Mb041	Micaschist	40	40	330	10	35° 07′ 46.69″ N; 24° 38′ 40.43″ E	505
Mb042	Metapelite, paraamphibolite etc.	50	40	340	20	35° 07′ 52.51″ N; 24° 38′ 40.32″ E	498
Mb043	Metapelite, paraamphibolite etc.	20	55	340	40	35° 07′ 55.31″ N; 24° 38′ 34.88″ E	492
Mb044	Metapelite, micaschist	20	45	320	30	35° 08′ 03.94″ N; 24° 38′ 34.16″ E	475
Mb045	Metapelite marble	50	30	340	20	35° 08′ 14.47″ N; 24° 38′ 39.32″ E	448
Mb046	Metapelite marble	20	50	330	35	35° 08′ 16.94″ N; 24° 38′ 32.24″ E	427
Mb047	Metapelite, marble	50	35	330	10	35° 08′ 16.77″ N; 24° 38′ 17.78″ E	410
Mb048	Metapelite, marble	40	20	330	10	35° 08′ 24.59″ N; 24° 38′ 14.46″ E	413
Mb049	Paraamphibolite, marble	40	20	340	10	35° 07′ 44.07″ N; 24° 37′ 23.87″ E	433
Mb050	Paraamphibolite, marble	220	25	140	15	35° 07′ 42.91″ N; 24° 37′ 32.11″ E	464
Mb051	Metapelite	70	30	200	30	35° 07′ 39.28″ N; 24° 37′ 39.97″ E	463
Mb052	Metapelite	30	50	350	40	35° 07′ 37.87″ N; 24° 37′ 55.46″ E	500
Mb053	Serpentinite, orthogneiss	30	50	350	40	35° 07′ 39.88″ N; 24° 37′ 57.73″ E	515
Mb054	Paraamphibolite	290	20	330	10	35° 07′ 43.89″ N; 24° 37′ 55.26″ E	493
Mb055	Metasediments	60	20	140	15	35° 07′ 50.67″ N; 24° 37′ 45.30″ E	453
Mb056*	Plutonic rock					35° 07′ 35.93″ N; 24° 38′ 23.10″ E	726
Mb057*	Granitic dyke					35° 07′ 45.58″ N; 24° 38′ 11.48″ E	728
Mb058	Orthogneiss, marble	350	15			35° 07′ 47.91″ N; 24° 38′ 13.17″ E	716
Mb059	Orthogneiss, marble	030	40	340	30	35° 07′ 41.70″ N; 24° 38′ 11.84″ E	747
Mb060	Orthogneiss, marble					35° 07′ 37.17″ N; 24° 38′ 20.18″ E	740
Mb061	Metapelite	030	30	330	20	35° 07′ 39.72″ N; 24° 38′ 22.06″ E	763
Mb062	Metapelite, granitic dyke	010	40	330	25	35° 07′ 42.48″ N; 24° 38′ 29.90″ E	631

* One or more samples have been taken from these outcrops to the Goethe-Universität Frankfurt for further investigations thin section investigations.

Table B2.2 Summary of measurements on tapering quartz boudins within metapelite of the Asterousia Crystalline Complex west of Melambes and calculation of the aspect ratio.

Outcrop	Length	Width	Aspect ratio		
Mb027	3.6	1.5	2.4	35° 08′ 01.60″ N; 24° 37′ 07.86″ E	377
	1.3	0.4	3.3		
	3.7	1.0	3.7		
	3.5	1.7	2.1		
	14.0	2.8	5.0		
	11.2	2.4	4.7		
	2.0	0.6	3.3		
	3.5	0.8	4.4		
	3.7	1.0	3.7		
	4.0	1.3	3.1		
	4.0	1.7	2.4		
	3.5	1.0	3.5		
	2.7	1.2	2.3		
	5.3	1.5	3.5		
	6.0	2.8	2.1		
	11.5	3.5	3.3		
	7.2	2.2	3.3		
	6.2	2.0	3.1		
	8.0	1.5	5.3		
	10.8	2.4	4.5		
	3.8	0.7	5.4		
	4.8	1.4	3.4		
	3.2	1.0	3.2		
	1.5	0.5	3.0		
	2.9	0.6	4.8		
	2.1	1.0	2.1		
	3.6	1.2	3.0		
	16.3	4.7	3.5		
	2.3	0.5	4.6		
	6.3	1.7	3.7		
Mb032	7.7	2.1	3.7	35° 08′ 13.83″ N; 24° 36′ 57.85″ E	376
	1.5	0.8	1.9		
	5.4	2.1	2.6		
	4.9	1.5	3.3		
	6.3	2.6	2.4		
	6.0	0.9	6.7		
	4.1	1.4	2.9		
	3.6	0.8	4.5		
	1.6	0.4	4.0		
	3.0	1.4	2.1		
	5.5	1.4	3.9		
	5.1	1.9	2.7		
	2.0	1.0	2.0		
	1.6	0.5	3.2		
	10.5	2.6	4.0		
	13.6	3.1	4.4		
	7.8	2.8	2.8		
	6.6	2.0	3.3		
Mb044	9.5	3.9	2.4	35° 08′ 03.94″ N; 24° 38′ 34.16″ E	475
	16.1	4.2	3.8		
	11.1	3.6	3.1		
	8.0	2.8	2.9		
	8.4	3.0	2.8		
	3.8	1.4	2.7		
	1.0	0.5	2.0		
	7.7	2.5	3.1		
	3.8	1.1	3.5		
	10.2	3.9	2.6		
	4.6	1.2	3.8		
	6.8	1.9	3.6		
	3.5	1.2	2.9		
	2.3	0.7	3.3		
	6.0	3.4	1.8		
	4.3	1.6	2.7		
	2.2	0.6	3.7		
	4.2	1.0	4.2		
	2.8	0.7	4.0		
	2.6	1.1	2.4		
	3.4	0.9	3.8		
	4.7	1.9	2.5		
	2.8	1.3	2.2		

	8.2	3.8	2.2		
	9.9	3.1	3.2		
	2.9	0.6	4.8		
	11.2	2.7	4.1		
	7.7	1.5	5.1		
	6.5	3.6	1.8		
	5.7	1.9	3.0		
	57.2	15.2	3.8		
	13.9	4.9	2.8		
	7.0	3.6	1.9		
	2.5	0.6	4.2		
	7.6	3.0	2.5		
	9.5	2.4	4.0		
	4.7	2.0	2.4		
	5.9	2.1	2.8		
	3.2	0.9	3.6		
	2.0	0.7	2.9		
	2.4	0.8	3.0		
	3.6	1.4	2.6		
	7.7	1.2	6.4		
	2.6	1.3	2.0		
	7.8	2.7	2.9		
	6.8	3.2	2.1		
	3.5	0.8	4.4		
	9.8	2.7	3.6		
	6.5	2.0	3.3		
	2.2	0.9	2.4		
	3.4	1.0	3.4		
	2.9	0.9	3.2		
	12.2	5.3	2.3		
	6.3	1.9	3.3		
	3.4	1.1	3.1		
	4.0	1.1	3.6		
Mb048	8.6	3.0	2.9	35° 08′ 24.59″ N; 24° 38′ 14.46″ E	413
	3.0	1.6	1.9		
	5.2	1.6	3.3		
	4.2	1.7	2.5		
	4.0	2.1	1.9		
	1.6	0.7	2.3		
	8.6	2.1	4.1		
	7.1	2.2	3.2		
	7.8	2.3	3.4		
	6.2	1.8	3.4		
	11.8	4.4	2.7		
	5.5	1.9	2.9		
	3.6	1.2	3.0		
	8.1	2.4	3.4		
	6.5	2.6	2.5		
Mb027	3.6	1.5	2.4	35° 08′ 01.60″ N; 24° 37′ 07.86″ E	377
	1.3	0.4	3.3		
	3.7	1.0	3.7		
	3.5	1.7	2.1		
	14.0	2.8	5.0		
	11.2	2.4	4.7		
	2.0	0.6	3.3		
	3.5	0.8	4.4		
	3.7	1.0	3.7		
	4.0	1.3	3.1		
	4.0	1.7	2.4		
	3.5	1.0	3.5		
	2.7	1.2	2.3		
	5.3	1.5	3.5		
	6.0	2.8	2.1		
	11.5	3.5	3.3		
	7.2	2.2	3.3		
	6.2	2.0	3.1		
	8.0	1.5	5.3		
	10.8	2.4	4.5		
	3.8	0.7	5.4		
	4.8	1.4	3.4		
	3.2	1.0	3.2		
	1.5	0.5	3.0		
	2.9	0.6	4.8		
	2.1	1.0	2.1		
	3.6	1.2	3.0		

	16.3	4.7	3.5		
	2.3	0.5	4.6		
	6.3	1.7	3.7		
Mb032	7.7	2.1	3.7	35° 08′ 20.74″ N; 24° 37′ 04.90″ E	360
	1.5	0.8	1.9		
	5.4	2.1	2.6		
	4.9	1.5	3.3		
	6.3	2.6	2.4		
	6.0	0.9	6.7		
	4.1	1.4	2.9		
	3.6	0.8	4.5		
	1.6	0.4	4.0		
	3.0	1.4	2.1		
	5.5	1.4	3.9		
	5.1	1.9	2.7		
	2.0	1.0	2.0		
	1.6	0.5	3.2		
	10.5	2.6	4.0		
	13.6	3.1	4.4		
	7.8	2.8	2.8		
	6.6	2.0	3.3		
Mb044	9.5	3.9	2.4	35° 08′ 03.94″ N; 24° 38′ 34.16″ E	475
	16.1	4.2	3.8		
	11.1	3.6	3.1		
	8.0	2.8	2.9		
	8.4	3.0	2.8		
	3.8	1.4	2.7		
	1.0	0.5	2.0		
	7.7	2.5	3.1		
	3.8	1.1	3.5		
	10.2	3.9	2.6		
	4.6	1.2	3.8		
	6.8	1.9	3.6		
	3.5	1.2	2.9		
	2.3	0.7	3.3		
	6.0	3.4	1.8		
	4.3	1.6	2.7		
	2.2	0.6	3.7		
	4.2	1.0	4.2		
	2.8	0.7	4.0		
	2.6	1.1	2.4		
	3.4	0.9	3.8		
	4.7	1.9	2.5		
	2.8	1.3	2.2		
	8.2	3.8	2.2		
	9.9	3.1	3.2		
	2.9	0.6	4.8		
	11.2	2.7	4.1		
	7.7	1.5	5.1		
	6.5	3.6	1.8		
	5.7	1.9	3.0		
	57.2	15.2	3.8		
	13.9	4.9	2.8		
	7.0	3.6	1.9		
	2.5	0.6	4.2		
	7.6	3.0	2.5		
	9.5	2.4	4.0		
	4.7	2.0	2.4		
	5.9	2.1	2.8		
	3.2	0.9	3.6		
	2.0	0.7	2.9		
	2.4	0.8	3.0		
	3.6	1.4	2.6		
	7.7	1.2	6.4		
	2.6	1.3	2.0		
	7.8	2.7	2.9		
	6.8	3.2	2.1		
	3.5	0.8	4.4		
	9.8	2.7	3.6		
	6.5	2.0	3.3		
	2.2	0.9	2.4		
	3.4	1.0	3.4		
	2.9	0.9	3.2		
	12.2	5.3	2.3		
	6.3	1.9	3.3		

	3.4	1.1	3.1		
	4.0	1.1	3.6		
Mb048	8.6	3.0	2.9	35° 08′ 24.59″ N; 24° 38′ 14.46″ E	413
	3.0	1.6	1.9		
	5.2	1.6	3.3		
	4.2	1.7	2.5		
	4.0	2.1	1.9		
	1.6	0.7	2.3		
	8.6	2.1	4.1		
	7.1	2.2	3.2		
	7.8	2.3	3.4		
	6.2	1.8	3.4		
	11.8	4.4	2.7		
	5.5	1.9	2.9		
	3.6	1.2	3.0		
	8.1	2.4	3.4		
	6.5	2.6	2.5		

B3 Field data from the area of Pefkos, Kalamos and Sykologos

Table B3.1 Summary of data collected during fieldwork in the area of Pefkos, Kalami and Sykologos Viannos Municipality) south of the Dikti Mountains from the Pindos flysch, Arvi unit, Theodorii Greenschist and Asterousia Crystalline Complex.

Outcrop	Rock type(s)	Planes		Lines		Coordinates	Height [m]
		Strike	Dip	Trend	Plunge		
Pf001	Serpentinite	002	40	342	37	35° 01′ 26.03″ N; 25° 30′ 27.60″ E	587
		004	42	338	37		
Pf002*	Micaschist, chiastolite hornfels	142	35	225	25	35° 01′ 25.04″ N; 25° 30′ 29.66″ E	595
		138	30	220	20		
		140	34	224	24		
		140	25	228	30		
		150	30	212	14		
	Calcsilicate rock	180	25	158	15		
		150	68	212	14		
		144	34	230	26		
		142	36	236	25		
		144	36	228	25		
		198	50	158	34		
Pf003	Micaschist, chiastolite hornfels, paragneiss	236	25	240	18	35° 01′ 25.14″ N; 25° 30′ 27.51″ E	593
		240	25	240	24		
		230	20	238	20		
		236	28	240	20		
Pf004*	Serpentinite, micaschist, paragneiss	352	81			35° 01′ 25.38″ N; 25° 30′ 26.56″ E	592
		192	25	210	25		
		204	25	215	24		
		208	24	216	26		
		206	22	214	25		
Pf005	Micaschist, paragneiss?	210	26	192	18	35° 01′ 26.04″ N; 25° 30′ 37.31″ E	598
		214	24	200	22		
		212	25	196	20		
Pf006*	Marble, micaschist, paragneiss	296	16	320	15	35° 01′ 22.44″ N; 25° 29′ 53.70″ E	457
Pf007*	Calcsilicate rock	150	28	218	10	35° 01′ 21.68″ N; 25° 29′ 55.38″ E	449
		140	24	208	15		
		146	20	212	12		
		148	26	218	10		
		144	24	218	14		
	Marble			200	06		
	Quartzite			220	15		
Pf008	Chert, marble	016	32	336	28	35° 01′ 27.10″ N; 25° 29′ 53.89″ E	452
Pf009	Marble	226	35	182	40	35° 01′ 28.18″ N; 25° 29′ 53.98″ E	450
		224	32	180	36		
Pf010	Arvi slate	304	30	310	32	35° 01′ 37.31″ N; 25° 29′ 56.94″ E	449
		300	30	308	35		
		302	30	312	32		
		300	32	306	35		
Pf011*	Arvi slate	312	24	328	12	35° 01′ 36.31″ N; 25° 29′ 57.19″ E	448
		318	15	316	10		
		314	16	320	12		
Pf012	Arvi slate	278	20	294	05	35° 01′ 35.44″ N; 25° 29′ 59.22″ E	447
		288	15	300	10		
Pf013*	Basalt, Arvi slate	300	18	294	15	35° 01′ 38.65″ N; 25° 29′ 58.03″ E	461
		298	16	298	14		
Pf014	Arvi slate	118	20	124	18	35° 01′ 36.79″ N; 25° 30′ 00.72″ E	469
		116	18	120	20		
Pf015*	Arvi slate	118	20	110	28	35° 01′ 37.54″ N; 25° 30′ 00.31″ E	479
		114	22	114	24		
Pf016	Arvi slate	018	36	312	08	35° 01′ 39.64″ N; 25° 30′ 00.73″ E	490
		016	34	312	06		
		208	15	302	10		
		222	18	122	20		
		198	24	302	05		
		198	15	320	08		
		210	25	132	28		
		240	24	324	12		
		236	14	322	16		
Pf018	Arvi slate, basalt	120	20	118	22	35° 01′ 52.88″ N; 25° 30′ 01.34″ E	509
		118	14	112	10		
		122	18	104	14		
		182	24	106	06		
		112	22	116	26		
		160	22	118	15		
Pf019	Arvi slate	172	28	120	10	35° 01′ 38.04″ N; 25° 30′ 01.60″ E	477
		160	22	108	12		

		146	18	110	12		
Pf020*	Orthoamphibolite	138	06	132	05	35° 01′ 54.47″ N; 25° 28′ 55.08″ E	663
		124	15	140	14		
		136	14	128	10		
		118	02	134	05		
		130	04	126	04		
		124	02	136	02		
		126	16	138	14		
		160	24	130	14		
		132	20	132	15		
		112	12	128	10		
		124	10	130	08		
Pf021*	Orthoamphibolite	130	14	144	04	35° 01′ 52.08″ N; 25° 28′ 53.11″ E	657
		158	18	138	08		
		150	16	140	12		
		164	15	136	10		
		138	10	144	10		
		152	20	132	18		
		120	10	140	04		
		128	18	142	14		
		148	12	146	08		
		136	14	148	14		
		160	02	132	02		
Pf022	Orthoamphibolite	158	12	146	15	35° 01′ 50.29″ N; 25° 28′ 52.17″ E	677
		144	32	148	34		
		150	04	140	06		
		154	24	146	24		
		166	24	152	20		
		132	32	156	20		
		170	20	136	12		
		152	06	150	08		
		160	14	138	10		
		152	12	140	18		
		224	25	230	06		
		315	40	150	20		
Pf023	Orthoamphibolite	156	14	148	16	35° 01′ 47.65″ N; 25° 28′ 53.81″ E	642
		150	22	148	18		
		164	20	138	12		
		156	15	148	20		
		166	22	150	16		
		160	16	150	20		
		144	16	152	15		
		156	18	146	12		
		150	20	140	16		
		164	20	148	18		
Pf024	Orthoamphibolite, greenschist	302	40			35° 01′ 46.76″ N; 25° 28′ 54.63″ E	644
Pf025*	Micaschist	156	20	162	15	35° 01′ 24.21″ N; 25° 29′ 12.16″ E	608
		090	12	172	02		
		160	16	166	18		
		150	25	162	80		
		158	28	170	15		
		178	25	176	25		
		154	20	160	12		
		160	15	168	10		
		164	20	154	15		
Pf026	Arvi					35° 01′ 15.40″ N; 25° 29′ 04.58″ E	583
Pf027	Orthoamphibolite	094	20	154	24	35° 02′ 08.18″ N; 25° 28′ 35.12″ E	586
		096	30	156	14		
		082	35	152	12		
		082	22	156	04		
		096	28	160	12		
		076	32	154	10		
		088	22	142	12		
		078	10	140	12		
		072	06	134	04		
		084	14	148	12		
Pf028	Orthoamphibolite	146	04	158	06	35° 02′ 05.69″ N; 25° 28′ 36.59″ E	571
		112	08	162	06		
		120	10	154	08		
		098	24	156	06		
		118	18	152	12		
		112	08	162	04		
		96	15	154	05		
		108	12	158	02		
		106	10	154	06		

		112	04	156	04		
Pf029	Orthoamphibolite	110	10	158	02	35° 02′ 04.41″ N; 25° 28′ 32.76″ E	565
		098	04	150	02		
		102	02	156	02		
		100	05	152	02		
		128	06	150	06		
		120	08	156	10		
		112	04	148	02		
Pf030	Orthoamphibolite	138	28	156	15	35° 02′ 00.48″ N; 25° 28′ 27.00″ E	563
		140	20	150	16		
		108	22	160	10		
Pf031	Orthoamphibolite	140	10	148	06	35° 01′ 57.32″ N; 25° 28′ 23.76″ E	568
		136	06	152	02		
		146	06	154	06		
		138	02	154	08		
Pf032	Orthoamphibolite	166	22	146	06	35° 01′ 50.33″ N; 25° 28′ 13.70″ E	578
		172	20	138	16		
		176	25	138	20		
		166	24	148	12		
		170	22	138	24		
Pf033	Orthoamphibolite	108	22	138	04	35° 01′ 47.76″ N; 25° 28′ 14.72″ E	611
Pf034	Orthoamphibolite	102	14	152	12	35° 01′ 34.99″ N; 25° 28′ 05.47″ E	571
		100	12	148	12		
		152	16	140	15		
Pf035*	Orthoamphibolite	166	32	150	30	35° 01′ 30.87″ N; 25° 28′ 06.91″ E	572
		172	30	148	26		
		168	15	152	10		
		174	22	148	20		
		162	34	152	30		
Pf036*	Micaschist	310	14	12	04	35° 01′ 24.77″ N; 25° 27′ 53.10″ E	571
		312	12	08	04		
		304	18	08	14		
		306	20	02	10		
		290	14	06	04		
Pf037*	Marble	192	28			35° 01′ 46.25″ N; 25° 28′ 06.47″ E	612
Pf038*	Quartzite	192	48	258	38	35° 01′ 18.11″ N; 25° 30′ 47.18″ E	587
		230	34	214	30		
		212	30	218	32		
		224	35	222	25		
		232	26	260	15		
		240	30	230	32		
		186	28	218	04		
		238	30	242	28		
		012	14	042	06		
		212	24	230	20		
		222	18	220	12		
		234	20	220	18		
		244	38	242	36		
		182	04	212	02		
		240	30	232	30		
		332	42	044	26		
		248	14	238	12		
		222	16	232	12		
		236	30	240	26		
		208	14	220	15		
		196	36	208	34		
		208	38	232	30		
		222	35	228	28		
		222	30	218	20		
		234	26	230	20		
		210	48	206	42		
		230	30	232	30		
		232	28	240	30		
		240	36	242	32		
		262	40	240	36		
		248	15	138	10		
		188	42	122	02		
		282	40	318	30		
		304	14	340	14		
		274	24	302	26		
		320	16	316	16		
		120	10	134	26		
		108	06	120	06		
		300	08	304	10		
		184	16	130	04		

		132	20	152	14		
		172	12	142	05		
		180	20	302	20		
		298	40	314	32		
		292	32	310	30		
		310	08	306	08		
		304	12	306	14		
		320	06	308	02		
		316	14	338	14		
		284	28	314	16		
		330	10	320	10		
		142	04	138	02		
		320	16	318	15		
		265	28	304	18		
Pf039*	Quartzite	220	25	058	08	35° 01′ 08.90″ N; 25° 30′ 46.94″ E	571
		302	15	084	15		
		266	24	244	16		
		266	24	224	10		
		204	24	228	15		
		232	04	240	04		
		262	26	238	18		
		052	05	054	05		
		258	02	250	02		
		240	40	212	24		
		250	42	226	34		
		240	40	230	35		
		068	04	062	02		
		248	02	240	04		
		028	28	070	14		
		046	24	048	28		
		325	10	334	02		
		318	50	310	48		
		316	52	314	35		
		108	24	116	22		
		142	46	112	24		
		304	40	308	45		
		190	25	112	06		
		324	10	336	05		
		316	14	332	10		
		132	28	166	28		
		148	08	156	04		
		322	45	314	44		
		320	46	326	40		
		326	26	346	16		
		108	30	122	32		
		160	14	138	12		
		318	46	308	42		
		330	44	336	40		
		348	34	332	26		
		150	34	128	26		
		314	45	322	46		
		318	52	294	40		
	Pindos flysch	284	65				
Pf040*	Chiastolite hornfels	76	12	134	28	35° 01′ 09.40″ N; 25° 30′ 07.26″ E	411
		82	52	112	28		
Pf041	Arvi slate			140	50	35° 01′ 00.70″ N; 25° 29′ 19.28″ E	465
Pf042	Quarzite	246	16	294	08	35° 01′ 28.60″ N; 25° 30′ 16.50″ E	570
Pf043	Quarzite	168	52	124	26	35° 01′ 27.92″ N; 25° 30′ 14.10″ E	559
Pf044*	Chiastolite hornfels	252	40			35° 01′ 09.69″ N; 25° 30′ 08.88″ E	401
		220	35				
		232	40				
		224	30				
		208	30				
		230	28				
		226	30				
		230	38				
		210	42				
		218	42				
		208	58				
		210	34				
		220	30				
		224	34				
		228	34				
		208	26				
		208	22				

		212	40				
		218	36				
		194	45				
		252	40				
		212	25				
		208	24				
Pf045	Chiastolite hornfels					35° 01′ 07.80″ N; 25° 30′ 08.24″ E	396
Pf046	Metapelite, calcsilicate rock, marble	308	22	232	12	35° 01′ 08.99″ N; 25° 30′ 05.20″ E	392
		294	20	242	10		
		304	22	232	22		
		300	15	228	15		
		296	18	224	18		
		310	16	240	08		
		290	20	222	12		
		298	14	230	14		
		292	32	334	08		
		290	34	324	16		
		175	56	140	50		
Pf047	Metapelite, calcsilicate rock, marble					35° 01′ 10.55″ N; 25° 30′ 03.91″ E	412
Pf048*	Arvi slate	282	34	334	18	35° 02′ 36.60″ N; 25° 24′ 08.17″ E	514
		274	32	308	22		
		282	32	342	14		
		302	24	348	16		
		322	28	346	22		
Pf049	Arvi limestone					35° 02′ 22.62″ N; 25° 24′ 02.47″ E	511
Pf050*	Arvi slate	328	36	22	34	35° 02′ 12.77″ N; 25° 24′ 46.70″ E	581
Pf051	Serpentinite					35° 02′ 36.49″ N; 25° 25′ 02.16″ E	641
Pf052	Metapelite, calcsilicate rock, marble					35° 01′ 17.50″ N; 25° 31′ 08.63″ E	581
Pf053*	Metapelite	210	15	208	16	35° 01′ 27.63″ N; 25° 30′ 50.42″ E	612
		216	10	206	12		
		196	22	204	24		
		208	20	210	16		
		210	20	218	18		
		148	18	202	8		
		190	28	208	18		
		188	24	194	18		
		196	20	200	24		
		190	20	202	32		

* One or more samples have been taken from these outcrops to the Goethe-Universität Frankfurt for further investigations thin section investigations.